

Dissertation
submitted to the
Combined Faculty of Mathematics, Engineering and Natural Sciences
of Heidelberg University, Germany
for the degree of
Doctor of Natural Sciences

Put forward by M.Sc. Jannis Oliver Weimar

Born in Breisach, Germany

Oral examination: 21.07.2022

Advances in Cosmic-Ray Neutron Sensing

by

Monte Carlo simulations and neutron detector development

by

M.Sc. Jannis Oliver Weimar

supervised by

Prof. Dr. Ulrich Schmidt

Reviewers:

Prof. Dr. Ulrich Schmidt (Physikalische Institute, Heidelberg University)

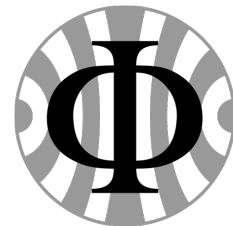
Prof. Dr. Werner Aeschbach (Institute of Environmental Physics, Heidelberg University)

Thesis Committee:

Prof. Dr. Matthias Bartelmann (Institute of Theoretical Astrophysics, Heidelberg University)

Prof. Dr. Lucas Menzel (Institute of Geography, Heidelberg University)

*Physikalisches Institut
Fakultät für Physik und Astronomie
Ruprecht-Karls-Universität
Heidelberg
Germany*



Defense: July 21st, 2022

Abstract

Epithermal cosmic-ray neutrons are widely used as a proxy for environmental hydrogen content for an area of up to 20 hectares, reaching maximum soil penetration depths of 80 cm. The present work deploys the multi-particle Monte Carlo code MCNP6 to simulate neutron production via cosmic-ray particles and their transport processes at the land-atmosphere interface. The simulation setup was validated against measured neutron flux attenuation in water, air and soil and shows an accurate reproduction of the data sets. This led to simulation-fitted analytical functions that are designed for soil moisture sensing below the soil surface and snow water equivalent monitoring via cosmic-ray neutron detectors. Additionally, the influence of a homogeneous snow cover on the intensity and transport dynamics of the airborne epithermal neutron flux was examined and approximated by analytical functions.

The limitations of standard cosmic-ray neutron detectors and the shortage of ^3He have led to a novel gaseous ^{10}B -lined neutron detector design specifically tailored to the needs of Cosmic-Ray Neutron Sensing. The system features high count rates as well as an adapted energy response, dedicated readout electronics and low pressure neutron counters, which results in low statistical and systematic errors of the epithermal neutron flux measurement. Two systems, stationary and mobile, proved to be able to capture soil moisture dynamics on the hectare and square kilometre scale.

Zusammenfassung

Epithermale, kosmische Neutronen werden erfolgreich dazu genutzt den Wasserstoffgehalt in einer Umgebung von bis zu 20 Hektar und einer maximalen Bodeneindringtiefe von 80 Zentimeter zu ermitteln. Die vorliegende Arbeit setzt den Mehr-Teilchen Monte-Carlo-Code MCNP6 ein, um die Neutronenproduktion, durch andere kosmische Strahlung, und ihre Transportprozesse an der Schnittstelle zwischen Boden und Atmosphäre zu simulieren. Der Simulationsaufbau wurde anhand gemessener Neutronenabschwächungslängen in Wasser, Luft und Boden validiert, was eine präzise Reproduktion der Datensätze ergab. Dies führte zu simulationsbasierten, analytischen Funktionen, die für Bodenfeuchtemessungen unterhalb der Bodenoberfläche und für Messungen des Schneewasseräquivalents einer Schneedecke mit Hilfe von Neutronendetektoren genutzt werden können. Zusätzlich wurde der Einfluss einer homogenen Schneedecke auf die Intensität und Transportdynamik des luftgetragenen epithermalen Neutronenflusses untersucht und durch analytische Funktionen genähert.

Die Limitationen bestehender Neutronendetektoren und der Mangel an ^3He haben zu einem neuartigen, ^{10}B basierten Neutronendetektor-Design geführt, das speziell auf die Bedürfnisse der Bodenfeuchtemessung anhand kosmischer Neutronen zugeschnitten ist. Das System zeichnet sich durch hohe Zählraten sowie einer angepassten Energieauflösung, dedizierten Ausleseelektronik und Niederdruck-Neutronenzähler aus, was zu geringen statistischen und systematischen Fehlern der epithermalen Neutronenflussmessung führt. Mit einer stationären und einer mobilen Ausführung dieses Detektortyps konnte die Bodenfeuchtedynamik auf der Hektar- und Quadratkilometerskala erfolgreich gemessen werden.

Contents

1	The context of this work	1	detectors	25
2	Background on cosmic-ray neutrons	3	3.1 Neutron converters	25
2.1	Neutron-matter interaction: units and parameter definitions	3	3.2 Interaction of charged particles with matter	26
2.1.1	The neutron	3	3.2.1 Heavy charged particles	26
2.1.2	Neutron energies	3	3.2.2 Electrons	27
2.1.3	Interaction types and cross section	4	3.3 Gas ionisation and gain	28
2.1.4	Neutron flux	6	3.3.1 Filling gas	28
2.1.5	Neutron transport equation	7	3.3.2 Charge amplification	30
2.2	Definition of environmental quantities	7	3.4 Ion drift and event time signature	30
2.3	The physics of secondary cosmic-ray neutron production and propagation	8	3.5 Solid neutron converters	31
2.3.1	Primary cosmic rays and cut-off rigidity	8	3.6 Gaseous proportional counter	32
2.3.2	Galactic cosmic-ray modulation by the sun	9	4 MCNP Model setup	35
2.3.3	Neutron monitor data base	10	4.1 Using Monte Carlo toolkits to describe environmental neutron transport	35
2.3.4	Generation of unbound neutrons within the Earth system	11	4.1.1 URANOS	35
2.3.5	Slowing down of evaporation and epithermal neutrons	14	4.1.2 MCNP	36
2.3.6	Thermal neutron interactions	16	4.1.3 Why MCNP?	36
2.4	Cosmic-Ray Neutron Sensing: Using epithermal neutrons as a proxy for ambient hydrogen content	17	4.1.4 Previous studies	36
2.4.1	The cosmic-ray neutron spectrum above the soil	17	4.2 Domain setup	37
2.4.2	Epithermal neutron intensity - soil moisture transfer function	18	4.3 Particle source terms	37
2.4.3	The standard cosmic-ray neutron probe	20	4.4 Other simulated particle species	39
2.4.4	Footprint of epithermal neutrons at the land-atmosphere interface	21	4.5 Transport description	39
2.4.5	Other parameters that influence the epithermal neutron intensity	23	4.6 Visualization of the domain setup and particle propagation	40
3	The physics of gaseous neutron		5 Neutron sources within the simulation domain	43
			5.1 Soil	43
			5.1.1 Elemental composition dependence	43
			5.1.2 Effect of the incoming particle distribution	45
			5.2 Atmosphere	48
			5.3 Water and snow	49
			5.4 Contribution of individual neutron source terms to the soil moisture signal	49
			5.4.1 Elemental composition dependence	49
			5.4.2 Particle species contribution to the soil moisture signal	51

6 MCNP model validation, calibration and application	53	7.2.5 Simple snow cover inhomogeneities	95
6.1 Atmospheric propagation: Neutron intensity above lakes and glaciers	53	7.2.6 Experimental evidence	97
6.1.1 Simulation setup	53	8 Concepts of developing dedicated cosmic-ray neutron detector systems	101
6.1.2 Glacier setup measurement and simulation comparison	54	8.1 The ^3He crisis as the onset for neutron detector development	101
6.1.3 Lake-side snap shots	56	8.2 Specific demands on neutron detectors in the context of Cosmic-Ray Neutron Sensing	102
6.2 Deep soil intrusion: Groundwater shaft soil moisture sensing	59	8.3 Neutron measurement uncertainty and its propagation onto the soil moisture retrieval	102
6.2.1 Intensity relation	61	8.4 Reducing statistical uncertainty: count rate enhancement	104
6.2.2 Footprint dynamics	63	8.5 Optimizing the moderator dimensions for an existing neutron counter	106
6.2.3 Comparison to field site measurement data	66	8.6 Improving the cosmic-ray neutron probe's signal-to-noise ratio	107
6.3 Below the water table: buried cosmic-ray sensors	69	8.6.1 Optimised energy resolution of the cosmic-ray neutron probe	107
6.3.1 Calibration of MCNP input parameters	70	8.6.2 False positive detections - Neutron counter efficiency to other types of radiation	110
6.3.2 SWE measurements by soil-buried neutron detectors	73	9 Large-scale boron-lined cosmic-ray neutron probes	111
6.3.3 Footprint dynamics	76	9.1 Description of the detection system	111
7 Neutron transport dynamics above snow-covered soil	81	9.2 Readout electronics	113
7.1 Neutron footprint dynamics above snow covers	83	9.2.1 Analog input stage and digitising unit	114
7.1.1 Footprint definition	83	9.2.2 Board design	116
7.1.2 Radial footprint as a function of SWE, air and soil moisture content	84	9.2.3 Pulse shape analysis	117
7.1.3 Radial footprint dimensions expressed in R_{86}	86	9.2.4 Potential of the two-dimensional pulse discrimination tool	120
7.1.4 Radial footprint as a function of detector height z_{eff}	87	9.3 Field data of a stationary probe	121
7.1.5 Neutron emission by snow and footprint comparison to snow-free footprint dynamics	88	9.4 Mobile measurement campaign	122
7.2 Snow cover influence on the above-ground neutron flux	89	10 Conclusion and Outlook	125
7.2.1 Neutron spectra above snow layers	89	A Bibliography	127
7.2.2 Detector-measured intensity as a function of soil moisture and snow cover	91	B Appendix	138
7.2.3 High-energy neutron intensity above the snow cover	94		
7.2.4 Intensity relation as a function of effective detector height	94		

B.1	Thermal neutron intensities 500 cm below the soil surface . . .	138	B.2.1	Detected neutron intensities above snow covered soil . . .	140
B.2	Fitting of neutron dynamics above snow covered soils. . . .	139	B.3	Neutron counter and copper foil	141
C Acknowledgements				142	

Comprehensive and accurate monitoring of water resources is crucial to understand and predict heat and water fluxes at the land-atmosphere interface. These influence, both, weather dynamics (Whan et al., 2015) and agricultural yield (Vergopolan et al., 2021). The soil is the most important storage of water resources at this interface and of key importance in the description of these fluxes. Hence, soil moisture was recognised an essential climate variable in the IPCC, 2014.

Soil moisture shows high spatial variability between the soil pore and regional scale and is influenced by many environmental parameters. The challenge remains to link all involved processes at different scales in order to understand soil moisture dynamics. A critical horizontal scale appears to be that of several ten to hundreds of hectares because it shows the highest variability in space and time (Crow et al., 2012). Moreover, typical horizontal correlation lengths range from few to several hundred meters (Western et al., 2004, and references therein). Additionally, measurement techniques that reach far into the soil are sought-after in order to accurately describe the hydrology of the complete vadose zone, which is in particular advantageous for agricultural use cases. Besides the importance of the spatial scale, temporal variability of soil moisture also covers a large range of scale lengths from hours to decades (Bogena et al., 2015). In the context of agriculture and micro-climate modelling it is most important on the hour-to-day scale.

Conventional soil moisture monitoring techniques range from local measurements with high temporal resolution to large scale satellite-based remote sensing methods with long measurement intervals. In between these spatial scales only few measurement techniques exist. While satellite-based instruments are developed to finer spatial resolution (e.g. the Sentinel mission), they still lack the ability of penetrating far into the soil (Fang et al., 2014). On the other hand, measurements at the local scale are usually not representative enough and, thus, not usable for upscaling to large-scale applications (Blöschl et al., 1995). Bogena et al., 2015 discussed potential measurement methods to close this spatial gap. Candidates reach from GNSS reflectometry, gamma ray intensity monitoring, ground based microwave radiometry, gravimetry and Cosmic-Ray Neutron Sensing (CRNS), see also Fig. 1.1. The latter combines all desired properties mentioned above. It monitors the above-ground cosmic-ray neutron flux, which inversely relates to the surrounding environmental hydrogen content. Ever since it has been first introduced by Zreda et al., 2008, it has gained a steady rise in soil moisture sensing applications due to the following reasons:

1. It features a large support volume: Averaging soil moisture over 10–20 hectares with penetration depths of up to 80 cm.
2. It is passive and non-invasive.
3. It works autarkic, usually combined with several other sensor powered by a solar panel with low maintenance.
4. Its signal only depends on the environmental hydrogen content independent on the state of matter.
5. It has a temporal resolution of few hours to minutes depending on the sensor type.
6. Mobile measurements can extend the spatial coverage up to areas of several 10 km².

Due to being sensitive to hydrogen in general, CRNS has also been successfully deployed as a snow cover sensing technique (Schattan et al., 2017; Schattan et al., 2019). The use case

1. The context of this work

of CRNS for snow monitoring is in particular beneficial in alpine regions due to the strong heterogeneity in snow cover. This heterogeneity is mainly induced indirectly by the topology, which in turn influences e.g. wind displacement, snow accumulation and melting by solar radiation.

Nevertheless, CRNS is a highly complex technique combining disciplines from geography, hydrology and neutron physics. There are still many open research questions since it is a comparatively new approach that has been tackled by a small community from 2008 till 2018. In 2018 the german branch of the community realised that the attempts of the individual disciplines needed to be coordinated in order to guarantee an efficient progress of the understanding of CRNS. The deutsche Forschungsgesellschaft (DFG) recognized this endeavour by funding the research unit (Forschergruppe) FOR 2694 Cosmic Sense¹. Cosmic Sense unites researchers from eight institutes in Germany that cover the disciplines of remote sensing, hydrological modeling and monitoring and neutron physics. It was granted a second phase for another three years of funding starting in 2022 with the University of Innsbruck, Austria as a new partner with focus on snow monitoring via CRNS.

This thesis was conducted in the framework of this research group with emphasis on deepening the understanding of the transport mechanisms of cosmic-ray neutrons and improving cosmic-ray neutron detectors. At the same time a strong focus was set on an interdisciplinary exchange including several combined efforts with researchers of the FOR 2694 and beyond. I spent one-and-a-half years in Innsbruck, where I tackled neutron dynamics above snow covers in close cooperation with Paul Schattan (alpS GmbH and University of Innsbruck).

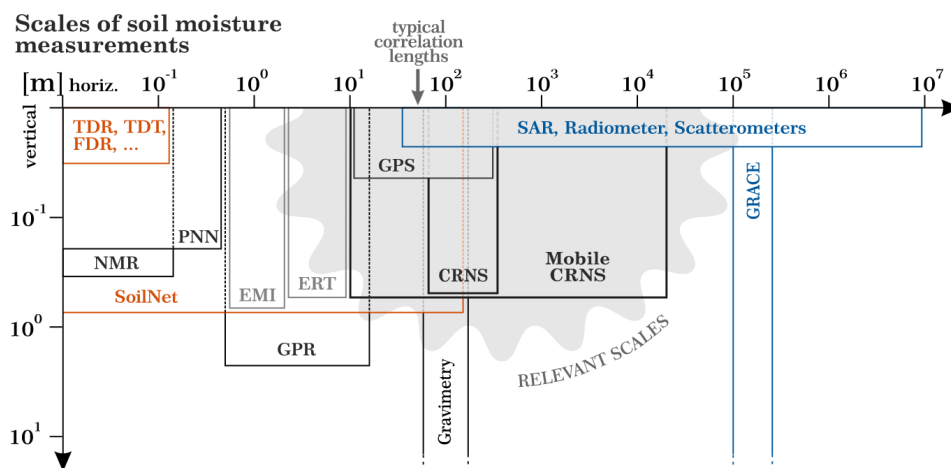


Figure 1.1: A summary of soil moisture sensing techniques and their respective measurement scales (taken from Schrön, 2016 with typical correlation lengths of soil moisture patterns according to Western et al., 2004). Invasive, non-invasive and remote-sensing techniques are colour-coded in brown, black and grey, respectively. Refer to Bogena et al., 2015 and Schrön, 2016 for a detailed description on the different methods.

¹<https://www.uni-potsdam.de/de/cosmicsense/about/overview>

2

Background on cosmic-ray neutrons

2.1 Neutron-matter interaction: units and parameter definitions

2.1.1 The neutron

Mass	1.00866491588 (5) u 939.5654133 (58) MeV/c ²
Spin	1/2 $h/2\pi$
mean lifetime	879.6 (8) s
magnetic moment μ_n	-1.91304273(45) μ_N

Table 2.1: Basic properties of the neutron according to Particle Data Group, 2020.

In 1932 James Chadwick was the first to propose the existence of a neutron (Chadwick, 1932). He also concluded that this neutral particle should be of similar mass than the proton from the kinetic energies of recoil protons released by neutrons. In fact, its mass is slightly higher than that of the proton by approximately one per mill. For this reason, free neutrons are able to decay via weak interaction into a proton, an electron and antineutrino



The neutron, a spin 1/2 fermion, features a small magnetic moment μ , thus indicating it has a charged substructure even though it does not hold a net charge. The magnetic interactions are about seven orders of magnitude weaker than the nuclear interactions for non-ferromagnetic materials. That is why, the neutron mostly interacts with the nuclei of atoms via the nuclear force. Therefore, neutrons exhibit distinguished interaction schemes with matter as most other particles prevalently interact with the electrons of the atoms. The neutron has a charge radius of roughly 1 fm.

2.1.2 Neutron energies

The neutron kinetic energy E primarily determines its interaction type with matter. In the context of this work, it is appropriate to restrict the energy classification to four regimes, that deviate from the typical naming, as is shown in Tab. 2.2. The energy classes are also linked to the neutrons velocity v and de Broglie wavelength λ_B , which are useful quantities to describe neutron interactions and transport mechanisms. Besides spallation neutrons the classifications are all in the non-relativistic regime described by

$$v = \frac{2E}{m}, \quad (2.2)$$

$$\lambda_B = \frac{h}{p}, \quad (2.3)$$

with m and p being the neutron rest mass and momentum and h the Planck constant.

2. Background on cosmic-ray neutrons

	thermal	epithermal	evaporation	spallation
Kinetic energy [eV]	10^{-3} – $3 \cdot 10^{-1}$	$3 \cdot 10^{-1}$ – $3 \cdot 10^4$	$3 \cdot 10^4$ – $2 \cdot 10^7$	$> 2 \cdot 10^7$
velocity [m/s]	440–7600	7600– $3 \cdot 10^6$	$3 \cdot 10^6$ – $6.2 \cdot 10^7$	$> 6.2 \cdot 10^7$
wavelength [Å]	9–0.5	0.5– $1.3 \cdot 10^{-3}$	$1.3 \cdot 10^{-3}$ – $6.4 \cdot 10^{-5}$	$< 6.4 \cdot 10^{-5}$

Table 2.2: Neutron energy classification adapted to the context of this work.

The temperature related naming of thermal neutrons refers to the fact, that these are in thermal equilibrium with the environment and can be described by a Maxwell-Boltzmann distribution:

$$f_E(E) = 2\sqrt{\frac{E}{\pi}} \left(\frac{1}{k_B T}\right)^{3/2} \text{Exp}\left(-\frac{E}{k_B T}\right). \quad (2.4)$$

The most probable energy E_{\max} obtained by a thermal neutron, is linked to the environmental temperature via $T = E_{\max}/k_B$, where k_B is the Boltzmann constant.

2.1.3 Interaction types and cross section

The neutron almost exclusively interacts via the nuclear force, which can be described via the exchange of a pion between nucleus and neutron. The resulting Yukawa potential of the nucleus is short ranged (few fm) due to the large rest mass of the pion ($\approx 140 \text{ MeV}/c^2$). Furthermore, above thermal energies the neutron's interaction time with the nucleus is short due to its short de Broglie wavelength. This leads to low interaction probabilities and neutrons can travel large distances through matter without interacting in it.

Two general types of interaction schemes can be distinguished: scattering and absorption. Neutron reactions are denoted by (n, X) , where n indicates the incident neutron and X the reaction product(s). Scattering is subdivided into direct elastic scattering, resonance elastic scattering, inelastic scattering and coherent scattering, where the latter is only significant in the thermal neutron energy regime. **Direct elastic scattering (n,n)** represents a neutron-nucleus collision wherein the neutron is deflected at the nucleus. It can be described by a hard sphere model and therefore resembles a classical billiard-type collision. During **inelastic reactions (n,n'+X)** the kinetic energy of the system is not conserved leading to an excitation of the target nucleus or emission of numerous inelastic reaction products, which mainly depends on the incoming neutron's energy. See section 2.3.4 for a detailed description on deep inelastic scattering spallation processes. **Resonance scattering (n,n/n')** occurs when the neutron's kinetic energy is such that absorption of the neutron in the nucleus produces a bound excited state, called compound nucleus. Thus, the incident neutron's energy has to coincide with an excitation state of the nucleus which leads to a distinct formation of resonance peaks. Resonance scattering can be both elastic, when the compound nucleus deexcites via releasing a neutron with the same energy as the incident neutron, or inelastic via the emission of a less energetic neutron and a gamma-ray.

During **absorption processes (n,X)** the neutron is captured by the target nucleus forming a compound nucleus. Its deexcitation is accompanied by the emission of particle(s) X . This process can be subdivided into neutral, photonic or charged branches with the emission of neutron(s), photon(s) or charged particles, respectively.

The interaction probability is defined by the **cross section** σ , which is sometimes specified as the sum of all elastic and absorption cross sections $\sigma_t = \sigma_s + \sigma_a$. The cross section takes the units of an area, which is usually specified in barn ($1 \text{ barn} = 10^{-24} \text{ cm}^2$). Fig. 2.1 depicts the

total cross section of the four most prevalent isotopes at the atmosphere-land interface as a function of energy. Three regions are identified: Thermal neutrons exhibit a long interaction time with the Yukawa potential, which increases their interaction probability. The interaction time scale can be estimated by the inverse of the neutron's de Broglie wavelength, which in turn leads to an inverse relation between cross section and neutron velocity v . Thus, this low energy regime is commonly referred to as the $1/v$ region. This region is subject to both elastic scattering and absorption, while the dominant interaction process depends on the target nucleus.

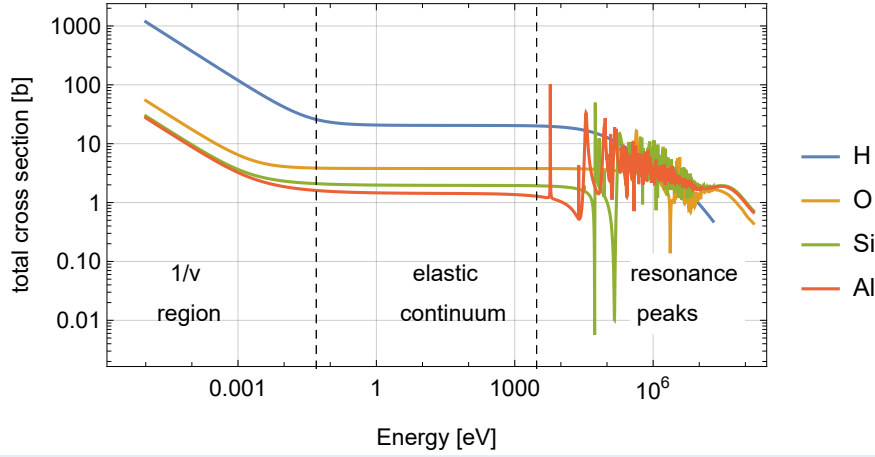


Figure 2.1: Comparison of energy-dependent total neutron cross sections σ_t of hydrogen (blue), oxygen (orange), silicon (green), and aluminum (red) for incident neutron energies between 10 meV and 150 MeV (except for hydrogen, which cross section is only tabulated up to 20 MeV). The data is taken from the ENDF-VIII nuclear data base (Brown et al., 2018). Three characteristic energy regions are marked that show different underlying physics.

For intermediate energies, the neutron-nucleus interaction shows a relative constant probability, which is dominated by elastic scattering. This continuum is overlaid by the resonance region described above. It is important to note that the number and location of the resonance peaks is a result of all possible excited states of the nucleus. This region shifts to lower energies the heavier the target nucleus.

The cross section also exhibits an angular dependence denoted as the differential cross section $\frac{d\sigma}{d\Omega}$ where Ω is the solid angle between the neutron's incident and scattered direction. The total cross section is then recovered by integrating $\frac{d\sigma}{d\Omega}$ over all angles

$$\sigma_t = \oint_{4\pi} \frac{d\sigma}{d\Omega} d\Omega. \quad (2.5)$$

Frequently, the cross section is translated to a **macroscopic cross section** defined as

$$\Sigma(E) = \sum_{i=1}^N n_i \sigma_{i,t}(E), \quad (2.6)$$

where n_i and $\sigma_{i,t}$ are the number density (n/cm^3) and the total cross section of the i -th isotope of a material consisting of N isotopes. The macroscopic cross section has the unit

2. Background on cosmic-ray neutrons

of an inverse length and can be considered as the probability that the neutron is scattered or absorbed in a path of 1 cm. It should be noted, that Σ is frequently defined independently for scattering and absorption $\Sigma_t = \Sigma_a + \Sigma_s$.

Following that, one can define the inverse quantity of Σ : the **mean free path** L , which describes the average distance covered by a particle traversing a target medium before interacting with it:

$$L(E) = \frac{1}{n\sigma_t(E)} = \frac{1}{\Sigma(E)}. \quad (2.7)$$

Above several 10 MeV the cross sections fall off and the mean free path of the neutron increases. When looking at the full ensemble of a particle beam traversing a medium, the **attenuation length** λ states the penetration depth into the medium where the beam's intensity I has dropped to $1/e$ of its initial intensity I_0 . Relating λ to the Beer-Lambert law one obtains the beam intensity at **depth** d :

$$I(d) = \text{Exp}(-d/\lambda). \quad (2.8)$$

The neutron beam attenuation depends on the medium's density ρ in g/cm^3 , i.e. the number of nuclei the neutrons pass. Thus, penetration depth (or simply depth) and attenuation length are usually denoted in units of g/cm^2 . These units facilitate the attenuation comparison of media with different density. The attenuation length can be specified for the entire particle beam but is frequently used to describe the intensity decay within an energy regime. This serves as a measure for the interaction processes at these energies.

2.1.4 Neutron flux

The scalar quantity neutron flux

$$\Phi(\vec{r}, E, t) = \bar{v}n(\vec{r}, E, t) \quad (2.9)$$

describes the number of neutrons n with energy E travelling through an area per time at a location \vec{r} [$\text{n cm}^{-2}\text{s}^{-1}$] with average velocity \bar{v} . The neutron energy spectrum at \vec{r} can be specified by two descriptions. Firstly, by a derivative of Φ

$$\phi'(\vec{r}, E) = \frac{d\Phi(\vec{r}, E)}{dE}. \quad (2.10)$$

However, most neutron-nucleus interactions lead to an energy transfer proportional to the initial energy of the neutron. On average this leads to a constant logarithmic energy loss, in particular in the epithermal and evaporation energy regime (see section 2.3.5). This mechanism suggests an energy weighting of the neutron spectrum as follows:

$$\phi(\vec{r}, E) = \frac{E d\Phi(\vec{r}, E)}{dE}. \quad (2.11)$$

This representation holds the benefit that equivalent values of ϕ per logarithmic energy decrement represent the same total particle flux. It therefore directly depicts the particle fluxes in a logarithmic energy plot, which is especially useful for a cosmic-ray neutron spectrum that

covers more than ten orders of magnitude in energy. Neutron spectra shown in this work, therefore, follow this representation.

2.1.5 Neutron transport equation

The neutron transport equation describes the balance of the neutron number $n(\vec{r}, \Omega, E)$ at the location \vec{r} in the volume element V , in flight direction of the solid angle Ω and with energy E in accordance to the Boltzmann transport equation. Four terms are identified that lead to a change in $n(\vec{r}, \Omega, E)$:

1. Generation of neutrons of this energy interval in the volume by a source $S(\vec{r}, \Omega, E)$,
2. Scattering into the volume from an initial solid angle Ω' or scattering into the energy range from an initial energy E' ,
3. Loss due to absorption or scattering out of the volume or energy range,
4. leakage out of the volume.

The neutron number, therefore, changes in time according to

$$\begin{aligned} \frac{dn(\vec{r}, \Omega, E)}{dt} = & S(\vec{r}, \Omega, E) \\ & + \int_{4\pi} \int_0^\infty \Sigma_s(\Omega' \rightarrow \Omega, E' \rightarrow E) v n(r, \Omega', E') d\Omega' dE' \\ & - (\Sigma_a(E) + \Sigma_s(E)) v n(\vec{r}, \Omega, E) \\ & - v \Omega \nabla n(\vec{r}, \Omega, E), \end{aligned} \quad (2.12)$$

where the four terms appear in the same order as in the list above. While, no exact general solution for the neutron transport equation exists, it can be solved in some particular cases. For example, the transport of monoenergetic neutrons in a purely scattering medium without energy loss can be reduced to a simple diffusion process, which can be used to describe the transport of thermal neutrons.

2.2 Definition of environmental quantities

Here a short list of environmental quantities, that are used frequently in this work, is presented:

1. The **volumetric soil moisture** θ describes the volume percentage covered by water in soil. It is either specified in units of cm^3/cm^3 or in Vol-%, which is used for this work.
2. **SWE [mm]** describes the equivalent amount of liquid water stored in the snow pack. It is the product of snow height and density and is commonly referred to in applications where the total water stored in snow covered areas is of major importance e.g. flood forecasting, water driven power plants and irrigation control.
3. The water mass per volume stored in air is described by the quantity **absolute humidity** h_{abs} [**g/m³**]. It can be inferred from the air temperature T in $^\circ\text{C}$ and relative humidity RH in %, which can be monitored with standard meteorological sensors, via

$$h_{\text{abs}} = \frac{RH \cdot e_s(t)}{R_{\text{H}_2\text{O}}(T+273.15)} = \begin{cases} \frac{RH \cdot 6.112 \text{Exp}\left(\frac{17.62T}{243.12+T}\right)}{R_{\text{H}_2\text{O}}(T+273.15)} & , \text{ above water} \\ \frac{RH \cdot 6.112 \text{Exp}\left(\frac{22.46T}{272.62+T}\right)}{R_{\text{H}_2\text{O}}(T+273.15)} & , \text{ above snow} \end{cases}$$

2. Background on cosmic-ray neutrons

with e_s being the saturated water vapour pressure [hPa] approximated using the Magnus formula above water and ice/snow surfaces (WMO, 2014).

4. The density of the dry soil matrix is denoted by the quantity **bulk density** $\rho_{b,r}$ commonly specified in the units of g/cm^3 .

2.3 The physics of secondary cosmic-ray neutron production and propagation

2.3.1 Primary cosmic rays and cut-off rigidity

A comprehensive treatment that goes beyond this brief overview on cosmic rays can be found in Blasi, 2013 and Ziegler, 1996. Primary cosmic rays are almost exclusively charged particles. Thus, they are subject to the Lorentz force when directed at the Earth inflicted by the its magnetic field. This results in an energy selection of the incoming cosmic-ray flux that depends on the magnetic field's inclination angle. The quantity, vertical cut-off rigidity $r_c(E)$ describes the minimum energy of an incident particle in order to pass the Earth's magnetic field and impinge on the atmosphere divided by its charge (Gerontidou et al., 2021). The Earth's magnetic field is well described by a dipole which is tilted by ≈ 10 degrees to its rotational axis. Thus, r_c is to first order a function of latitude that ranges between few hundred MV and 18 GV between the poles and the equator (see Fig. 2.2).

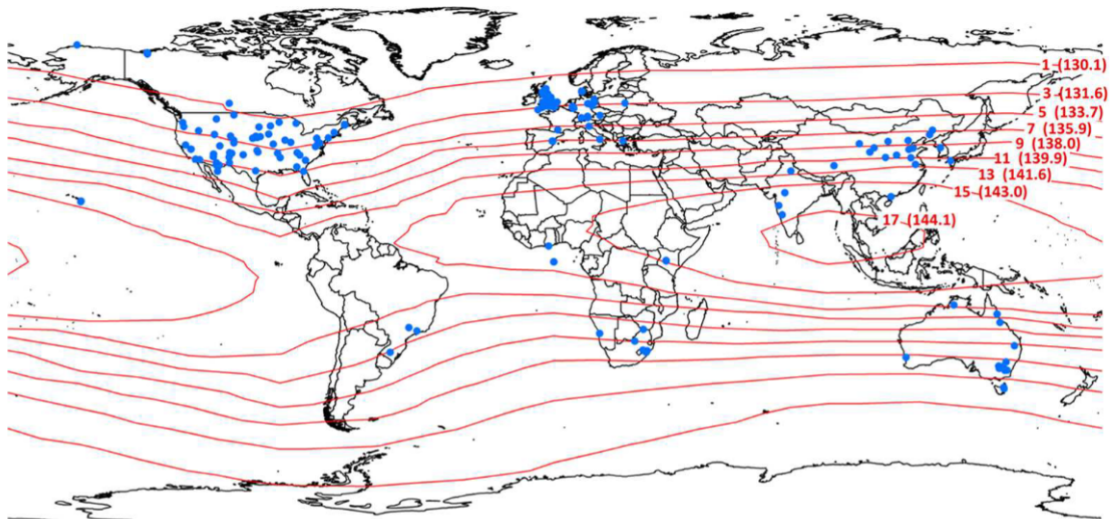


Figure 2.2: Vertical cut-off rigidities indicated by the red contour lines and given in GV. The values are calculated for the year 2010 based on Smart et al., 2004. Atmospheric neutron attenuation lengths are given in paranthesis based on Desilets et al., 2006. The blue points indicate cosmic-ray neutron stations. The figure is taken from Andreasen et al., 2017a.

Thereby, the solar wind, which makes up for most of the cosmic-ray flux density directed at the Earth is deflected and partly captured by the van Allen radiation belt because it features low energies peaking at several keV (Mewaldt, 2017). Cosmic-rays that overcome this shielding effect of the magnetic field are mostly of galactic origin with the majority being protons that make up $\approx 90\%$ of the total flux (see Fig. 2.3). Most studies point at supernovae remnants as the main acceleration source for these galactic cosmic rays (see e.g. Nikolić et al., 2013; Hillas, 2005; Bustamante et al., 2010). These feature shock regions with strong local magnetic gradients. Each time cosmic rays penetrate these highly magnetized domains they are accelerated in bursts. This process is called diffusive shock acceleration (for

a detailed description of the processes see Bykov et al., 2018). The acceleration continues until the particle reaches a high enough energy that leads to its escape from the shock region. However, Abramowski et al., 2016 argued that the super-massive black hole at the centre of our galaxy can accelerate protons to energies beyond those which can be achieved in the shock fronts of supernovae. Fig. 2.3 shows that the cosmic-ray spectrum peaks at ≈ 1 GeV and then decreases strongly following a power law of $E^{-2.7}$ for $E < 10^6$ GeV. This energy value is referred to as the knee and is believed to mark the separation point between galactic and extra-galactic cosmic rays, since no objects that are able to accelerate cosmic-rays to these energies can be found in our galaxy according to Hillas, 2005. Cosmic rays of extra galactic origin account for few particles per year and cm^2 . The majority of the cosmic-ray flux is, therefore, made up of particles in the GeV to TeV energy range.

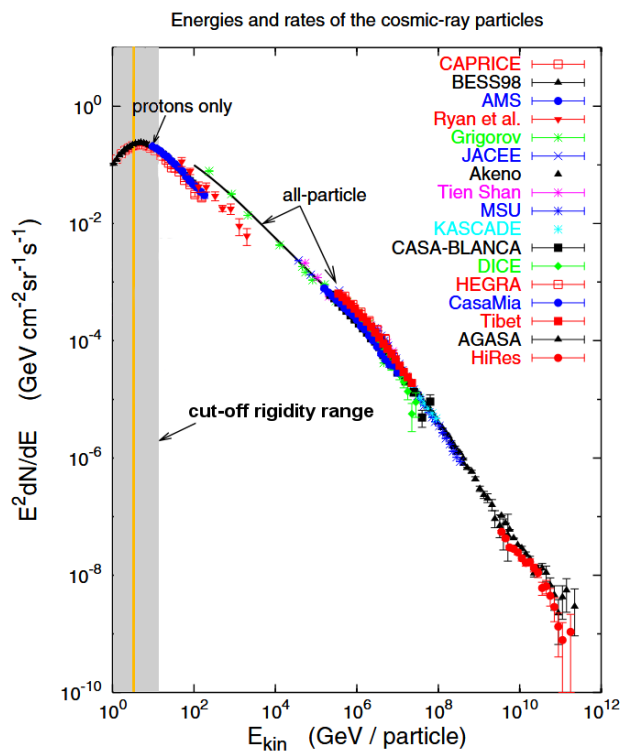


Figure 2.3: Energy spectrum of primary cosmic rays at the top of the atmosphere inferred from several experiments listed on the right (figure adapted from Gaisser, 2006). The grey shaded area indicates the range of vertical cut-off rigidities for a single-charged particle such as a proton for the Earth magnetic field, while the orange line denotes the vertical cut-off rigidity at Heidelberg, Germany.

2.3.2 Galactic cosmic-ray modulation by the sun

Cosmic rays are also deflected by the solar magnetic field leading to a modulation of their intensity according to solar activity. This effect shows a periodic regulation of the cosmic-ray flux that amounts to 20 % and in extreme cases 30 % signal change and consists of a manifold of frequencies (see Fig. 2.4). The most prominent are the 11-year and 22-year cycles which designate time periods of the oscillation of the solar magnetic field. A shorter cycle is caused by the sun's differential rotation which features a 27 day period (Dorman, 2004). Among these processes, corona mass ejections (CME) can lead to a strong increase in solar magnetic field strength that shields cosmic-rays and leads to a galactic cosmic-ray flux drop during few hours to days, called Forbush decreases (Cane, 2000). However, these CME's have been reported to lead to ground-level enhancements (GLE) in the cosmic-ray neutron flux occasionally (Moraal et al., 2012).

2.3.3 Neutron monitor data base

In the 1950s a neutron monitor network was established that provides real-time data on cosmic-ray flux variations¹ and covers a broad range of cut-off rigidity values. It deploys two types of lead covered neutron detectors (Krüger et al., 2008), that convert cosmic-ray nucleons with energies of several GeV into evaporation neutrons (see section below 2.3.4). These detectors are, therefore, suitable means to monitor changes in the galactic cosmic-ray flux. Fig. 2.4 shows data of the neutron monitor at Jungfraujoch, Switzerland, which has been used to account for changes in the incoming cosmic-ray flux for most cosmic-ray neutron studies located in the Alps or Southern Germany.

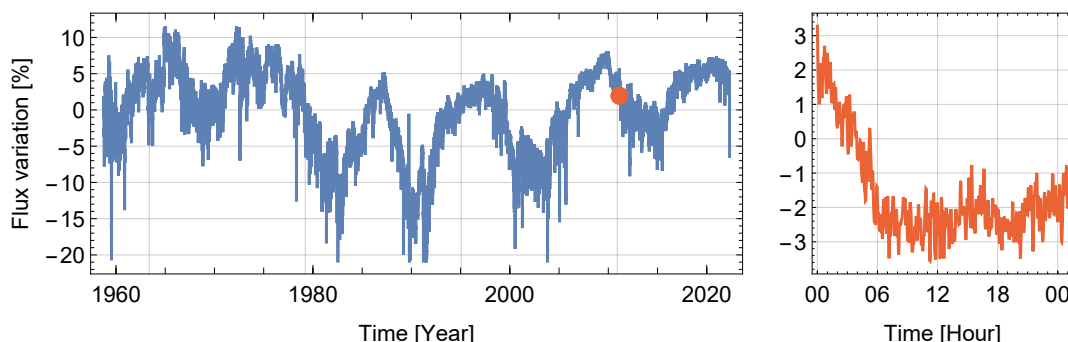


Figure 2.4: Signal changes in the high-energy cosmic-ray nucleon flux recorded at the Sphinx Observatory, Jungfraujoch, Switzerland. **Left:** Long term variations recorded since the deployment of the neutron monitor exhibit the dominant 11 and 22-year cycles. **Right:** Short-term nucleon flux drop due to a Forbush decrease during 18th of February, 2011.

¹<https://www.nmdb.eu/>

2.3.4 Generation of unbound neutrons within the Earth system

Secondary cosmic-ray neutrons are constantly produced when primary cosmic rays collide with nuclei in the atmosphere and soil below. The only effective channel to generate unbound neutrons is via releasing them from nuclei. Here several mechanisms can be distinguished. This chapter does not aim on a comprehensive description of all neutron production channels but rather focuses on a qualitative description of those relevant for the flux of secondary cosmic-ray neutrons at the land-atmosphere interface.

2.3.4.1 Neutron production in hadronic showers

For a more detailed description on hadron-nucleon interactions see e.g. Gandini et al., 1998; Ferrari, 2011. Among other processes mediated by the Coulomb force, highly energetic hadrons undergo inelastic nuclear collisions when hitting nuclei. The microscopic cross section approximately scales with $A^{2/3}$ leading to much more pronounced reaction rates with heavy nuclei. These processes lead to a forward directed emission of secondary particles, which in turn, if energetic enough, interact inelastically and produce further particles. This multiplication process that converts the incoming particles energy into particles ceases when their energy falls below the pion production threshold, which lies at approximately 300 MeV.

The transverse momentum of secondary particles stays almost constant throughout all energies leading to a narrowing of the emission angle with energy. It is important to note that within these cascades a large fraction of the incoming particle's energy is deposited via neutral pion production. These trigger electromagnetic showers, which feed only small amounts of energy back into hadronic production processes. Although one of those weaker channels, i.e. muon interactions, plays a key role in cosmic-ray neutron production (see section 2.3.4.2 below).

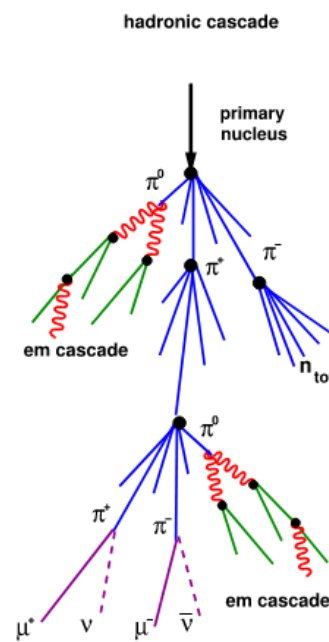


Figure 2.5: Schematic development of hadronic air showers. The black dots mark the target air nuclei while the blue, red and green lines represent hadrons, photons and leptons (figure is taken from Mollerach et al., 2018).

The intra-nuclear processes of these inelastic interactions are called spallation reactions ("to spall" is "to produce fragments"). They are usually described by a sequence of stages that occur at different time scales, according to Serber, 1947 who was the first to propose this scheme:

1. **Fast intra-nuclear cascade** (INC, see 1. in Fig. 2.6): If the incident particle's energy exceeds approximately 100 MeV, its de Broglie wavelength ($\lambda = h/\sqrt{2mE}$) falls below 1 fm. Thus, the particle does not interact with the whole nucleus but penetrates it while successively colliding with its nucleons on a time scale of $\approx 10^{-22}$ s. Depending on its energy, additional particles are created during this stage within the nucleus that are mainly pions and to a smaller extend kaons, further nucleons and heavier particles.

2. Background on cosmic-ray neutrons

This results in high-energy nucleons being ejected from the nucleus, as these are the target particles, and with minor yield the particles described above. The multiplicity of the emitted particles scales with the logarithm of the incoming particle's energy. The highly energetic emitted nucleons can combine to create heavier particles, which is called coalescence. This stage is directly followed by a pre-equilibrium phase during which the nucleus may break into two or more fragments and, thereby, releases further highly energetic particles.

2. **Slow deexcitation of the residual nucleus** (2. in Fig. 2.6): After the INC the compound residual nucleus remains in an excited and partly equilibrated state. Its deexcitation process is much slower than the INC (10^{-16} – 10^{-18} s) and is therefore decoupled of the previous excitation processes. During this stage the hot remnant nucleus isotropically emits lower energetic particles. This process resembles the release of droplets and is therefore called evaporation. Heavier nuclei with $Z > 64$ also experience fission that leads to further particle emission. However, fission is omitted in the context of this work since these elements are rare in the Earth system.

Neutrons are emitted during both stages with different energy emission spectra. The first process releases high-energy neutrons peaking at few 100 MeV up to several GeV (indicated by the neutron highlighted in red in Fig. 2.6). These neutrons are referred to as spallation neutrons in this work. The nucleus' excitation during the second stage amounts to several MeV/nucleon, just below their binding energy (Kowalczyk, 2007). The deexcitation results in the emission of neutrons with energies of typically few MeV, subsequently called evaporation neutrons (indicated by the neutron highlight in blue in Fig. 2.6). It is important to note, that the emission of neutrons is favoured over protons during these processes, in particular for heavy nuclei. That is because the target nucleus is rich in neutrons as compared to possible final states of the nucleus after these processes.

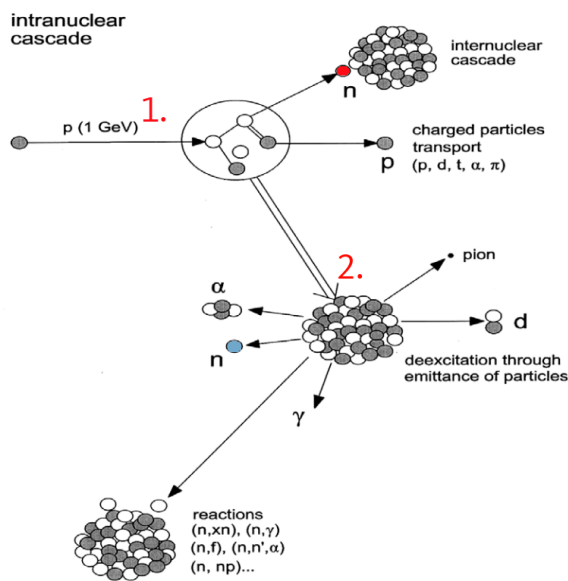


Figure 2.6: Simplified spallation reaction scheme triggered by an incident proton with $E = 1$ GeV adapted from Yasin et al., 2010. The figure excludes fission processes which occur for nuclei with $Z > 64$ and are therefore negligible for atmospheric cosmic-ray shower propagation. Spallation and evaporation neutrons are indicated in red and blue, respectively.

2.3.4.2 Muogenic neutrons

Cosmic-ray induced spallation almost exclusively takes place in the hadronic part of the particle cascades. However, neutrons can also be generated via muon-matter interactions described in more detail in Manukovsky et al., 2016a and Wang et al., 2001a. Muogenic neutron production plays a minor role in the Earth's atmosphere but becomes the dominant neutron source between a few meters to several 10 m below the soil surface (Esch, 2011). The dominant neutron generating channel by muons above soil depths of several ten meter is muon capture mediated by a W-boson and described by



where the second reaction refers to the radiative muon capture that also releases a gamma photon. This nuclear interaction results in a compound nucleus and subsequent emission of evaporation neutrons with low multiplicity.

2.3.4.3 Cosmic-ray fluxes in the atmosphere

The processes within hadronic and electromagnetic showers lead to a formation of particle fluxes as they penetrate through the atmosphere. Fig. 2.7 indicates how primary galactic cosmic-rays (protons, α particles and others) are attenuated by the atmospheric mass. Their attenuation leads to the production of secondary cosmic-rays inside the particle showers (neutrons, electrons, photons and muons; note that this list is not complete as many hadronic particles are produced to lesser extend in the cascades). In the upper layers of the atmosphere the flux of secondary cosmic rays increases to higher depth because the primary flux that sources the secondary flux is still large. Their intensity peaks at the Pfozter maximum (at (50–100) g/cm² atmospheric depth according to Pfozter, 1936, while Nesterenok, 2013 inferred a value of (30–150) g/cm²). Below that the particle loss due to the propagation through the atmospheric medium overcomes the source term and the neutron flux decreases (close to) exponentially by several orders of magnitude.

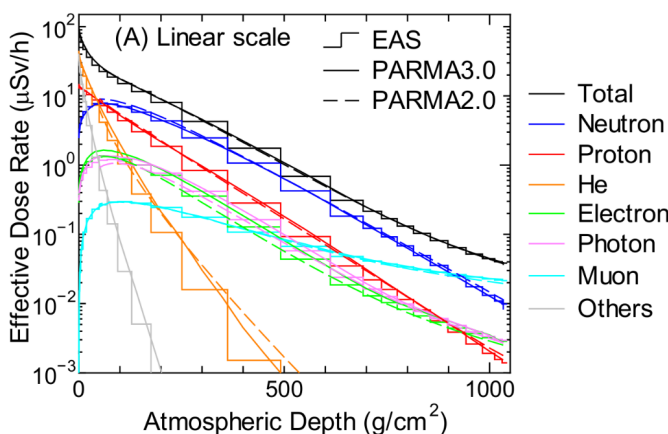


Figure 2.7: Cosmic-ray fluxes in the atmosphere as a function of atmospheric depth calculated using PARMA2.0/3.0 (solid lines) at $r_c = 0$ GV for various particles species (Sato, 2015). These spectra are used as source terms for the Monte Carlo simulations in this work (see chapter 4)

2.3.4.4 Cosmic-ray fluxes below the ground level

When the cosmic-ray particle fluxes impinge soil or water at ground level their intensity rapidly decreases due to the material density increase. Especially, the hadronic showers decrease strongly within the first 5 m causing a decline in total neutron flux of approximately two orders of magnitude. However, neutrons are still produced at large depths. The cosmic-ray

2. Background on cosmic-ray neutrons

muon flux reaches far into the ground where it induces further neutrons. At a certain depth, which strongly depends on the ground material, natural radioactivity becomes the dominant source of neutrons.

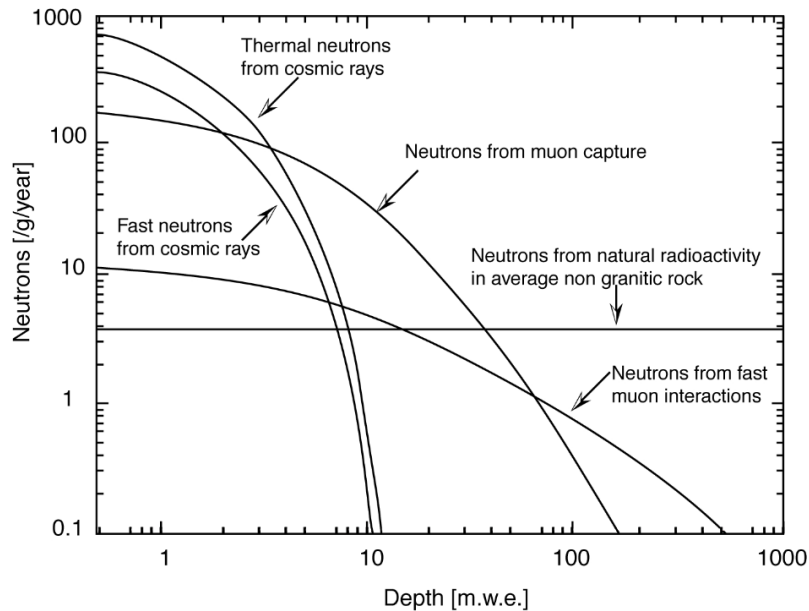


Figure 2.8: Sources of the neutron flux below the soil surface as a function of depth in mass water equivalent. Figure adapted from Esch, 2011

2.3.5 Slowing down of evaporation and epithermal neutrons

Evaporation and epithermal neutrons primarily scatter elastically when interacting with nuclei. Their energy is high enough to assume the target nucleus to be at rest. Thus, these scattering events lead to a constant slowing down of neutrons within this energy regime, called moderation. It is instructive to examine the properties of this moderation process in more detail since it is the underlying mechanism of Cosmic-Ray Neutron Sensing.

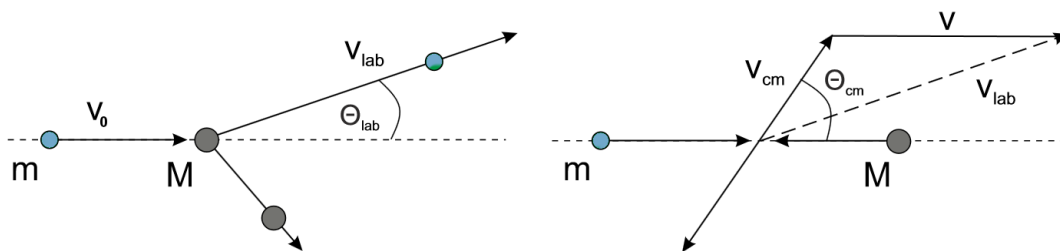


Figure 2.9: Elastic scattering of a neutron at a nucleus of mass M in the lab frame (left panel) and centre of mass frame (right panel). Adapted from Köhli, 2019.

The calculus can be treated non-relativistically at these energies and only s -wave scattering contributes to the scattered wave function, leading to an isotropic scattering function. The relative masses of the interaction partners are usually given in multiple of the neutron mass, i.e. $m=1$ and $M=A$ in Fig. 2.9. Transforming to the centre of mass frame the velocity of the neutron v_{cm} and the nucleus' velocity V become

$$v_{\text{cm}} = \frac{A}{A+1} v_0, \quad (2.15)$$

$$V = \frac{1}{A+1} v_0, \quad (2.16)$$

with v_0 being the incident neutron's velocity. The neutron's center of mass velocity retains after the collision while it is deflected by the angle Θ_{cm} . The neutrons velocity is transferred back into the lab frame by using the cosine law (see Fig. 2.9, right panel) and substituting Eq. 2.15 to obtain

$$(v_{\text{lab}})^2 = \left(\frac{A}{A+1}\right)^2 v_0^2 + \left(\frac{1}{A+1}\right)^2 v_0^2 - 2\frac{A}{(A+1)^2} v_0^2 \cos(\pi - \Theta_{\text{cm}}). \quad (2.17)$$

The relative kinetic energy change of the neutron then takes the form

$$\frac{E}{E_0} = \left(\frac{v_{\text{lab}}}{v_0}\right)^2 = \frac{A^2 + 1 + 2A\cos(\Theta_{\text{cm}})}{(A+1)^2}, \quad (2.18)$$

with $E_0 = \frac{1}{2}mv_0$. The energy of the scattered neutron is limited within the range

$$\left(\frac{A-1}{A+1}\right)^2 E_0 < E < E_0, \quad (2.19)$$

where the lower and upper limit correspond to $\cos(\Theta_{\text{cm}})$ equals -1 and 1. The average neutron energy loss strongly depends on the mass of the target nucleus and for neutron scattering at a hydrogen nucleus, i.e. $A=1$ and $m \approx M$, Eq. 2.19 transforms to

$$0 < E < E_0. \quad (2.20)$$

That means that the entire kinetic energy of the neutron is transferred to the nucleus in head-on neutron-proton collisions. Eq. 2.18 implies that neutrons loose energy via elastic scattering in fractions of their initial energy E_0 . This is expressed by the quantity lethargy

$$u = \ln \frac{E_0}{E}, \quad (2.21)$$

which describes the logarithmic energy loss for a single scattering event. Taking the isotropic scattering function into account the average lethargy, can be expressed by

$$\xi = \overline{u(\theta)} = \int \ln \frac{(A+1)^2}{A^2 + 1 + 2A\cos(\Theta_{\text{cm}})} \frac{d\cos(\Theta_{\text{cm}})}{2} = 1 + \frac{(A-1)^2}{2A} \ln \frac{A-1}{A+1}. \quad (2.22)$$

Furthermore, it is instructive to calculate the average number of neutron-nucleus collisions n_{mod} , needed to decelerate neutrons with energy E_0 to a certain final energy E_f . It is a function of ξ defined by

2. Background on cosmic-ray neutrons

$$n_{\text{mod}} = \frac{1}{\xi} \ln \frac{E_0}{E_f} = \frac{u}{\xi}, \quad (2.23)$$

and describes the moderation ability of a certain isotope. For a mixed-isotope material each average lethargy of the individual isotopes ξ_i must be weighted according to their elastic scattering cross section σ_i :

$$\overline{n_{\text{mod}}} = \ln \frac{E_0}{E_f} \left(\frac{\sum_i \sigma_i \xi_i}{\sum_i \sigma_i} \right)^{-1}. \quad (2.24)$$

Isotope	Mass [u]	ln energy loss ξ	n_{mod} (2 MeV \rightarrow 25 meV)
^1H	1	1	18
^{14}N	14	0.134	135
^{16}O	16	0.12	153
^{27}Al	27	0.0723	255
^{28}Si	28	0.0698	264

Table 2.3: Moderation power of most abundant elements at the land-atmosphere interface. The isotopes' mass is given in atomic mass. The isotope specific moderation ability is indicated by the average collision number n , which is needed to slow evaporation neutrons ($E = 2$ MeV) down to the thermal energy regime ($E = 25$ meV).

2.3.6 Thermal neutron interactions

The theory of thermal neutron scattering has been comprehensively illustrated by Squires, 1978 and Wirtz et al., 1964, while here only a brief outline of the topic is given. The simple scheme of elastic scattering as shown above loses its validity if the neutron reaches an energy comparable to

1. the kinetic energy of the target atom set by the temperature of the medium,
2. the molecular binding energies.

The first criterion refers to the assumption that the target nucleus cannot be considered at rest. This leads to a higher mean energy transfer and finally to the thermalisation of the neutron adopting the kinetic energy of the environment. At this stage no energy transfer occurs on average during neutron-nucleus scattering.

At thermal energies, neutrons probe the structure of the medium and are therefore sensitive to its degrees of freedom, e.g. vibration, rotation and translation excitation processes of the molecules (Kimura et al., 2020). This fact is quantized by a double differential cross-section for neutrons with incident energy E_i and final energy E_f defined as

$$\frac{d^2\sigma}{d\theta dE_f} = \frac{\sigma_b}{4\pi k_B T} \sqrt{\frac{E_f}{E_i}} S(\alpha, \beta, T), \quad (2.25)$$

where σ_b denotes the scattering cross section of the target nucleus bound in a specific molecule and k_B and T are the Boltzmann constant and temperature. The parameters α and β represent the dimensionless momentum and energy transfer of the scattering process. The term $S(\alpha, \beta, T)$ describes the scattering kernel for this specific isotope-molecular binding combination at a certain temperature. These kernels are used as tabulated matrices to

calculate neutron transport dynamics. The dependence on α and β expresses that some energy transitions are favoured above others depending on the initial energy of the neutron and the excitation states of the molecule.

Several isotopes show a significant deviation in total cross section between unbound or bound states at thermal energies. Hydrogen, for example, exhibits an unbound cross section of ≈ 30 b at $E = 25$ meV, which is increased in its bound state in polyethylene or light water by a factor of ≈ 2 and 4, respectively (Brown et al., 2018).

Additionally, thermal neutrons experience a significant absorption probability, which for some isotopes dominates over the scattering processes. Thus, the total thermal neutron intensity is largely determined by the ratio of Σ_s/Σ_a with respect to the medium.

2.4 Cosmic-Ray Neutron Sensing: Using epithermal neutrons as a proxy for ambient hydrogen content

2.4.1 The cosmic-ray neutron spectrum above the soil

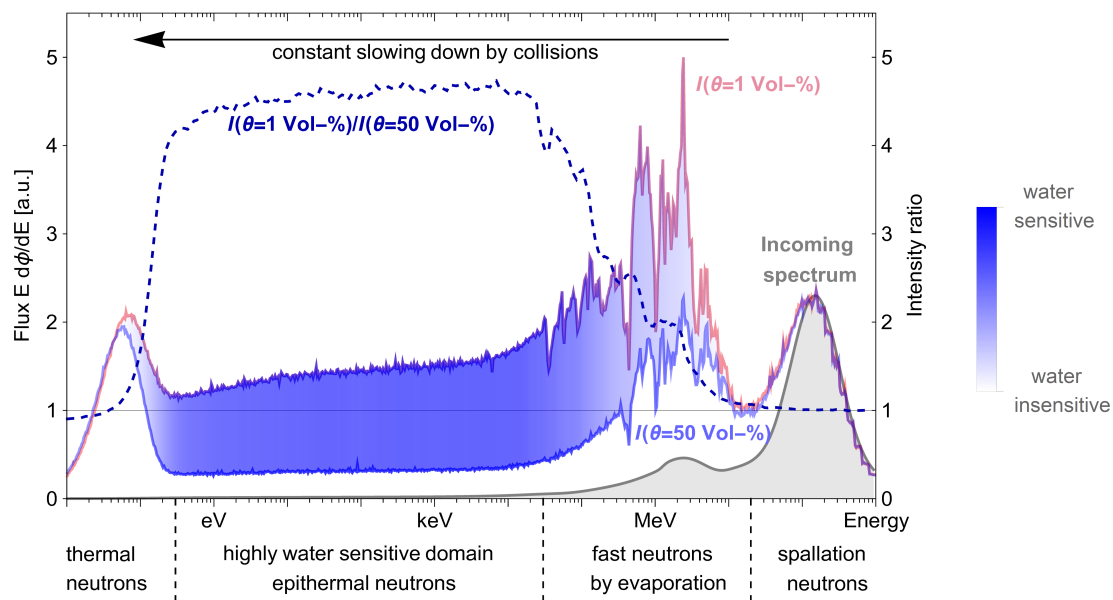


Figure 2.10: Simulated cosmic-ray neutron energy spectra using the Monte Carlo toolkit MCNP6 (Goorley et al., 2012). An evaluated input spectrum, according to Sato, 2015 (gray curve), is released in 450 m height and propagated towards the soil. Above-ground neutron intensities in 1.5 m height are shown for dry (light red) and moist conditions (light blue) referring to 1 Vol-% and 50 Vol-% volumetric soil moisture content, both at an air humidity of 1 g/m^3 . The intensity ratio between dry and moist soils (dashed blue curve and color-coded filling between the two spectra) reveals the hydrogen-sensitive domain. The figure is adapted from Weimar et al., 2020.

The cosmic-ray neutron spectrum above the land-atmosphere interface exhibits features according to the processes described above (see Fig. 2.10). The neutron production within the atmosphere leads to a spectrum indicated in grey that is directed at the interface. It is dominated by a characteristic high-energy peak of spallation neutrons that build up in the cosmic-ray showers and makes up three quarters of the spectrum. Evaporation neutrons compose another $\approx 20\%$ of the spectrum, while epithermal neutrons are scarce contributing

2. Background on cosmic-ray neutrons

a few percent of the total flux.

The soil likewise acts as a neutron source in analogy to the atmosphere. The neutron spectrum above the land-atmosphere interface is a result of the incoming neutron flux, neutrons produced in the soil and the neutron interaction processes at this interface domain (indicated by the red and blue curve in Fig. 2.10). The spallation neutron peak is mainly composed of the incident atmospheric spectrum because the high-energy flux produced in the soil is strongly collimated downwards. After evaporation, the neutrons experience a constant slowing down due to elastic scattering in the soil and air volume until they finally thermalise. Thermal neutrons commonly undergo several ten to hundred scattering events before being absorbed. That is because, typical elements at the land-atmosphere interface feature much lower absorption than scattering cross sections, which leads to a build up of a thermal peak. Both the evaporation and thermal regime confine the region most affected by ambient hydrogen between 300 meV and 30 keV.

2.4.2 Epithermal neutron intensity - soil moisture transfer function

Comparing neutron spectra above dry to wet soils reveals a strong intensity decline with soil moisture increase which is most apparent in the epithermal energy regime (indicated by the dashed blue line in Fig. 2.10). This strong relation between epithermal neutrons and ambient hydrogen content is determined by three factors:

1. The extraordinary high moderation power of hydrogen in the elastic scattering regime due to (nearly) the same mass of neutron and proton.
2. The high scattering probability for neutrons at hydrogen nuclei as compared to other isotopes abundant at the land-atmosphere interface (indicated in Fig. 2.1).
3. The large change in number density n of hydrogen between dry and wet conditions directly translates into a substantial variation in macroscopic cross section Σ of the soil.

Thus, the ambient hydrogen moderation decelerates epithermal and evaporation neutrons leading to their thermalisation and an intensity decrease in the respective energy regimes. For common conditions of the land-atmosphere interface, most hydrogen is bound in water in the soil leading to a strong correlation between the soil's water content and the albedo epithermal neutron intensity.

Evaporation neutrons are equally sensitive to hydrogen content as epithermal neutrons, because the elastic scattering processes dominate these energies as well. However, a large fraction of evaporation neutrons are produced in the atmosphere and in the soil, leaving the soil without interacting in it. These neutrons have not been in contact with the soil and were not influenced by its moisture content which results in a large soil moisture independent offset. Thermal neutrons show a more complex response to soil moisture. For wet conditions the soil efficiently slows down neutrons transferring epithermal neutrons to the thermal energy regime, however, the epithermal neutron density is low. For dry conditions the much higher epithermal intensity competes with the poor moderation capability of the soil in absence of hydrogen. Both conditions show a similar thermal neutron flux above the soil. Between 5 and 10 Vol-% soil moisture content a thermal intensity maximum arises for sufficiently high epithermal neutron flux and average moderation power.

Referring to Tab. 2.3, it is important to remark that hydrogen dominates the total ambient moderation power even at few Vol-% soil moisture content (for a more detailed description see Zreda et al., 2012). Assuming that the epithermal neutron flux Φ_{epi} is proportional to the moderation power of dry soil added by a fraction w of water (the air is neglected due to

its low density) one yields by using Eq. 2.24

$$\Phi_{\text{epi}} \propto n_{\text{mod,soil}} \propto u \frac{\Sigma_s + w\Sigma_w}{\Sigma_s \xi_s + w\Sigma_w \xi_w}, \quad (2.26)$$

where $n_{\text{mod,soil}}$ is the average collision number needed to thermalise evaporation neutrons indicated by Tab. 2.3, Σ_s and Σ_w the macroscopic cross sections of dry soil and water and u and ξ lethargy and average lethargy. Tab. 2.3 shows that $\xi_w = 1$ and $\xi_s \approx 0.1$, which results in a hyperbolic relationship between epithermal neutron intensity N above the soil and its water content. Desilets et al., 2010 and Bogena et al., 2013 identified that concept and proposed a simple transfer function

$$\theta(N) = \rho_{b,r} \left(\frac{a_0}{N/N_0 - a_1} - a_2 \right), \quad (2.27)$$

with θ being the volumetric soil moisture, $\rho_{b,r}$ the soil's bulk density and N refers to the neutron count rate of an epithermal neutron detector. Desilets et al., 2010 deduced the parameter set $(a_1, a_2, a_3) = (0.0808, 0.372, 0.115)$ semi-empirically and N_0 is the count rate at $\theta = 1.4$ Vol-%. The parameter N_0 is site and neutron detector specific and demands for a single calibration measurement (Schrön et al., 2017). However, several studies concluded that individual site conditions could not be fully captured by N_0 and inferred adapted parameter sets a_i for their specific sites (see e.g. Heidbüchel et al., 2016; Iwema et al., 2015; Rivera Villarreyes et al., 2011). Recently, Köhli et al., 2021 revised the transfer function by a combination of the two Monte Carlo tool kits MCNP and URANOS². They combined the influence of the soil moisture and atmospheric water content in one equation. The hitherto used approach corrected for the influence of atmospheric humidity using a linear function, independent of the soil's moisture content according to Rosolem et al., 2013. Köhli et al., 2021 argued that for dry soil conditions the influence of air humidity is larger than for wet soils and proposed the *universal transport solution (UTS)*

$$N(\theta, h) = N_D \left(\frac{p_1 + p_2 \theta}{p_1 + \theta} (p_0 + p_6 h + p_7 h^2) + \text{Exp}(-p_3 \theta) (p_4 + p_5 h) \right), \quad (2.28)$$

with N_D being the new calibration constant. The effect of atmospheric water content is twofold. It pre-moderates the incoming atmospheric neutron flux and furthermore it also slows down the albedo epithermal and evaporation neutron flux. Köhli et al., 2021 were able to show that the soil moisture retrieval can be improved significantly at dry soil conditions. For wet soils this approach and the hitherto-used standard show similar results. The technique that uses above-soil epithermal neutrons as a proxy for environmental hydrogen content is called Cosmic-Ray Neutron Sensing (CRNS).

²The author of this work contributed as second author to the realization of this article by conducting the MCNP Monte Carlo simulations. Since, the topic was comprehensively treated and no new findings have been acquired ever since the publication, the author decided to not include these findings to this work.

2.4.3 The standard cosmic-ray neutron probe



Figure 2.11: Field measurements during a joint-field campaign of the Cosmic Sense research unit from May to July, 2019 in Fendt, Bavaria, Germany (picture is taken from the article on this field campaign Fersch et al., 2020). A roving unit, used for mobile measurements, is placed on a hand wagon on the left. In the middle, one of 24 stationary cosmic-ray neutron probes deployed during this campaign is positioned. The two white tubes are neutron detectors. The scaffolding on the right holds a third sensors that was used to intercalibrate the 24 probes.

Cosmic-ray neutron probes (CRNP) are designed to measure the albedo epithermal neutron flux. They are usually mounted on a pole 1.5 m above the soil surface (see Fig. 2.11). The system works autarkic by using a solar panel that powers the electronics used to read out and process the recorded data (see chapter 9 for a more detailed description on the setup of such systems). Neutron detectors used in the context of CRNS exclusively rely on neutron absorption processes to detect the neutron indirectly (see section 3.1). However, neutron absorption is only efficient in the thermal energy regime.

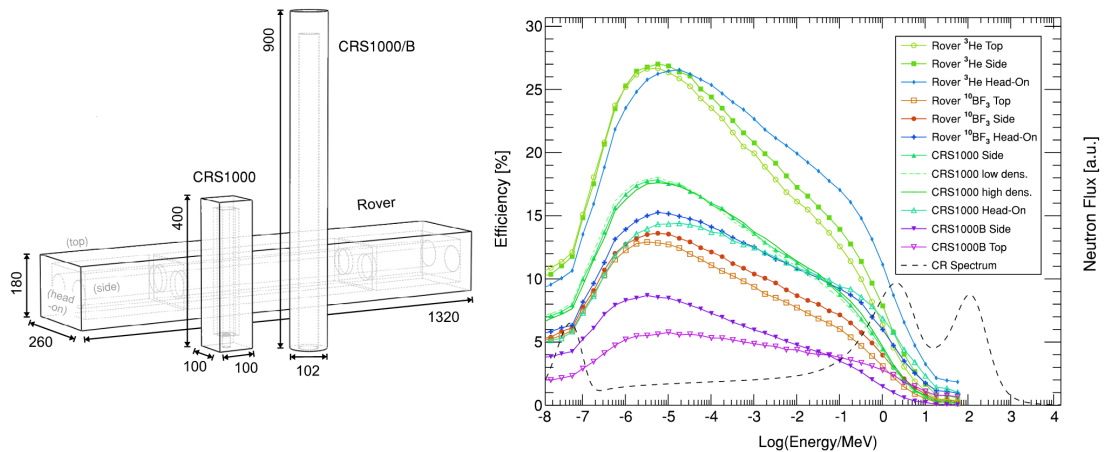


Figure 2.12: Cosmic-ray neutron probes (CRNP) and their response functions (both figures are taken from Köhli et al., 2018a). **Left:** Schematic setup of a selection of CRNPs. The dashed profiles indicate the thermal neutron detector, which is surrounded by a polyethylene moderator indicated by the solid shapes. The rover unit consists of two thermal neutron detectors. **Right:** Detector response functions of the models in the left panel irradiated with neutrons from the side (large surface) and top.

Thus, epithermal neutrons are shifted to thermal energies by using a hydrogen-rich material as moderator, which encloses the thermal neutron counter from all sides. The effective energy resolution of the thermal detector-moderator combination is primarily determined by the moderator's hydrogen content per area, i.e. its thickness. Standard CRNPs consist

of a cylindrical neutron counter inside a 25 mm thick polyethylene moderator housing (see Fig. 2.12 left). It is important to realize, that the moderation process is of probabilistic nature. Some neutrons that hit the moderator casing are reflected back into the air, some scatter few times until reaching the neutron detector, others undergo more than a hundred collisions before entering the inside of the moderator casing. This leads to a broad energy sensitivity of the CRNP, called the detector response function (DRF). The DRF denoted as $R(E, \phi)$ describes the probability to detect a neutron with energy E that hits the moderator casing in the angle ϕ to the moderator surface normal (Köhli et al., 2018a). It can be separated into two terms that describe the angular and energy dependence independently. Several $R(E)$ are depicted in Fig. 2.12 that all combine thermal counters with 25 mm moderator shielding (with ϕ equals 0). They feature similar shape for differently sized systems indicating that the geometry of the detector has a minor effect. The CRNP is most sensitive in the epithermal energy regime but shows significant contamination of evaporation and in particular thermal neutrons, which is discussed in chapter 8.

2.4.4 Footprint of epithermal neutrons at the land-atmosphere interface

The footprint is defined as the spatial distribution of the signal contribution. In the case of CRNS, the footprint $F(\vec{r})$ describes the influence of a soil moisture pattern located at point \vec{r} on the detected epithermal neutron flux at location $\vec{r} = \vec{0}$. It results from the transport processes of epithermal neutrons at the land-atmosphere interface. These scatter isotropically and can switch between the soil and the atmosphere compartment several times before being thermalised (Köhli et al., 2015). Epithermal neutrons cover much larger distances in the air than in soil because it is less dense by a factor of ≈ 1000 . Therefore is instructive to look at the neutron transport in air in order to determine their range that directly relates to the footprint. The integral version of the transport equation Eq. 2.12 can be solved for a point source, which radiates neutrons isotropically, in an infinite medium. If isotropic scattering is assumed, the system is spherically symmetric and the neutron flux can be reduced to a radial flux (see for a comprehensive derivation Wirtz et al., 1964 and references therein)

$$\Phi(r) = S \frac{\text{Exp}(-\Sigma_t r)}{4\pi r^2} + \int_{r'} \Sigma_s \Phi(r') \frac{\text{Exp}(-\Sigma_t |r - r'|)}{4\pi (|r - r'|)^2} dV', \quad (2.29)$$

$$= \Phi_{\text{geometric}}(r) + \Phi_{\text{diffusive}}(r). \quad (2.30)$$

The first term describes a geometric transport of neutrons from the source with strength S to a sphere's surface with radius r in straight lines without any interaction in the medium. The attenuation length of this direct transport is the inverse of the macroscopic cross section of the medium, which is the mean free path of the neutrons. This term only contributes to the flux in the close vicinity of the point source. A diffusive-type transport is described by the second term, which takes the asymptotic solution (Glasstone et al., 1952)

$$\Phi_{\text{diffusive}}(r) \approx \frac{\text{Exp}(-r/L_d)}{r}, \quad (2.31)$$

in the limit of large distances r . The parameter L_d is the diffusion length of the medium, which is characterised by the ratio Σ_s/Σ_a . For $\Sigma_s \gg \Sigma_a$ it takes the form

$$L = \sqrt{3\Sigma_a \Sigma_t}, \quad (2.32)$$

2. Background on cosmic-ray neutrons

but for strongly absorbing media the asymptotic solution is never reached. That is because the neutrons are absorbed before being able to travel large distances. The epithermal neutron transport in air may be visualised by Eq. 2.30, as epithermal neutrons scatter isotropically and air shows small absorption capability. The soil surface can then be assumed to act as an ensemble of point sources for neutrons by evaporation or scattering into a certain energy range, while emitting these neutrons into the air. These are the neutrons of interest as they probed the soil. Placing a detector above this soil surface, one would infer a similar transport scheme: a direct short-ranged transport of neutrons from the soil surface to the detector in addition to a diffusive-type mechanism that transports neutrons over large distances.

Indeed, the footprint function inferred by Köhli et al., 2015 shows these two characteristic transport regimes (see Fig. 2.13, left panel). Although, the picture drawn above can visualize and motivate a rough radial footprint distribution, it is oversimplified because neutrons traverse the atmosphere-soil interface several times. Hence, much of the transport occurs at the interface and in both media for which no exact solution can be calculated. Furthermore, inhomogeneous source distribution terms in soil and air, as well as the energy dependent cross sections lead to a complicated transport description.

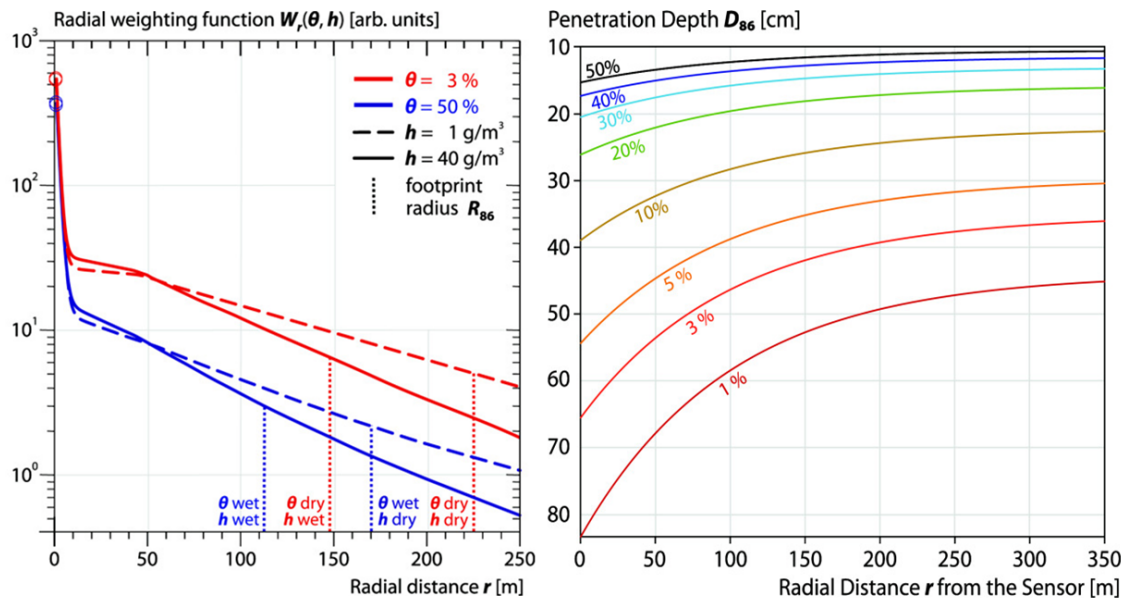


Figure 2.13: Footprint dynamics of epithermal neutrons at the soil-atmosphere interface. **Left:** Radial weighting functions as detected neutron intensity over distance between detection and origin in the soil of epithermal neutrons for dry and wet conditions. The dotted lines denote the R_{86} quantiles. **Right:** The vertical penetration depth, described by the 86 % quantile of the vertical signal contribution D_{86} , as a function of radial distance r is shown for several soil moisture values.

Therefore, Köhli et al., 2015 analysed the CRNP's footprint by means of probabilistic Monte Carlo simulations above wet soils assuming homogeneous conditions in both soil and air volume (see chapter 4 on Monte Carlo codes). They fitted their simulation results which lead to analytical functions that describe the radial weighting of soil moisture patterns at a distance r from the detector. These functions are comprised of a sum of equations that resemble Eq. 2.30. Moreover, they were able to show that the moderation ability of ambient hydrogen strongly influences the range of epithermal neutrons and thereby the footprint. The atmospheric moisture content almost exclusively affects the long term transport, while

soil moisture controls the whole transport regime. They also reduced the radial weighting function to a single distance R_{86} that covers 86 % of all signal contributions. This 86 % quantile refers to a two e-fold decline in signal contribution. It has been regarded as the single quantity that describes the radius of the CRNP support volume, ever since Desilets et al., 2013 introduced CRNP footprint estimations for the first time. The values of R_{86} range between 120 and 230 m for moist and dry conditions at 1013 hPa, corresponding to an area of approximately 5 and 17 ha. Atmospheric pressure also strongly influences the footprint as it directly relates to the mean free path of the neutrons. This can be treated by a scaling factor in order to rescale R_{86} to a given pressure by:

$$f_p = \frac{0.5}{0.8647 - \text{Exp}\left(-\frac{p}{p_0}\right)}. \quad (2.33)$$

This correction factor is applied linearly and R_{86} becomes:

$$R_{86}(p) = f_p \cdot R_{86}(p_0). \quad (2.34)$$

The effective penetration depth of epithermal neutrons into the soil also strongly depends on its moisture content and is a function of radius (indicated by Fig. 2.13, right panel). It is defined in analogy to the horizontal transport as the quantile D_{86} that covers 86 % of the vertical signal contribution. It is on the order of few 10 cm and therefore covers the root zone of a multitude of plants, in particular during dry conditions. The large horizontal and vertical footprint of epithermal neutrons represents the key advantage of Cosmic-Ray Neutron Sensing over other techniques for some hydrological topics.

2.4.5 Other parameters that influence the epithermal neutron intensity

Besides the ambient hydrogen content several other parameters control the epithermal neutron flux N_{raw} . Correction functions are the standard approach to account for these influences by

$$N_{\text{cor}} = N_{\text{raw}} \cdot f_p \cdot f_i, \quad (2.35)$$

with f_p being the pressure correction and f_i the incoming correction factor. The corrected count rate N_{cor} is then applied to Eq. 2.28 to retrieve the soil moisture.

The neutron monitor data base records variations in the high-energy nucleon flux that is believed to directly relate to the flux of incoming galactic cosmic-ray (see section 2.3.3). Most importantly, their intensity is not dependent on the land-atmosphere interface's state parameters such as soil moisture. The variation of the high-energy nucleon flux is a proxy of the galactic ray flux that sources the production of cosmic-ray neutrons. The standard approach to correct for these variations is

$$f_i = 1 + \gamma \left(\frac{I_{\text{ref}}}{I} - 1 \right), \quad (2.36)$$

with I_{ref}/I being the normalized count rate variations of a neutron monitor located at a similar cut-off rigidity than the CRNP. The parameter γ can be used to adjust the correction factor according to the difference in cut-off rigidity between the local site and the reference neutron monitor (Schrön, 2016).

2. Background on cosmic-ray neutrons

Below the Pfozter maximum, the flux of cosmic-ray nucleons that produce evaporation downstream is attenuated quasi exponentially by the atmospheric mass. The change in neutron flux can be corrected using the atmospheric depth d with

$$f_p = \text{Exp} \frac{d - d_{\text{ref}}}{\lambda}, \quad (2.37)$$

where λ describes the atmospheric attenuation length and d_{ref} a reference depth at a certain time. The attenuation length strongly depends on the altitude and cut-off rigidity and is therefore a location dependent parameter that varies between (130–165) g/cm² according to several studies (e.g. Desilets et al., 2006; Dunai, 2000). The atmospheric depth directly relates to the barometric pressure via $p = d \cdot g$ in hPa with $g = 9.81 \text{ m/s}^2$. Since the atmospheric pressure is the more accessible parameter by measurements the correction factor is commonly translated to pressure by $\lambda'[\text{hPa}] \rightarrow \lambda[\text{g/cm}^2] \cdot g$.

In addition to that, static hydrogen pools also affect the epithermal neutron intensity. These include for example vegetation cover θ_{veg} and lattice water θ_{lw} . According to Bogena et al., 2013 these can be added up to

$$\theta = \theta_{\text{mob}} + \theta_{\text{veg}} + \theta_{\text{lw}}. \quad (2.38)$$

The quantity θ_{mob} represents the accessible amount of water present in soil. The assessment of static hydrogen pools and d_{ref} and I_{ref} is usually carried out at the point of calibrating N_D (N_0).

3 The physics of gaseous neutron detectors

3.1 Neutron converters

Particle detection relies on the interaction of a particle with an appropriate detection substance. Subsequently, the energy change triggered via this reaction is recorded. Most commonly, particles deposit energy within the detector's volume via ionisation. However, neutrons are non-ionising particles and, therefore, cannot be detected directly by means of standard particle detectors. Efficient neutron detectors almost exclusively rely on neutron converters¹. These are materials that comply three criteria:

1. Neutron converters possess a high absorption cross section for thermal neutrons.
2. They instantaneously decay into short-ranged ionising radiation most commonly charged core fragments.
3. The reaction products feature high kinetic energy that induces a large ionisation signature.

Therefore, neutron converters possess a high probability to induce a strong ionisation signal via neutron absorption. However, as was discussed above, absorption processes are only significant in the thermal energy regime (see Fig. 3.1).

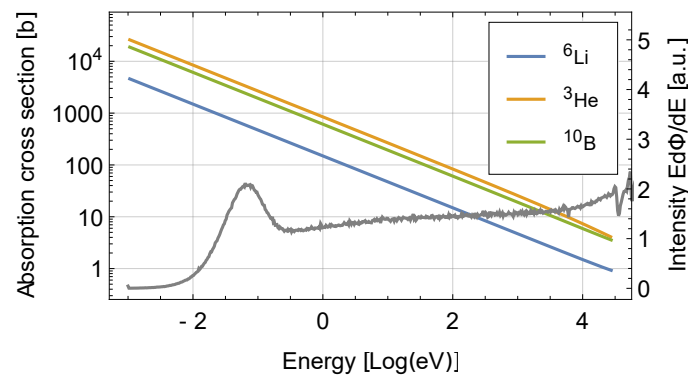
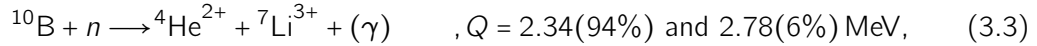
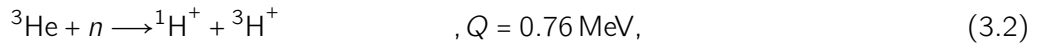
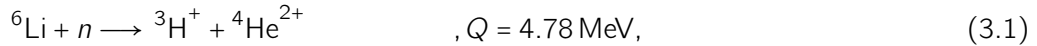


Figure 3.1: Cross sections for neutron absorption by ${}^6\text{Li}$, ${}^3\text{He}$ and ${}^{10}\text{B}$ indicated by Eq. 3.1–Eq. 3.3 as a function of energy (left logarithmic y-axis). The thermal and epithermal part of a cosmic-ray neutron spectrum at dry conditions is plotted in grey for better orientation (right y-axis).

Thus, neutron detectors, which rely on such converters, are called thermal neutron detectors. The most relevant isotopes used as neutron converters, in general but also in the context of CRNS, are ${}^3\text{He}$, ${}^6\text{Li}$ and ${}^{10}\text{B}$ with the following neutron absorption reactions

¹Evaporation and epithermal neutrons may be detected indirectly by light recoil nuclei via elastic scattering (see section 2.3.5), which in turn induces an ionisation signature within the detection volume. However, the efficiency for detecting neutrons by elastic scattering is ≈ 2 orders of magnitude lower than the efficiency for absorption of thermal neutrons

3. The physics of gaseous neutron detectors



where the Q value denotes the energy released within these exothermic reactions transferred to the reaction products as kinetic energy. Note that 94 % of the conversion reaction via ${}^{10}\text{B}$ are accompanied by the emission of a γ -ray resulting in a smaller kinetic energy of the alpha particle and the ionized lithium core. The reaction fragments are emitted back to back due to the much higher Q value than the thermal neutron's kinetic energy. The kinetic energy is split according to momentum conservation and the rest mass of the product core fragments. In the case of the ${}^{10}\text{B}$ conversion process the fragments ${}^4\text{He}^{2+}$ and ${}^7\text{Li}^{3+}$ carry 1.472/1.776 MeV and 0.84/1.013 MeV, respectively, where the first value corresponds to more probable decay including a γ -ray.

The absorption cross sections at room temperature ($E = 25 \text{ meV}$) amount to approximately 930, 5310 and 3840 b for ${}^6\text{Li}$, ${}^3\text{He}$ and ${}^{10}\text{B}$, respectively. Several isotopes feature even larger absorption cross section such as ${}^{113}\text{Cd}$ and ${}^{157}\text{Gd}$ with 21,000 and 255,000 b at 25 meV, respectively. However, the compound nucleus decays via a γ -ray, which features a weak ionisation signature and, therefore, induces only a small signal in the detector. These isotopes are frequently used to absorb the thermal neutron flux in various applications.

3.2 Interaction of charged particles with matter

Charged particles steadily dissipate energy as they traverse a medium via electronic, radiative or nuclear interactions. The dominant processes depend on the particle species but even more so on its energy. To lower energies electronic excitation and ionisation dominate, followed by radiative losses like Bremsstrahlung and pair production. Above these energies nuclear interactions as described in section 2.3.4 are the prevalent interaction mechanism. Energy loss due to relativistic processes is omitted in this work (for a more detailed work on this topic please refer to Lechner, 2018 and Eidelman et al., 2006).

A frequently used term to describe the mean energy loss of a charged particle in a certain material is the mass stopping power defined as

$$S(E) = -\frac{1}{\rho} \frac{dE}{dx}, \quad (3.4)$$

with dE/dx being the energy loss of the particle per distance, called stopping power, and ρ the density of the material.

3.2.1 Heavy charged particles

In the intermediate energy range, heavy charged particles like protons, alpha particles and atomic ions primarily lose energy due to electron excitation and ionisation. Muons behave similarly but exhibit a much lower nuclear interaction probability because they are leptons. Qualitatively, muons show similar energy dissipation behaviour as hadronic charged particles with lower absolute values. Heavy charged particles traverse the medium in relatively straight lines due to their much higher mass than the mass of the electrons they interact with. In the regime between few MeV to several 10 GeV or higher for heavier particles, their energy loss

can be approximated via the Bethe equation. Here, several parameter dependencies of the Bethe formula are examined without looking at the whole formula in detail:

$$-\frac{1}{\rho} \frac{dE}{dx} \propto \frac{Z}{A} \frac{z^2}{\beta^2} \ln \left(\frac{\beta^2}{l(1-\beta^2)} - \beta^2 \right), \quad (3.5)$$

with z being the charge of the incident particle in elementary charges, Z and A are the atomic number and atomic mass number of the medium, $\beta = v/c$ with v being the particles velocity and l the mean excitation potential. Thus, multiple charged particles like ${}^4\text{He}^{2+}$ and ${}^7\text{Li}^{3+}$ dissipate their whole energy in short path lengths. The target material influences dE/dx via Z/A and the mean excitation potential, which scales almost linearly with Z . At non-relativistic energies dE/dx is proportional to v^{-2} , however, to relativistic energies dE/dx increases logarithmically. In between a point of minimum ionisation arises at the energy $E_{\min} = 3Mc^2$, with M being the particle's rest mass. Thus, E_{\min} equals approximately 0.31, 2.81, 11.2 and 19.6 GeV for μ^- , protons, alpha-particles and ${}^7\text{Li}^{3+}$. Apart from this shift in energy the mass stopping power of heavy charge particles follows a similar pattern depicted exemplarily for μ^+ in Fig. 3.2.

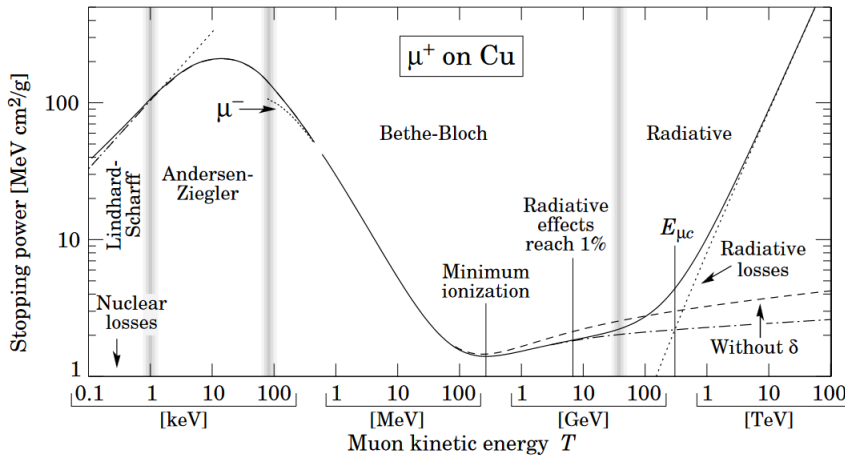


Figure 3.2: Mass stopping power of positively charged muons in copper. The solid, dotted and dash-dotted lines describe the total mass stopping power, the radiative and the electronic stopping power according to Bethe (Groom et al., 2001).

3.2.2 Electrons

Electrons are leptons and therefore behave much like a light version of a muon. When interacting with the bound electrons of nuclei they are on average deflected at larger angles than heavy charged particles because their mass is equal to that of the orbital electrons (see e.g. McMullan et al., 2009). For electrons radiative losses start to dominate at energies of few 10 MeV.

Aside from radioactive β^- -decay and cosmic-rays, unbound electrons are also ejected via Compton scattering. Compton scattering is the dominant photon interaction process at the MeV energy regime and shows cross sections of few μb to few mb in Argon between 1 and 10 MeV. That corresponds to a macroscopic cross section on the order of 10^{-7} – $10^{-5}/\text{cm}$. The ejected electrons can carry a large fraction of the initial energy of the photon, following a continuous spectrum that terminates at the Compton edge. Typical energies of Compton electrons amount to several 100 keV. It should be concluded that although the probability for

3. The physics of gaseous neutron detectors

Compton scattering is rather low, the relatively high flux of cosmic-ray photons as compared to neutrons and natural γ -ray decay may still lead to a significant amount of ionisation events in gaseous detectors (Crane et al., 1991).

3.3 Gas ionisation and gain

Gaseous neutron detectors make use of the ionisation by the neutron conversion products within a gas volume. Typically, a strong electric field is applied in order to separate the produced gas ions and electrons. Subsequently, the electrons are multiplied by acceleration and further ionisation via the electric field and then collected as a small electric current. This section aims at describing the underlying processes briefly.

Fig. 3.3 shows the mass stopping power of several charged particles. The ^{10}B conversion products are emitted with energies at approximately 1 MeV and, therefore, experience a strong energy dissipation in gaseous Argon. Their range amounts to less than 1 cm resulting in a dense ionisation signature (see also Köhli et al., 2016).

The other three species represent ionising particles with a significant flux intensity at the land-atmosphere interface as cosmic rays or in the case of e^- also as a product of radioactive decay. All three species feature a similar mass stopping power of $\approx 1.9 \text{ MeV cm}^2/\text{g}$ at their respective cosmic-ray energy spectrum intensity peaks (see also chapter 4 and Fig. 4.1 therein). In gaseous Argon with a density of $1.78 \cdot 10^{-3} \text{ g/cm}^3$ at 1 bar pressure this results in an energy deposition of 3.382 keV/cm indicating the low ionisation capability of cosmic-ray muons, protons and electrons. The depicted mass stopping powers exhibit the pattern shown in Fig. 3.2, where the minimum ionisation energy is located according to the particle mass (only visible for e^- , μ^- and p^+).

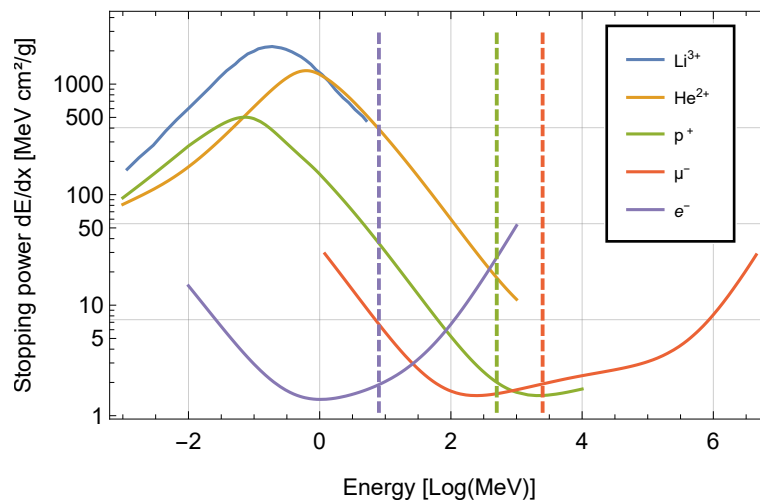


Figure 3.3: Mass stopping power in gaseous argon for the ^{10}B conversion products $^4\text{He}^{2+}$ and $^7\text{Li}^{3+}$ as well as e^- , p^+ and μ^- . The dashed lines in purple, green and red indicate the energy value for which the cosmic-ray electron, proton and muon fluxes show the highest intensity (see also Fig. 4.1). The data for e^- , p^+ and $^4\text{He}^{2+}$ is taken from Berger et al., 1999, for μ^- from Groom et al., 2001 and the $^7\text{Li}^{3+}$ stopping power from Paul et al., 2001, i.e. the MSTAR code referenced therein.

3.3.1 Filling gas

Gaseous neutron detectors are usually filled to a large portion with a noble gas. Monoatomic noble gases are beneficial because the conversion products kinetic energy is deposited only in ionisation, translation and electron excitation. Molecular gases on the other hand exhibit a

	He	Ar	Ne	Xe	CO ₂	CH ₄
W [eV]	41	26	36	22	33	28

Table 3.1: Mean energy dissipation for ion-electron pair creation W of selected gases according to Leo, 1994. The value W already accounts for energy dissipation via other channels than ionisation.

multitude of vibrational and rotational excitation modes, which leads to a larger percentage of energy deposition not resulting in ionisation, as indicated by Fig. 3.4. This characteristic is described by the value W that defines the average energy dissipation per ion-electron pair creation (see Tab. 3.1). Furthermore, noble gases are inert and the filling gas returns to its initial state after an ionisation event. Fig. 3.4 indicates an undesirable high excitation cross section for $E < 10$ eV that competes with the ionisation process in the case of argon. The excited atom emits a γ -ray which can ionise the gas at another location by ejecting a bound electron via Compton scattering. This leads to an ionisation process shifted in time, which cannot be attributed to the initial neutron conversion process. In order to reduce this effect a quench gas is added. This is a polyatomic gas that can absorb γ -rays and subsequently distribute the energy via various excitation modes and, therefore, is less ionised by γ -rays than noble gases (see Fig. 3.4 right panel). Common quench gases are CO₂ or methane and typically compose 10–20% of the total gas mixture. Argon is the most widely used noble gas due to its low cost.

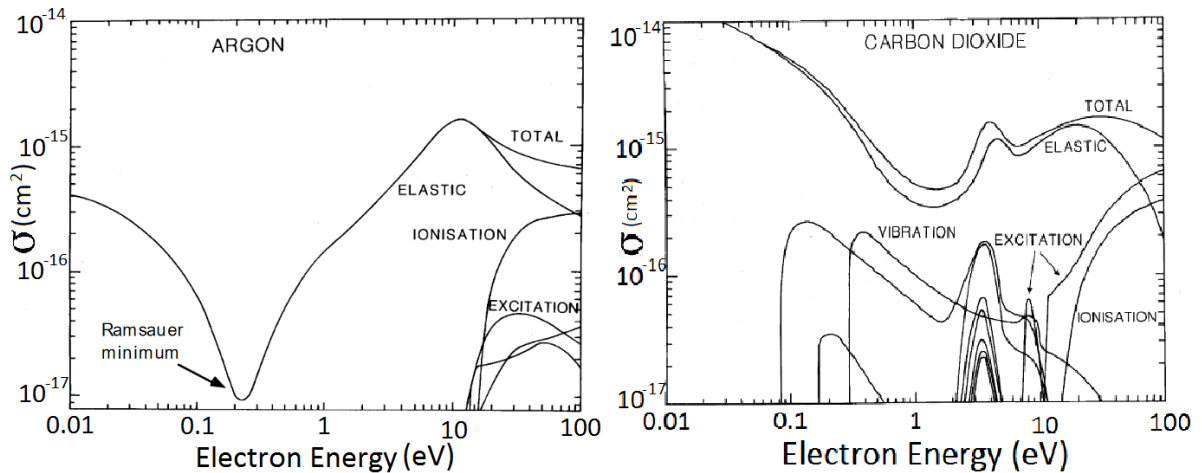


Figure 3.4: Electron cross sections for gaseous Argon (left) and CO₂ (right). Below 20 eV elastic scattering is the dominant process for both gases with a minimum interaction probability at the Ramsauer minimum. Both figures are taken from Sharma, 1998.

3.3.2 Charge amplification

A neutron conversion product with a typical kinetic energy of 1 MeV creates approximately 37,000 ion-electron pairs in a 90 % Argon and 10 % CO₂ gas mixture. Such low numbers of electrons are usually not sufficient for detection by an electronic readout device. In the presence of a strong electric field, free electrons produced by the neutron conversion products can be accelerated to ionisation energies themselves. This leads to an avalanche sequence, which results in an amplification of the primarily produced ion-electron pairs typically of the order of 10³–10⁶. The high field strengths necessary for such an avalanche formation can be induced in the vicinity of a conducting wire put on high voltage (see Fig. 3.5). The charge amplification per distance can be expressed via

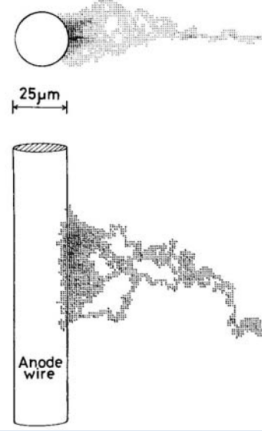


Figure 3.5: Simulated charge avalanche formation in the vicinity of a wire with an diameter of 25 μm (Byun, 2016). The gray pixels indicate electron trajectories.

$$\frac{dN}{dr} = \alpha(r)N(r), \quad (3.6)$$

with $\alpha(r)$ being the Townsend coefficient which depends on the field strength at the location r and the gas mixture (Auriemma et al., 2003). The total amplification factor G is usually referred to as gain with

$$N_{\text{tot}} = N_0 \text{Exp} \left(\int_{r_1}^{r_2} \alpha(r) dr \right) = G N_0. \quad (3.7)$$

3.4 Ion drift and event time signature

The critical quantity to describe the kinematics of charged particles in a gas volume is the ion mobility μ defined as

$$\mu = \frac{u}{|\vec{E}|}, \quad (3.8)$$

with u [cm/s] being the drift velocity and $|\vec{E}|$ the electrical field strength [V/cm]. In the case of ions μ is a linear function of $|\vec{E}|/p$, while for electrons it is a complex function of the gas mixture. In general, drift velocities are small for ions compared to their thermal velocity even at high field strengths. After charge avalanche formation the electrons collected at the wire are held in place due to the electrical field induced by the ion image charges. The drift velocity of the ions, therefore, determines the velocity at which the electrons can be drained off by the readout electronics, which in turn controls the time signature of the recorded pulse (see p. 138 ff Leo, 1994).

3.5 Solid neutron converters

The neutron converter material can be either applied in the gas phase of the detector or as a solid layer. However, only ionisation that occurs in the gas phase of the detector contributes to the signal. In the case of a solid neutron converter the conversion products deposit a fraction of their kinetic energy in the solid material before entering the gas volume. This restricts the maximum thickness of the converter layer due to the short range of the conversion products. The ${}^4\text{He}^{2+}$ and ${}^7\text{Li}^{3+}$ released via the ${}^{10}\text{B}$ absorption process feature a maximum range of 2 and 4 μm in solid boron (Köhli et al., 2016). Thus, solid converter layers exhibit a maximum efficiency for neutron detection as the thickness of the converter layer directly relates to its neutron absorption (see Fig. 3.6). The maximum efficiency per layer amounts to approximately 7 % and 24 % for solid ${}^{10}\text{B}$ and ${}^6\text{Li}$ layers, respectively, which are the most common solid converter materials.

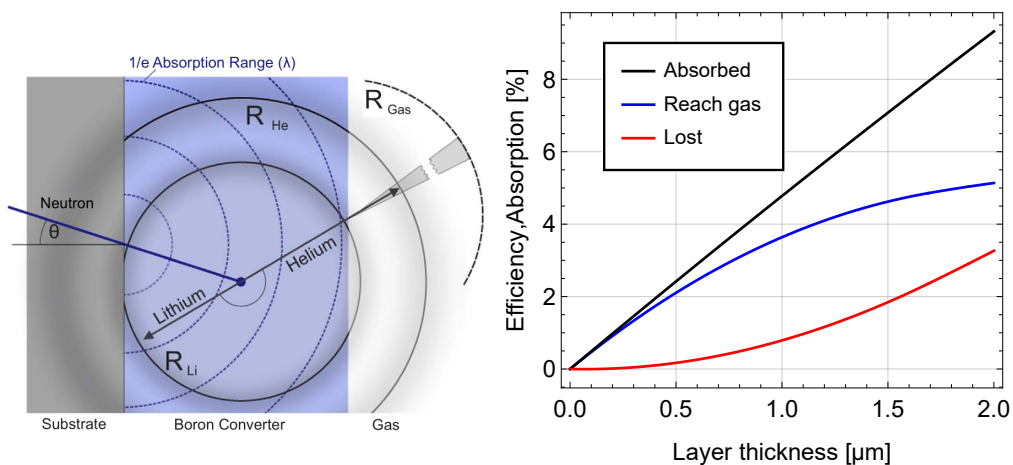


Figure 3.6: Neutron conversion process within a solid boron layer. **Left:** An incident neutron is converted into ${}^4\text{He}^{2+}$ and ${}^7\text{Li}^{3+}$ ions, which are emitted back to back in the layer with different maximum range indicated by R_{He} and R_{Li} . Only one of the reaction products may leave the boron layer and deposit its remaining kinetic energy in the gas volume via ionisation (figure taken from Köhli et al., 2016). **Right:** Efficiency of a boron carbide layer (${}^{10}\text{B}_4\text{C}$) as a function of layer thickness. Boron carbide is favoured over pure boron due to the production process of such layers. The neutron absorption in the layer follows the Beer-Lambert law, which behaves quasilinear in this low absorption regime (black curve). The blue curve denotes neutron absorption that leads to gas ionisation, while those neutrons that trigger ${}^4\text{He}^{2+}$ and ${}^7\text{Li}^{3+}$ ions that do not leave the solid layer are indicated with the red curve. The latter are lost because only ionisation within the gas volume can be detected.

Moreover, the fraction of energy that is deposited by one of the conversion products in the gas volume also strongly depends on the layer thickness. However, it also depends on the location of the conversion inside the layer and the emission angle of the fragments. In the case of thick conversion layers, the result is a rather broad distribution which describes the probability that a neutron conversion leads to a certain total energy deposition in the gas. Such is shown in Fig. 3.7 for a ${}^{10}\text{B}$ layer of 1.7 μm thickness. The spectrum features two distinct edges at energies of 1.47 and 0.84 MeV that correspond to the kinetic energies carried by the ${}^4\text{He}^{2+}$ and ${}^7\text{Li}^{3+}$ fragments for 94 % of all decays. The small cluster that reaches to an energy of roughly 1.8 MeV represent ${}^4\text{He}^{2+}$ particles emitted via the decay channel that

3. The physics of gaseous neutron detectors

has a probability of 6 %.

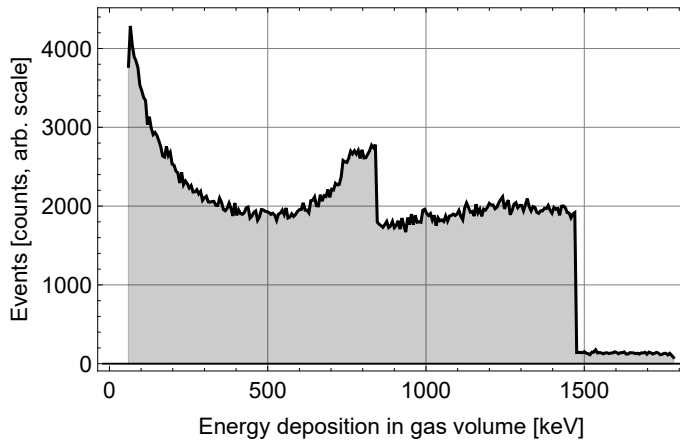


Figure 3.7: Simulated distribution for the energy deposition in the gas volume of the conversion products of a solid ^{10}B layer with a $1.7\ \mu\text{m}$ thickness. Credit: The simulation was carried out by Markus Köhli using the URANOS transport code (see section 4.1.1).

3.6 Gaseous proportional counter

Proportional counters are widely-used neutron detectors making use of neutron converters either in the gas phase or as a solid coating at the inner wall of the counter (see Fig. 3.8). They are mostly designed as a hermetically sealed cylinder with a thin wire in its centre and follow the general detection steps described above. A high voltage V_0 is applied to the wire which conducts a radially symmetric electrical field $E(r)$ at distance r from the wire that can be described by

$$E(r) = \frac{1}{r} \frac{V_0}{\ln\left(\frac{r_{\text{cyl}}}{r_{\text{wire}}}\right)}, \quad (3.9)$$

in the case of an infinitely long cylinder. Where r_{cyl} and r_{wire} denote the radii of the cylinder and the wire, respectively. In the case of a finite cylinder boundary effects lead to a reduced field strength, which results in less efficient charge separation and avalanche formation at the cylinder edges. The high voltage applied to the wire is chosen in such a way that the number of electrons generated within the charge avalanche is increased by a constant gain factor. Hence, the amount of electrons collected at the wire is proportional to the amount of primarily generated electrons, which are in turn proportional to the energy deposited by the charged particle e.g. the neutron conversion product. This linear mapping between energy deposition of a charged particle and the amount of electrons is the key characteristic of a proportional counter. It allows for discrimination between neutron conversion that deposits large amount of energies within the gas as compared to less ionising particles as muons and electrons. It is also important to note that the energy deposition spectra shown in Fig. 3.7 is amplified linearly and can be read out in this shape via appropriate readout electronics. The recorded spectrum is, therefore, a suitable indication for the performance of the proportional counter.

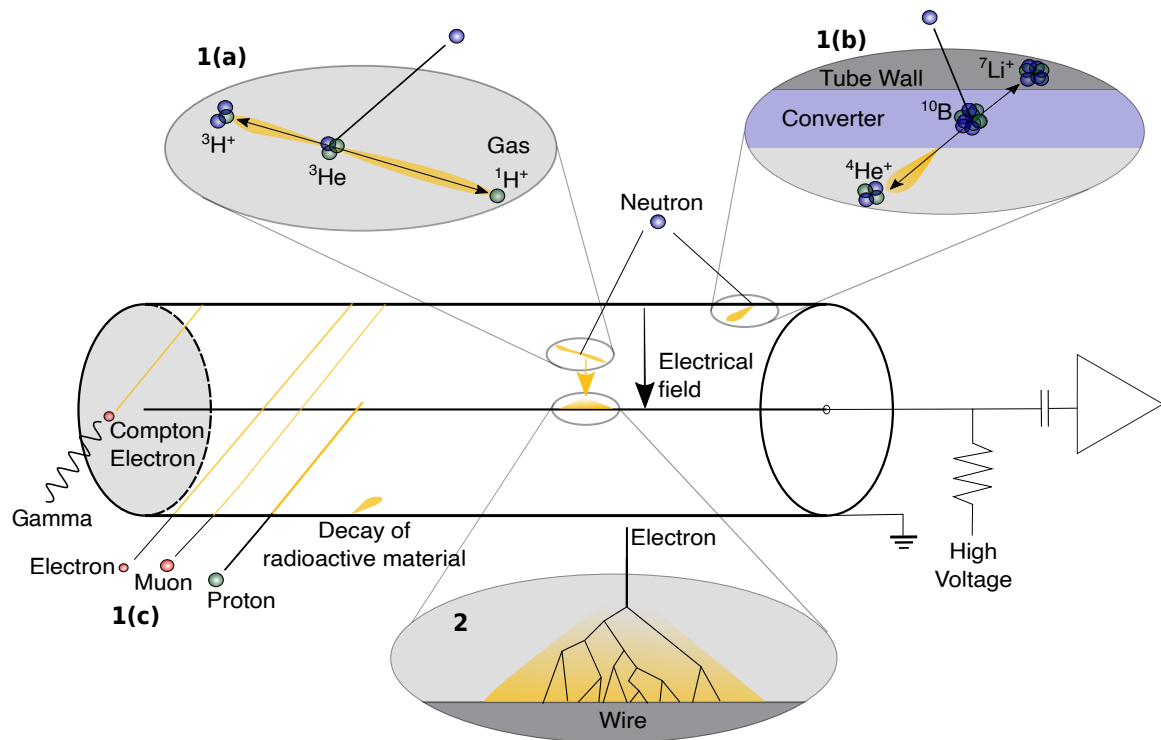


Figure 3.8: Detection principle of a proportional counter. Neutron conversion into ionizing radiation takes place in either the solid material via ^{10}B (1(b)) or for comparison to the old standard in the gas phase via ^3He (1(a)). The fragments of the conversion process are emitted in opposite directions. The ionization trace is indicated in yellow. An electric field between the tube wall and the axial wire accelerates the generated electrons towards the wire. In the vicinity of the wire, the electrons reach the gas ionization energy and charge multiplication takes place (2). The resulting pulse is then read out by a charge sensitive amplifier. 1(c) indicates other types of radiation that may induce a signal. The thickness of the tracks indicate the ionization energy deposition. Figure and caption are taken from Weimar et al., 2020.

4

MCNP Model setup

4.1 Using Monte Carlo toolkits to describe environmental neutron transport

The physics of a single neutron-nucleus interaction process within the energy range of cosmic-ray neutrons is relatively well understood. Over the past decades, a large number of dedicated experiments has accumulated, constantly refining the understanding of these processes. These findings are tabulated in data bases (see also section 4.5) that list highly resolved energy and angular dependent cross sections for the interaction between a neutron and a large variety of isotopes. The crux is to find an appropriate tool to translate the microscopic understanding of neutron physics to the transport processes of a neutron ensemble in a complex geometry consisting of a variety of isotopes, e.g. at the atmosphere-land interface.

Although, deterministic transport codes exist that aim at solving the neutron transport equation numerically they usually exhibit high uncertainty at complex setups. The probabilistic method of Monte Carlo simulations has proven to be an appropriate tool to compute neutron transport. The method samples randomly from prefixed initial conditions. In this case a particle is released at a certain location according to a given energy and angular spectrum and then propagated probabilistically through a simulation domain according to the microscopic cross sections. This method is beneficial for several reasons: (1) single neutron tracks are simulated, which helps to visualize their movement and to identify objects that influence their transport; (2) simulating a multitude of neutron trajectories results in a neutron flux representation with appropriate statistical accuracy; (3) The computational effort of Monte Carlo codes is relatively low compared to other codes. However, a Monte Carlo simulation is a heuristic approach, which does not directly yield an analytical relation between variables of the simulated domain. It requires the user to carefully choose an appropriate simulation setup in order to be able to retrieve the desired functional dependencies.

The main ability of a Monte Carlo transport code in the context of Cosmic-Ray Neutron Sensing is, therefore, the reproduction of the influence of environmental parameters on the neutron flux above the atmosphere-land interface. The results are used to infer analytical transfer functions that describe the behaviour of the neutron flux in relation to certain state parameters, e.g. soil moisture.

4.1.1 URANOS

URANOS (**U**ltra **R**apid **N**eutron-**O**nly **S**imulation) is a neutron-only Monte Carlo simulation toolkit based on a voxel engine designed by Markus Köhli at the Physikalische Institut, Heidelberg University. It is specifically designed for simulating neutron transport at the land-atmosphere interface and neutron detector analysis. It is freely available while most other codes fall under strict export restrictions. Moreover, it was designed to offer an alternative in view of modern code standards and multi-threading to other standard codes, which were mostly designed in the last century. URANOS outperforms older packages in terms of amount of particles simulated per time. A graphical user interface displays the results of a on-going simulation and facilitates the use of the toolkit. Complex geometry input is realized via an import option for images or tables that describe the structure of the simulation setup. That is why URANOS is now used in the majority of neutron transport studies in the context of CRNS (see also below). Total and angular cross sections are taken from a combination of the data bases ENDF-VIII (Brown et al., 2018) and JENDL-HE (Watanabe et al., 2011). Furthermore, URANOS makes use of effective models that describe neutron production within

its simulation domain via other particle species as their transport is not included.

4.1.2 MCNP

MCNP (**M**onte **C**arlo **N**-**P**article) was developed at the Los Alamos National Laboratory, USA with the most recent version being MCNP6.2 (which is also deployed in this work). Historically, MCNP evolved from neutron and photon transport description dating back to 1977. It is a general purpose software package able to simulate the coupled transport of 36 particles species and heavy ions. Moreover, MCNP features a wide range of input options, which include complex geometry setup, heat transfer by particles, particle tracking including their precursor particles in e.g. particle showers or several variance reduction methods. Similarly, many parts of the toolkit can be excluded from the current simulation in order to reduce computational effort. This has led to a wide spread application of the code ranging from reactor and accelerator design to particle therapy or other medical use cases. It also provides an optional galactic cosmic-ray source and is therefore capable of simulating the whole propagation of particle showers in the atmosphere. Still, MCNP is not considered a standard for high-energy particle interactions beyond the GeV range and is historically more tailored to lower energies. However, the latest versions have seen several improvements on the code part that treats high energies extending its energy range to 1 TeV.

4.1.3 Why MCNP?

MCNP includes all particle species that significantly contribute to the cosmic-ray neutron flux via the processes described in section 2.3.4. Moreover, historically MCNP was tailored to describe neutron transport and has been validated against multiple neutron experiments including the thermal and high-energy transport (see e.g. Mashnik, 2011; Degenaar et al., 2004). The MCNP toolkit is therefore capable to comprehensively simulate cosmic-ray neutron generation and propagation at the land-atmosphere interface.

One specific use case is the comparison and validation of neutron transport simulations carried out by URANOS. Such has been done and published in Köhli et al., 2021. Moreover, URANOS relies on input data that describes neutron production via spallation and evaporation events at the land-atmosphere interface. While such processes are already implemented, dedicated MCNP simulations may help to further improve these subroutines of URANOS. MCNP is in particular beneficial when the effective neutron transport through dense material is simulated. For example, the neutron flux a few meters deep into the soil is entirely generated in the soil volume itself because the airborne neutron flux is completely attenuated. In such cases a precise simulation of the particle cascades that generate these neutrons is crucial and MCNP is favoured over URANOS.

4.1.4 Previous studies

The analytical function presented by Desilets et al., 2010 that links the above-ground epithermal neutron flux to soil moisture was derived experimentally and by means of Monte Carlo simulations. It has been the main pillar of the method but was subject to refinement through simulations conducted by Köhli et al., 2021. Since then, Monte Carlo codes have been the main tool to determine and quantitatively analyse other variables that influence the neutron signal. These studies examined the influence of atmospheric water vapour (Rosolem et al., 2013; Köhli et al., 2021), vegetation cover (Andreasen et al., 2017b; Baatz et al., 2017; Jakobi et al., 2018), footprint dynamics (Köhli et al., 2015; Desilets et al., 2013; Jakobi et al., 2021), fractional snow cover in a complex alpine terrain (Schattan et al., 2019) and also detector development (Köhli et al., 2018b; Weimar et al., 2020). Some Studies aimed at inferring correction factors that improve the soil-moisture retrieval, while others focused on retrieving other parameters from the neutron signal. For example, the

above-mentioned studies on vegetation cover used the ratio of thermal to epithermal neutrons as a proxy to disentangle the vegetation cover and soil moisture signal. It must be noted that the list above makes no claim to be complete but shall give a broad overview on the topics.

4.2 Domain setup

The neutron transport is simulated in a domain that covers the soil and atmosphere, while additional layers such as snow, vegetation, rivers and so on may also be integrated. The spatial dimension of the domain is confined by several parameters:

1. The larger and the more complex the domain, the higher the computational effort. Domain size inversely relates to the counting statistics and therefore the simulation error per unit area.
2. The ratio between detector and domain size geometrically determines to first order the flux that reaches the detector volume. The smaller the ratio the more particles have to be simulated in order to achieve a certain statistical error. The size of the virtual detector may also exceed its real dimensions. However, this leads to a changing influence of closely located hydrogen pools due to the blurring of their distance to the detector. Thus, the simulated detector size is a compromise between statistical and systematic error. Homogeneous setups allow for a detector layer which covers the whole horizontal range of the domain.
3. The domain should cover most of the detector's footprint in order to capture all objects that influence the signal. That results in domain radii of approximately 500 m. However, some setups, e.g. those featuring homogeneous topologies, offer the opportunity to apply reflecting or periodic vertical boundary conditions. The footprint also defines a minimum soil thickness in the vertical dimension: Neutrons that evaporated at approximately 1.5 m below the soil surface unlikely penetrate the whole soil column and escape into the air volume.
4. For most setups a rotationally symmetric domain is most suitable, especially for homogeneous topologies where no lateral direction is favoured and the detector's footprint becomes a function of radius.
5. The atmosphere covers a source layer where the initial particles are released, located between 100 and 500 m above the soil surface (see below). The atmosphere extends to around 1000 m above this source region. The layer between source and upper domain boundary allows for the diffusive part of the neutron flux that enters this part of the atmosphere to be backscattered in direction of the soil surface.

4.3 Particle source terms

Two general approaches of cosmic-ray neutron flux simulations can be distinguished. Firstly, a comprehensive simulation of atmospheric particle showers by releasing primary galactic cosmic rays at the top of the atmosphere. The complexity of the particle cascades and the huge model dimensions introduce large uncertainties and demand for extensive computational efforts. The second approach uses validated particle spectra computed by a transport code tailored to high-energy particle cascades. This allows for particles to be released above the land-surface interface in mid-air. This approach is chosen for this work for a couple of reasons: (1) While MCNP features a galactic cosmic-ray input source and can treat high-energy particle cascades, it is a code mainly specialised for lower energies. (2) Virtually all parameters simulated within the scope of this work are covered within the vicinity of the land-atmosphere interface. Thus, simulating the upper atmosphere holds no benefits. (3) The

4. MCNP Model setup

computational effort is decreased by approximately two orders of magnitude (this estimate on the computational overhead is based on the calculations of section 6.1).

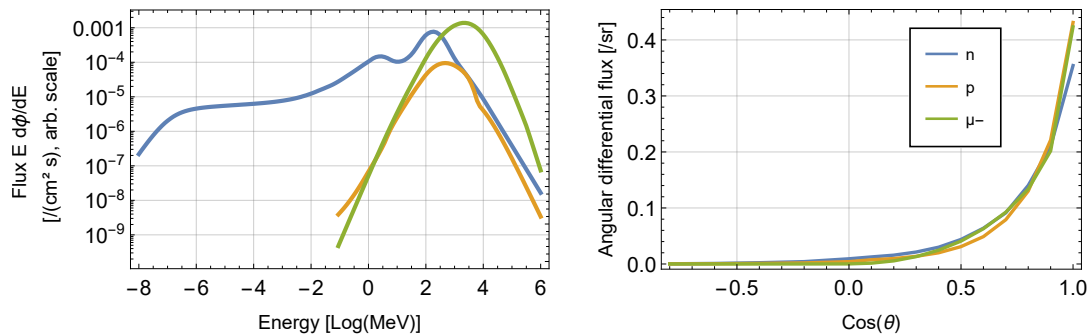


Figure 4.1: Particle source characteristics at a cut-off rigidity of ≈ 3.7 GV and an elevation of 110 m, which corresponds to Heidelberg, Germany (Sato, 2015; Sato, 2016). **Left:** Energy spectra of neutrons (n), protons (p) and muons (μ^-) that are released as source particles in the simulations of this work. Note that the spectra are in relative scale to each other: At the chosen location muons, neutrons and protons amount to approximately 63, 33 and 4 % of the total flux. **Right:** Angular distribution as a function of the cosine of the zenith angle: a value of 1 corresponds to the downward direction. The distribution for neutrons (blue) only covers the high-energy part with $E \geq 20$ MeV. The lower energetic neutrons are released isotropically.

The source particle energy spectra and their corresponding angular distributions are taken from Sato, 2015 and Sato, 2016. Both works used PARMA (Sato et al., 2008) a follow-up development of the PHITS code (Iwase et al., 2002). Their results are accessible via their Excel-based EXPACS tool. EXPACS offers spectra and angular distributions for a large variety of particles and a large parameter range. It covers atmospheric depths between 0.15–1095 g/cm² corresponding to 0–63 km height for any given latitude and longitude. Among the particle spectra offered by EXPACS those have to be chosen that contribute the most to the neutron flux above ground. Three particle source species are selected (see Fig. 4.1):

1. **Neutrons:** The atmospheric neutron spectrum already contains evaporation neutrons and to a smaller amount epithermal neutrons, i.e. those most important to Cosmic-Ray Neutron Sensing. Moreover, the spectrum mainly consists of spallation neutrons at energies of approximately 100 MeV that can trigger further neutrons via spallation and evaporation.
2. **Protons:** Neutrons are mainly produced via hadronic showers. Apart from short-lived mesons, protons contribute the most to neutron production in the hadronic showers. The proton energy spectrum has a larger mean energy value than that of neutrons which leads to intensive particle cascades even at high atmospheric depths.
3. **Muons:** Muons possess a much larger attenuation length than protons and neutrons. At sea level muons are approximately twice and 15 times as abundant as cosmic-ray neutrons and protons, respectively. As indicated in section 2.3.4.4 their contribution to neutron production is relatively low at the soil surface but dominates production few meters below the ground level.

The neutron production mechanisms of these three particle species within the simulation domain will be discussed in detail in section 5.1.2. Other cosmic-ray particles that are also abundant like photons and electrons contribute insignificantly to the neutron production while

strongly increasing the computational effort.

The source particles are released in 450 m height above the soil surface. A certain height is needed to moderate the incoming neutron flux as EXPACS assumes a dry atmosphere defined by Minzner, 1977. If not stated otherwise, the simulation batches shown in this study involved 100 million initial source particles.

4.4 Other simulated particle species

In addition to the three source particle species, positive and negative pions were simulated as well. They are numerous produced within the particle cascades due to their low rest mass of $139.6 \text{ MeV}/c^2$ that lies well below the peak energies of the neutron and proton spectrum. Charged pions possess a short mean life time and primarily experience a leptonic decay to a muon and muon neutrino. However, if interacting with nuclei before decaying, they can spall these and thereby contribute to the neutron flux (Mancusi et al., 2017): they act as intermediate cascade agents. On the other hand, neutral pions only contribute to the electromagnetic branch of particle cascades and are therefore excluded from the simulation setup. Other mesons like kaons are heavier ($m \approx 500 \text{ MeV}/c^2$) and are composed of quarks of the second generation. Due to colour charge conservation a second meson has to be produced making their production less likely in particle showers located in the lower atmosphere. Heavier baryons than neutrons and protons as well as light nuclei are also excluded for analogue reasons. Alpha particles are included as intermediate particles as well as they may emerge as spallation products and then induce further spallation or nuclei excitation.

4.5 Transport description

MCNP features several input options that control the physics of particle transport in various energy regimes. Different cross section data bases can be included after being converted to the MCNP-inherent ACE format (Conlin et al., 2019). These cross sections are limited to low energies and usually do not extend beyond 150 MeV for most elements (JENDL-4/HE marks an exception to that rule by extending up to 3 GeV (Watanabe et al., 2011)). This work mainly focuses on the use of the ENDF-VIII nuclear cross section data base (Brown et al., 2018). Some setups were also run implementing the JEFF 3.2 (Koning et al., 2011), JENDL (Shibata et al., 2011) and the precursor version of ENDF-VIII the ENDF-VII (Chadwick et al., 2011) databases and the results were compared and published in Köhli et al., 2021. These data bases also cover thermal neutron scattering kernels that describe the neutron cross sections at energies close to atomic binding energies.

To higher energies, MCNP makes use of so called event generators. These codes predict interaction probabilities and spallation progeny for collisions of incident particles with energies up to 1 TeV. Their prediction is based on the interaction stages described in section 2.3.4. Several model combinations can be chosen that treat the lower and higher energy part of the intra-nuclear cascade and the deexcitation process for different incident particles separately. The choice of these high-energy models determines the propagation of particle cascades in the domain.

In each case nucleon, pion and light ion interactions are computed by LAQGSM (Gudima et al., 2001) above energies of 3.5 GeV, 2.5 GeV and 940 MeV, respectively. Below that Isabel (Yariv et al., 1979) or CEM03.03 (Mashnik et al., 2012) control light ions, in this case alpha particles. Nucleons might be controlled by Bertini (Bertini, 1963) or CEM below the 3.5 GeV threshold. While CEM03.03 has its own built-in evaporation and fission model, Bertini and Isabel invoke the Dresner evaporation (Dresner, 1962) and RAL (see e.g Armstrong et al., 1984) fission model which can be changed to Abla (Junghans et al., 1998) comprising both evaporation and fission models. Although the MCNP manual recommends

4. MCNP Model setup

to use a combination of CEM03.03 and LAQGSM (Werner et al., 2017), this work has studied the influence of high-energy input models in the context of Cosmic-Ray Neutron Sensing and compared it to measured data in order to determine a suitable model combination for this specific neutron transport case.

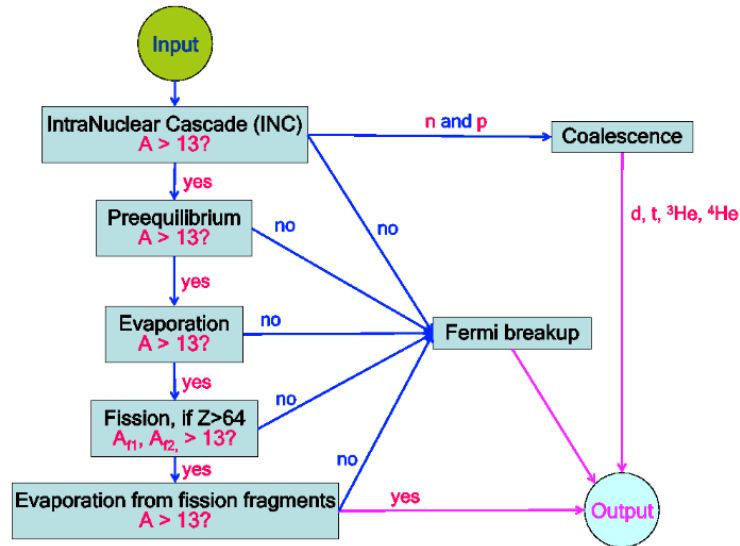


Figure 4.2: Schematic outline of a high-energy nuclear reaction calculation by CEM03.03 (Mashnik et al., 2012). The Fermi breakup model describes the process of light nucleus disassembling into two or more fragments during the pre-equilibrium stage that is directly followed by the intra-nuclear cascade.

4.6 Visualization of the domain setup and particle propagation

Fig. 4.3 depicts a typical domain setup used in the context of this work. The three source terms and all relevant processes including evaporation (red dots) and detection (blue dots) are schematically illustrated. Fig. 4.4 shows a specific neutron track including its precursor particle, a proton, demonstrating the particle track ability of MCNP.

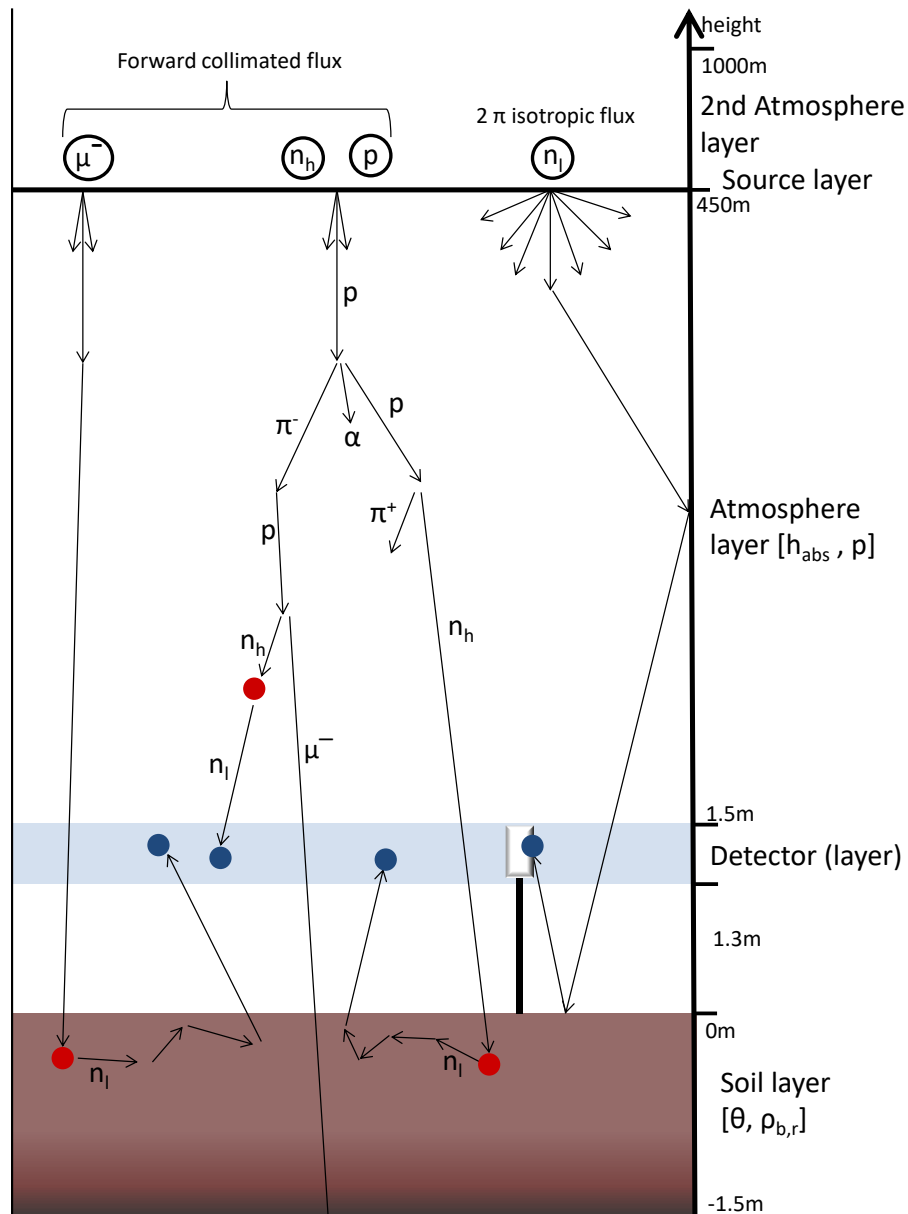


Figure 4.3: Schematic setup of a minimal simulation domain as a default for the Monte Carlo studies of this work. Several particle tracks are shown schematically and are reduced to few participating particles. The high-energy neutron (n_h) and proton (p) source particle terms are summed up as a hadronic part. Neutron evaporation events are shown as red dots. The detection of an epithermal neutron, either by a detector or a virtual detector layer, is marked by a blue dot. The parameters in parentheses indicate the most important environmental variables to the neutron flux propagation: soil moisture (θ), soil bulk density ($\rho_{b,r}$), atmospheric water content (h_{abs}) and pressure (p).

4. MCNP Model setup

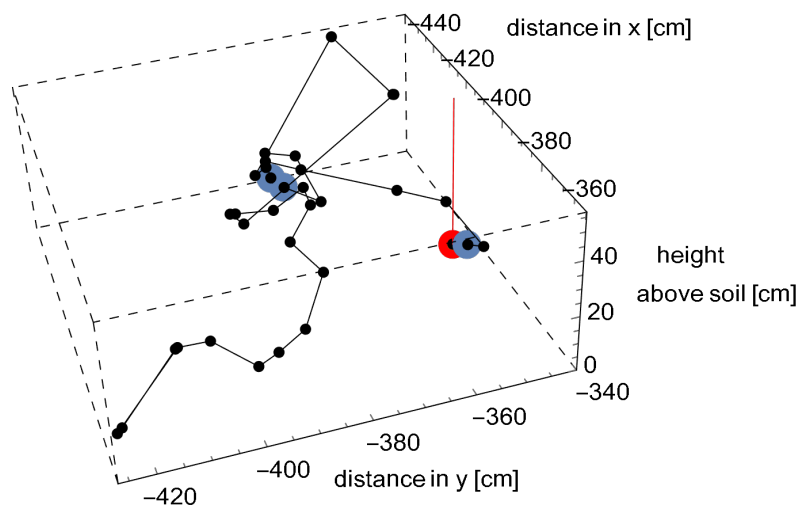


Figure 4.4: Example of a typical particle track that leads to crossings in a detector layer as displayed in Fig. 4.3. The initial particle is a proton which is released with an energy of approximately 66 MeV in 450 m height. It loses energy with few interactions in air and soil (red line) and then triggers the evaporation of a neutron with $E = 1.9$ MeV (red dot). This neutron scatters 45 times in soil and air crossing the detector layer in 2 m height 3 times (blue dots) until it thermalises in the soil. It subsequently scatters 69 times in the soil in close distance due to its low energy and after that is absorbed. Because the soil's density is approximately 1000 times as high as that of air, which directly relates to the neutrons mean free path, all scattering points in the soil volume appear as one on this scale.

Neutron sources within the simulation domain

Cosmic-ray neutrons are not only produced within the upper layers of the atmosphere but also at the land-atmosphere interface in the soil and air volume. It is important to understand how neutrons are produced in the various compartments as their origin, i.e. point of evaporation, also strongly determines the impact of hydrogen on their trajectory through the domain. Thus, any above-ground epithermal neutron flux representation needs to accurately take these neutron source terms into account. This chapter aims at revealing the spatial distribution of neutron production at this interface and how it is influenced by certain initial conditions like soil or source particle composition. Moreover, the angular distribution of the neutron production processes is examined in order to elaborate how these neutrons are transported from the soil to the air volume. The chapter also targets the penetration of the neutron flux into shallow soil of up to several meters. In fact, this region is poorly covered by other literature. Larger depths of several ten to hundreds of meters have gained more popularity due to low background experiments (e.g. Cooper et al., 2011; Manukovsky et al., 2016b). A standard setup as visualised in Fig. 4.3 is used releasing the source particles in 450 m height according to Fig. 4.1. The atmospheric water content and pressure are set to 10 g/m^3 and 1013 hPa, respectively. The high-energy particle transport is treated with a combination of the event generators CEM03.03 and LAQGSM, following the recommendation of the MCNP manual.

5.1 Soil

5.1.1 Elemental composition dependence

At the land-atmosphere interface the target material for the high-energy cosmic-ray flux changes significantly. The material's density increases by three orders of magnitude. However, the spallation, evaporation, scattering and absorption characteristics are not changed by a density change. The more relevant change that influences the neutron production and their transport mechanisms is the change in elemental composition. Firstly, soils may possess a much higher relative hydrogen content than air making the soil volume a more efficient moderation region. At the same time dry soils have a higher mean atomic number than dry air. As a rule of thumb, neutron evaporation increases with increasing atomic number while spallation does not follow this trend (see Fig. 5.1, left).

The right panel of Fig. 5.1 highlights a strong energy dependence of the angular distribution of the emitted neutrons: while evaporation neutrons are emitted mostly isotropically with a slight focus to the downward direction into the soil, neutrons with $E > 20 \text{ MeV}$ are strongly collimated downwards. That is mainly due to the strong focus on the downward direction of the incident high-energy particle flux. The spallation neutrons triggered by these particles are emitted mostly in the same direction due to momentum conservation. Some of these reactions eject more than one particle. In these cases, one of the lower energetic spallation neutrons may be ejected in backward direction while momentum is still conserved. This energy dependent angular distribution has several implications for CRNS. Even though soil produces a similar amount of spallation and evaporation neutrons, only 20 % of the first but more than 40 % of the latter are emitted back into the direction of the air volume. Even further spallation reactions become likely for particles with $E > 500 \text{ MeV}$. However, these neutrons are almost exclusively emitted in downward direction with $\approx 0.7 \%$ being emitted upward. Thus, the neutron flux emitted in soil in upward direction has almost no capability for

5. Neutron sources within the simulation domain

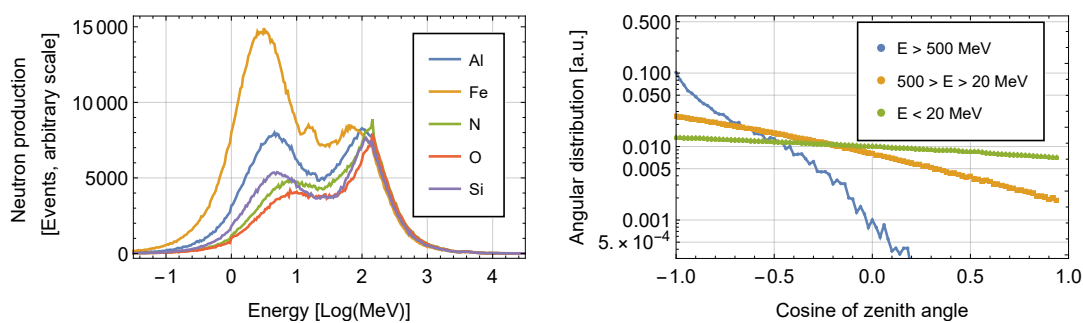


Figure 5.1: Neutron emission at various target materials when exposed to a high-energy flux composed of neutrons, protons and muons. **Left:** Absolute generated neutron flux production spectra of some of the most prominent soil constituents are shown: Aluminium (Al), iron (Fe), oxygen (O) and silicon (Si). Nitrogen is added due to its high abundance in air. While the production of highly energetic neutrons with $E > 20$ MeV is almost equal for each element, the evaporation probabilities increase significantly with increasing atomic number. The small peak at around 10–20 MeV, most prominent in the iron production spectrum (Fe), is a simulation artefact due to the limited range of the ENDF/B-VIII data base. It contains several (z, xn) neutron production cross sections that are only defined between 10 and 20 MeV, in the case of iron, or 30 MeV for lighter elements. **Right:** Angular distribution of the emitted neutron flux split into three energy regimes via thresholds of 20 and 500 MeV. The cosine of the zenith angle is positive for an upward emission in the direction of the air volume above the soil and negative for an emission deeper into the soil. A value of zero corresponds to an emission parallel to the soil surface.

reverse particle showers. The emission probability of the spallated neutron flux back into air is further decreased because these mostly interact inelastically. That means most interactions lead to the neutrons annihilation while producing further particles as evaporation neutrons. Their mean free path fixes the layer thickness from where such neutrons may be emitted into the air resulting in a strong suppression of slant trajectories as indicated in Fig. 5.2, right panel. This effect competes with the suppression of direct upward emission which is unfavourable because of the low phase space.

Evaporated neutrons show a similar qualitative behaviour. However, in this energy regime elastic scattering is the dominant interaction type, which is only slightly focused to the forward direction for energies of several MeV. These neutrons may scatter multiple times at the nuclei of the single-material soils presented here without losing much energy. The angular distribution of the neutrons with $E < 20$ MeV emitted from soil is therefore defined by their last scattering event in ground. Their shorter mean free path length than that of spallated neutrons and the constant redirection of slant angles lead to an angular emission that is focused upward until at approximately 70 degrees the phase space restricts the emission probability again.

The energy spectra of the emitted neutrons by bare soil reveal a strong correlation between atomic mass number and emission capability (see Fig. 5.2, left). These numbers are summarized in Tab. 5.1 and added by further soil constituents. The atomic abundance refers to the percentage of atoms and was taken from the statistics chapter of the Geochemical Atlas of Europe (Salminen et al., 2005). This data reveals that the main soil constituents, oxygen and silicon, show a very similar neutron production ability. Anomalous high values of iron lead to a substantially enhanced neutron production in the soil. To the other end, thick

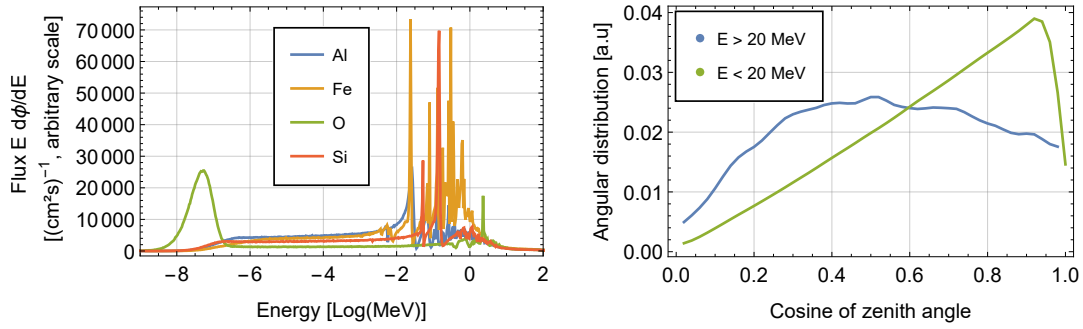


Figure 5.2: Neutron emission of single-material soils into the air volume. **Left:** Energy spectra of the neutrons released into air for the same materials as shown in Fig. 5.1. The highly structured spectra in the evaporation energy regime resemble the inverse of the corresponding element’s scattering cross section. The oxygen spectrum shows a thermal peak due to its anomalously low absorption cross section. **Right:** Angular distribution of the neutron emission of single-material soils for two energy regimes. The angle orientation is defined as in Fig. 5.1.

humus layer with high carbon and nitrogen content result in a poorly neutron-emitting soil. Of course, the emission spectrum changes significantly once soil moisture is added to the simulation setup due to its high moderation power. The angular distribution, however, remains similar.

Element	Main compound	Atomic fraction [%]	Total flux	$E < 20 \text{ MeV}$	$E > 20 \text{ MeV}$
O	SiO_2	57.7	0.607	0.601	0.006
Si	SiO_2	22.4	0.621	0.615	0.006
Al	Al_2O_3	5.5	0.760	0.753	0.006
Fe	Fe_2O_3	1.3	1.000	0.992	0.008
C	TOC	1.2	0.401	0.395	0.006
Ca	CaO	1.0	0.572	0.566	0.006
K	K_2O	0.8	0.682	0.676	0.006

Table 5.1: Neutron flux emitted by single-material soils into the air volume. The numbers are normalized to the total flux emitted by a target soil consisting solely of iron. Main compound refers to the most frequent chemical compound of this element, while atomic fraction indicates the relative percentage of this element of all atoms in the top 25 cm of the soil. The data is taken from Salminen et al., 2005 and the values correspond to the mean values for all analysed sites, which are located at various places in Europe. TOC refers to total organic carbon.

5.1.2 Effect of the incoming particle distribution

The neutron spectrum produced in the soil and then emitted into the air volume does not only depend on the soil composition itself. But also on the incident particle type and energy distribution. This is especially important since the relevant particle species show different attenuation lengths. The fraction on the total incoming particle flux of each species therefore changes with altitude and latitude. The latter is strongly connected to the

5. Neutron sources within the simulation domain

cut-off rigidity which also influences the attenuation of the particles within the atmosphere. In the following the soil is composed of 75 Vol-% SiO_2 and 25 Vol-% Al_2O_3 with a porosity of 50 %, i.e. a bulk density $\rho_{b,r}$ of 1.43 g/cm^3 .

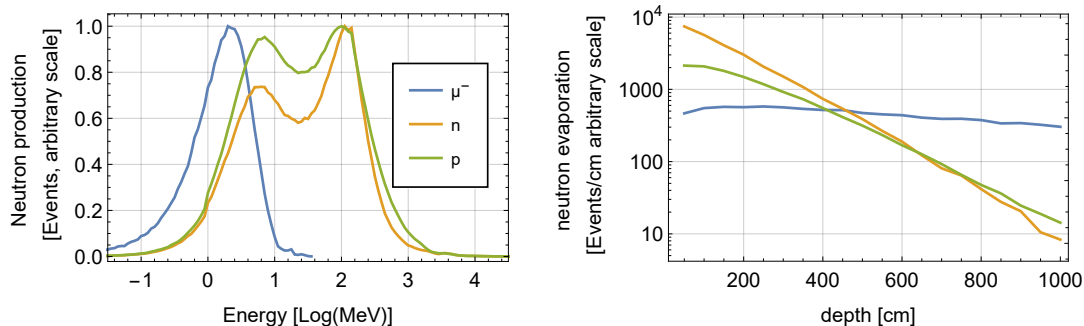


Figure 5.3: Production of neutrons by incoming cosmic-ray muons, protons and highly energetic neutrons. **Left:** Energy spectra of neutron production by selected particle species normalized to their maximum. Muons virtually only produce neutrons via muon capture while protons and neutrons also contribute by spallation processes. The muogenic evaporation peak appears at lower energies because it is not shifted by an underlying spallation peak. **Right:** Depth-dependent evaporation neutron production. The distributions are not to scale, the muogenic and proton neutron production are increased here for better visibility. The absolute numbers depend on the location and elevation of the site.

Fig. 5.3 shows the production probability distributions within the first ten meters of dry soil for the three different particle species. The main neutron production channel of muons is muon capture and subsequent evaporation. Very few muons also induce higher energetic neutrons through direct spallation. However, only 0.5 % of all muogenic neutrons produced in MCNP6 within the first 10 m of soil are spallation products. It is noted that, this percentage increases with depth as the muogenic spectrum hardens (Wang et al., 2001b). The hadronic showers induce slightly more high-energy neutrons with $E > 20 \text{ MeV}$ than evaporation neutrons. High-energy cosmic-ray neutrons induce approximately 20 % more spallation than evaporation neutrons while for protons it is only elevated by 10 %. At a cut-off rigidity of $\approx 3.7 \text{ GV}$ and an elevation of 110 m (corresponding to Heidelberg, Germany) the incoming particle flux is made up of 63 % muons, 33 % neutrons and 4 % protons. Taking that into account 69, 25 and 6 % of all evaporation neutrons produced in dry soil of 10 m depth are triggered by high-energy neutrons, protons and muons, respectively. However, the production in the uppermost meter of soil is most important for above-ground neutron intensities since evaporation neutrons possess attenuation lengths in this order of magnitude and will unlikely leave the soil if produced below 1 m depth. For the uppermost soil layer with 1 m thickness the fractions take the values 78, 20.5 and 1.5 % for neutron, proton and muon induced evaporation neutrons. On average, each proton produces 0.2 neutrons in the first 1 m of dry soil. This value is 0.09 and 0.003 for high-energy neutrons and muons, respectively. Cosmic-ray protons possess a much higher average energy than neutrons and are, therefore, capable of inducing more secondary particles in cascades when penetrating soil. Muons on the other hand have a much smaller interaction probability and penetrate deeper into the soil before interacting.

These properties also determine the shape of the depth distributions shown in Fig. 5.3,

right. The flux of the incoming particles is attenuated with increasing penetration depth into the soil. Evaporation triggered by high-energy neutrons falls off exponentially, while the more energetic protons generate cascades that also trigger more spallation particles. The spatial extension of these cascades and the induced evaporation events lead to a build-up of evaporation centres in the first meter of soil, after which the proton-induced neutron evaporation also decays exponentially. Muons show a virtually constant neutron production within the first three meters, which then decreases in a non-exponential fashion.

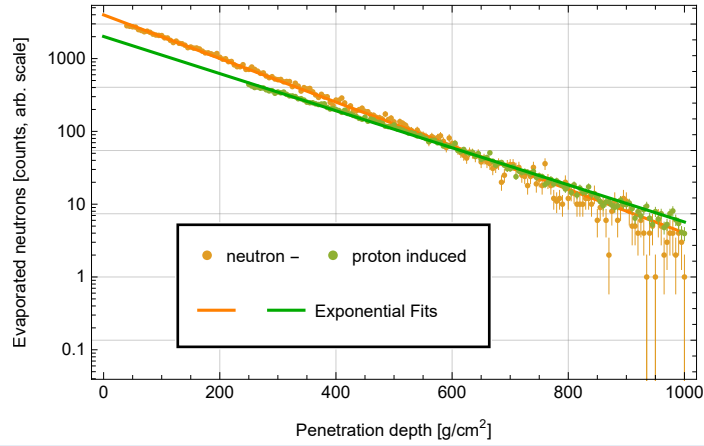


Figure 5.4: Exponential decay of neutron evaporation via cosmic-ray neutrons and protons with dry soil penetration depth. For the fit of the proton contribution only data deeper than 250 g/cm^2 were taken into account as the shallower production shows a non-exponential behaviour.

The exponential decay of neutron and proton-triggered neutron evaporation is depicted in more detail in Fig. 5.4 and fitted by the function

$$N_{n/p} = N_{0,n/p} \text{Exp}\left(-\frac{l}{\lambda_{l,n/p}}\right) = N_{0,n/p} \text{Exp}\left(-\frac{d}{\lambda_{d,n/p}}\right), \quad (5.1)$$

where the attenuation length can be specified in λ_l [cm] for this specific soil ($\rho_{b,r} = 1.43 \text{ g/cm}^3$) or in a more general term λ_d [g/cm^2]. A larger attenuation length appears for the proton attenuation with $\lambda_{d,p} = (170.4 \pm 0.9) \text{ g/cm}^2$ than for the neutron part $\lambda_{d,n} = (145 \pm 0.7) \text{ g/cm}^2$. This is again mainly a consequence of the higher mean energy of the cosmic-ray protons. This behaviour is also observed in Fig. 5.5: In shallow depths high-energy neutrons are the main trigger for evaporation until at approximately 660 g/cm^2 their contribution equals that of protons. Even before that, around 550 g/cm^3 the muogenic equals the hadronic contribution, while to larger depths the neutron evaporation is dominated by the incoming muon flux (this qualitatively coincides with Fig. 2.8, which indicates hadronic and muogenic neutron production equality at similar depths).

5. Neutron sources within the simulation domain

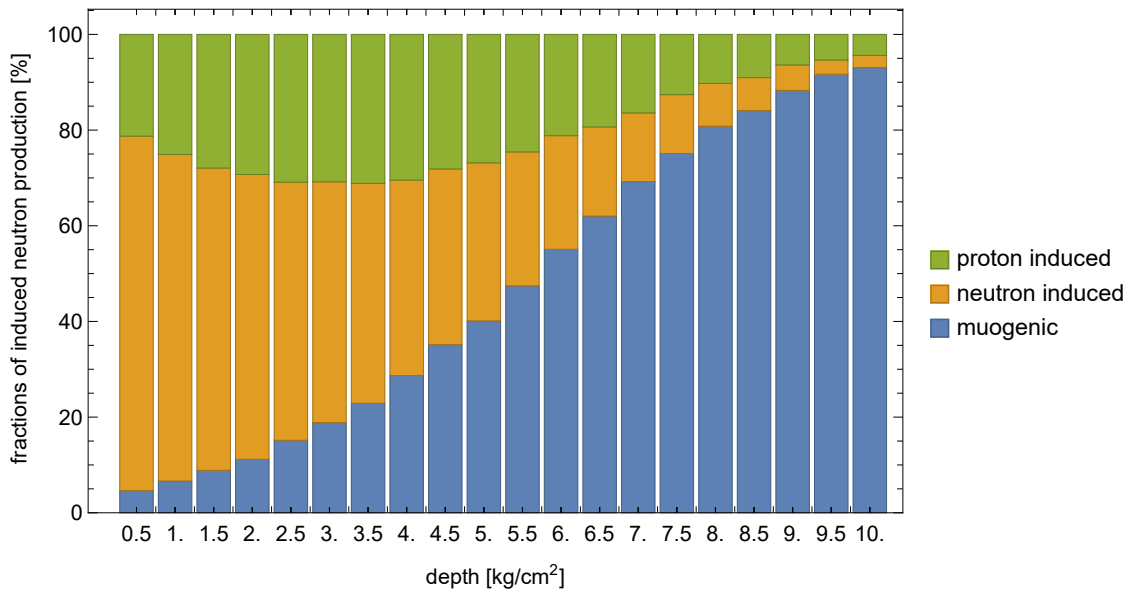


Figure 5.5: Percentage of precursor particles that trigger evaporation neutrons as a function of soil depth. These absolute numbers refer to incoming spectra at a cut-off rigidity of ≈ 3.7 GV and an elevation of 110 m. The dry soil has a density of 1.43 g/cm^3 , thus, 1 kg/cm^2 refers to approximately 7 m depth.

5.2 Atmosphere

Along the trajectory of the high-energy incoming cosmic-ray flux the atmosphere is located upstream. That means that the mainly downward collimated high-energy neutron flux with energies higher than 20 MeV has a strong focus towards the land-atmosphere interface, the region of interest. Opposed to the soil volume where most of the high energetic neutron flux is directed deeper into the ground.

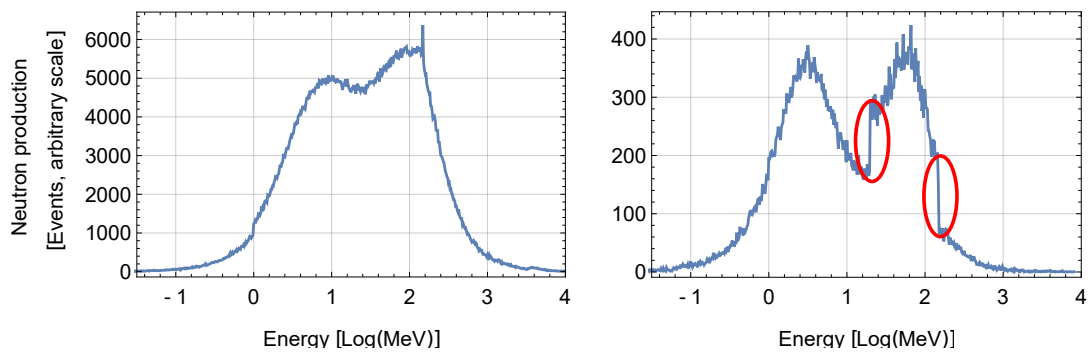


Figure 5.6: Neutron emission energy spectra in air. **Left:** Neutron production in dry air with elemental composition of 78 % N_2 , 21 % O_2 and 1 % Ar. **Right:** Neutron production spectrum induced by Argon nuclei with red ellipsoids that mark two points of a discontinuity.

An undesired feature of MCNP6 invokes a discontinuity in the neutron production spectra of ^{40}Ar at these high energies (marked with red ellipsoids in Fig. 5.6). Its source within the code can be tracked back to a tabulated neutron generation via a subroutine called INTRCT. A closer inspection of the fortran code leads to the suspicion that this part of the code is called

up twice in some circumstances leading to an overestimation of neutron emission between 20 and 150 MeV. However, this feature virtually disappears when computing the emission spectra of dry air as ^{40}Ar only makes up around 0.5 % of the atmosphere's atoms. It is still an undesirable systematic error that could not be resolved in the scope of this work.

5.3 Water and snow

At energies well above molecular binding energies nuclear interactions are unaffected by the state of matter: water and snow become equivalent targets to the high-energy flux. In general, water is a poor neutron source. The hydrogen nucleus solely consisting of a proton is not able to emit evaporation neutrons. Hence, more than 90 % of water's neutron production and virtually all its evaporation potential is made up by oxygen.

The effect of soil moisture on the above-ground epithermal neutron flux is therefore twofold: it moderates atmospheric neutrons and those created in dry soil to thermal energies, but at the same time it is such a poor neutron source itself that it contributes much less to flux than other soil constituents, while shielding their neutron production via moderation. Both mechanisms lead to a decline in the epithermal neutron flux.

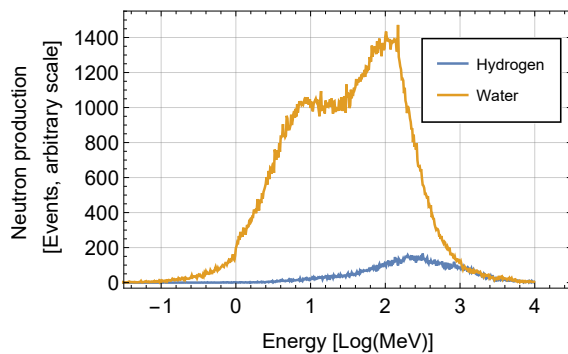


Figure 5.7: Neutron emission spectra in water (orange curve). The contribution of hydrogen to the neutron production in water is shown in blue.

5.4 Contribution of individual neutron source terms to the soil moisture signal

5.4.1 Elemental composition dependence

The above-mentioned source domains, i.e. soil, water and atmosphere, provide evaporation neutrons at the land-atmosphere interface, which are moderated and thereby contribute to the above-ground epithermal neutron intensity. After discussing each source domain separately, it is important to highlight the relative contribution of each domain to the above-ground epithermal neutron flux.

Fig. 5.8 reveals the contribution of the evaporation sources to the detected flux as a function of soil moisture. The results refer to a homogeneous setup as described in chapter 4. Fig. 5.8, left reveals that for dry regions the soil acts as the major emitter for the detected neutron flux. However, the percentage of these evaporation neutrons which are moderated below epithermal energies decreases strongly as the soils hydrogen content increases. Moreover, the additional water content itself acts as a poor evaporation source. Consequently, the soil's sourcing capability for the above-ground neutron flux decreases strongly until at approximately 20 Vol-% soil moisture content the atmospheric contribution equals that of the soil.

Fig. 5.8, right indicates the intensity of above-ground epithermal neutrons separated their evaporation origin in either the soil or atmosphere. Evidently, evaporation in the soil itself is affected most by its moisture content: Neutrons that evaporate in the soil are less likely to reach the air volume above thermal energies with increasing soil moisture content. But it is important to note that the atmospheric source term also shows a significant dependence on

5. Neutron sources within the simulation domain

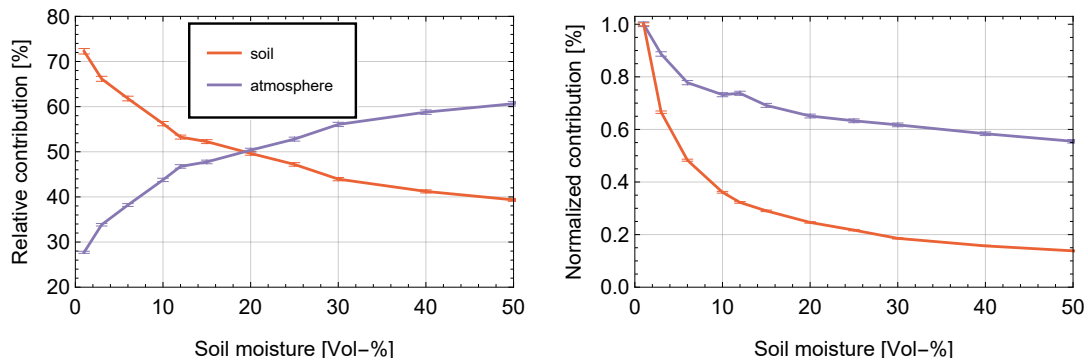


Figure 5.8: The evaporation location of detected neutrons is traced back in order to quantify the sources of the detected above-ground epithermal neutron flux. A neutron is detected when crossing the detector layer located between 1.9 and 2 m above the ground and having an energy $100 \text{ eV} < E < 10 \text{ keV}$. The atmospheric pressure and humidity content are fixed to 1013.15 hPa and 10 g/m^3 , respectively. **Left:** Relative evaporation contribution to the above-ground epithermal flux of the soil and atmosphere, which combines the source input in 450 m height and the evaporation inside the air volume, as a function of soil moisture. **Right:** Source contributions normalized to their maximum value as a function of soil moisture.

soil moisture as large parts of these neutrons penetrate the soil on their way to the epithermal energy regime. Above-shown simulations are rerun while adding iron to the soil, which is the strongest evaporation source in the soil compartment. The iron atomic abundance is set to 5.8% in dry soil, which is indicated as the maximum value found in Salminen et al., 2005. The total number of atoms per volume is kept constant. Hence, this example shows an extreme case of how changes in the soil composition can change the soil moisture retrieval.

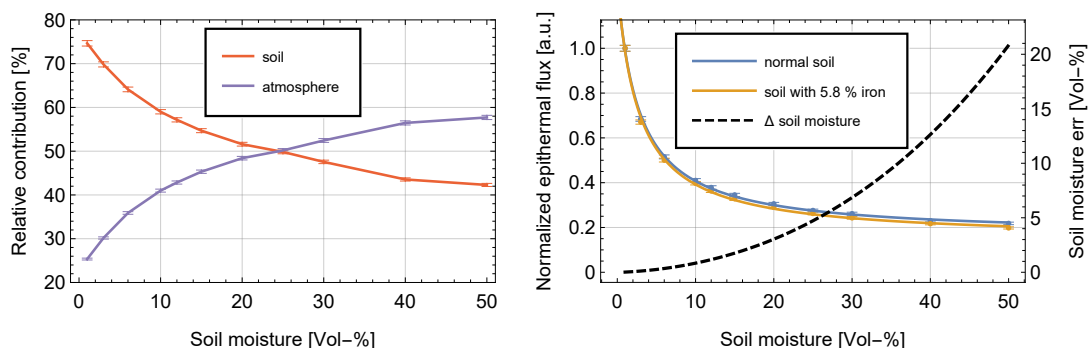


Figure 5.9: Source contribution of a soil with 5.8% iron atomic abundance (setup analogue to Fig. 5.8). **Left:** Relative evaporation contribution to the above-ground epithermal flux of the soil and atmosphere. **Right:** Detected epithermal neutron flux of soils without iron and 5.8% iron atomic abundance. The black, dashed curve indicates the error in soil moisture retrieval if the site specific transfer function between epithermal intensities and soil moisture is not adjusted (note the second y-axis on the right).

The iron nuclei enhance the soil's capability as a source, leading to an increase of the soil's relative contribution to the above-ground epithermal neutron flux by approximately 2.5% (compare Fig. 5.8 and Fig. 5.9). These neutrons experience a stronger influence by soil

moisture content than the airborne flux, which leads to a slight shift in the transfer function (see Fig. 5.9, right): The transfer function steepens. However, this introduces a relatively large soil moisture retrieval error to high moisture values due to the flattening of the hyperbolic relation. For example, if the non-iron transfer function is assumed (blue curve) and the actual soil moisture amounts to 50 Vol-%, a value of approximately 70 Vol-% is retrieved. Note that this assumes a calibration at completely dry conditions. If the calibration would be done at high soil moisture values, which corresponds to normalising the blue and orange curve in Fig. 5.9 to be the same at this moisture value, would lead to a less pronounced overestimation in the wet region but to an underestimation in the dry region.

5.4.2 Particle species contribution to the soil moisture signal

Section 5.1.2 discussed how the three different particle species, introduced as source terms, show slightly different behaviour in neutron production in the soil. These differences are mainly a consequence of the different attenuation lengths. An examination of the direct and indirect contributions to the above-ground epithermal neutron flux by the three particle species reveals how their different production patterns lead to a flux change induced by the species. The neutron source term contains a significant part of evaporation and epithermal neutrons that were already produced in the upper layers of the atmosphere (see Fig. 4.1). These neutrons directly contribute to the signal but are influenced strongly by the moderation power of the atmosphere's hydrogen content, which is also shown by Tab. 5.2. The high-energy part of the neutron spectrum triggers neutron evaporation in the soil that is more focused to the upper layers as compared to proton and muon-induced evaporation (see Fig. 5.4). As the soil moisture content increases, neutrons that are generated in the lower soil layers are more effectively prevented from exiting the soil as those produced in the upper layers. The contribution of protons and muons to the above-ground epithermal neutron flux, therefore, experiences a stronger decline with soil moisture content increase. The contribution of charged pions as intermediate particle cascade agents follow similar pattern. These are mainly produced in cascades triggered by rather high-energy neutrons and protons, which penetrate deeper into the soil than their lower energetic counterparts. At dry conditions ($\theta = 1$ Vol-% and $h_{\text{abs}} = 1 \text{ g/m}^3$) intermediate pion production contributes approximately 6% to the above-ground epithermal neutron flux and then drops to 3.5% at wet conditions ($\theta = 50$ Vol-% and $h_{\text{abs}} = 35 \text{ g/m}^3$). In summary: The involved particle species not only contribute to the total above-ground epithermal neutron flux but also show varying response to the environmental hydrogen pools.

(θ, h_{abs})	n	p	μ^-
(1,1)	66.6	29.1	4.3
(1,35)	65.7	29.8	4.5
(50,1)	76.4	21.9	1.7
(50,35)	75.3	22.9	1.8

Table 5.2: Epithermal neutron flux above moist soil triggered by the different particle species. Four different soil moisture (θ) and atmospheric absolute humidity content (h_{abs}) values are given that span a typical range of these parameters. θ is given in Vol-%, h_{abs} in g/cm^3 and the relative contributions to the epithermal flux of the particle species in %.

Conclusion

This chapter reveals how neutron production depends on the elemental composition of the soil and the composition of the source particle species. The latter changes with cut-off rigidity and altitude. The fraction of muons of the total cosmic-ray flux changes significantly with those two parameters, while the high-energy proton and neutron flux ratio experiences only slight changes (see section 2.3.4.3). It is, furthermore, indicated that neutron evaporation below 550 g/cm^2 depth in the soil is dominated by muons. Thus, any simulation that targets the flux description at these depths should use site-specific muon, proton and neutron source spectra. Moreover, the chapter discusses how the contribution of particle species to the above-ground epithermal neutron flux show a different response to soil moisture and air humidity. This implies that an accurate description of the influence of different hydrogen pools on the neutron flux needs to take all three particle species into account.

It is also shown, that a different elemental soil composition leads to a slightly different site-specific transfer function between the above-ground epithermal neutron flux and soil moisture, which was reported by several studies (see section 2.4) and motivated here. Soil constituents that act as a strong or poor neutron source lead to a steep or flat transfer function as compared to standard soil, respectively.

The neutron production mechanisms revealed in this chapter could be used as model input for other toolkits such as URANOS, which relies on effective models to describe neutron generation via spallation and evaporation.

MCNP model validation, calibration and application

This chapter aims at examining the use of MCNP for Cosmic-Ray Neutron Sensing by combining Monte Carlo simulations with dedicated neutron measurements. The goal is to indicate how MCNP may be employed to understand the cosmic-ray neutron transport dynamics within the simulation domain, i.e. the atmosphere, soil and water bodies. The experimental setups were chosen such that they hold appropriate data sets to calibrate the MCNP high-energy event generator input option in order to determine the model that describes the particle cascade, i.e. neutron production within the domain, best in the context of CRNS (see also section 4.5). This high-energy model calibration is beneficial because it features higher uncertainties as compared to the lower energetic neutron transport description. However, the scenarios described below do not merely hold the opportunity to calibrate and validate Monte Carlo toolkits but also offer various applications of cosmic-ray neutron detectors beyond the standard operation.

6.1 Atmospheric propagation: Neutron intensity above lakes and glaciers

Disclaimer: This chapter is the result of a close cooperation with Paul Schattan from alpS GmbH and University of Innsbruck, Austria. He contributed equally in terms of the conceptual ideas on this topic, the detector installation on the glacier and had a valuable share in the simulation setup discussions.

The concept of measuring the epithermal neutron flux above water surfaces traces back to Schrön, 2016. Epithermal neutron intensity changes are dominated by soil moisture dynamics. A constant 'soil moisture' effect is achieved easiest above lakes or glaciers. The signal saturates if the water column or ice sheet is thick enough so that additional hydrogen content, e.g. due to precipitation, does not change the epithermal neutron flux above the water/ice-surface. These conditions bear the opportunity to monitor second-order effects on the epithermal signal. However, some of these show significant cross correlation with soil moisture, which is the case for the influence of air humidity. The incoming atmospheric downward-propagated high-energy particle flux, however, is not affected by the underlying material. The magnitude of this flux is determined by the incoming galactic cosmic-ray flux, which acts as the primary source for secondary cosmic-rays, and the air column that attenuates the flux. The air column or atmospheric depth, given in g/cm^2 , can be monitored via the atmospheric pressure. The larger the depth the stronger the attenuation of the high-energy cosmic-ray flux. This section aims at utilizing saturated data sets in order to calibrate and validate the simulated atmospheric propagation. The measured data also provides the possibility to rank atmospheric attenuation lengths from existing literature and compare them to MCNP simulation results.

Two data sets are presented: Firstly, a long-term and local measurement above the Stubai glacier. It spans several months during winter and spring in 2019/2020 but covers a small pressure range due to its static location. Secondly, snap-shot measurements above lakes at different altitudes in summer 2020 featuring single measurements at large pressure variations within few days.

6.1.1 Simulation setup

MCNP6 features a built-in galactic cosmic-ray source (McKinney et al., 2012) which enables users to simulate particle propagation through the whole atmospheric column. The input parameters of this option are location and date in order to account for cut-off rigidity and

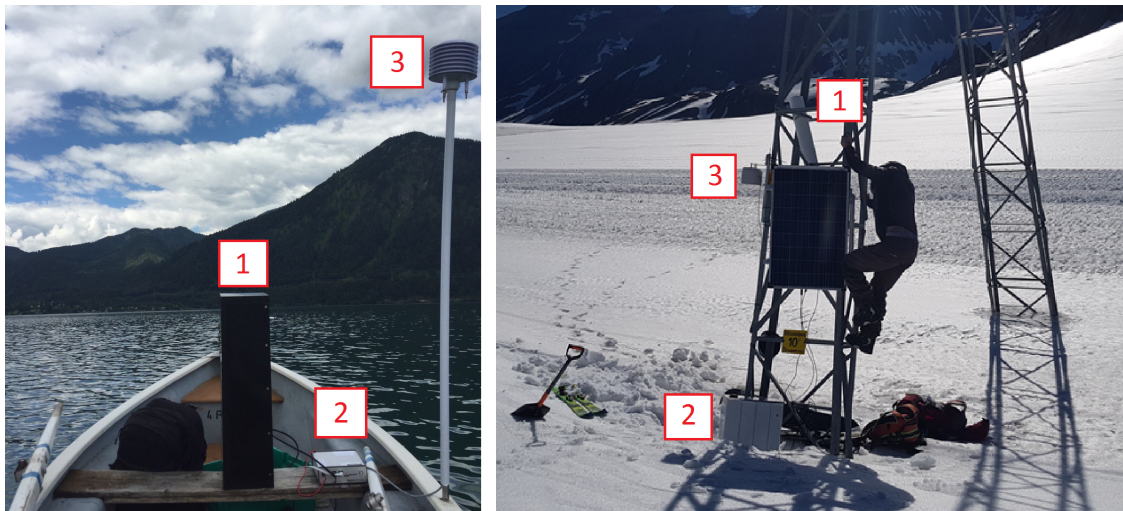


Figure 6.1: Field measurement setup: The equipment involves a standard cosmic-ray neutron detector (label in red as 1), a data logging device (2) and a pressure, relative humidity and temperature sensor, covered by a Stevenson screen (3). **Left:** Snap-shot experiment at Walchensee, Bavaria, Germany. The lake is located at approximately 800 m above sea level (a.s.l.), which corresponded to 925 hPa during the day of measurement (25th July 2020). **Right:** Maintenance at the Stubai glacier field site during approximately maximum snow cover. The white data logger box is partly covered by the snow (located below the yellow sign). The equipment is situated almost exactly 3000 m a.s.l.

terrestrial and solar modulation cycles. Furthermore, the galactic cosmic-ray particle composition can be chosen. These particles are released at the MCNP6 default height of 65 km and propagated through an atmosphere composed of several homogeneous layers with temperature T_i , pressure p_i and absolute humidity h_i . Pressure and temperature height dependence are chosen according to the international standard atmosphere (Minzner, 1977) with a lapse rate $dT/dz = -6.5 \text{ K/km}$ and a pressure scale height of 8.5 km. An air humidity profile is set in accordance to Tomasi, 1984 who suggested a scale height of approximately 2 km for absolute humidity. Simulation batches are run in order to determine the robustness of the simulation setup. It is found that the number of atmosphere layers had insignificant effect on the neutron flux if it is higher than 40. The difference between a setup of 40 and 100 atmospheric layers is purely statistical when simulating 5 mio. galactic cosmic rays. To limit computational effort each of the following setups features a 40-layer atmosphere of equal thickness in terms of penetration depth (g/cm^2). Also the galactic cosmic-ray source is chosen to only consist of protons and alpha particles since adding heavier ions also seems to have virtually no effect. However, both restrictions have only small effects on the computational time accounting to few per cents.

Several simulation batches are run featuring a variety of MCNP configuration options that control the high-energy physics beyond the ENDF-VIII cross-section data base (see section 4.5) in order to find the model that describes the atmospheric propagation the best.

6.1.2 Glacier setup measurement and simulation comparison

In accordance with the Stubai glacier ski resort, a standard cosmic-ray neutron detector was deployed at a pole of the Gamsgarten ski lift (coordinates: lat=46.98206, long=11.11265, see Fig. 6.1). High count rates are achieved at this measurement site due to the high elevation. These in combination with long-term monitoring offer the possibility of tight data

selection while still attaining low statistical uncertainty. In this case, the selection criteria are set such that only data points with air humidity lower 2 g/m^3 were allowed and a period of low precipitation is chosen in order to keep the influence of the effective height of the detector minimal (see section 7.2.4). The data is also limited to high snow cover periods because the area spanned by the detector's footprint shows some shallow-iced and even some small ice-free patches in the summer.

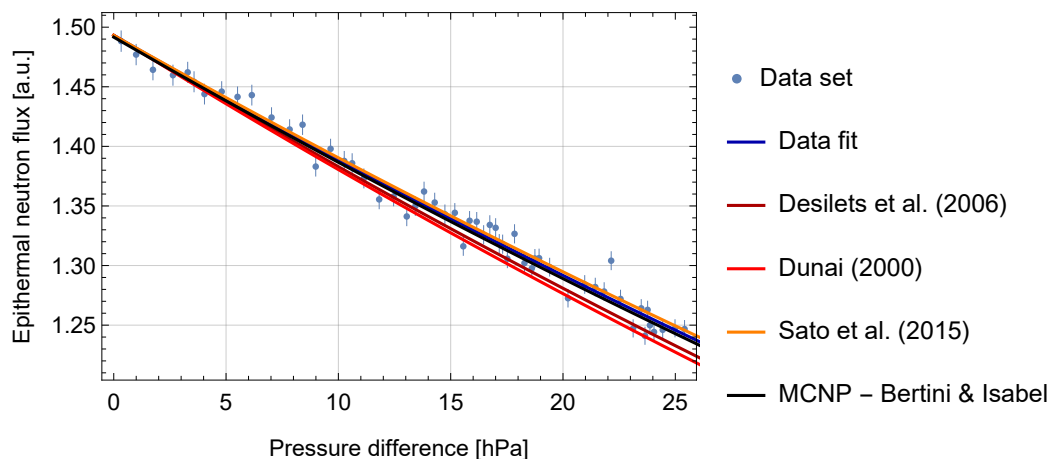


Figure 6.2: Normalized detected neutron counts as a function of air pressure at the stubai glacier field site. The recorded data and its exponential fit are indicated by the blue dots and line. The attenuation lengths of the works of Desilets et al., 2006, Dunai, 2000 and Sato, 2015 are listed alongside the high-energy model combination of the MCNP simulation batch that fitted the data the best. Zero pressure difference corresponds to an absolute value of 690 hPa.

The field data is then used to calculate an atmospheric attenuation length (λ_h), which is given in g/cm^2 . This attenuation length is normally used for correcting the epithermal neutron flux for pressure variations (see section 2.4.5). Thus, this data not only allows for validating MCNP simulations and calibrating them in terms of the high-energy model choice but also to validate existing attenuation length values from the literature. Dunai, 2000 and Desilets et al., 2006 provide analytical functions to derive location-dependent attenuation lengths. Their values are scaling factors of cosmogenic nuclide production which is mostly due to spallation by cosmic rays and for fewer cases due to thermal neutron absorption. Because the spallation rate also controls the cosmic-ray neutron production, their attenuation length values are believed to describe pressure-induced signal variations accurately. Desilets et al., 2006's functions are the standard for pressure correction in the context of CRNS. Sato, 2015 provide complete atmospheric neutron spectra as a function of location. Their work also comprises spectra above moist soil and water. These spectra are then weighted using a detector response function (see section 2.4.3), which results in an attenuation length adapted to the CRNS energy range.

The results are displayed in Tab. 6.1 and Fig. 6.2 and indicate an underestimation in attenuation length by Desilets et al., 2006 and especially Dunai, 2000. The inferred attenuation length by weighting Sato, 2015's neutron spectra agrees well with the measured data. Attenuation lengths deduced by MCNP simulation vary significantly indicating the importance of the correct model choice. Using a combination of the Bertini model to simulate nucleon and pion transport below 3.5 GeV along with the Dresner evaporation model, the Isabel model for low energy light ion transport below 940 MeV and the LAQGSM treating all particles above

Data set		λ_h [g/cm ²]
Measurement	Stubai glacier	142.9 (28)
	Lakes	143.4 (72)
MCNP6 (this study)	Bertini + Dresner	141.2 (17)
	Isabel + Dresner	134.5 (15)
	CEM03.03	137.1 (18)
	Isabel + Abla	134.9 (17)
Literature	Dunai, 2000	130
	Desilets et al., 2006	133
	Sato, 2015	143

Table 6.1: Comparison of effective neutron attenuation lengths in the atmosphere. The fit error of the simulation results is given in brackets.

these energy thresholds, resulted in an attenuation length that agrees with the measured data within the uncertainty range (see also section 4.5 on the high-energy model options).

6.1.3 Lake-side snap shots

Four one-day measurement campaigns were conducted at Lake Garda ((lat,long)=(45.55270, 10.71062), 65 m a.s.l.), Lake Constance ((47.55150, 9.66767), 395 m a.s.l.), Lake Walchen ((47.59214, 11.34794), 801 m a.s.l.) and Lake Sils ((46.42270, 9.73679) 1,797 m a.s.l.) that cover a large range of altitudes, i.e. atmospheric pressure states, and a vertical cut-off rigidity range from 4.2 to 4.8 GV. In addition to the altitude, the four lakes were selected because their surface area is big enough to cover the detector's R_{86} footprint radius at least twice at saturated conditions (see also section 7.1) in order to guarantee insignificant influence of the dry lake shore. The detector was mounted 30–50 cm above the water surface on rented boats. The statistical uncertainty of the measurements strongly depends on the lake's altitude, due to the exponential increase in the neutron flux with altitude. Each lake-side campaign is treated as a single measurement point. The detector system's count rate was then inter-calibrated to that of the Stubai glacier during two days. The Stubai data set covers a lot of data around 715 hPa. That pressure state is added to four lake data points. All data is corrected for atmospheric humidity using Köhli et al., 2021 in the limit of 100 Vol-% soil moisture.

A MCNP simulation batch is run, using the setup described above, simulating the epithermal neutron flux weighted with the detector response function above an infinitely expanded water surface at pressure states that cover the whole range of the lake campaign and values in between (see Fig. 6.3). This section only covers the high-energy model combination that fitted the glacier data set best. The inferred intensity pressure relation slightly deviates from a strict exponential decline, indicating a change in attenuation length with altitude. This change is to be expected as the various precursor particles that contribute to the neutron flux generation possess different attenuation lengths and is also included in the values provided by the other studies. Note that, although a relatively large altitude range was covered, the range in atmospheric depth only amounts to 300 g/cm². A second exponential, featuring a much larger attenuation length, contributes to less than 4 % of the decline. This indicates that in the pressure range presented here, a pure exponential function is suitable to describe the data. However, the resulting data fit shows a larger error than that of the Stubai data set due to high statistical uncertainty of the lake measurements at low altitudes.

Fig. 6.3 confirms that Desilets et al., 2006 and Dunai, 2000 propose attenuation lengths too short to reproduce the data presented here. The neutron spectra provided by Sato, 2015 reproduce the measurements better than the previous two but also show an underestimation of the attenuation length. The best reproduction was achieved with MCNP. The simulation results as well as the functions provided by the literature were normalised to the Stubai measurement point (pressure difference equals 25 hPa) because it shows the lowest statistical uncertainty.

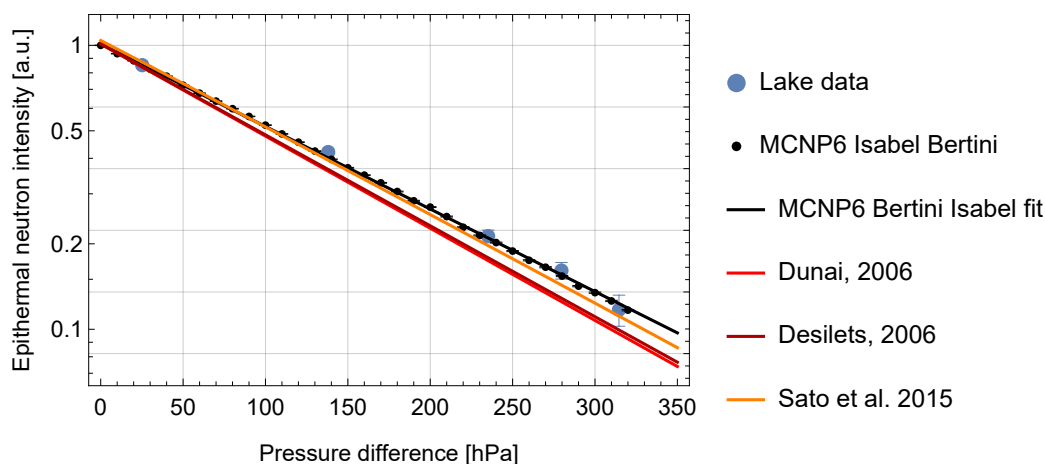


Figure 6.3: Normalized neutron intensity at saturated conditions as a function of atmospheric pressure. Measured data covering five pressure states is compared to a MCNP simulation batch and attenuation length values from Desilets et al., 2006, Dunai, 2000 and Sato, 2015. Zero pressure difference corresponds to an absolute value of 690 hPa.

Fig. 6.4, left displays the difference between MCNP simulation results and Sato, 2015's functions compared to the measured data relative to the latter. Negative values correspond to measured count rates exceeding simulated data. Both show similar discrepancies pointing to systematic errors in the measurements. The lake Sils data point features a measured count rate that significantly exceeds the predicted values for both models. It is the smallest of the four lakes with a maximum distance to the shore line of approximately 400 m. Lake Sils is also subject to strong winds during many days a year as was the case during the recording, which lead to a strong wind-induced displacement throughout the measurement. The detector's location was tracked via GPS during the recording revealing a minimum distance of 300 m for short time periods. Thus, a small contamination of the lake shore enhancing the neutron flux could have occurred. Schattan et al., 2019 also concluded that complex topology can influence the neutron flux. They used Monte Carlo simulations to show that dry uphill terrain such as near-by hills or mountains contributed to the neutron flux over a snow pack by directing neutrons to the detector's location. A similar situation could give rise to the high count rates of Lake Sils as it is surrounded by mountains that tower over the lake.

Fig. 6.4, right compares simulated neutron spectra above Lake Sils calculated with MCNP and taken from Sato, 2015. Although the spectra coincide roughly, there are still some qualitative differences worth noticing. The ratio between the high-energy and evaporation peak is lower in their function indicating different spallation and evaporation behaviour. The highly structured evaporation peak of the MCNP simulation is due to the resonance peaks of the oxygen cross section. Sato, 2015 show similar features in their simulation results, however, their analytical functions do not cover these structures. In the epithermal energy

6. MCNP model validation, calibration and application

regime MCNP's calculated intensity flattens while Sato, 2015 suggest a steady increase of flux with energy. As this domain is dominated by elastic scattering that constantly moderates neutrons to lower energies where absorption increases, a decline in intensity to lower energies is expected. This behaviour of MCNP is also observed in section 7.2.2. The slightly lower peak in the thermal energy regime points to an enhanced absorption in MCNP simulations.

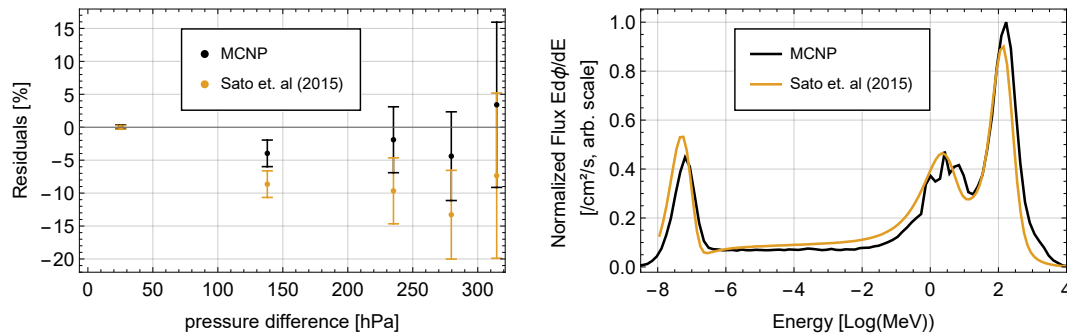


Figure 6.4: Comparison of neutron fluxes by simulating the whole atmospheric column between MCNP and PARMA/EXPACS (Sato, 2015) **Left:** Difference of measured minus model-predicted intensity relative to the measured intensity as a function of pressure difference. Zero pressure difference corresponds to an absolute value of 690 hPa. **Right:** Cosmic-ray neutron spectra at saturated conditions and approximately 830 hPa atmospheric pressure inferred from MCNP simulations and EXPACS. This pressure state relates to that of the Lake Sils data set.

6.2 Deep soil intrusion: Groundwater shaft soil moisture sensing

Disclaimer: This chapter is the result of a close cooperation with Daniel Rasche from GFZ, Potsdam, who carried out all the field measurements mentioned below and contributed many ideas to the simulation setup.

In the 1950s active neutron probes were first engaged to measure moisture contents below the soil surface (Gardner et al., 1952). This method incorporates an active neutron source and measures the moderation capability of the soil that directly relates to its hydrogen content: Evaporation neutrons with energies around a few MeV, depending on the exact source type, are emitted towards the soil and a thermal neutron detector monitors the intensity of slowed down and backscattered neutrons (Ferronsky, 2015). Beyond that, active neutron probes have been applied in oil, uranium and detection of explosives (Oraby et al., 1990; Woolson et al., 1980; Vourvopoulos et al., 2001) or even on Mars for water exploration (Mitrofanov et al., 2016). The advantage of an active neutron probe against other in-situ soil moisture measurements is the large support volume, empirically estimated by Ølgaard's equation to (in Kristensen, 1973; Gardner, 1986)

$$R_{95} = \frac{100}{1.4 + 0.1 \cdot \theta}, \quad (6.1)$$

where θ is the volumetric water content Vol-% and R_{95} denotes the radius of a sphere from which 95 % of the soil moisture response originates. This sphere's radius therefore varies significantly between approximately 70 and 14 cm for $\theta = 1$ and 60 Vol-%. Van Bavel et al., 1956 concluded similar footprint dimensions. The large footprint is mainly due to the high energy of the neutrons emitted by the source, which allows them to travel deep into the soil. A drawback of using an active neutron probe are the high precautions one needs to take handling the neutron source (IAEA, 1970). Consequently, active neutron probes are solely deployed as a non-continuous measurement technique.

Instead of an active probe, cosmic-ray neutrons can also be used as a passive proxy of moisture content at various depths in the soil. Shafts, such as groundwater access tubes, can be utilized to lower a neutron detector into the soil volume. This faces the main challenge of high statistical uncertainty as the neutron flux decreases with soil depth. At the same time, the temporal variability of soil moisture decreases with depth, which allows for longer integration time periods. The thermal or epithermal neutron intensity $I(z) = I(d(z), \theta(z))$ z cm below the ground level then becomes a function of soil depth d [g/cm²] and moisture content θ in the vicinity of the detector. The soil depth d , i.e. the material mass column above the sensor, determines the attenuation of the high-energy flux that creates evaporation neutrons in the vicinity of the neutron sensor. It is defined as the integral from the soil surface down to the centre of the neutron detector over the total material by

$$d(z) = \int_0^z [\theta(z^*)\rho_w + \rho_{b,r}(z^*)] dz^*, \quad (6.2)$$

where $\rho_{b,r}$ is the bulk density in g/cm³ and $\rho_w = 1$ g/cm³ the density of water. The hydrogen content $\theta(z)$ around the detector moderates these evaporation neutrons down to thermal energies and, thereby, influences the neutron flux that reaches the sensor.

The estimation of d marks a difficulty as $\theta(z^*)$ and $\rho_{b,r}(z^*)$ need to be known precisely to calculate d . This suggests an iterative measurement approach starting from shallow soil intrusions because the deeper regions can only be monitored accurately with the knowledge of the overlying soil layers.

The field measurements were carried out at the Serrahn observation site, which is part

6. MCNP model validation, calibration and application

of the Terrestrial Environmental Observatory TERENO and was described in more detail by Bogena et al., 2022. The soil setup and sedimentological profile was intensively studied during the drilling of a groundwater observation well. Profiles for the bulk density, lattice water and organic matter were taken in February, 2019. Furthermore, in-situ point-scale soil moisture sensor profiles (Truebner GmbH, 2021, type SMT100) are installed in a distance of $\approx 20\text{--}30$ m from the groundwater shaft at depths of 70, 130, 200 and 450 cm below the soil surface. This allows for a precise estimation of the penetration depth d and provides a validation data set.



Figure 6.5: Measurement setup at the Serrahn field site. The white box houses the data logging electronics which is connected via long ethernet wires, covered by the black cable conduit, to the thermal neutron detectors and their read-out electronics. These are lowered inside the groundwater shaft which is composed of a stainless steel cylinder. Air humidity, pressure and temperature is monitored with the sensor mounted on an additional pole.

In this study a thermal, ^3He based, instead of an epithermal neutron detector is used for three reasons: (1) An epithermal neutron detector would not fit into the groundwater shaft due to the additional PE moderator needed; (2) very low count rates are expected deep in the soil and a thermal neutron detector is expected to measure higher overall count rates due to its higher efficiency and the built-up of a large thermal peak; (3) As the thermal energy regime is sustained by the moderation of epithermal neutrons, the thermal intensity fades slower with soil depth than the epithermal intensity. The drawback of using a thermal neutron detector is the higher susceptibility to trace elements in soil. Especially boron and gadolinium act as strong absorbers in the thermal energy regime and are contained in small traces in some soils.

The overall simulation setup is schematically shown in Fig. 6.6. The soil composition is chosen to be 75 Vol-% SiO_2 and 25 Vol-% Al_2O_3 in order to test the robustness of a more general simulation approach, which can be transferred to other sites. The moisture content is distributed homogeneously in the soil and the atmospheric pressure and humidity content are set to 1013.25 hPa and 5 g/m^3 , respectively. The simulated parameter set involved all combinations of ten soil moisture values ranging from 0.5 to 50 Vol-% and 14 depth values ranging from 50 to 1500 g/cm^2 .

The measurements deployed two thermal detectors simultaneously at different depths in order to enhance the count and depth sampling rates. Previous, to the groundwater shaft measurement campaign, both detectors were placed above a water surface at a lake. This

was done for two reasons: (1) as an intercalibration between the two detectors and (2) as an approach to a non-site specific calibration method. Alternatively, one could measure thermal neutron intensities at the site itself in order to link below soil intensities to simulation results.

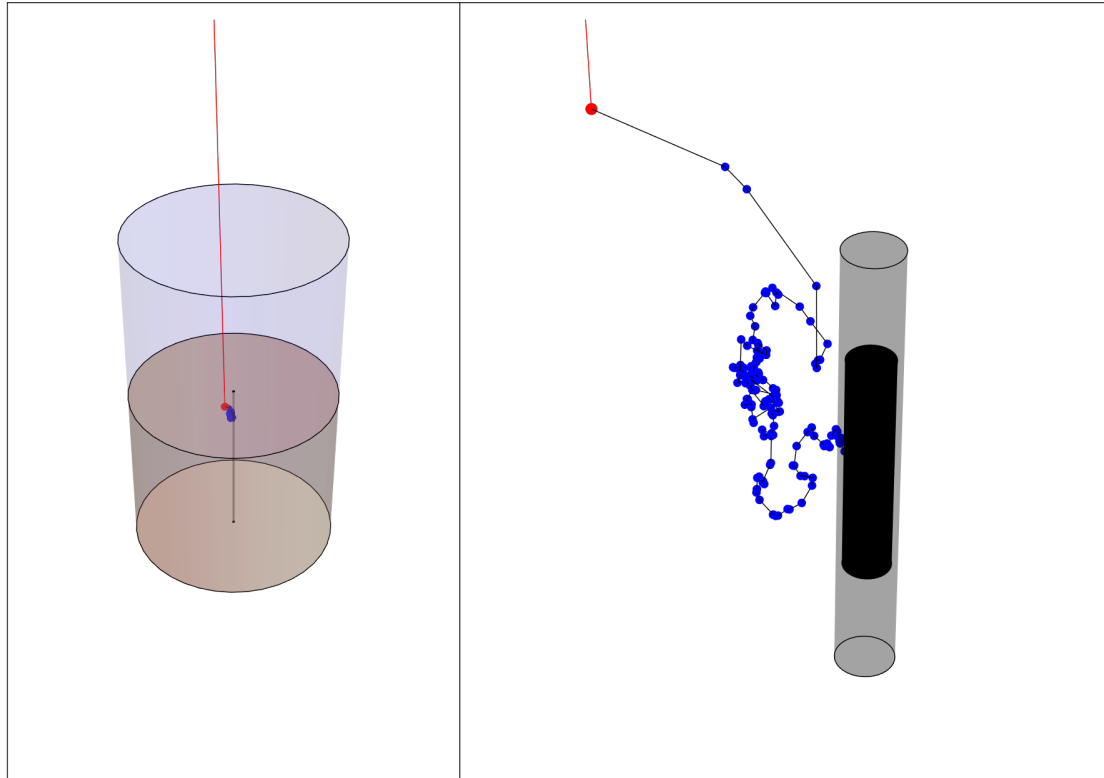


Figure 6.6: Monte Carlo simulation setup for groundwater shaft measurements. **Left:** The setup comprises a long cylinder along the z-axis with a radius of 6 m. The air volume extends to 1000 m height and has a cosmic-ray neutron, muon and proton source set at 450 m height. Below that the soil extends to 10 m depth. The thermal neutron detector contains 1.5 bar ^3He , is 50 cm high and has a radius of 5 cm. It is embedded in a PVC groundwater access tube with an inner radius of 5.75 cm and a thickness of 5 mm. In this example, the center of the detector is located at approximately 186 cm depth and the surrounding soil has a moisture content of 18 Vol-%, leading to an overall depth of 300 g/cm^2 . The path of a detected neutron is shown: Red dots mark the interaction of the precursor neutron with $E = 2.6\text{ GeV}$, which triggers the evaporation of a 10 MeV neutron at an oxygen nucleus. This neutron then scatters more than 150 times in the soil while being moderated down to thermal energies and is finally absorbed by the detector (indicated via the blue dots). The **right** panel shows a close-up of the moderation process: As the neutron's energy decreases the mean free path also decreases, leading to a contraction of the path lengths between scattering events.

6.2.1 Intensity relation

This section presents a function for the thermal neutron intensity at a depth d below the ground surrounded by a soil with moisture content θ . It is compared to measured neutron intensities but also allows for soil moisture estimation if the thermal neutron flux and the depth of the detector are known. The depth dependent thermal intensity relation can be subdivided into three parts as is indicated by Fig. 6.7.

6. MCNP model validation, calibration and application

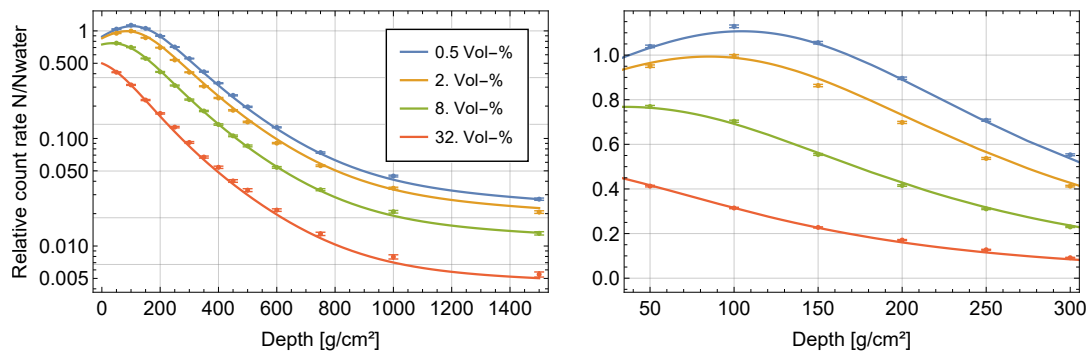


Figure 6.7: Left: Depth dependence of simulated thermal neutron intensities for various soil moisture contents. Count rates are normalized to the thermal intensity above a water surface, that acts as a calibration measurement. The dots mark the simulated flux values and the line the fitted functions described by Eq. 6.3. **Right:** Zooming in on shallow soil depths reveals a moderation optimum for low moisture contents.

At shallow soil intrusions, soils with different moisture content show a non-linear behaviour. Dry soils possess very little moderation power to slow down epithermal neutrons down to thermal energies. This is why, in these dry cases, the neutron flux needs to penetrate into the soil by a significant distance in order to build up the thermal neutron flux before it decreases. At higher moisture levels this moderation optimum shifts to lower depths as the soil moisture increases and finally vanishes at around $\theta = 5$ Vol-%. Below these depths, the thermal neutron flux exhibits an exponential decrease that is due to the reduction of neutron production via hadronic showers in soil that shows a similar depth dependent pattern as described in section 5.1.2. Around 600–800 g/cm² a tipping point occurs and the attenuation is lowered because muons become the key neutron production agent.

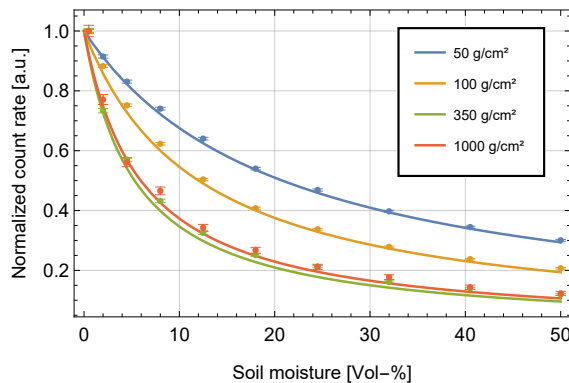


Figure 6.8: Thermal neutron intensity as a function of soil moisture at various penetration depths.

For a fixed penetration depth, the intensity shows a hyperbolic dependence on soil moisture similar to that of above ground epithermal neutrons. However, this hyperbola is changing, revealing that a clear separation approach is not valid for shallow soil intrusions ($I(z) \neq I(d) \cdot I(\theta)$). This effect saturates at around 200 g/cm², which also marks the depth at which virtually all detected neutrons evaporated in the soil volume. Above this depth threshold, a part of the thermal flux evaporated in the air volume or at least interacted in it. This leads to an atmospheric signal interference, i.e. parts of the detector's footprint show a constant moisture content, which in turn results in a lower effect of the changing soil moisture content. The result is a flattening of the soil moisture dependence curve. Additionally, the dry soil's bulk density $\rho_{b,r}$ plays a key role. The neutron moderation ability of the soil directly relates to

parameter	p_1	p_2	p_3	p_4	p_5
value	0.2449	$-1.289 \cdot 10^{-2}$	$2.341 \cdot 10^{-3}$	$-1.417 \cdot 10^{-4}$	0.1156
parameter	p_6	p_7	p_8	p_9	p_{10}
value	$-5.206 \cdot 10^{-3}$	$6.762 \cdot 10^{-2}$	-110.67	0.4022	$-1.3974 \cdot 10^{-2}$

Table 6.2: Fitted parameters of Eq. 6.3–Eq. 6.5 against above shown simulation results.

the ratio of dry material, at which neutrons scatter but barely lose energy, and hydrogen that slows neutrons down. For a given volumetric moisture content, moderation is more efficient if the density of the dry soil matrix is low.

The simulated thermal neutron intensity as a function of depth and local soil moisture content can be described by

$$I(d, \Theta) = \frac{F_1(d)}{F_2(d) + \Theta}, \quad (6.3)$$

with the function definitions

$$F_1(d) = \frac{\rho}{1.43} [p_1 \text{Exp}(p_2 d) + p_3 \text{Exp}(p_4 d) + p_5 \text{Exp}(p_6 d)], \quad (6.4)$$

$$F_2(d) = \frac{\rho}{1.43} [p_7 \text{Exp}(p_8 d) + p_9 \text{Exp}(p_{10} d)], \quad (6.5)$$

where d , Θ and ρ are the dimensionless parameter of depth/(g/cm²), θ /(Vol-%), and $\rho_{b,r}$ /(g/cm³). The fitted parameters are tabulated in Tab. 6.2.

6.2.2 Footprint dynamics

Passive below-ground-surface soil moisture monitoring by cosmic-ray neutrons exhibits a few drawbacks when compared to other techniques. These are in particular high statistical uncertainties due to the low neutron flux, expensive equipment, accessibility (shaft or similar needed). On the other hand, the advantages of the method are similar to those of above-ground neutron sensing: it is mostly sensitive to hydrogen and features a large footprint as estimated by Ølgaard's equation Eq. 6.1. Although, it is important to note that in the case of thermal neutron sensing, as in this case, soil trace elements obtain a more significant role as they can act as strong absorbers. Here, the footprint characteristics are discussed in more detail since this can be the main reason for a future usage of in-soil cosmic-ray neutron sensing. In general, an even larger footprint than the one proposed by Ølgaard is to be expected. That is because in the case of an active probe, the neutrons have to travel from the shaft into the soil where they are backscattered to the detector, traversing the support volume twice. In the case of passive neutron sensing, neutrons are evaporated within the soil volume and therefore only need one transit.

Historically, the neutron detector's radial footprint has been described via the R₈₆ quantile, as the region where 86 % of all detected neutron originate from (Desilets et al., 2013). When Köhli et al., 2015 revised the above-ground footprint, they argued that the origin of the detected neutron has the most influence on the measured signal. Thus, they only accounted for the origin in their radial footprint calculations. In this case, the origin would correspond to the

evaporation location of the detected neutron. Here another approach is chosen: Every elastic interaction above the thermal energy regime is taken into account because these interactions determine the moderation of the neutron. This definition leads to a smaller footprint than only using the origin. Here both definitions are examined and Köhli et al., 2015's approach leads to a larger footprint by 35–70 %. Where the smaller value corresponds to dry and the larger to wet conditions. In the following, the term footprint always refers to the definition that takes into account the whole moderation process.

The footprint was calculated for a depth of 300 g/cm^2 . As mentioned above, depths smaller than 200 g/cm^2 involve atmospheric interference leading to an enlarging of the footprint, because of the low density of air. Hydrogen contained in the air and biomass then plays a significant role. Hence, measurements close to the soil surface are harder to interpret. Below that the footprint should not change significantly until the muogenic neutrons dominate.

Fig. 6.9 shows the scattering locations of detected neutrons as a function of radial (left panel) and vertical distance (right panel) to the detector's centre during dry conditions. This reveals a support volume that rather resembles an ellipsoid or egg than a sphere. Due to the decreasing neutron evaporation rate with depth, this ellipsoid's centre is located above the detector's centre. Thus, one probes a part of the soil that is located above the detector itself.

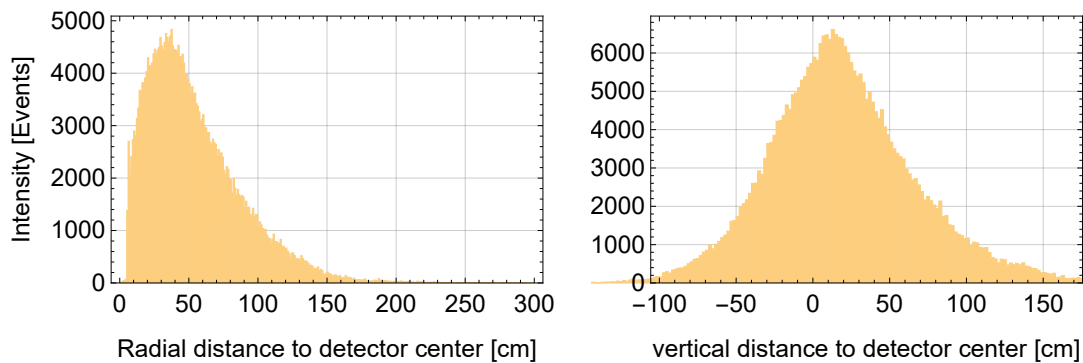


Figure 6.9: Footprint characteristics at 300 g/cm^2 below the soil surface with a surrounding moisture content of 4.5 Vol-% within a soil matrix with a bulk density of 1.43 g/cm^3 . Histograms of the radial (**left**) and vertical (**right**) distance indicate the detector's support volume.

Both, radial and vertical, coverage strongly depend on the soil moisture content. As the pore space fills with water, the moderation capability of the soil is increased and the footprint shrinks. Fig. 6.10 and Fig. 6.11 show the soil moisture dependence of the 86 % quantile of the radial (R_{86}) and the vertical footprint (V_{86}) as well as the centre of the vertical footprint (V_c) with respect to the detector's centre for a soil with a bulk density of 1.43 g/cm^3 .

Further simulation batches are run featuring soils with bulk densities ($\rho_{b,r}$) of 1.1 and 1.8 g/cm^3 . As discussed above, $\rho_{b,r}$ adds to total soil material that shields the neutron radiation. Larger $\rho_{b,r}$ values, therefore, lead to smaller footprints. Taking $\rho_{b,r}$ and θ into account, the 86 % quantiles show a hyperbolic relation:

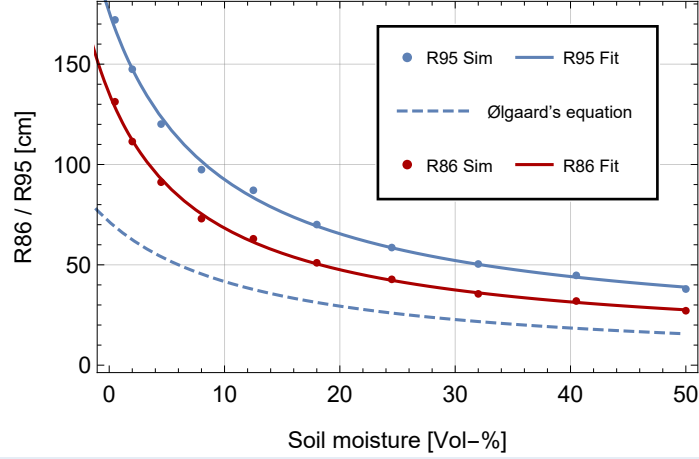


Figure 6.10: Radial footprint characteristics at 300 g/cm^2 below the soil surface with $\rho_{b,r} = 1.43 \text{ g/cm}^3$.

$$R_{86}(\rho, \Theta) = \frac{c_1}{\rho(1 + c_2\Theta)} + c_3\rho^2, \quad (6.6)$$

$$V_{86}(\rho, \Theta) = \frac{a_1}{\rho^{1.2}(1 + a_2\Theta)} + a_3\rho^{0.5}, \quad (6.7)$$

where R_{86}/V_{86} are given in cm, Θ and ρ are again dimensionless parameter as defined above and a_i and c_i are tabulated in [Tab. 6.3](#). Both R_{86} and V_{86} describe radial distributions that are the semi-axes of the footprint ellipsoid. They converge to limit values for $\theta \rightarrow 100 \text{ Vol-}\%$. In the vertical footprint's case this limit takes the value of the detector's dimension: a_3 equals half of the detector's height. The radial footprint's limit correlates to $\rho_{b,r}^2$, this may point to the enhanced evaporation capability in the presence of more dry soil material. [Fig. 6.10](#) reveals a larger footprint of the passive neutron sensing method as compared to the active probe as is expected due to the reasons mentioned above.

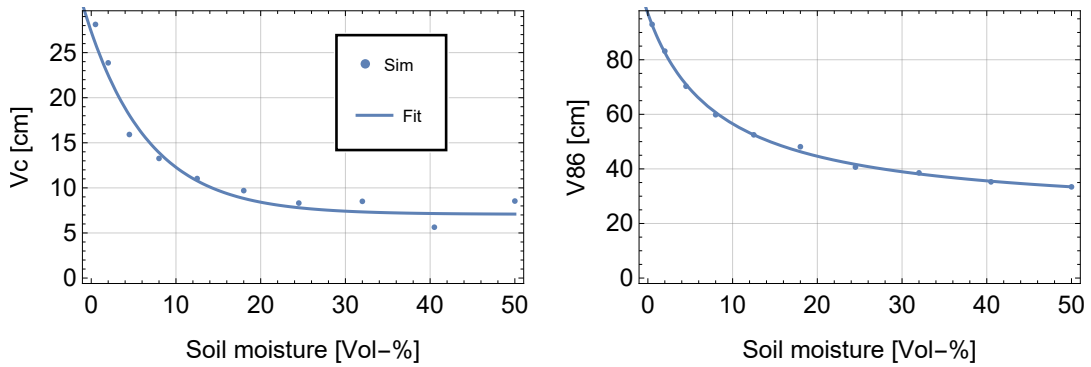


Figure 6.11: Vertical footprint characteristics at 300 g/cm^2 below the soil surface with $\rho_{b,r} = 1.43 \text{ g/cm}^3$

The position of the footprint's centre with respect to the detector's centre features a steeper correlation to the soil moisture content and saturates for $\theta > 20 \text{ Vol-}\%$. It is best described by an exponential law:

$$V_c(\rho, \Theta) = \frac{b_1 \text{Exp}\left(-\frac{\Theta}{b_2}\right)}{\rho} + b_3 \rho^{0.7}, \quad (6.8)$$

where V_c takes the units cm. All fit parameters are listed in Tab. 6.3. The exponential relation of V_c and soil moisture leads to a large shift of the actual measurement depth during dry conditions. The simulated value of V_c for $\theta = 0.5 \text{ Vol-}\%$ and $\rho_{b,r} = 1.1 \text{ g/cm}^3$ approximates 35 cm. This is due to the large distances covered by the neutron tracks, also indicated by R_{86}/V_{86} and the strong decline of the evaporation potential with soil layer depth. This footprint shift has to be taken into account when one retrieves soil moisture values.

$V_{86} - V_c$, par	a_1	a_2	a_3	b_1	b_2	b_3
value	$1.01 \cdot 10^2$	$1.21 \cdot 10^{-1}$	19.4	28.5	6.51	5.51
R_{86}, par	c_1	c_2	c_3			
value	$1.80 \cdot 10^2$	$1.13 \cdot 10^{-1}$	4.05			

Table 6.3: Fitted parameters of equations Eq. 6.6, Eq. 6.7 and Eq. 6.8. The parameters a_1 , a_3 , b_1 , b_3 take the units cm.

6.2.3 Comparison to field site measurement data

The procedure to compare the in-situ measured and CRNS retrieved soil moisture values was conducted as follows. First, the soil moisture content at the depth of the thermal neutron detector was estimated by simple interpolation between the nearest FDR probes in terms of depth. The actual probing depth of the neutron detector was then calculated using Eq. 6.8. The interpolated soil moisture value of the FDR probes at this actual probing depth is the value the CRNS retrieved moisture content is compared to. The depth in g/cm^2 of the neutron detector's location was estimated using the soil moisture and bulk density profiles added by 1.9 g/cm^2 , which accounts for the above-ground forest biomass. This value is time dependent according to the soil moisture variations. The CRNS soil moisture content was calculated by numerically inverting Eq. 6.3 in combination with the detector's count rate divided by the above-lake count rate and the inferred detector depth in g/cm^2 . Both pressure and incoming correction were applied to the measure neutron count rate. However, the effect of air humidity was assumed to be negligible as the neutrons' trajectories between evaporation and detection lie within the soil volume.

Fig. 6.12 shows the measured soil moisture dynamics at an actual measurement depth of 88 cm below the soil. On average 100 neutrons were detected per hour. A moving average of 48 hours was applied to the count rate in order to filter spikes due to the high statistical uncertainty. The CRNS predicted values show a bias to dry conditions as compared to the FDR values. During the campaign the total precipitation amounted to 416 mm leading to a wetting of the soil, which is captured by both data sets. Both sets show similar dynamics that are smoothed out in the case of the neutron retrieved values due to the temporal averaging.

An analogue measurement was conducted during the same time interval using a second detector at 200 cm below the soil surface (see Fig. 6.13). This data set shows a bias to higher soil moisture values of the CRNS retrieved data, which might lead to the assumption that the neutron flux decrease with depth is not well covered in Eq. 6.3. However, a third data set at 500 cm depth again reveals a slight underestimation of the CRNS soil moisture values as compared to the FDR data (see Appendix B.1). Both time series indicate a slow increase in moisture content similar to the shallower data set. However, the CRNS values

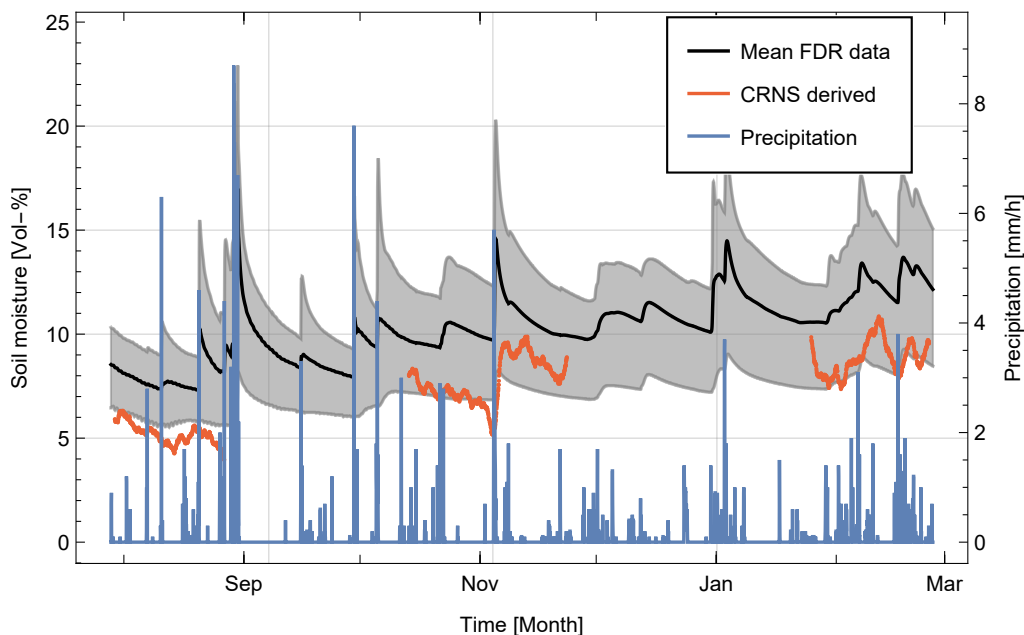


Figure 6.12: Measured soil moisture dynamics at 100 cm below the soil surface corresponding to ≈ 88 cm or 130 g/cm^2 actual probing depth of the neutron detector. The campaign was conducted during the winter 2021/22. Note the two y-axes, indicating soil moisture (left) and precipitation (right). The gray area spans the minimum and maximum FDR-interpolated soil moisture content at 85 cm and the black curve their mean value. Sensor failure appeared during several periods (see red curve). A two-day moving average was applied to the neutron count rate due to low statistics.

exhibit much more pronounced dynamics, e.g. after the rain event at the end of August, 2021. It is not clear whether this event lead to significant water intrusion to these depths or not.

Both depth time series reveal a prominent dip in CRNS retrieved soil moisture prior to the rain event 5th–6th of November, 2021. This increase in count rate seems unrelated to soil moisture variations since it is not captured by the FDR probes and a drying process is expected to show slower dynamics. One reason for this pattern might be due to leaching of airborne radioactive isotopes into the soil when captured by rain drops indicated by several studies on gamma-ray activity (e.g. Serafini et al., 2020; Bottardi et al., 2020). An increase in gamma-ray activity at these specific days was also reported by the ODL network of the BFS (Bundesamt für Strahlenschutz) at three stations located within 25 km distance to the field site (Lychen, Wesenberg, Godenswege)¹. Other rain events during the field campaign show much lower dose rate amplitudes according to this network, which coincides with this work's measurements. Bottardi et al., 2020 indicated that several decay products that can be allocated to the ^{222}Rn i.e. the ^{238}U decay chain exhibit an intensity increase at the ground level after rain fall. These include ^{222}Rn , ^{218}Po and ^{210}Pb , which emit alpha particles above 5 MeV. Mendoza et al., 2020 argued that for low neutron flux conditions, (α, n) reactions could significantly increase the neutron flux. The cross section for this reaction at 6 MeV accounts to 25 and 3 mb for ^{27}Al and ^{28}Si but is negligible for ^{16}O . If the increase in these radioactive isotopes is high enough during such rain events in order to explain the observed rise in neutron flux by this mechanism is not examined here but may be targeted by

¹<https://odlinfo.bfs.de>

future works. The count rate might also be enhanced directly by gamma ray induced false positive events, however the gamma-ray sensitivity of these neutron detectors is $\approx 10^{-5}$.

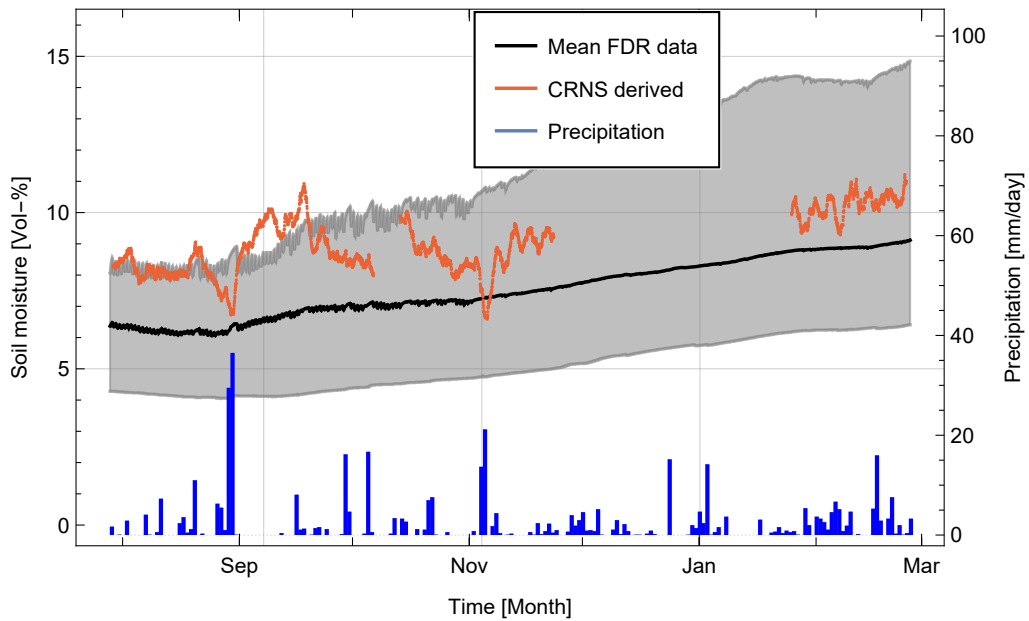


Figure 6.13: Measured soil moisture dynamics at 200 cm below the soil surface corresponding to ≈ 182 cm or 300 g/cm^2 actual probing depth of the neutron detector. See caption of Fig. 6.12 for more information.

6.3 Below the water table: buried cosmic-ray sensors

In recent years, snow-buried sensors have gained a lot of popularity as snow monitoring devices (see e.g. Gugerli et al., 2019; Howat et al., 2018; Wallbank et al., 2021). However, its first application dates back to Kodama et al. (1979) who may have been the first to use cosmic-ray neutrons as a proxy for environmental hydrogen content. The standard sensor applied in this context goes by the name SnowFox™ (Desilets, n.d.). It features the standard 25 mm polyethylene moderator housing, thus, being most sensitive in the epithermal energy regime.

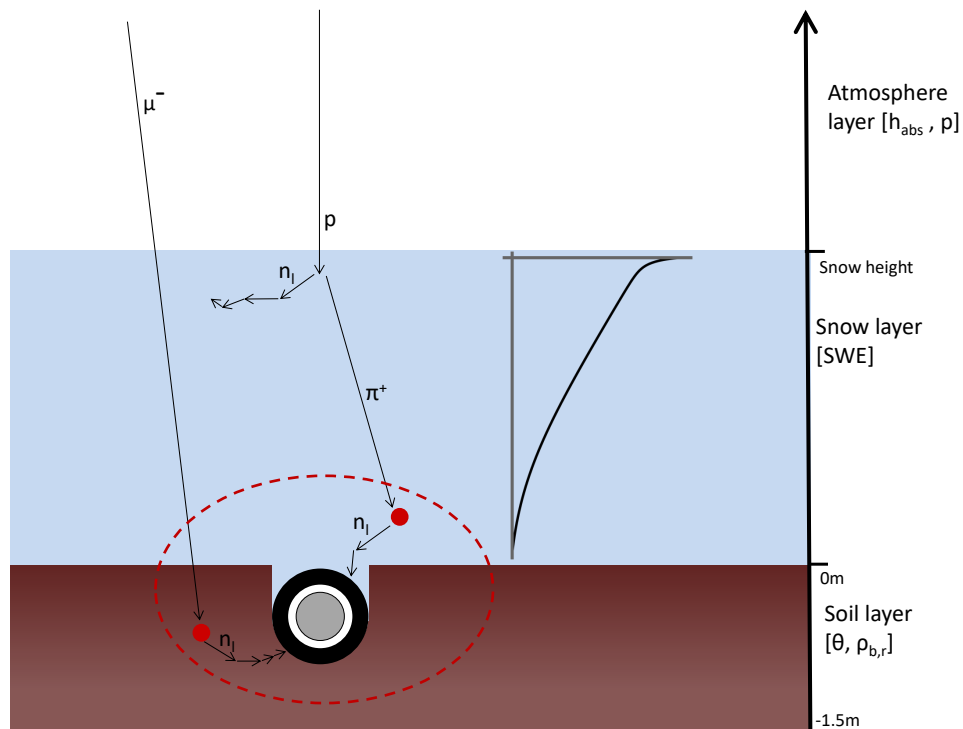


Figure 6.14: Schematic cross section through snow water equivalent measurements by buried cosmic-ray neutron sensors. The snow pack attenuates incoming cosmic-ray particles (the attenuation is indicated by the curve on the right hand side). These particles can trigger spallation and evaporation within the snow or soil volume. Neutrons can impinge on the detector (grey cylinder, surrounded by a black polyethylene shield) if they get evaporated (red dots) within a certain distance of the detector. This distance is marked as a dashed line and represents the range of evaporated neutrons in water/snow and soil. The detector is placed within the soil volume parallel to the interface in order to not disturb snow accumulation.

The snow water equivalent (SWE) of the snow column above the buried sensor attenuates the transmission of the incoming neutron flux (see Fig. 6.14). Inversely, the neutron flux intensity measured by the detector is used to estimate the snow cover thickness or better its SWE value.

The epithermal neutron flux below a snow pack depends on the transmission and moderation of mid-air evaporation and epithermal neutrons at shallow snow cover. Towards thicker snow packs all the detected neutrons are evaporated within the snow or soil volume below. The intensity change per mm SWE increment is then directly related to the attenuation of

the hadronic and muon flux that trigger these evaporation events. A snow-buried sensor, therefore, presents an appropriate experimental device in order to not only validate MCNP simulations but also to calibrate its high-energy models. Compared to the above-ground sensing method², buried sensors feature a much smaller footprint due to the forward-directed high-energy flux and the low range of the isotropic low-energy neutron flux in dense snow. Qualitatively, the dynamics are similar to those described in section 6.2. On the other hand, its sensitivity to SWE reaches far beyond that of above-ground epithermal neutron sensing since the high-energy neutrons, protons and most of all muons can evaporate significant amounts of neutrons deep inside the snow column.

Most model background on the application of buried sensors as well as the neutron intensity - SWE transfer functions are provided by the manufacturer of the SnowFox™ itself. These functions are a combination of empirical and simulation-based results and are only applicable to one soil type. Additionally, footprint characteristics of a buried sensor were never examined and it has been assumed that the detector measures rather locally. The following results present an extract of an article about this topic, which is planned to be published shortly after this work. The findings presented here, are the result of a close cooperation with Paul Schattan (AlpS and University of Innsbruck, Innsbruck Austria), Rebecca Gugerli (University of Fribourg, Switzerland), Benjamin Fersch (KIT alpine Campus, Garmisch Partenkirchen, Germany) and Martin Schrön (UFZ Leipzig, Germany).

6.3.1 Calibration of MCNP input parameters



Figure 6.15: Setup of the field site: The neutron detector enclosed by a black cylinder features a standard moderator with a thickness of 25 mm. It is lowered via a rope winch of a floating pedestrian bridge at the Elephant Butte Lake in New Mexico, USA (courtesy D. Desilets, Hydroinnova).

Regarding simulation calibration and validation, soil-buried sensors introduce significant uncertainties due to the unknown soil composition. Glacier-based sensors, as described by Gugerli et al., 2019, present a much more simple setup in terms of reproducibility because

²Similar to soil moisture sensing, above-ground epithermal neutrons are also used to monitor SWE above the snow pack, which is described in more detail in section 7.2

they are completely surrounded by water (in the form of snow and ice). Errors can still arise due to the measurement of the snow pack's SWE. Reference SWE might be measured by other snow monitoring devices or most commonly through snow pits by recording snow height and density profiles. None of these uncertainties occur in measuring the neutron flux attenuation in water by lowering a sensor into a lake. The water column height above the sensor is measured easily and the sensor is only surrounded by water (neglecting trace components). Additionally, the water column above and below the sensor is constant as opposed to a melting or accumulating snow pack. Thus, single data points can be recorded within longer time scales achieving low statistical uncertainty. It should be pointed out that above thermal energies snow and water feature the same neutron cross sections and the results gained from a water measurement can be directly transferred to the snow case.

The data set chosen for this study was recorded at the Elephant Butte lake (lat=33.24474, long=-107.17044) by Darin Desilets (Hydroinnova LLC). The lake itself is located at approximately 1350 m a.s.l. in New Mexico, USA. The high elevation of Elephant Butte lake comes with a high count rate in comparison to sea level, thus, lowering statistical uncertainty. This is especially useful for deep-penetration measurements as the neutron flux decreases strongly with depth. The setup is shown in Fig. 6.15. The data shown in Fig. 6.16 suggests that the attenuation of the neutron flux in water follows a two-region pattern. In deep water levels a third region appears (not shown here but similar to that in soil, see section 6.2).

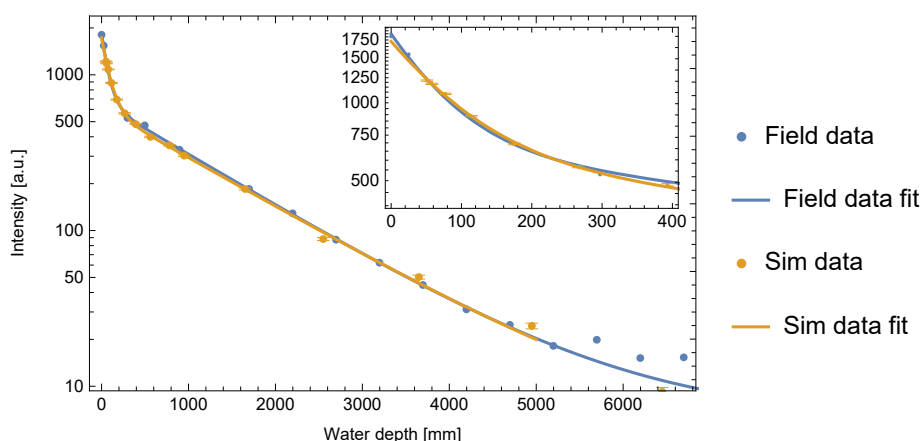


Figure 6.16: Comparison of the simulated and measured attenuation of the epithermal neutron flux through water. The data was recorded at the Elephant Butte lake, New Mexico, USA, during several days. The fit function follows Eq. 6.9.

The attenuation curve qualitatively follows that in soil. Within the first ≈ 270 mm a strong decrease of the neutron flux can be observed with λ_n equals 17 and 18.5 mm for the simulated and measured data set, respectively. This is due to the attenuation of the above-water evaporation and epithermal neutron flux, i.e. neutrons with energies below ≈ 20 MeV. This flux behaves like a neutron gas due to the rather isotropic scattering function. It consists of (1) the incoming low energy neutron flux and (2) production and moderation of neutrons within a large footprint (see section 7.1). Neutrons of that energy regime can travel large lateral distances above the water surface and are still able to penetrate the water to these depths. However, the deeper the water level the higher the neutron energy required to penetrate it.

Below 300 mm virtually all neutrons are generated in the water column itself. The high-energy neutrons and protons are attenuated exponentially by the water column and thus the

6. MCNP model validation, calibration and application

production of lower energy neutrons, as their progeny, declines in a similar manner. The muon flux, on the other side, declines much less leading to a source of muogenic neutrons that stays almost steady within the first 4 m (similar to the dynamics in dry soil, see section 5.1.2). Thus, the second region is dominated by the exponential decrease of the hadronic neutron sources with a small offset of muogenic neutrons.

Around 6 m below the water table half of the neutrons are generated indirectly by cosmic muons. At this stage, the effective neutron attenuation flattens due to the high attenuation length of muons and their increasing production ratio. Compared to dry soil where muogenic and hadronic neutron equality is reached at around 550 g/cm², water shows a muogenic dominance on the neutron flux at similar depths. The simulated and measured data sets agree well up to approximately 5 m water depth. Below that the measured neutron flux flattens supposedly due to the neutron counters background.

The attenuation of the neutron flux intensity is described by

$$N(d) = N_m + N_h \text{Exp}\left(-\frac{d}{\lambda_h}\right) + N_n \text{Exp}\left(-\frac{d^{0.7}}{\lambda_n}\right), \quad (6.9)$$

where the first term describes muogenic background, which is approximately constant within the range of the data set. The second term describes the neutrons created in the hadronic showers featuring an attenuation length of λ_h . Because of the strong directional bias of this high-energy flux, this part can be described via a Beer-Lambert law. The third term adds the attenuation of the mostly diffusive neutron flux with the effective attenuation length λ_n . The diffusive-type movement leads to non-straight trajectories amplifying the effective path length of these neutrons. This is accounted for by the exponent 0.7 which lies between a straight transport (1) and a pure random walk (0.5). The setup is resimulated while only one particle species was embedded as a source term. Fig. 6.17, left reveals the depth-dependent contribution of the different source particle species to the total flux. Fig. 6.17, right shows the muogenic percentage of the total flux that shows a similar distribution as in dry soil (see Fig. 5.5).

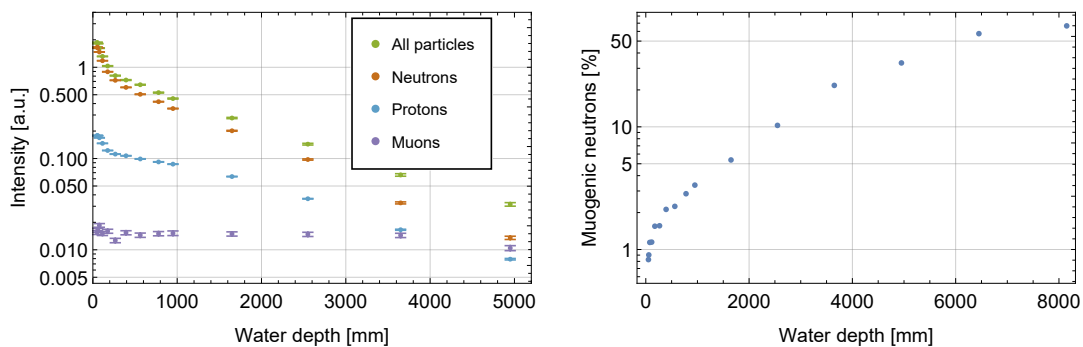


Figure 6.17: Simulation runs of the Elephant Butte site with various particles source permutations. **Left:** The green curve features a simulation with a muon, proton and neutron source in mid air and therefore shows the same data as is depicted in Fig. 6.16. The brown, blue and violet curve show the neutron flux for simulation runs with only the neutron, proton or muon source turned on. **Right:** The contribution of the muogenic neutron flux, i.e. the neutron flux that is indirectly triggered by a source muon, to the total neutron flux is shown as a function of water depth.

The simulation of the first stage of the neutron attenuation exhibits the smallest uncertain-

ties. The cross sections and the physics for neutrons below 20 MeV are well understood. Still, even at smaller water depths many neutrons are evaporated within the domain by high-energy processes.

On the other hand, the attenuation of the high-energy flux below 300 mm requires a rigorous treatment of the intranuclear processes involved. Thus, the second region is suitable to compare the different high-energy models that are included in MCNP. The water depth range is chosen to be 400–4000 mm. For lower values the intensity function is dominated by the sub-20 MeV physics and to higher values the measured data set flattens.

Tab. 6.4 shows the fit results of the measurement data set in comparison to that of MCNP simulation batches and literature values. The data set provided by D. Desilets agrees well with all MCNP simulations within the error margins. The attenuation length proposed by Nesterenok et al. (2012) shows a small deviation to the data set.

Data set		λ_h [cm]
Measurement	Elephant Butte Lake	136(4)
MCNP6 (this study)	Bertini + Dresner	132(3)
	Isabel + Dresner	136(3)
	CEM03.03	136(2)
	Isabel + Abla	134(2)
Literature	Nesterenok et al. (2012)	130
	Kodama et al. (1979)	173
	Zweck et al. (2013)	109
	Delunel et al. (2014)	148(1)

Table 6.4: Comparison of effective neutron attenuation lengths in water. The uncertainty is given as fit errors. The simulations covered a total of 10^8 source particles that resulted in a statistical uncertainty of few per mil to approximately one per cent to deeper water levels. See section 4.5 for more detailed information on the built-in high-energy models of MCNP.

6.3.2 SWE measurements by soil-buried neutron detectors

6.3.2.1 Intensity relation

Many sensors that measure the snow cover thickness via the neutron flux transmission are buried in soil. Thus, the measured neutron intensity is a function of both SWE and soil moisture changes. This mixed signal is examined in this section.

Since the detector is mostly encompassed by soil (see Fig. 6.14), most of the scattering events between evaporation and detection take place in the soil: For shallow snow cover (SWE= 8 mm) soil scattering is by a factor of approximately 30 more likely than snow scattering. This ratio decreases with snow pack thickness and finally reaches a value of 7 to 8.

For this study, batches that comprise all permutations of 7 soil moisture and 14 SWE values are simulated. Exemplary particle tracks of the three snow height stages of detected neutrons and their precursor particles are shown in Fig. 6.18 in order to visualize the particle transport dynamics.

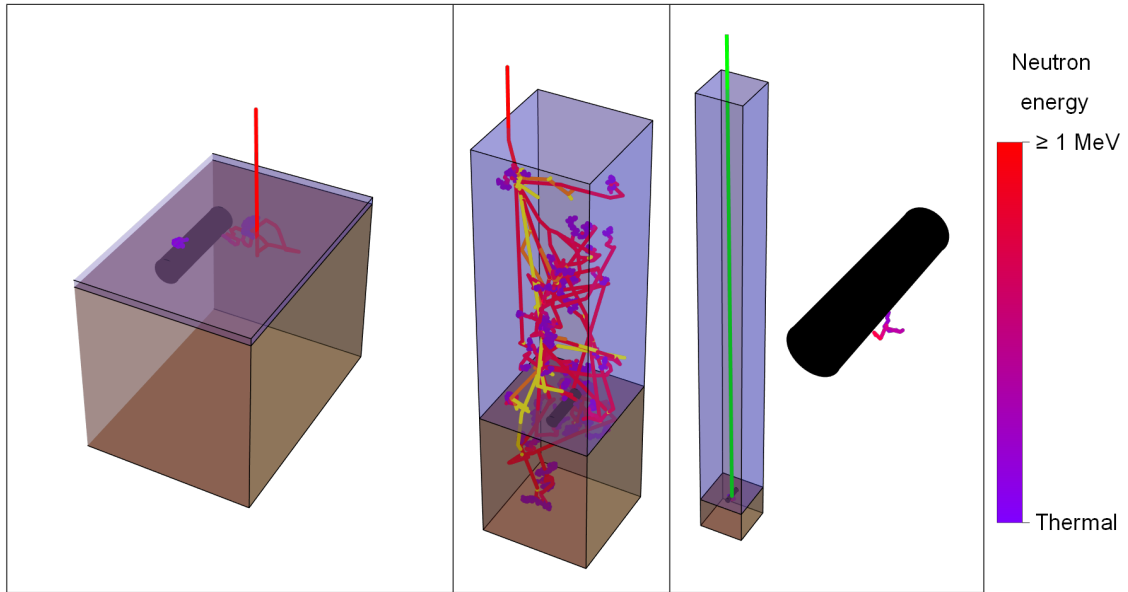


Figure 6.18: Particle tracks at the snow cover-soil interface (the snow layer is marked in light blue). The detector (black cylinder) is embedded in soil (brown volume) with $\theta = 50$ Vol-% and $\rho_{b,r} = 1.43$ g/cm³. The whole particle cascade triggered by one incoming high-energy particle is shown. In each case one of the evaporated neutrons leads to a detection. The particle species shown involve protons (yellow lines), $\pi^{+/-}$ (orange), μ^- (green), alpha particles (not visible at this scale) and neutrons, which are colour-coded according to their logarithmic energy (see bar legend at the right side). **Left:** A neutron with an energy of 110 MeV penetrates the snow cover (SWE= 30 mm) and excites a nucleus within the soil that evaporates two neutrons. As these lose energy due to elastic scattering, their mean free path length shrinks strongly. This leads to agglomerated tracks when neutrons reach thermal equilibrium (violet colour code). **Middle:** A rare high-energy neutron ($E = 15$ GeV) transits the snow surface and invokes a multi-particle spallation and evaporation centre, which in turn leads to subsequent particle production. This particle cascade leads to more than 40 neutron evaporations in the snow and soil volume, one of which leads to a detection (SWE=2,500 mm). **Right:** A muon passes the whole snow layer with SWE= 10,000 mm and invokes a single neutron evaporation directly beneath the detector. The neutron scatters approximately 50 times after which it penetrates the moderator casing (shown in the close up on the right side).

Evaluating the simulation batches confirms the strong influence of soil moisture on the detected epithermal neutron signal (see Fig. 6.19, left). The set of curves can be described by Eq. 6.9, however, with varying factors N_i indicating a soil moisture scaling function independent of SWE. This scaling function can be described by a hyperbola, i.e. shows the same response to soil moisture as above-ground epithermal neutrons:

$$N(\Theta) = b_1 \frac{b_2 + b_3 \Theta}{b_2 + \Theta}, \quad (6.10)$$

where Θ is the dimensionless value $\theta/\text{Vol-\%}$. However, a signal deviation remains for shallow snow cover and dry soils even after applying this scaling function as indicated by Fig. 6.19, right. It can be accounted for by adapting λ_n , which describes the intrusion of the diffusive airborne neutron flux through the snow volume to the detector. These neutrons' trajectories

can pass the soil volume and are therefore moderated by its hydrogen content as well. Although the intensity at the soil-snow interface is higher for dry soil, it experiences a stronger decrease with snow cover than moist soils. Similar patterns can be found for mixed signals between air humidity and soil moisture or in snow and soil moisture signals when monitoring above-ground neutron intensities (see section 7.2.2). These also show cross correlations of different hydrogen pools which is particular noticeable in case one of these features dry conditions. λ_n can be approximated by a bounded growth as to larger depths the neutron signal scales purely with Eq. 6.10.

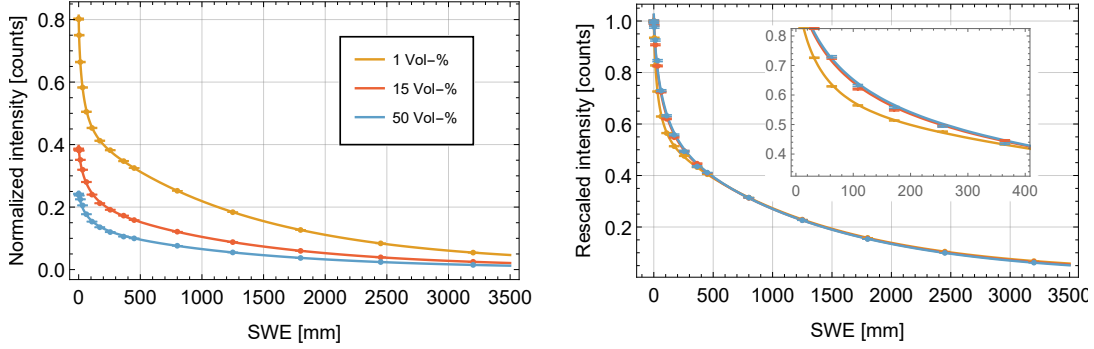


Figure 6.19: Simulated neutron intensities at the snow-soil interface as a function of the snow pack's SWE and for three soil moisture conditions. The intensities are determined by weighting the neutron spectra with the standard detector response function. Both simulation results, indicated by the points with error bars, and the corresponding fit, described by Eq. 6.11 and Eq. 6.12, are shown. **Left:** Intensity normalized to the driest state of the simulation batch ($\theta = 1$ Vol-% and SWE=5 mm). **Right:** The rescaled intensity, divided by Eq. 6.10, reveals a second order effect for shallow snow cover above dry soil.

and the overall intensity transfer function then becomes

$$N(h_{\text{swe}}) = N_{\text{max}} \frac{a_0 + a_1 \Theta}{a_0 + \Theta} \left[N_m + N_h \cdot \text{Exp} \left(-\frac{h_{\text{swe}}}{\lambda_h} \right) + N_n \cdot \text{Exp} \left(-\frac{h_{\text{swe}}^{0.7}}{\lambda_n(\Theta)} \right) \right], \quad (6.11)$$

with

$$\lambda_n(\Theta) = a_2 - (a_2 - a_3) \cdot \text{Exp}(-a_4 \cdot \Theta), \quad (6.12)$$

where h_{swe} is the dimensionless parameter SWE/mm. Both, soil moisture dependent parameters and their corresponding fits are shown in Fig. 6.20. The parameter set determined from these fits is tabulated in Tab. 6.5.

Fit parameter	Value
N_m	0.019 (0.001)
N_n	0.468 (0.007)
N_h	0.513 (0.001)
λ_h	1341 (15) mm
$\lambda_n (\theta > 15 \text{ Vol-}\%)$	20.2 (1.1) mm
a_0	3.48 (0.48)
a_1	0.21 (0.02)
a_2	20.2 (1.1) mm
a_3	10.9 (0.3) mm
a_4	0.12 (0.01)

Table 6.5: List of all parameters needed to describe equation Eq. 6.11. Note that a_2 describes the limit of λ_n towards moist soils and thus takes the same form as λ_n ($\theta > 15 \text{ Vol-}\%$). The uncertainty stated in parentheses is the fit error.

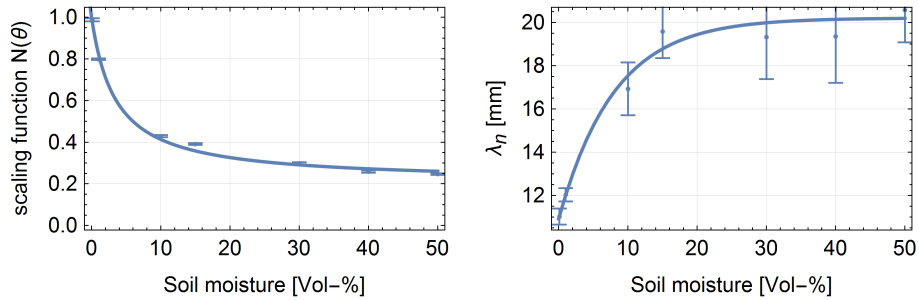


Figure 6.20: Fitting of soil moisture dependent parameters of equation Eq. 6.11. **Left:** The sum over N_i indicates the overall neutron intensity scaling with soil moisture. It follows a hyperbola, similar to that of the above-ground sensing method. **Right:** The soil moisture dependence of the attenuation length of the diffusive neutron flux and the corresponding fit is shown.

6.3.3 Footprint dynamics

So far, neutron detectors buried below the snow pack have been widely regarded as local snow measurement devices with an estimated footprint at the meter scale (Gugerli et al., 2019). However, no study has analysed the support volume of the buried cosmic-ray neutron detector in detail. As was shown before, the neutron intensity to SWE correlation is not only determined by the sub MeV neutron transport but also by the attenuation of high-energy particles. Former analyses of the above ground/snow neutron detector's footprint mainly focused their examination on the epithermal neutron flux. Hence, for the buried sensor a new approach has to be chosen. Here, every scattering event of a detected neutron from evaporation to detection or thermalization, if the neutron reaches thermal equilibrium before detection, is included in the footprint analysis. Thermalization is completed when the neutron reaches an energy below 300 meV as suggested by Weimar et al., 2020. Moreover, every interaction of its precursor high-energy particle(s) is accounted for as well. Thus, the complete particle track from detection through all stages of the particle showers within the snow volume is reconstructed backwards. All events are weighted equally. The following

section is based on simulations of a neutron detector mounted in soil with 50 Vol-% moisture content. The simulation domain had a radial extent of 150 m.

6.3.3.1 shallow snow

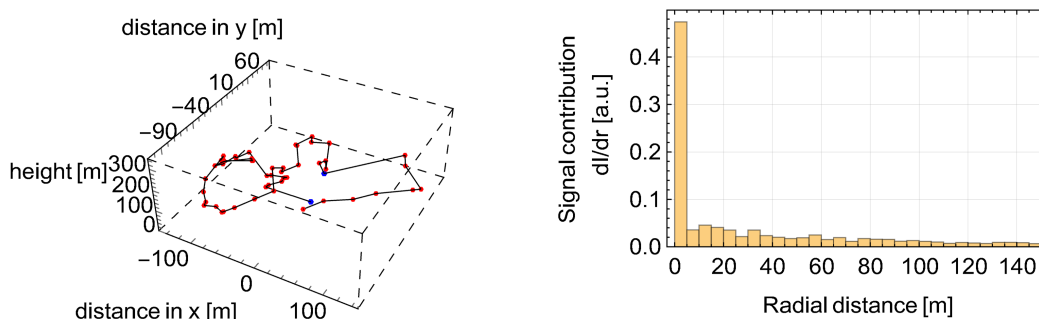


Figure 6.21: Signal influence of a shallow snow cover. **Left:** Scattering centres of a single neutron track. The neutron detector is embedded at the graph's origin in a soil with 50 Vol-% moisture content and covered by a 8 mm thin snow cover of a density of 0.5 g/cm^3 . Red dots mark scattering events in air and blue dots indicate interactions in the snow cover or soil. The incoming neutron possesses an initial energy of 26 MeV. Multiple interactions occur at both locations where it penetrates the snow and soil volume. However, the various blue dots are indistinguishable at this scale because of the short interaction length in the dense material. The distance between the two blue penetration locations is approximately 50 m. **Right:** Intensity contribution as a function of radius in meter of detected neutrons for the same simulation setup.

For shallow snow covers ($\text{SWE} < 300\text{ mm}$), a significant amount of the detected neutrons have energies below 20 MeV while still travelling through the air volume. The neutrons mean free path in air is a lot larger than in soil or snow due to the air density being approximately three orders of magnitude smaller. Additionally, these neutrons possess a rather isotropic scattering function. Therefore, they can change their direction multiple times in air while travelling large distances between scattering events. During the neutron's trajectory, it can also impinge the snow or soil volume, re-enter the air volume and finally penetrate the snow cover once more to reach the detector.

Fig. 6.21 shows an example of this kind of neutron transport in the shallow snow cover regime. These multiple snow cover penetrations and the large distance transport within the air volume lead to a wide spread signal influence. In the case of a very thin snow cover of 4 mm SWE, 24 % of all detected neutrons penetrated the snow volume at a distance larger than 20 m from the sensor. This percentage decreases to 21, 15, 7, 3 and 2 % for snow covers with 14, 32, 63, 158 and 172 mm SWE. Therefore, a strong decline in the radial footprint can be observed with a snow cover increase (see Tab. 6.6). The source particles that trigger neutron detections also change with snow cover increase. Their mean energy doubles from 14 to 108 mm SWE and also experiences a shift towards a more pronounced muogenic and proton-induced flux.

The atmospheric pressure and humidity in these simulation setups were set to 1013 hPa and 3 g/cm^2 , respectively. The radial footprint is expected to expand with decreasing air pressure for shallow snow covers as the air density decreases and therefore the mean free path of the diffusive neutron flux therein increases. For the snow free case, the formulas in Köhli et al. (2015)'s work can indicate suitable scaling functions for the footprint change with pressure and air humidity. The behaviour of these scaling functions with increasing snow

shallow snow				deep snow	
SWE [mm]	R_{63} [m]	R_{86} [m]	precursor (n, p, μ) [%]	SWE [mm]	$R_{86,He}$ [mm SWE]
4	25	73	(88, 11, 1)	365	580
14	4.7	57	(88, 10, 2)	450	760
32	0.4	27	(87,11,2)	864	920
63	0.3	0.5	(87,10,3)	1372	1010
108	0.3	0.4	(82,16,2)	2450	1350
172	0.3	0.4	(82,14,4)	4050	1920

Table 6.6: Footprint characteristic of a neutron detector embedded in soil with 50 Vol-% moisture content and buried below a snow layer. **shallow snow:** R_{63} and R_{86} declare the quantiles in which 63 % and 86 % of the cumulative interaction centres are located, respectively. The ratio of source particle species that trigger a neutron detection is shown (precursor). **deep snow:** $R_{86,He}$ is the cumulative 86 % quantile in mm water equivalent of the radial distribution of the detected precursors' interaction locations.

cover demands for another large scale simulation campaign and is left for future studies.

6.3.3.2 Deep Snow

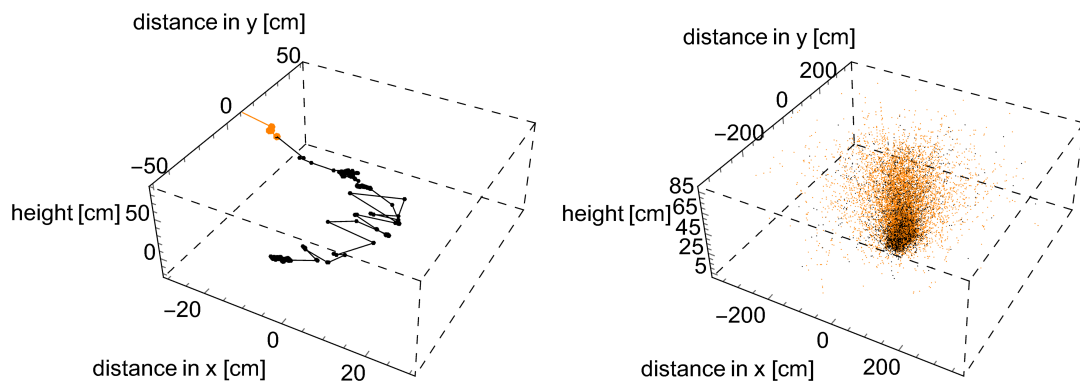


Figure 6.22: **Left:** Trajectory of a single track of a detected neutron (black dots and lines) and its precursor particle, in this case another neutron (orange). The particles pass a 90 cm snow layer with a density of 0.5 g/cm^3 . The neutron detector is embedded at the graph's origin in soil with 50 Vol-% moisture content. **Right:** Interaction centres of ≈ 7300 neutron tracks that lead to a detection. Orange dots mark interactions of highly energetic particles that induce a neutron detection further down the particle cascade. Black dots mark scattering events of detected neutrons following their evaporation centre to their point of thermalisation.

In the case of snow covers with $\text{SWE} > 300 \text{ mm}$, the diffusive neutron flux above the snow surface cannot penetrate the snow layer all the way to the detector. The whole trajectory between evaporation, moderation and detection of a neutron takes place in the snow and soil layer in the vicinity of the detector. The 86 % quantile of the radial footprint of the diffusive neutron flux then shrinks to approximately 50 cm in a snow layer with 0.5 g/cm^3 or 250 mm water equivalent. At these depths the neutron signal is dominated by the at-

tenuation of the highly energetic flux of the detected neutrons' precursors. Therefore, their trajectories and interaction locations inside the snow have to be taken into account for the footprint considerations. These particles have large mean free path lengths due to their high energy and therefore interact a lot less per distance travelled as compared to the lower energetic diffusive neutron flux. However, the deeper the snow layer, the larger the distance the neutrons' precursors travel vertically and, therefore, also horizontally even though their scattering function is collimated to the forward direction. Taking the high-energy interactions into account, therefore, leads to a widening in the radial footprint function as indicated in Fig. 6.22, Fig. 6.23 and Tab. 6.6.

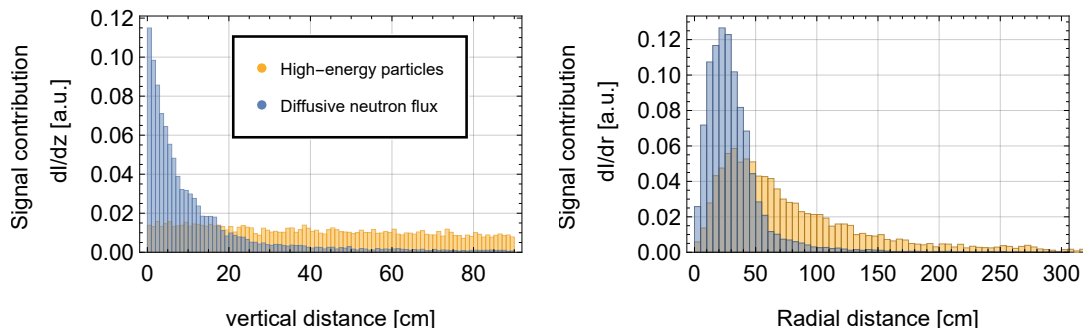


Figure 6.23: Footprint characteristics of a cosmic-ray neutron sensor buried below a 90 cm snow layer with a density of 0.5 g/cm^3 , embedded in soil with 50 Vol-% moisture content. **Left:** Event interaction probability in the snow layer over vertical distance above the detector. The yellow bars illustrate the, mostly inelastic, high-energy interactions of the detected neutrons' precursors, while the blue bars visualize the scattering events of the diffusive neutron flux. **Right:** Interaction probability in the snow layer over radial distance to the detector's center.

The vertical signal contribution is relatively constant throughout the whole snow cover in Fig. 6.23, which holds true for the whole SWE range simulated in this study. A slight focus to smaller vertical distances is observed due to the energy loss and mean free path length decrease along the neutron precursor's trajectory.

Conclusion

This chapter shows that MCNP is able to reproduce the effective attenuation of the cosmic-ray neutron flux within the atmosphere and a water or snow volume. The MCNP high-energy model configuration using a combination of the Bertini, Isabel, Dresner and LAQGSM event generators is well suited for the transport description of both cases. This model choice shows similar attenuation lengths as those inferred from Sato, 2015's functions in the atmospheric study ($\lambda = 143 \text{ g/cm}^2$) and that of Nesterenok et al., 2012 for the snow case ($\lambda = 136 \text{ g/cm}^2$). The difference between the two values might be explained by the fact that the snow volume is located downstream in the high-energy particle flux. The decrease in mean energy of the precursor particles of neutron evaporation with depth leads to a lower attenuation length. The chapter, furthermore, reveals that snow-buried sensors exhibit a local footprint in the case of intermediate to deep snow (SWE > 100 mm) as was suspected by several studies. However, in the case of shallow snow cover the radial footprint extends to several 10 metres. Reproducing thermal neutron intensities below the soil surface shows higher model uncertainty. The simulation-inferred function that describes the thermal flux as a function of depth and soil moisture reproduces general trends in FDR moisture data, which it is com-

6. MCNP model validation, calibration and application

pared to. However, the CRNS inferred soil moisture also exhibits dynamics that seem to be unrelated to actual soil moisture changes. An increase in local radioactive isotopes is suspected to influence the detector's signal. Apart from that, the soil features several unknown state parameters that could influence the thermal intensity such as strong neutron absorbers as trace elements.

7

Neutron transport dynamics above snow-covered soil

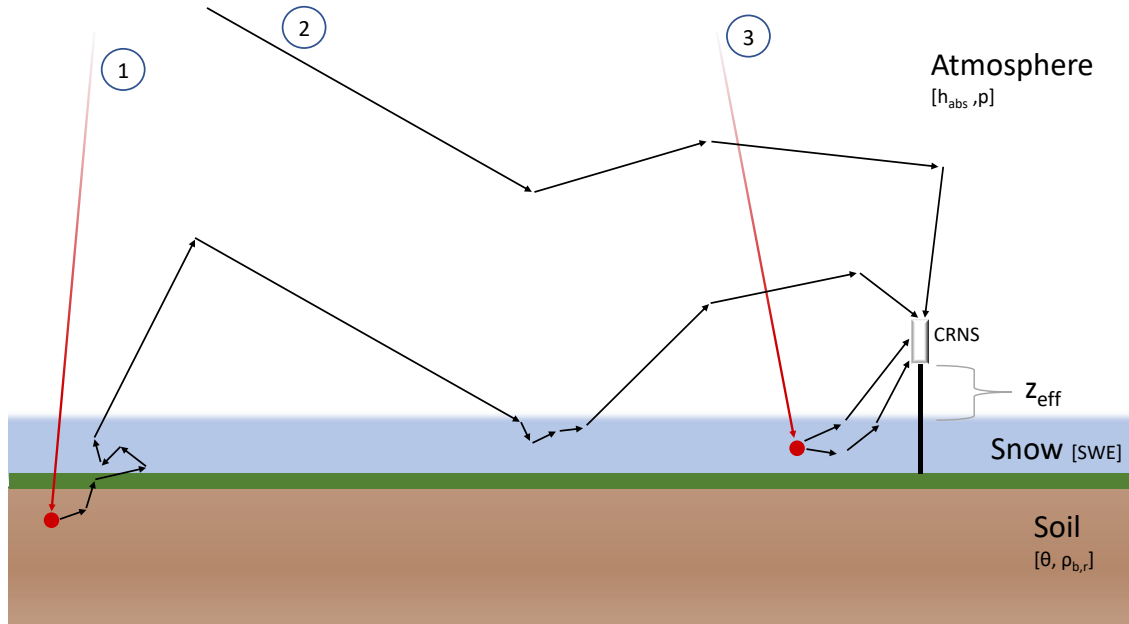


Figure 7.1: Cosmic-ray neutron detection scheme above a snow-covered soil. The figure shows all relevant environmental parameters that are integrated into the MCNP simulation batches of this chapter. The detected neutron flux originates from mainly three different transport patterns: (2) The incoming neutron spectra already contains epithermal and evaporated neutrons. These can be transported through few scattering events inside the air or even snow volume towards the sensor. However, a large part of the detected neutron flux is generated in the dense material, i.e. snow or soil, of the simulation domain (tracks 1 and 3). (1) The high-energy particle flux excites a nucleus and thereby triggers an evaporation of a neutron. Neutrons, which leave the dense material and enter the air volume, can travel large distances in the atmosphere, which is less dense than snow or soil by a factor of $\approx 10^3$. Large travel distances are especially achieved if the neutron crosses the snow-air interface with a large energy in the order of MeV or higher.

The conceptual ideas of this chapter and their implementation were carried out in close cooperation with Paul Schattan from AlpS gmbH and University of Innsbruck, Innsbruck, Austria.

The transport mechanics of epithermal neutrons above snow-covered soils resemble similar behaviour like those above bare soil. However, this kind of discrete two-layer setup features significant differences to those of discretely layered soils (see Fig. 7.1). Firstly, the ratio between hydrogen as a moderator and other elements that scatter neutrons but barely decelerate them is much higher than in soil. Hence, above-ground epithermal and evaporation neutrons are moderated down to thermal energies much more efficiently. Furthermore, snow covers shield the signal influence of the underlying soil until the signal saturates. Signal saturation takes place when the underlying soil has virtually no effect on the epithermal intensity in the air volume. When no airborne epithermal neutron has ever probed the soil, a further increase in snow cover does not change the measured signal. Moreover, the snow layer is a poor evaporation domain due to its high hydrogen content. Also oxygen has a lower evaporation

7. Neutron transport dynamics above snow-covered soil

probability than silicon or aluminium due to its lower atomic number (see section 5.3). Since epithermal neutrons are most sensitive to hydrogen, the relevant parameter for their intensity is the total water column content of the snow layer, the snow water equivalent (SWE). The epithermal flux above snow-free soils is generated to a large extent by evaporation inside the soil. A snow cover therefore decreases the epithermal neutron intensity dramatically because of (1) its high moderation power for air-borne neutrons that penetrate the snow layer on their way to the detector and (2) its shielding capability of the soil as a neutron source while (3) being a poor neutron source itself. These factors lead to a signal drop in the epithermal energy regime from snow-free conditions to SWE equals 600 mm above a soil with 1 Vol-% moisture content by a factor of approximately seven. This signal change can be expected in alpine regions where snow accumulates on bedrock, which features very low hydrogen content. In comparison to snow free conditions, going from 1 to 50 Vol-% soil moisture content leads to a signal drop of about 4.5 (Köhli et al., 2021).

Schattan et al., 2017 empirically showed that the transfer function between the above-snow epithermal neutron flux and the SWE of the snow cover can be approximated by a hyperbolic function similar to that for soil moisture. Their transfer function still showed significant variability and saturated above 600 mm SWE when snow cover changes finally became unresolvable. Later on, they concluded that the heterogeneous snow cover of their site had a strong impact on the SWE retrieval: Snow-free patches contribute much more to the signal than the overall area-average SWE value would suggest due to the highly non-linear, hyperbolic transfer function. These patches act as strong neutron sources and weak moderation spots.

A distinct difference to the standard soil moisture sensing technique is the changing sensor height. The snow cover approaches the sensor as snow accumulates and thereby decreases the effective detector height above the snow surface (z_{eff}). This mainly affects the direct geometric neutron transport from snow surface to detector without any scattering event in-between (see track 3 in Fig. 7.1): The area covered by a certain solid angle decreases with increasing snow height and decreasing effective detector height. Köhli et al., 2015 already showed the large influence of this geometric transport on the signal, while Schrön, 2016 was able to demonstrate the detector's height influence on footprint dynamics in the context of airborne applications. Both, the support volume and the transfer function that links neutron counts and snow water equivalent, are therefore dependent on z_{eff} .

When reaching thermal energies, the neutron becomes sensitive to the bonding and aggregate state of water. Hence, this section applies the thermal scattering kernel of ice water (h-ice.87t in Brown et al., 2018) in order to achieve accurate thermal neutron intensities above the snow layer. The simulation setup comprises a homogeneous snow layer on top of a soil, which is composed of dry material, consisting of 75 % SiO_2 and 25 % Al_2O_3 with a bulk density of 1.43 g/cm^3 with a thickness of 3 m. The sensor is embedded in an air volume at a certain pressure p with an atmospheric moisture content h_{abs} .

7.1 Neutron footprint dynamics above snow covers

One key component to the success of Cosmic-Ray Neutron Sensing is the large support volume. Köhli et al., 2015 comprehensively studied the footprint function above moist soils and were able to show that especially the long-ranged transport mechanisms are largely governed by the moisture content of the soil and air as both domains can be crossed several times by the neutrons' trajectories. Schattan et al., 2017 suspected that the footprint function above snow could be approximated by using Köhli et al., 2015's results in the limit of $\theta \rightarrow 99$ Vol-%. In their follow-up study, Schattan et al., 2019 calculated the footprint for their specific field site. However, it was never examined in detail and from a more general perspective taking the mixed signal of snow cover, soil moisture and air humidity into account.

The value of an accurate description of the CRNP footprint is manifold: It assigns a representative area to the measurement, which is for example useful when integrated into hydrological models. In such cases it is useful to condense the complicated footprint function to a single value e.g. the quantile that comprises 86 % of the signal contribution R_{86} . However, an explicit distribution of the signal contribution as a function of radial distance from the sensor holds numerous benefits. It can be used to weight soil or snow reference measurements according to their distance to the sensor as was described by Schrön et al., 2017. They suggested an improved validation and calibration procedure for CRNS data based on the findings of Köhli et al., 2015 on the footprint above moist soils. Moreover, a radial footprint function can be used to estimate the influence of certain structures on the signal, for example roads, rivers or buildings.

7.1.1 Footprint definition

This section focuses on homogeneous snow conditions as spatial heterogeneous conditions are manifold and cannot be captured comprehensively in this context. Although homogeneous snow covers are rather sparse in alpine regions, homogeneous footprint functions are still beneficial to users of the method to estimate the footprint of their specific case. In homogeneous snow conditions the footprint function should be rotationally symmetric and therefore only a function of the radial distance.

There are numerous possible definitions for the method's footprint as the area that affects the measured signal. Köhli et al., 2015 looked at the distance between the neutron's origin and the point of detection, where the neutron's origin is the point of the first interaction in soil (or snow in this case). This definition is slightly redefined here: The first elastic scattering in the soil or snow volume is selected as the origin. This redefinition is beneficial for two reasons. Firstly, the dominant neutron moderation ability of hydrogen only occurs through elastic scattering. Secondly, MCNP triggers a small amount of highly energetic neutrons emitted from soil or snow back into the air volume. Although being quite rare, they travel over large distances in air and therefore stretch the tail of the footprint distribution. These high-energy neutrons scatter twice as likely inelastically at nuclei than elastically. Inelastic interactions are not hydrogen dominated, which is why these should be excluded from the footprint definition if the latter should not be overestimated.

Another possible footprint definition could cover all elastic interactions within the snow or soil volume that contribute to the moderation process (this definition was chosen in section 6.2). Thereby, more scattering events closer to the point of detection are taken into account, which leads to a reduction in footprint size. In this section, the footprint is calculated according to the definition of Köhli et al., 2015 in order to make the results comparable.

The point of detection is defined as the point where a neutron traverses a detector layer in a certain height with an energy within the sensitivity regime of the neutron detector. The track is then weighted according to the detector's energy response function (see section 2.4.3).

Thereby, neutrons can be counted multiple times. Köhli et al., 2015 claim that simulation tests confirm that multiple counts of single neutrons at different positions equal the detection of a neutron density at a single position. The distance distribution between origin to the point of detection makes up the radial footprint.

It is also important to note that the atmospheric pressure for the following calculations was set to 1000 hPa. It is therefore suggested to use the scaling factors inferred by Köhli et al., 2015 and given in Eq. 2.33 and Eq. 2.34 in section 2.4.4 to rescale the functions given below to a specific pressure state.

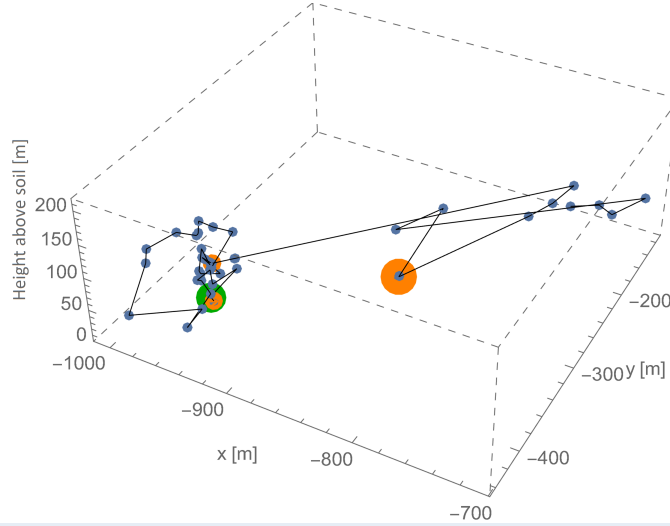


Figure 7.2: An exemplary neutron track that leads to detection is shown: A neutron is evaporated with $E \approx 1.3$ MeV in air, approximately 100 m above ground. It transverses the thin snow layer (SWE equals 20 mm) and then enters the soil volume. The first scattering in the dense material is marked as the origin with a large orange point. Subsequent scatterings in soil or snow cover appear in smaller orange dots. Finally the neutron traverses the detector layer while having an energy in the sensitive regime of the detector and is detected. The detection event is highlighted by the green dot. The distance between origin and detection is approximately 150 m.

7.1.2 Radial footprint as a function of SWE, air and soil moisture content

The findings presented below are based on a broad Monte Carlo campaign featuring a total of 192 simulation setups covering four values for soil moisture ranging between 10–70 Vol-%, four values for absolute humidity between 1–12 g/m³ and 12 SWE values covering the range of 0.5 to 864 mm. The simulation domain has a horizontal extend of 5x5 km. The results shown below are fitted within the value range for the radius between 0 and 400 m.

The signal weighting as a function of radius r [m], of a detector located at a constant $z_{\text{eff}} = 2.7$ m above the snow surface, can be approximated via

$$F(r) = a_6 \text{Exp}\left(-\frac{r}{a_{61}}\right) \left[1 + \text{Exp}\left(-\frac{r^{a_4}}{a_5}\right) (a_3 + r)^2 + a_{11} \text{Exp}\left(-\frac{r}{a_1}\right) (a_{13}r - a_{12}r^2 + r^3) \right], \quad (7.1)$$

in meter with the following definitions of parameters that show dependencies on the three hydrogen pools $h_{\text{SWE}} := \text{SWE}/\text{mm}$, $h_{\text{sm}} := \theta/\text{Vol-\%}$ and $h_{\text{air}} := h_{\text{abs}}/(\text{g}/\text{cm}^3)$:

$$a_6(h_{\text{swe}}, h_{\text{sm}}, h_{\text{air}}) = 0.0686 + 0.0667 \cdot \text{Exp}\left(-\frac{h_{\text{swe}}^{0.4}}{1.87}\right) (1 - 0.01h_{\text{sm}})(1 + 0.0038h_{\text{air}}), \quad (7.2)$$

$$a_{61}(h_{\text{swe}}, h_{\text{sm}}, h_{\text{air}}) = 81.5 + 50.0 \cdot \text{Exp}\left(-\frac{h_{\text{swe}}^{0.4}}{3.3}\right) (1 - 0.0089h_{\text{sm}})(1 - 0.0056h_{\text{air}}) \quad (7.3)$$

$$- 0.26h_{\text{air}}, \quad (7.4)$$

$$a_1(h_{\text{swe}}) = 6.72 + 2.28 \cdot \text{Exp}\left(-\frac{h_{\text{swe}}^{0.5}}{0.42}\right), \quad (7.5)$$

$$a_3(h_{\text{swe}}, h_{\text{sm}}) = 2.65 - 0.89 \cdot \text{Exp}\left(-\frac{h_{\text{swe}}}{13.5}\right) (1 - 0.011h_{\text{sm}}), \quad (7.6)$$

$$a_5(h_{\text{swe}}) = 3.03 + 0.56 \cdot \text{Exp}\left(-\frac{h_{\text{swe}}^{0.5}}{0.49}\right), \quad (7.7)$$

where a_6 , a_{61} and a_1 take the units m, while the other parameters are dimensionless (see Appendix B.2 for detailed plots on the fits of a_i). Fixed parameters are tabulated in Tab. 7.1. Both, the local as well as the far field, of $F(r)$ are shown in Fig. 7.3 for four different snow pack configurations.

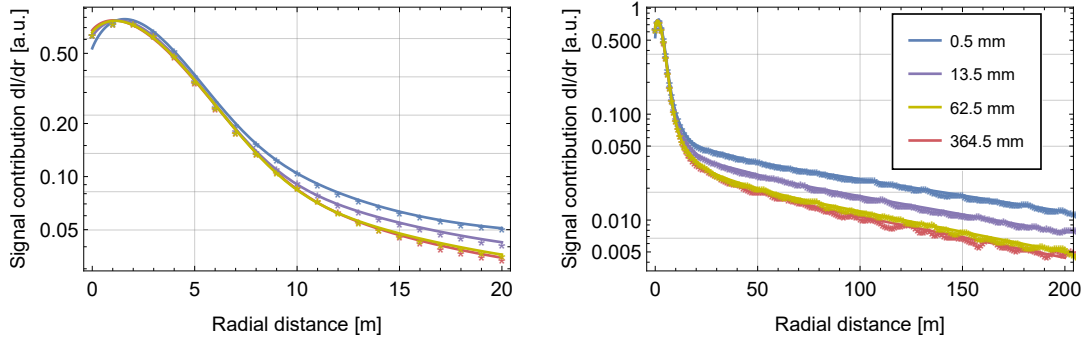


Figure 7.3: Selection of four radial footprint functions at the same soil moisture and air humidity conditions of 10 Vol-% and 1 g/cm^3 . Four different snow covers are shown that indicate how the radial weighting evolves with snow cover increase (SWE values are given in the legend box). Both the local peak at $r \leq 20 \text{ m}$ (left panel) as well as the far-field contribution (right panel) demonstrate the overall decrease of the effective support area with increasing snow cover. Dots mark the radial histograms inferred from neutron simulation while the lines indicate the corresponding fit described by Eq. 7.1

The far-field contribution is indicated by the first term, which is well described by an exponential decrease: a_6 and a_{61} show a strong decrease with increasing snow cover. Thin snow covers experience on average approximately 3 neutron penetrations into the snow and even soil on their way to the detector. Detected neutrons that cover large distances are likely to penetrate the dense material even more often. The higher the snow cover or the soil moisture content, the stronger the moderation of the neutrons when penetrating the dense material. That leads to a decrease in effective transport range as the ambient hydrogen content increases. The long trajectories through air of these neutrons result in a significant impact of air humidity which is present at all stages of snow-cover thickness. This is expressed in a_{61} , the attenuation length of the far field: Going from thin snow covers to saturated conditions (SWE $0.5 \rightarrow 600 \text{ mm}$ and θ equals 10 Vol-%) leads to a decrease in a_{61} from 117 to 82 m.

7. Neutron transport dynamics above snow-covered soil

The effect of air humidity is slightly higher for shallow snow and reaches a value of 0.4 % change in a_{61} each 1 g/m^3 for $\text{SWE} \geq 100 \text{ mm}$.

The local transport dynamics can be described by the two terms in the square parentheses. The radial dimensions of this peak shrink with increasing hydrogen content below the sensor. Both attenuation lengths of this regime a_1 and a_5 show strong SWE and weaker θ correlation. The atmospheric moisture content can be neglected in the near field as the path lengths in the air volume are short. To higher SWE values the transition region between near and far field slightly relocates to smaller radii. That is because the far field is more suppressed by large snow covers than the short-ranged transport. In general, Eq. 7.1 resembles the theoretically motivated footprint function described by Eq. 2.30 in section 2.4.4. Both functions show short and long-ranged transport mechanisms, which can be attributed to geometric and diffusive type transport processes. However, the deduced functions presented here are still significantly different in their shape, which should be a result of the distinct transport dynamics at a two-medium interface.

parameter	a_{11}	a_{12}	a_{13}	a_4
value	1.13E-3	39.4	596	1.35

Table 7.1: Fitted parameters of equation Eq. 7.1 against simulation results shown exemplary in Fig. 7.3.

7.1.3 Radial footprint dimensions expressed in R_{86}

It is instructive to reduce the detailed footprint formula $F(r)$ to a single value that corresponds to the area that affects the signal the most. The R_{86} [m] quantile, as described in section 2.4.4, can be estimated by the function

$$R_{86}(h_{\text{swe}}, h_{\text{sm}}, h_{\text{air}}) = 144.2 + 157.9(1 - 0.029h_{\text{sm}}^{0.7})(1 - 0.0085h_{\text{air}}^{0.8}) \cdot \text{Exp}\left(-\frac{h_{\text{swe}}}{5.51 - 0.012h_{\text{sm}}}\right) - 0.74h_{\text{air}}, \quad (7.8)$$

which takes the units of meter. Fig. 7.4 shows how the footprint shrinks as hydrogen is added to any of the three compartments. However, their impact on R_{86} behaves very differently. Snow and soil can be penetrated several times by a single neutron, which is then slowed down significantly and therefore loses range due to its smaller mean free path. The thicker the snow pack, the smaller the influence of soil moisture because less neutrons penetrate through the snow to scatter in the soil: The number of snow and soil interactions of detected neutrons are equal at $\text{SWE} = 40 \text{ mm}$, while the snow exceeds those in soil by a factor of 25 at $\text{SWE} = 350 \text{ mm}$. It must be pointed out, that even above really moist soils with 70 Vol-%, R_{86} still decreases by more than 50 m going from snow-free to saturated conditions. This emphasizes the strong moderation power of snow as compared to soil that contains a dry matrix.

Atmospheric humidity influences R_{86} strongest during dry conditions very similar to soil moisture. Its absolute effect is smaller than that of soil moisture by a factor of four within the value ranges chosen in this study. In addition to its effect on R_{86} that decreases with SWE, atmospheric moisture content shows a constant influence that describes its effect under saturated conditions. This might become relevant at field sites that encompass dry features within the detectors footprint, e.g. roads that are freed from snow while the landscaped

might be covered by thick layers. These structures' influence on the signal can then change due to air humidity variations.

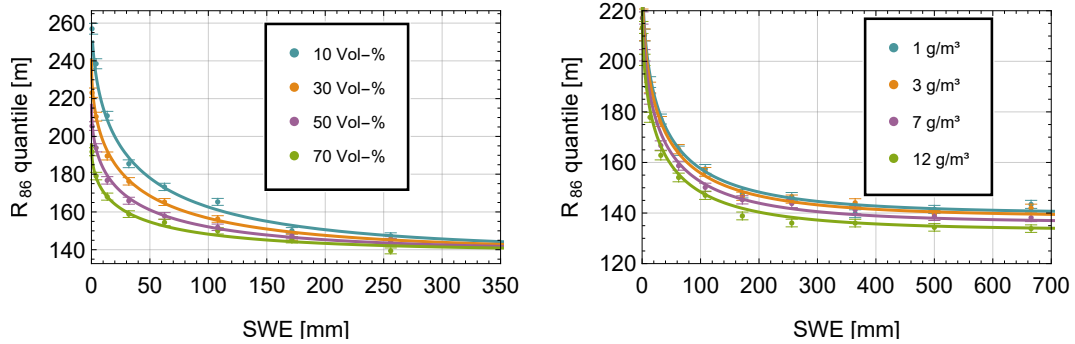


Figure 7.4: Radial footprint dimensions displayed as R_{86} , which denotes the radius that covers 86 % of all footprint events, are given as a function of SWE. **Left:** Four different soil moisture conditions are specified, while the absolute air humidity was set to 1 g/m^3 . **Right:** R_{86} as a function of air humidity with $\theta = 30 \text{ Vol-\%}$. Different scales are applied to both graphics in order to show the persistent effect of air humidity over all snow cover states. Dots denote the simulated R_{86} while the lines indicate the corresponding fit described by Eq. 7.8.

7.1.4 Radial footprint as a function of detector height z_{eff}

The influence of the effective detector height (z_{eff}) was examined by simulating a batch of snow layer setups with changing snow surface height while keeping SWE= 1000 mm as well as all other simulation parameters constant. z_{eff} , measured from snow surface to the lower end of the detector, was changed from 10 to 270 cm in steps of 20 cm.

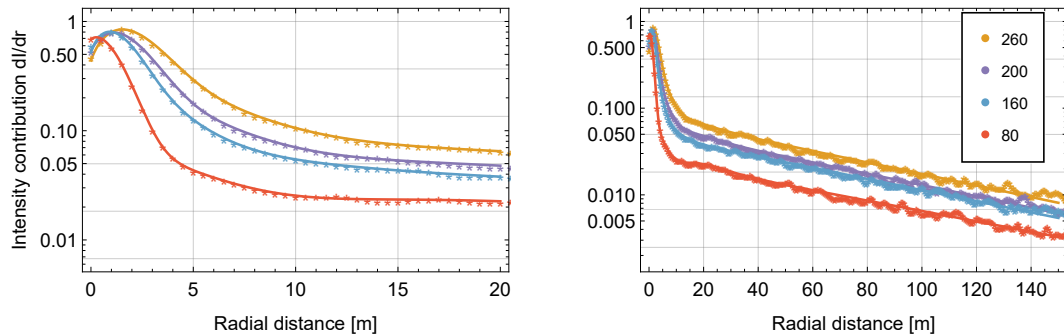


Figure 7.5: Radial footprint distributions as functions of effective detector height above the snow surface. **Left:** Extract of the near-field, which is most affected by changes in z_{eff} . **Right:** The complete footprint function for the first 150 m radial distance. The values in the legend box correspond to z_{eff} in cm.

Fig. 7.5 shows the resulting radial footprint as a function of distance to the sensor. A strong impact on the local peak of the footprint distribution can be observed. That is a pure geometric effect as this region is dominated by direct neutron transport from the snow surface to the detector. A decrease in z_{eff} leads to a compression of the snow surface area that is covered by a fixed solid angle: the field of view of the detector shrinks. The influence of the snow that is located in 6 m radius from the sensor drops by a factor of 6, for z_{eff} decreasing from 270 to 10 cm. To larger distances, this effect decreases but is still significant. Going

from z_{eff} equals 270 to 10 cm decreases the intensity contribution by 20 and 15 % in 30 and 100 m distance, respectively. This may point to a decrease of neutron intensity in the detector's sensitive energy regime close to the snow surface. It is important to note, that the long-range term only changes due to a change in a_6 , while a_{61} , the moderation length in air, stays the same.

The $R_{86}(z_{\text{eff}})$ can be linearised within the value range examined in this study by:

$$R_{86}(\Delta z_{\text{eff}}) = R_0 + 4.3\Delta z_{\text{eff}}, \quad (7.9)$$

where $R_{86}(z_{\text{eff}})$, R_0 and z_{eff} are given in m. R_0 can be any reference value within 10 to 270 cm due to the linearisation. This results in a R_{86} quantile change of 8 % for z_{eff} : 10 → 270 cm. The 63 % quantile, which mainly describes the near field, shows a much more pronounced variation with z_{eff} of ≈ 30 % between 10 to 270 cm.

As the footprint change with detector height is a geometric effect, similar considerations could also hold for the snow-free case and the detector installation height (which was considered also by Schrön et al., 2018).

7.1.5 Neutron emission by snow and footprint comparison to snow-free footprint dynamics

Previous studies that examined the footprint of CRNS by means of Monte Carlo codes focused on the snow-free soil moisture sensing case. It is still instructive to compare the above-shown results in the limit of $\text{SWE} \rightarrow 0$ mm to Desilets et al., 2013 and Köhli et al., 2015. The first used an earlier version of MCNP (MCNPX, Waters et al., 2007) while the latter revised their findings two years later using the URANOS Monte Carlo code. It must be noted that most recent findings of other studies suggest that Köhli et al., 2015's definition is able to explain measured footprint dynamics more accurately, especially regarding the near field.

Extrapolating above-discussed findings to 0 mm snow cover indicates a larger footprint, given in R_{86} , by around 22–25 % as compared to Köhli et al., 2015's results (this also takes into account the difference in detector height above the ground). This effect could be traced back to a higher mean energy of neutrons that are emitted from the soil or snow into the air volume (see Fig. 7.6). The higher the energy the larger the mean free path of a neutron in air. It should also be noted that R_{86} is very sensitive to the mean free path of the neutrons in air. That is mainly because the local peak already contains a large fraction of all detected neutrons. Thus, slight changes in the far-field description have strong impact on R_{86} . The difference in the soil emission spectrum is likely a consequence of the different Monte Carlo toolkits used. While URANOS does not eject neutrons with energies above 20 MeV from the soil into the air, MCNP shows a small contribution at these high energies. Even though inelastic scattering is more probable for $E > 20$ MeV, some of these neutrons also scatter elastically in the snow or soil volume and are then accounted for in the footprint calculations above. It is noteworthy, that this high-energy emission shows a less pronounced decline with snow cover than the lower energetic flux and sources the above-snow neutron intensity even to thick snow packs (see Fig. 7.6). That is also the reason why the detected signal above snow never fully saturates, see section 7.2. Köhli et al., 2015 also show a slightly higher influence of atmospheric humidity that amounts to a 10 m change in R_{86} per 4–6 g/m³ change in water vapour. This study's findings suggest a change of 10 m every 6–7 g/m³ which is in agreement with Desilets et al., 2013 who found a value of every 6 g/m³. The footprint above snow-free soil shrinks if elastic scattering by neutrons with energies higher than 20 MeV is excluded from the footprint calculations and exceeds the R_{86} values inferred by Köhli et al., 2015 by 5–7 %.

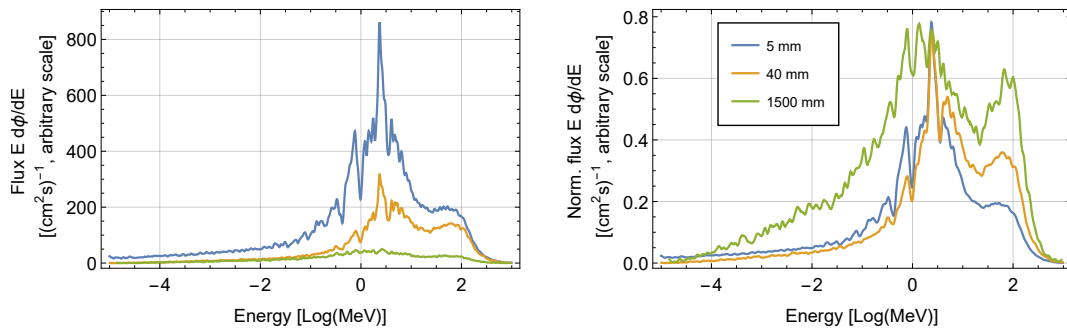


Figure 7.6: Spectra of neutrons that cross the snow-atmosphere interface with upward direction into the air volume for three snow cover thicknesses: 0.5, 32 and 665 mm SWE. The underlying soil has a moisture content of 10 Vol-% and the air volume is filled with 3 g/m^3 hydrogen content. **Left:** Total emitted neutron flux. The high peak at 2.35 MeV is due to a strong drop in the oxygen scattering cross section at this energy (Brown et al., 2018). Additionally, the hydrogen cross section falls off to these energies. Neutrons that leave the soil with this energy are likely to cross shallow snow covers without interacting with it. This complete transection of the snow cover becomes improbable for larger snow packs and the peak vanishes. **Right:** Normalized emitted neutron flux. The high-energy part of the spectrum ($E > 20 \text{ MeV}$) is emitted when more than one particle is produced in a spallation reaction. In such a case the less energetic particle can be emitted backwards, i.e. back in the direction of the air volume.

Fig. 7.6 reveals an important fact about snow: it is a very poor evaporation neutron emitter, as was also mentioned above. However, the snow volume also emits neutrons back in the air. Some of which are evaporated in the underlying soil and penetrate the whole snow pack. An emission window appears at around 2.35 MeV due to the low cross-section value of oxygen and hydrogen at this energy. This channel feeds the emission of soil-evaporated neutrons into air until around 500 mm SWE soil emission accounts to $\approx 1\%$ of the total emission of the dense material.

7.2 Snow cover influence on the above-ground neutron flux

7.2.1 Neutron spectra above snow layers

The cosmic-ray neutron spectrum above a snow-covered soil is dependent on all three hydrogen pools: atmospheric, snow and soil hydrogen content. Similar patterns as described in section 7.1 referring to the footprint dynamics are expected when looking at the intensity as well. However, this study excludes the influence of atmospheric water vapour on the intensity and refers to Rosolem et al., 2013 and Köhli et al., 2021. The findings of the latter study in the limit of $\theta \rightarrow 100\%$ can treat atmospheric water vapour influence while Rosolem et al., 2013 suggested a soil moisture independent water vapour correction factor. It must be noted, that this treatment is incorrect for shallow snow covers above dry soils that feature low hydrogen contents as compared to $\theta \rightarrow 100\%$. It is decided to omit atmospheric water vapour due to computational effort and due to the normally low values that are encountered at cold conditions above snow surfaces. In the simulations carried out for this section, the atmospheric water content was set to 3 g/m^3 . The values given as intensity, in this section, are spectra weighted with a detector response function as most neutron detectors deployed in this application field are standard CRNPs.

Fig. 7.7 shows the influence of snow cover and its SWE values on the neutron spectrum. In this case, the effective detector height (z_{eff}) and the snow layer height were kept constant. The corresponding SWE value was adjusted by the snow density. This was done in order to separate the influence of the hydrogen content of the snow layer and its height, i.e. z_{eff} , on the signal. Above dry soils, a moderation optimum in the thermal energy regime appears: small amounts of snow lead to an increase in thermalisation capability of the whole domain that overcomes the increase in absorption of thermal neutrons by hydrogen. This leads to a non-injective transfer function, which also appears in the snow-free case. Going to higher snow packs, the epithermal intensity saturates at shallower snow cover than the thermal intensity.

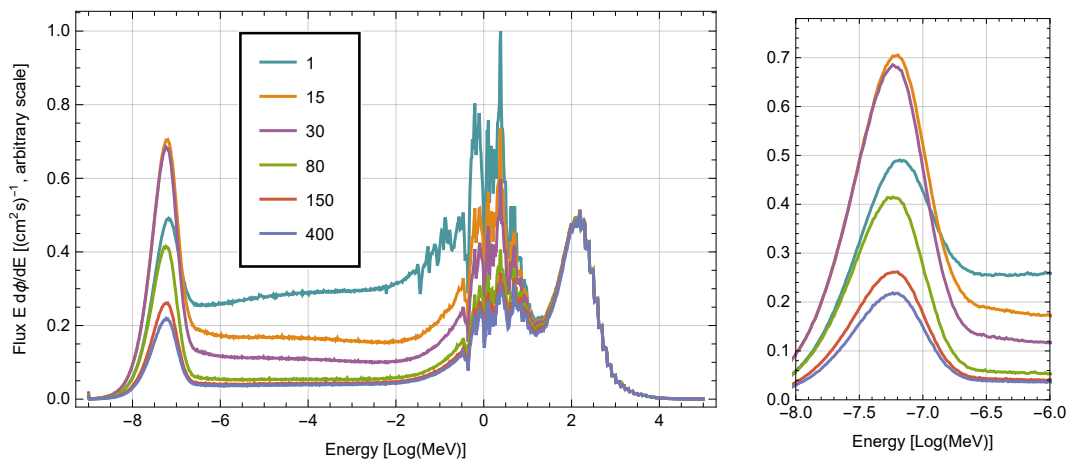


Figure 7.7: Cosmic-ray neutron spectra above a snow surface. The snow layer is located above a dry soil with 1 Vol-% moisture content and the detector layer 2.8 m above the snow surface. The SWE content varies between 1 and 400 mm, while the height of the snow pack was kept constant at 100 mm. The structure of the spallation peak is due to the logarithmic binning of the neutron input source in MCNP. **Left:** The whole spectrum reveals a similar influence of snow than that of soil moisture. **Right:** The thermal part shows a moderation optimum, which appears only in the case of dry soils.

Fig. 7.8, left benchmarks the spectrum above a snow cover of SWE equals 30 mm against a measured spectrum by Brall et al., 2021. They used 16 Bonner spheres that show different response functions to unfold the neutron spectrum (the unfolding process is described by Simmer et al., 2010). It was recorded at the research station Schneefernerhaus located 2650 m a.s.l. at the Zugspitze mountain (lat=47.41649, long=10.97938). The surrounding mountain site was covered in snow with SWE = 31 mm. The underlying rock can be considered dry, thus, their spectrum is compared to the dry ($\theta = 1$ Vol-%) case of these simulation batches also shown in Fig. 7.7. The spectra are normalized to each other by the neutron spallation peak. Their spectrum shows a stronger increase of intensity in the epithermal regime with decreasing energy. This is also observed in the MCNP spectra to shallower snow covers (see SWE equals 15 mm in Fig. 7.7). Note that the narrow structures in the evaporation peak cannot be resolved by the unfolding process. The spectra show significant difference in the ratio between the thermal and epithermal and evaporation energy regimes. The MCNP simulated spectrum at the thermal moderation optimum, which corresponds to SWE equals ≈ 17 mm at $\theta = 1$ Vol-%, also shows a lower ratio than the one measured by Brall

et al., 2021. As the thermal intensity is strongly determined by the ratio of the macroscopic scattering and absorption cross sections, while the epithermal and evaporation regime is solely governed by the scattering cross section, this might point to a slight overestimation of absorption processes within the MCNP simulation batch. However, it should be noted that the unfolding process of Bonner sphere spectra are accompanied with large uncertainties. Moreover, the Bonner sphere detectors feature small neutron count rates, which leads to significant statistical uncertainty.

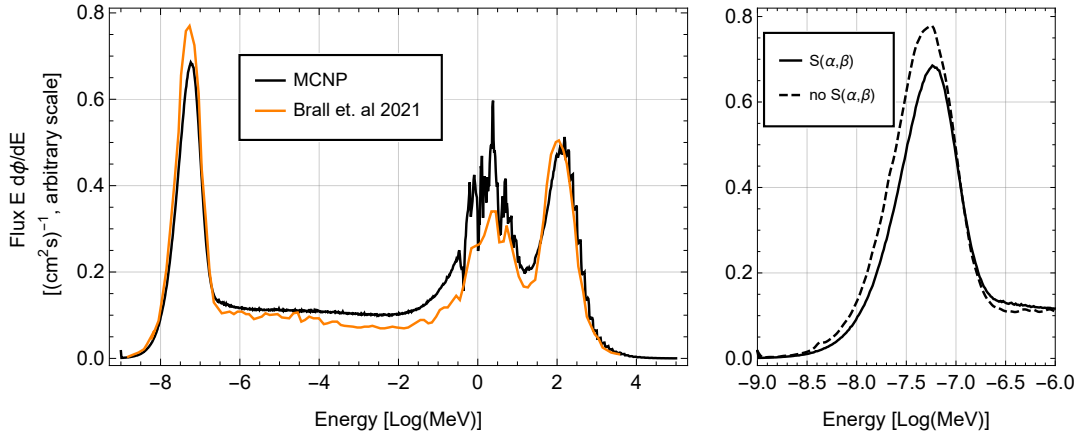


Figure 7.8: **Left:** Neutron spectrum measured at Schneefernerhaus, Zugspitze, Germany by Brall et al., 2021 surrounded by a snow cover with SWE equals 31 mm and a corresponding simulated spectrum with MCNP above SWE = 30 mm and dry soil ($\theta = 1$ Vol-%). **Right:** Thermal peak intensity of MCNP simulations for the same conditions with the thermal scattering kernel $S(\alpha, \beta)$ of ice turned on and without any scattering kernel visualised by the black and dashed curve, respectively.

Fig. 7.8, right displays the influence of the thermal neutron scattering kernel on the simulated spectrum (see section 2.3.6). Solid ice increases the cross section of hydrogen by a factor of approximately 3 at $E = 25$ meV, while that of oxygen remains equal. This results in an overestimation of thermal neutrons above snow by around 10 % if no scattering kernel is applied. This effect is constant throughout all stages of snow cover thickness examined here. It should also be noted, that the difference between the solid-ice and liquid-water kernel in the ENDF-VIII data base is negligible (see e.g. h-h2o.81t and h-ice.88t in Brown et al., 2018).

7.2.2 Detector-measured intensity as a function of soil moisture and snow cover

Schattan et al., 2017 empirically inferred a hyperbolic transfer function between SWE and detected neutron counts by a standard cosmic-ray neutron sensor. The results shown here suggest that an additional exponential term should be added to get a more representative intensity function $N(h_{swe}, h_{sm})$, where h_{swe} and h_{sm} are defined as above. A hyperbola fitted to the simulation results shows a less steep curve than the one suggested below (see Appendix B.2.1). A simulation batch covering 11 and 14 values of soil moisture and SWE was conducted. The resulting transfer function $N(h_{swe}, h_{sm})$ can be described by

$$N(h_{swe}, h_{sm}) = b_1 \frac{b_2 + b_3 h_{swe}}{b_2 + h_{swe}} \left[1 + b_4 \text{Exp} \left(-\frac{h_{swe}}{b_5} \right) \right], \quad (7.10)$$

where the first term resembles the soil moisture transfer function. All parameters show a

7. Neutron transport dynamics above snow-covered soil

dependence on soil moisture (see also Appendix B.2.1). For $h_{\text{swe}} = 0$ mm the transfer function equals the term $b_1 \cdot (1 + b_4)$, which should then become the hyperbolic expression described by Desilets et al., 2010 and revised by Köhli et al., 2021. Thus, both b_1 and b_4 can be expressed by a hyperbola by

$$b_1(h_{\text{sm}}) = 0.35N_0 \frac{5.08 + 0.589h_{\text{sm}}}{5.08 + h_{\text{sm}}}, \quad (7.11)$$

$$b_4(h_{\text{sm}}) = 2.39 \frac{7.46 + 0.044h_{\text{sm}}}{7.46 + h_{\text{sm}}}, \quad (7.12)$$

where N_0 is the site and detector-specific parameter that needs an initial calibration and

$$N_{\text{max}} = 0.35N_0(1 + 2.39), \quad (7.13)$$

where N_{max} denotes the detector's count rate at absolute dry conditions as defined by Köhli et al., 2021 (For $h_{\text{sm}} = h_{\text{swe}} = 0$). Fig. 7.9 compares this study's results in the limit of $h_{\text{swe}} \rightarrow 0$ mm to Köhli et al., 2021's findings that focused on the snow-free case. Their curve shows a slightly less intensity drop going from dry to moist conditions but the curves resemble each other in relative good agreement. The only difference in the setup of the two simulation batches is the detector height above the soil. Köhli et al., 2021 assumed 1.3 m distance between soil surface and lower detector end, while here this was chosen to be 2.8 m.

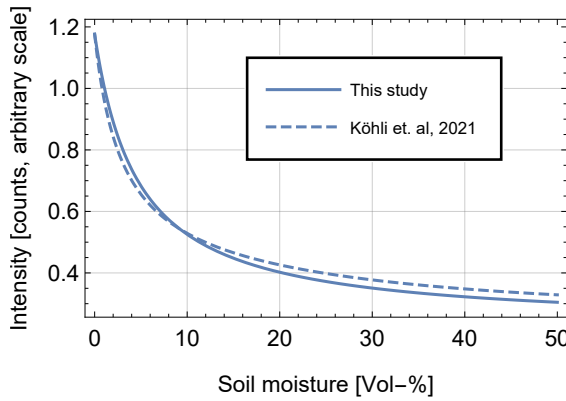


Figure 7.9: Neutron intensity $N(\theta)$ weighted with a standard detector response function compared to the results of Köhli et al., 2021. They offer four parameter sets that lead to slightly different $N(\theta, h_{\text{abs}})$, of which the 'MCNP detector response function' set was chosen because it assumes a similar setup as the one chosen for this study. The absolute humidity is set to 3 g/m^3 .

The other parameters' fit results are the following:

$$b_2(h_{\text{sm}}) = 38.9 - 23.4 \text{Exp}\left(-\frac{h_{\text{sm}}}{13.7}\right), \quad (7.14)$$

$$b_3(h_{\text{sm}}) = 0.79 - 0.24 \text{Exp}\left(-\frac{h_{\text{sm}}}{6.6}\right) + 0.002h_{\text{sm}}, \quad (7.15)$$

$$b_5(h_{\text{sm}}) = 45.0 - 6.4 \text{Exp}\left(-\frac{h_{\text{sm}}}{4.60}\right) + 0.058h_{\text{sm}}, \quad (7.16)$$

Simulated data and fit results are shown Fig. 7.10 for a variety of parameter settings. The fit residuals amount to less than 1 % over the whole parameter set but are largest for dry soil conditions. Fig. 7.10 reveals a strong influence of soil moisture until the signal saturates. A definition of signal saturation is introduced that marks the point at which a change in snow cover of $\Delta\text{SWE} = 10$ mm amounts to less than 1 per mil signal change, which is virtually not resolvable by any neutron detector. This point of saturation is reached at around 240 mm for any soil moisture state. Fig. 7.11 left panel, indicates how the signal varies when SWE

changes by 10 mm as a function of SWE. This ability to resolve changes in SWE decreases in a nearly exponential fashion.

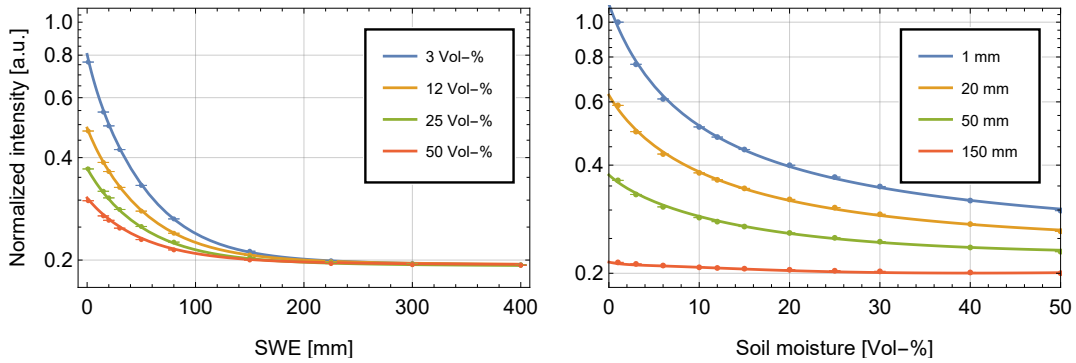


Figure 7.10: Neutron intensity functions weighted with a standard detector response function over a snow-covered soil as a function of SWE (left panel) and soil moisture (right panel).

Fig. 7.11 right panel displays the additional exponential term $b_4 \text{Exp}(-h_{\text{SWE}}/b_5)$ as a function of SWE. It strongly decreases with snow cover increase and also depends heavily on soil moisture. This additional term can be regarded as a soil neutron source term that feeds the above-snow epithermal neutron intensity. This assumption is supported by the fact that this additional term is weighted by $b_4(h_{\text{sm}})$, which decreases monotonously with soil moisture. $b_5(h_{\text{sm}})$ takes the physical meaning of an attenuation length of the soil source, attenuated through both, soil and snow volume.

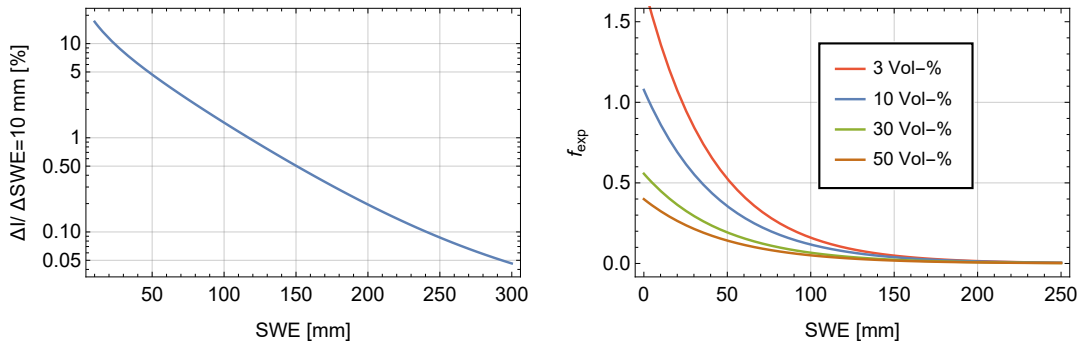


Figure 7.11: Left: Resolving capacity of 10 mm changes in SWE as a function of SWE. **Right:** Exponential term of the transfer function between snow cover and epithermal neutron intensity (see Eq. 7.10).

Parameters $b_2(h_{\text{sm}})$ and $b_3(h_{\text{sm}})$ feature a monotonous increase with soil moisture content leading to a less steep hyperbola described by b_1 , b_2 and b_3 . That is because the more hydrogen stored in the soil the smaller the effect of additional hydrogen in the form of snow. This relationship is a direct consequence of the non-linear correlation between hydrogen and epithermal neutron intensity. Köhli et al., 2021 discovered a similar pattern in the cross-correlation between h_{sm} and h_{abs} : the influence of atmospheric moisture content is highest when the soil moisture is lowest.

7.2.3 High-energy neutron intensity above the snow cover

The spallation peak of the above-snow neutron spectrum is relatively unaffected by snow cover changes (see Fig. 7.7). However, Fig. 7.6 suggests that snow acts as a neutron source even above 20 MeV. These neutrons are less attenuated by the snow cover due to their high energy even though their production is much more likely in the soil than in the snow volume. They can, therefore, source the neutron flux above the snow surface even at high cover thickness. This emission does not arise in URANOS and is therefore examined here briefly (see Fig. 7.12), which can be used as an input to other toolkits. The normalized intensity of this high-energy peak drops by 2.5–4 % depending on the soil moisture state and can be described by

$$I_{\text{he}}(h_{\text{swe}}) = c_1 \text{Exp} \left(-\frac{h_{\text{swe}}^{0.8}}{c_2} \right) + c_3. \quad (7.17)$$

The attenuation length $c_2 = 51.6$ and the minimum value above saturated snow $c_3 = 0.959$ are constant with soil moisture. The offset high-energy flux at snow-free conditions c_1 is a function of soil moisture and can be linearised between 1 Vol-% and 50 Vol-% by

$$c_1(h_{\text{sm}}) = 0.0403 - 2.81 \cdot 10^{-4} h_{\text{sm}}. \quad (7.18)$$

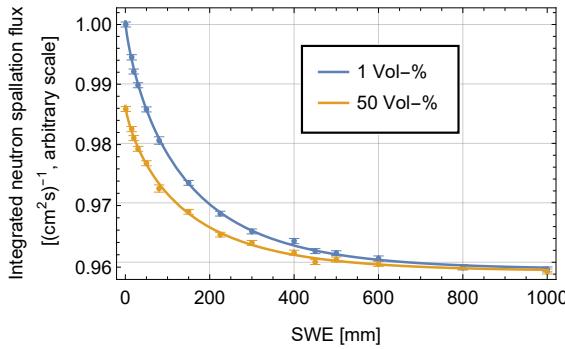


Figure 7.12: Integrated neutron flux above the energy threshold $E = 20$ MeV as a function of SWE for dry and wet soil conditions. The solid lines show the fits of the two curves described by Eq. 7.17. The values shown are normalized to the integrated flux above a snow cover with SWE equals 1 mm and $\theta = 1$ Vol-%.

It should be noted that the overall influence of the high-energy flux backward emission on the above-snow epithermal neutron intensity is larger than solely the part described here. That is because it can produce further evaporation neutrons at oxygen nuclei in the snow volume.

7.2.4 Intensity relation as a function of effective detector height

Above, in section 7.1, it was discussed how the effective detector height z_{eff} distorts the footprint function. The effect is strongest in the near field. The thermal neutron intensity is also mostly subject to the near field, as the low energy of these neutrons prohibit them to travel over large distances. Due to that, z_{eff} shows some effect on the thermal neutron intensity but very little on the epithermal intensity range (see Fig. 7.11). The simulation data indicates an increase in thermalisation capability of the detector's vicinity with decreasing z_{eff} . On the contrary, the epithermal neutron density decreases the smaller the distance to the snow pack. Due to the thermal contamination of the standard detector type, the neutron intensity weighted with the detector response function shows a mixed relationship to z_{eff} influenced by both energy regimes. While, in the thermal regime, the effect of the approaching snow cover is independent on its hydrogen content, the effect is two-dimensional in the epithermal regime. The effect of the snow layer's SWE saturates as the signal itself saturates. It is noteworthy, that in the thermal energy regime the effect opposes that of the

hydrogen in the snow cover: as snow accumulates, SWE increases, which leads to a signal drop, but z_{eff} decreases, which in turn leads to a small signal gain. In the thermal energy regime the effect of z_{eff} can be linearised, within the value range presented here, by

$$f_{\text{th}}(z_{\text{eff}}) = 1 - 1.99 \cdot 10^{-4} \Delta z_{\text{eff}}. \quad (7.19)$$

Combining simulated thermal intensities over a snow cover with constant height with this effect leads to a non-injective transfer function between snow cover and thermal neutrons at high SWE values. The right panel, bottom row of Fig. 7.13 combines both effects by assuming a snow density of 0.3 g/cm^3 , which links SWE and z_{eff} . For shallow snow the signal is dominated by the hydrogen content of the snow layer. However, as the signal saturates, the effect of the approaching snow cover takes over and, eventually, for SWE values larger 350 mm the thermal intensity experiences a gain with snow cover increase. The retrieval of SWE from thermal intensities is highly dependent on z_{eff} even before this intensity minimum. While Fig. 7.7 suggests a higher sensitivity of the thermal energy regime at high SWE values, this advantageous effect is diminished by the additional influence of z_{eff} . Epithermal neutrons are, thus, considered beneficial in the context of snow monitoring and the use of thermal neutrons is not recommended.

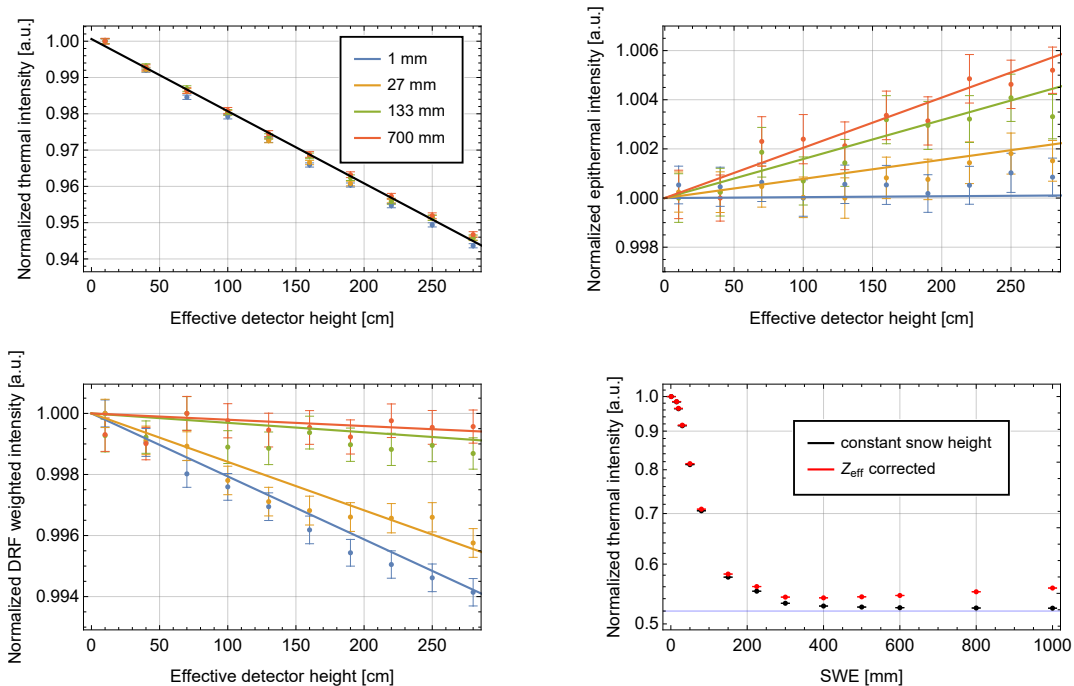


Figure 7.13: Influence of the effective detector height above the snow surface in the thermal and epithermal energy regime, shown in the top row left and right, respectively. The standard cosmic-ray neutron sensor is sensitive to both regimes and therefore shows combination of both patterns (bottom row, left). Bottom row, right: Combining the normal effect of a snow cover merely due to hydrogen (black curve) with the effect of z_{eff} assuming a snow density of 0.3 g/cm^3 (red curve).

7.2.5 Simple snow cover inhomogeneities

Schattan et al., 2017 indicated an upper SWE detection limit of 700 mm, which contradicts the results here (see Fig. 7.11). In their follow-up study (Schattan et al., 2019) based on the same field site, they showed that the signal could be reproduced by Monte Carlo simulations

7. Neutron transport dynamics above snow-covered soil

using the URANOS toolkit and pointed to the strong impact of the heterogeneity of the snow cover. Especially snow-free patches enhance the above-ground epithermal neutron intensity by a large fraction. This effect is to be expected because of the non-linear relation between θ , SWE and the neutron flux. Their simulated neutron fluxes could reproduce the signal dynamics until 400 mm SWE above which the simulation results saturated but the empirical data did not. As argued above, MCNP simulations generate an upward directed high-energy flux, which originates from the soil and enhances the evaporation in the snow layer and also in the air volume above. It might therefore be a promising candidate to explain such deviations.

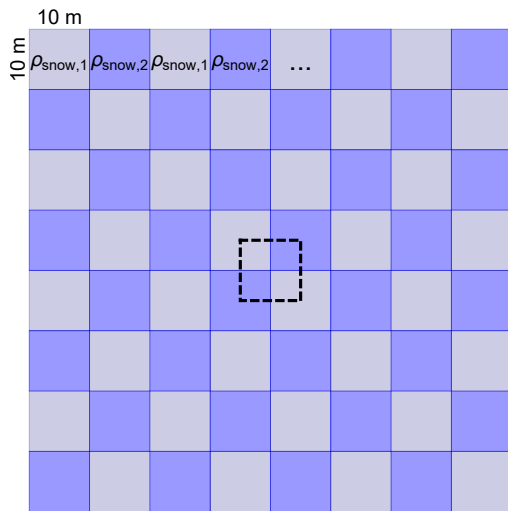


Figure 7.14: Schematic setup of a chequerboard pattern snow layer with constant snow height where the densities $\rho_{\text{snow},1}$ and $\rho_{\text{snow},2}$ control the SWE values of the two patch variants. The patches are $10 \times 10 \text{ m}^2$ in size. The neutron flux is recorded via a detector layer 2.8 m above the snow surface. The simulation domain consists of a base unit denoted as the black dashed rectangle with reflecting boundaries, thus, infinitely extending the chequerboard setup.

Instead of the specific field site focused in Schattan et al., 2019, a simple simulation setup of heterogeneous snow cover was chosen to reinforce this point: The snow layer is subdivided in a chequerboard grid with two different snow density states (see Fig. 7.14). An equal snow layer thickness is applied in order to exclude the effect of z_{eff} .

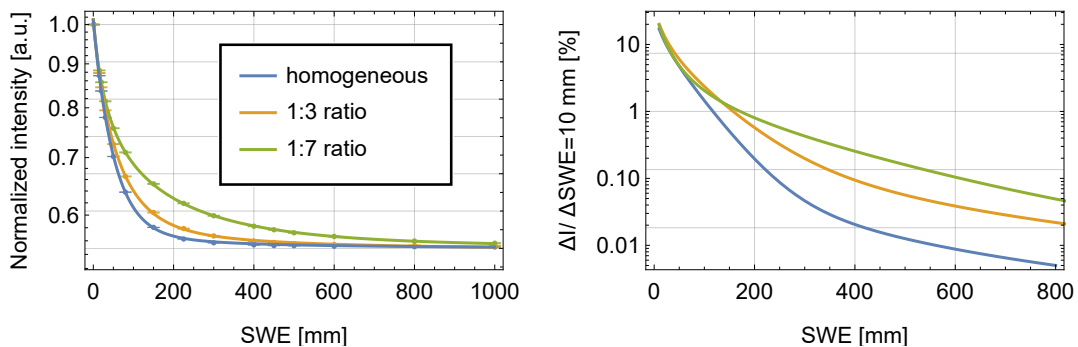


Figure 7.15: Simulated transfer functions between SWE of a heterogeneous snow layer and the above-ground weighted neutron flux using a standard detector response function. The SWE values are calculated as the average of the two snow grid cells defined in Fig. 7.14. The blue data denotes the homogeneous setup with $\theta = 30 \text{ Vol-\%}$, while orange and green represent heterogeneous snow cover. **Left:** The ratios in the legend box specify the degree of the density heterogeneity $\rho_{\text{snow},1}:\rho_{\text{snow},2}$. **Right:** Resolving capacity of 10 mm changes in SWE as a function of SWE analogue to Fig. 7.11.

The heterogeneities lead to a significant shift in the transfer function as indicated by Fig. 7.15

similar to that found by Schattan et al., 2019. In highly heterogeneous snow cover conditions the signal saturates beyond 800 mm SWE. The large difference between a density ratio of 1:3 and 1:7 indicates the strong non-linearity of snow cover heterogeneity on the epithermal neutron flux.

7.2.6 Experimental evidence



Figure 7.16: Setup of the Leutasch field site in Tyrol, Austria. Three neutron detectors are mounted on a pole and highlighted in red comprising an epithermal, standard and thermal detector, from left to right. A thin pole (yellow segment on top), located at the right side of the detectors, is used for snow depth measurements. The inset picture indicates a flat soil surface, while the large picture indicates a very homogeneous overlying snow cover.

This section shows preliminary data, which was recorded at Leutasch, Tyrol, Austria (lat=47.37540, long=11.16231). The site is located in a high valley approximately 1100 m.a.s. on a planar agricultural field. The Leutasch valley is protected to the south and north from the warm and cold foehn. This reduces wind-driven snow transport strongly and leads to a very homogeneous snow cover during winter. This presents an appropriate measurement setup to validate the transfer function Eq. 7.10.

The site features three neutron detectors: a standard CRNP, a thermal neutron detector and an epithermal neutron detector (see Fig. 7.16). The epithermal neutron detector comprises a standard CRNP enclosed in a thermal shield as described in section 8.6.1. For this preliminary analysis only the data of the standard CRNP is examined since Eq. 7.10 was tailored to this detector type. The station furthermore comprises a sensor that monitors atmospheric temperature, pressure and absolute humidity. In autumn 2020, four FDR in-situ soil moisture probes were deployed below the detectors in 5, 10, 15 and 45 cm depth.

7. Neutron transport dynamics above snow-covered soil

Time [date]	SWE [mm]	θ [Vol-%]	h_{abs} [g/m ³]	Pressure [hPa]
Jan 29th	186.6 ± 12.8	22.4	5.4	681
Feb 18th	197 ± 14.3	28.7	3.1	690
Mar 4th	153.7 ± 16.8	30.35	3.7	691
Mar 21st	235.2 ± 17.5	29.5	3.8	690

Table 7.2: SWE measurement campaigns during the winter in 2021 at the Leutsch site.

A field campaign with a mobile FDR sensor revealed a rather homogeneous soil moisture distribution for the top soil within a distance of 100 m with 5 Vol-% standard deviation. However, the soil in the very vicinity of the sensor exhibited lower soil moisture values by $\approx 10\%$, which might be due to bulking during the detector installation. During the winter 2020/21 four field campaigns were conducted measuring snow depth in a transect around the sensor with a snow measurement pole (see Tab. 7.2). The snow density was recorded once during each campaign in few meters distance to the sensor via snow tube sampling (the procedure is described in section 2 and 3 in Kinar et al., 2015).

For this analysis the SWE value is first estimated by taking the average over all snow depth measurements multiplied by the measured snow density. This SWE value along with the measured soil moisture and air humidity is then used to compute the radial footprint function Eq. 7.1 and weight the snow depth measurements accordingly. Although, the difference in SWE from the first to the second step only amounts to $\approx 4\text{--}5$ mm because of the homogeneous conditions. The detected neutron count rate is processed with standard corrections of air pressure, air humidity and incoming radiation and averaged over 12 hours in order to achieve a statistical error of 0.6%. This count rate is compared to Eq. 7.10, where the corresponding SWE and soil moisture values are inserted, in Fig. 7.17. For the soil moisture value only the uppermost FDR sensor in 5 cm depth is considered since the SWE values are high compared to the saturation limit of the epithermal neutron flux indicated by Fig. 7.11 and only the top soil should affect the epithermal neutron flux. However, a bias of 10 Vol-% was added due to the lowered soil moisture values in the vicinity of the detector pole. A good agreement between the simulated and measured values is observed except for the measurement point SWE=186.6 mm. Tab. 7.2 reveals that during this measurement campaign soil moisture, atmospheric humidity and pressure deviated slightly from the other days. This might point to either an incorrect treatment of the soil moisture influence in Eq. 7.10, an overestimation of the air humidity influence or underestimation of the pressure correction factor.

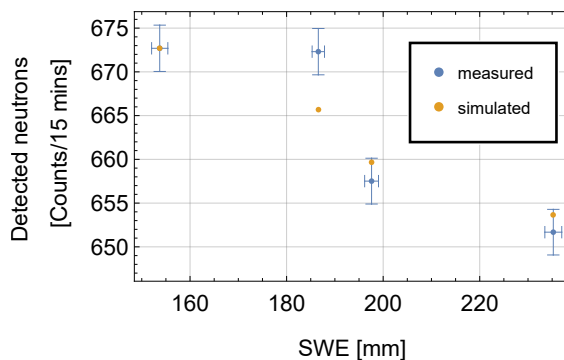


Figure 7.17: Comparison of measured (blue) and simulated (orange) neutron counts of a standard CRP probe at the Leutsch site. Measured and simulated count rates are normalized to the lowest SWE value.

Conclusion

This chapter presents a radial footprint function above snow-covered soils as a function of SWE, soil moisture and absolute humidity. While the snow cover reduces the influence of the soil moisture on the neutron transport dynamics as it increases, air humidity shows a relative constant influence on the footprint dynamics via the long-ranged transport. The function can be used for sample weighting of snow height and density measurements, as a measure for the representative area of the detector or to estimate the influence of structures on the signal. The effective height of the sensor above the snow surface has strong influence on the local neutron transport dynamics, while the long-ranged transport is less affected.

This mechanism also influences the thermal neutron flux above the sensor, which can lead to an intensity increase in this energy regime with snow cover increase for large snow packs. Thus, thermal neutrons show a non-injective relation to SWE. The simulated epithermal neutron flux weighted with a detector response function is best described with a combination of a hyperbola and exponential function, while previous, empirical studies suspected a purely hyperbolic relationship. In general, it is observed that the snow surface acts as a weak high-energy neutron source which is also motivated in chapter 5. This weak flux contribution is less shielded by the snow cover than lower energetic neutrons and, thus, sources the above-ground neutron flux even to large snow packs. Such a flux contribution could explain the difference between simulated and measured neutron intensities for large SWE values as was reported by Schattan et al., 2019.

Concepts of developing dedicated cosmic-ray neutron detector systems

8.1 The ^3He crisis as the onset for neutron detector development

Cosmic-ray neutron probes (CRNP) in CRNS have long relied on ^3He gaseous proportional counters (GE Energy, 2005) as did most of the neutron detection systems. However, virtually all ^3He is gained from the radioactive decay of tritium used in thermonuclear weapons. Its exploitation from natural sources has remained unprofitable as ^3He amounts to solely 1 ppm of all helium in the atmosphere (Aldrich et al., 1948). After the terrorist attack 9/11 in 2001, the anxiety of being the victim of a nuclear assault rose in the U.S. and neutron detectors were widely applied at its borders (Geelhood et al., 2003). The U.S. ^3He stockpile has since experienced a strong decline climaxing in 2010 followed by grave use restrictions on several sectors (Shea et al., 2010) and a price raise by more than one magnitude. This series of events has led to various development approaches in the sector of neutron detection to find alternatives to ^3He as a gaseous converter. Also CRNS has seen the introduction of $^{10}\text{BF}_3$ counters to the method. However, the toxicity of $^{10}\text{BF}_3$ had raised doubts about whether these detectors are suitable for outdoor applications. Moreover, their performance in terms of neutron count rates also left room for improvement.

Ever since Desilets et al., 2010 proposed to use cosmic-ray neutrons as a proxy for ambient hydrogen content, the method has steadily gained in popularity and so has the demand for neutron detection systems. In recent years several groups have started dedicated detector development advances, that tried to replace the first generation detection systems. Some of which again transferred over from neighbouring applications like homeland security but some also introduce approaches especially tailored to CRNS.

Gaseous multi-wire proportional counters using ^6Li metal as a solid converter have been introduced by Raymond et al., 2019 to CRNS and just recently Montag et al., 2019 presented a similar system. Thick converter layers can be afforded when using solid ^6Li due to its relatively high Q-value. That compensates for the lower absorption cross section as compared to ^{10}B or ^3He (see section 3.1). These systems therefore yield relatively high neutron count rates. Besides gaseous detectors, Stevanato et al., 2019 have launched a scintillator-based neutron detector followed by a similar endeavour by Stowell et al., 2021. Both use ^6Li in combination with a $\text{ZnS}(\text{Ag})$ scintillation material to convert neutrons into light. Moderator and detection volume are combined when using plastic scintillators. This may be used to enhance the count rate of smaller detectors but hinders the enlargement of the detector without shifting its energy response function. Scintillators come with an added application opportunity in the context of CRNS as they are decent muon detectors by default. Muons that are produced as secondary cosmic-rays alongside neutrons are not sensitive to ambient hydrogen content. Hence, the idea of using them as a proxy for the incoming galactic cosmic-ray flux that controls the neutron production circled the CRNS community for several years. Stevanato et al., 2022 argued that their integrated muon detector may be used to locally correct for the incoming flux instead of referring to a neutron monitor data base station.

Besides these, our group at Physikalisches Institut, Heidelberg has focused its experience in neutron detector design to develop a solid ^{10}B lined gaseous neutron detector system especially designed for the application of CRNS. The following chapter summarizes the findings that were already published in Weimar et al., 2020 appended by several recent results.

8.2 Specific demands on neutron detectors in the context of Cosmic-Ray Neutron Sensing

Neutron detectors applied in CRNS have to be improved in order to support a holistic progress of the method. In view of existing systems and the demands of CRNS on the neutron detector, three major challenges are identified:

1. **Count rate enhancement:** The neutron detector count rate directly relates to the time resolution by its statistical uncertainty. For typical systems and environmental conditions, neutron count rates have to be integrated over 4–12 hours in order to achieve a statistical precision of a few percent. While this is sufficient for many hydrological processes, it renders the method incapable of capturing interception or irrigation. But most certainly, large integration times impede mobile measurements where the area to be covered in a certain time is primarily restricted by the detector's count rate.
2. **Higher signal-to-noise ratio (SNR):** The SNR describes the ratio between the detected neutrons that relate to the environmental hydrogen content (signal) to such which do not (noise). It determines the change in detected neutron count rate per hydrogen content change. With increasingly moist conditions, the sensitivity to hydrogen content changes decreases steadily until it eventually saturates due to the hyperbolic relationship to θ . In close-to saturated conditions, i.e. humid forests (Bogena et al., 2013) and snow covered areas (Schattan et al., 2017), a high signal-to-noise ratio is critical for the assessment of water resources.
3. **Refinement of the energy sensitivity:** Some of the CRNPs come with two detectors, which feature peak sensitivities in the thermal and the epithermal energy regime, respectively. Recent studies tried to make use of spectral information (Baatz et al., 2015; Tian et al., 2016) by comparing the two signals. However, the moderated detector suffers from a thermal neutron contamination that constitutes up to 20 % of its signal (Köhli et al., 2018a). Moreover, preventing thermal neutron leakage is equivalently important for standard soil moisture sensing applications, since thermal neutrons exhibit a different and much smaller dependence on the environmental hydrogen content than epithermal-to-fast neutrons. Andreasen et al. (2016) and Desilets et al. (2010), therefore, already suggested to disentangle the signals to provide a higher contrast. The latter study also determined an appropriate moderator thickness of 25 mm through empirical studies. However, it might not be the ideal setup for any environmental condition and has not been further investigated by means of neutron modeling. Lastly, the spectral resolution can be extended by a modular multiple-counter detector system. Spectral information of higher energy neutrons can be used to actively correct for local effects (Schrön et al., 2018).

This listing might be expanded by a rather non-academical development topic: The ability of the detection systems for long-term measurements on the order of years in partly harsh environments. This additional requirement implicate further demands, such as low power consumption for autarkic use and a resilient electronics setup in terms of temperature, humidity influences and long-term drifts.

8.3 Neutron measurement uncertainty and its propagation onto the soil moisture retrieval

Precise measurements of environmental hydrogen content via cosmic-ray neutrons require low statistical uncertainty and a high signal-to-noise (SNR) ratio of deployed neutron detec-

tors. From a physical point of view signal may be defined as the detected epithermal-to-fast neutrons that penetrated the soil and underwent at least one scattering event. Following that, noise includes epithermal-to-fast neutrons which did not enter the soil volume, neutrons with different energy and detections that were erroneously assigned to a neutron event. Additionally, it comprises those evaporation neutrons that were created in the soil but leave it without any interaction. From a principle point of view, however, neutrons which were in contact with soil and those which did not are not distinguishable. Even with directional-sensitive detectors, it is not possible to trace back the location of the soil contact. That is because neutrons scatter multiple times in the air changing their direction with each scatter event. The following discussion, nonetheless, focuses on the former definition of SNR as the above mentioned limitation does not hold for Monte Carlo studies where neutrons can be tracked. Additionally to the systematic uncertainty introduced by noise σ_{ns} , another uncertainty is introduced by counting statistics σ_{stat} . The total uncertainty on the neutron count therefore becomes:

$$\sigma_N^2 = \sigma_{\text{stat}}^2 + \sigma_{\text{ns}}^2. \quad (8.1)$$

The detection of neutrons obeys Poisson statistics, where the variance σ_{stat}^2 equals the expected value N , which is the number of detected neutron events. Assuming a constant neutron flux under constant environmental conditions, the relative statistical uncertainty can be determined as:

$$\frac{\sigma_{\text{stat}}}{N} = \frac{1}{\sqrt{N}} \propto \frac{1}{\sqrt{t}}. \quad (8.2)$$

Hence, the statistical uncertainty can be reduced by prolonging the integration time of a single neutron measurement. Here, the propagation of the neutron measurement uncertainty onto the soil moisture retrieval is discussed briefly, before an appropriate strategy to build CRNS neutron detectors with low measurement uncertainty is discussed in more detail in the following sections. For simplicity, all hydrogen content is considered to be bound in soil moisture. The calculation still holds true if using the total water equivalent approaches like Franz et al., 2013 or Schattan et al., 2019. However, here the uncertainty analysis of specific further parameters such as air humidity or snow is neglected. Eq. 2.27 can be used to estimate the uncertainty σ_θ :

$$\sigma_\theta = \left| \frac{\delta\theta}{\delta N} \sigma_N \right| = \frac{a_0 \rho_{\text{bd}}}{N_0 \left(\frac{N}{N_0} - a_1 \right)^2} \sigma_N = \dots = \left(\frac{\theta}{\rho_{\text{bd}}} + a_2 \right)^2 \frac{\sigma_N \rho_{\text{bd}}}{a_0 N_0}. \quad (8.3)$$

It is important to note that σ_θ increases linearly with σ_N and quadratically with the hydrogen content. The ability to detect small hydrogen content variations in saturated environments is therefore strongly coupled to the measurement uncertainty of the neutron detector. Bogena et al. (2013) already discussed σ_θ with respect to the statistical uncertainty σ_{stat} . In the following sections the setup of gaseous neutron counters is described and each factor that may contribute to the noise is analyzed in view of detector design.

In the following the bare neutron detection device is referred to as neutron counter and the whole detection system including moderator, thermal shielding and electronics as neutron detector.

8.4 Reducing statistical uncertainty: count rate enhancement

The cosmic-ray neutron flux I_n at sea level integrated over all energies below 15 MeV is around 50–200 neutrons per second and m^2 , depending on the magnetic cut-off rigidity and hydrogen pools (Goldhagen et al., 2004; Nesterenok, 2013; Sato, 2015). For most CRNS systems that ensues integration times on the order of hours in order to reduce the relative statistical uncertainty on the neutron count rate to few per cents (Bogena et al., 2013; Schrön et al., 2018). Two parameters control the detector's count rate. Firstly, the flux impinging on the neutron detector is proportional to its surface area A . Secondly, the magnitude of the detector's response function $R(E, \phi)$, as discussed in section 2.4.3, is a measure for the efficiency of the system. Combining both one can define a pseudo efficiency ϵ_{pseudo} as

$$\epsilon_{\text{pseudo}} = \text{flux through detector [N/s]} \cdot \text{detection efficiency } (E, \phi) [\%] \quad (8.4)$$

$$\propto A [\text{m}^2] \cdot R(E, \phi) [\%] \cdot I_n(E) [\text{N}/(\text{s m}^2)],$$

which directly relates to the neutron count rate of the detector. Thus, this quantity should be maximized for minimal statistical uncertainty.

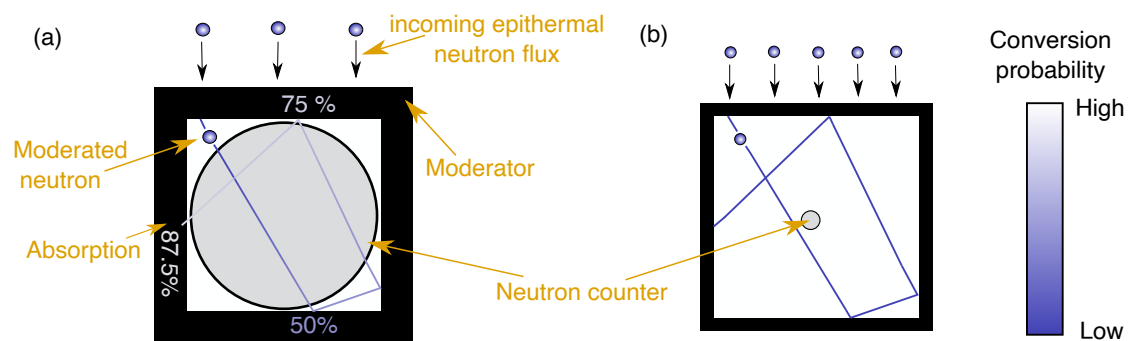


Figure 8.1: Schematic drawing of the interplay between surface area and response function. The cross sections through two combinations of a rectangular moderator and cylindrical neutron counter at thermal efficiency of 50 % are shown. Both figures are not to scale. A typical neutron track after thermalisation through the inside of the moderator is shown in blue with the colour saturation indicating the absorption probability by the converter material. (a) maximizes the response function but features the smallest surface area possible, while (b) has a large surface area compared to the neutron counter dimension. Configuration (b) therefore has a large neutron flux impinging the moderator but a low response function because of the lower probability for a counter transect (Weimar et al., 2020).

Surface area and energy response function anti correlate in the count rate optimization process at a fixed amount of converter material, see the conceptual idea in Fig. 8.1. An optimal compromise between the two in particular depends on the efficiency and dimensions of the neutron counter. Monte Carlo simulations reveal that a thermalised neutron entering the inside of the moderator casing transits the latter on average 3 times due to backscattering at the inner surface. It may, therefore, traverse the neutron counter inside the moderator several times. The smaller the counter compared to the volume enclosed by the moderator the lower the probability to hit the tube. However, for highly efficient counters multiple

traverses or large path lengths through the counter contribute less and less to the detection efficiency due to the exponential absorption law. For neutron counters with high efficiencies, it is advantageous to have a slightly bigger moderator casing, hence a larger surface area in exchange for a lower traverse probability, see Fig. 8.1. As the neutron converter usually makes up for most of the production costs, it is instructive to optimize the detector design for a certain amount of converter. Fig. 8.2 shows the interplay between the size of a cylindrical-shaped neutron counter inside a rectangular moderator casing and the system's efficiency calculated by means of Monte Carlo simulations.

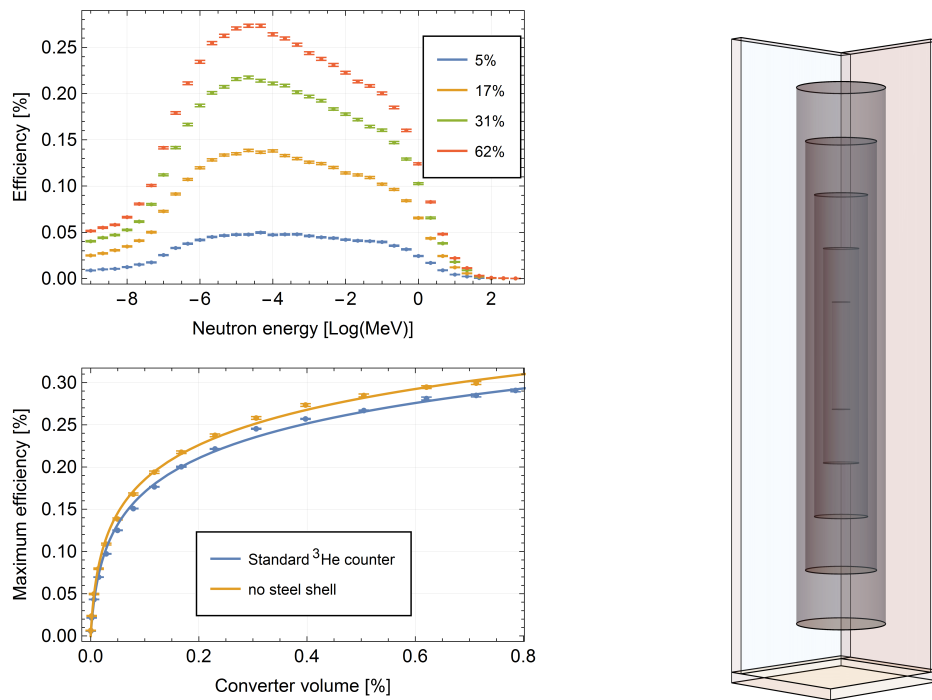


Figure 8.2: Overall detector efficiency as a function of the size of a neutron counter with constant ^3He amount. **Left, top:** Detector response functions (DRF) for several counter sizes. The values in the legend box indicate the counter's size expressed in percentage of the whole volume enclosed by the moderator casing. **Left, bottom:** Maximum value of the DRF as a function of counter size as defined before. Two scenarios are shown: In blue a realistic counter inside a stainless steel shell and in orange a counter solely consisting of ^3He . **Right:** Geometric setup of the simulation batch. The size of the cylindrical counter is changed both in radius as well as height (light gray cylinders). For better clarity only 3 moderator sheets are shown in order to indicate the dimension of the moderator casing. In the simulation setup the counter was surrounded by all six sides with a moderator of 25 mm thickness corresponding to the standard CRNP setup.

The overall amount of ^3He atoms in the counter was kept constant at 3.5 bar·l while its size was varied from 1–2700 cm³. It is also enveloped in a stainless steel shell according to GE Energy, 2005. The inner volume of the moderator casing was set to 3500 cm³, while having a thickness of 25 mm. In order to treat the transport of thermal neutrons correctly a thermal scattering kernel for hydrogen bound in polyethylene at $T = 293\text{ K}$ was used (Brown et al., 2018). Although, the differences in the simulated response function when using a

8. Concepts of developing dedicated cosmic-ray neutron detector systems

light water scattering kernel amounted to only few percent in its magnitude. The moderator was then radiated from the side with a neutron flux directed in 2π , i.e. any angle that points towards the moderator casing was weighted equally, in order to estimate the energy dependent detection efficiency (similar to the procedure proposed by Köhli et al., 2018a). The simulation results clearly confirm the conceptual idea of Fig. 8.1, while also quantifying the effect of a poorly spread converter within the inner moderation volume. In the ideal case, the converter is evenly spread throughout the inside of the moderator as opposed to a highly efficient but small counter with the same amount of converter. The detector's efficiency relates logarithmically to the counter's volume (see blue line in Fig. 8.2 bottom, left panel): the larger the volume the more converter nuclei are passed by the neutron, which add up to the overall absorption and conversion probability via the Beer-Lambert law. If less converter is available the curve shown scales approximately linearly to lower efficiency values.

It is also important to note that a large fraction of the neutron flux impinging the surface of the moderator does not penetrate through to the inner volume. Most of these neutrons are backscattered into the air, while a smaller part is absorbed within the moderator. That limits the maximum efficiency of a gaseous neutron counter inside a moderator casing. The maximum is only slightly higher than the values presented here: a neutron detector comprising a counter featuring 99 % absorption probability for thermal neutrons shows a maximum value of approximately 33 % indicating that two thirds of the incoming neutron flux is lost despite the counter's efficiency. In the context of CRNS, a cost-efficient detector design, therefore, is large in size while less efficient to maximize the use of its converter.

Fig. 8.1 reveals another important detail: Any other neutron absorber within the moderator casing competes with the neutron converter and reduces the thermalised neutron flux and thereby the count rate of the whole detection system (compare the two curves in the left, bottom panel). The choice of the material that composes the neutron counter therefore also has a strong effect on its efficiency. Stainless steel in particular consists of some moderate neutron absorbers like nickel, mangan and iron.

8.5 Optimizing the moderator dimensions for an existing neutron counter

The former standard CRNP comprised a ^3He neutron counter with usually 1.5 bar partial pressure of ^3He inside a stainless steel cylinder with a diameter of two inches and height of ≈ 30 cm. This configuration features an efficiency of over 60 % for thermal neutrons if the neutron penetrates the counter perpendicular to its barrel surface. These highly efficient counters offer the opportunity to enhance the system's count rate by enlarging the moderator casing because a reduction in the neutron's path length inside the converter volume is not linearly projected to a loss in conversion probability due to the exponential absorption law. The standard setup embeds the thermal counter tightly into a cuboid moderator casing, i.e. the outer moderator's dimensions are roughly $11 \times 11 \times 36$ cm.

The optimisation process is inverted to the above visualised by Fig. 8.2: The counter size is fixed and the moderator's dimensions are changed, while the thickness of the moderator is fixed to 25 mm. Since the neutron counter is circular symmetric, the moderators size in x and y direction is changed equally (the cylindrical neutron counter's symmetry axis is the z-axis), while its height, i.e. extension in the z-axis is changed independently. Neutrons are emitted on the surface of the cuboid moderator with a 2π -isotropic angular distribution. The four side panels of the moderator casing as well as the top and bottom panel share the same size. Hence all simulations were conducted emitting neutrons either from the side or the top and weighted according to the area fraction that is covered by either of these. The effective count rate normalized to the standard moderator casing can then be calculated by multiplying the surface area times the maximum efficiency (see Eq. 8.4), which is shown

in Fig. 8.3. Indeed, the effect of a higher flux throughput overcomes the efficiency loss with increasing moderator size, which yields a gain in count rate of approximately 2. Two characteristics of this optimisation process are noteworthy: Firstly, the inclination of the count rate gain is high when increasing the x/y dimension of the moderator, i.e. a cubic moderator casing is favored over a longitudinal arrangement. Cubes maximize the surface area for a given volume (assuming a cuboid shape) and thereby maximize the neutron's path length in the converter volume for a given surface area. Secondly, the count rate gain as a function of surface area can be described by a bound growth relationship that takes the limit of approximately 2.3. The efficiency gain saturates when the neutron's path length through the converter volume is so short that the exponential absorption law may be well linearised. By extending the standard dimensions to 40 × 40 × 40 cm a count rate gain by 50 % is yielded.

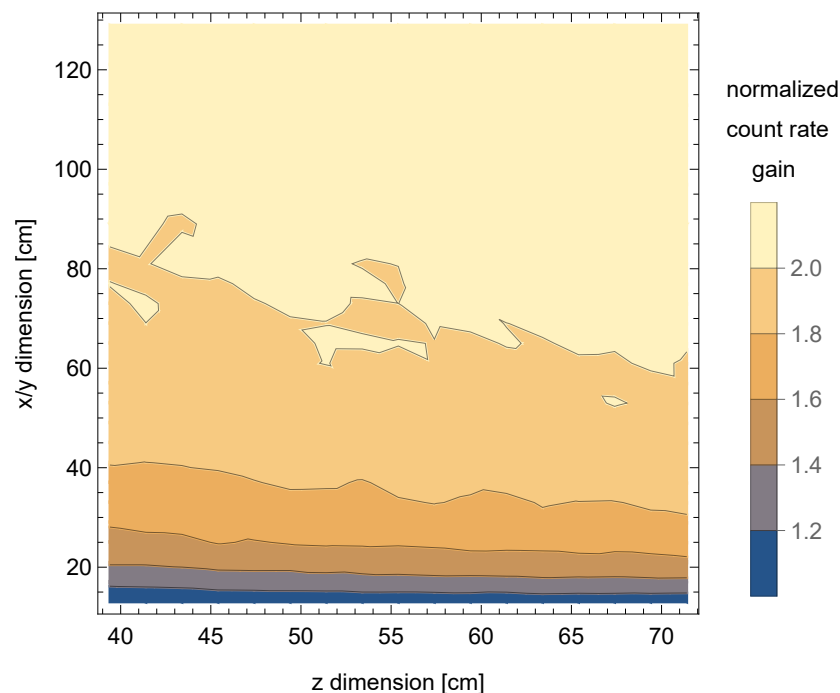


Figure 8.3: Normalized count rate of a ^3He neutron counter with 1.5 bar partial pressure enclosed in a cuboid moderator casing as a function of the moderator size. The count rate is normalized to a tightly fitted moderator casing of a minimal size of 11 × 11 × 36 cm. The cylindrical neutron counter is aligned along the z-axis.

8.6 Improving the cosmic-ray neutron probe's signal-to-noise ratio

8.6.1 Optimised energy resolution of the cosmic-ray neutron probe

Neutron absorption, including the conversion process, is most efficient for low-energy neutrons (see section 3.1). Therefore, the energy dependent detection efficiency of a bare neutron counter lies in the thermal energy regime, see the black curve in Fig. 8.4. The broad DRF of a standard cosmic-ray neutron probe as shown above, comes with the drawback that the environmental thermal neutron flux can partly leak into the moderator and increase the detector noise. This can be prevented by mounting a strongly absorbing material at the outside of the moderator case like cadmium, boron or gadolinium oxide (Gd_2O_3), further referred to as thermal shield. Moreover, the sensitivity reaches into the evaporation energy regime, which also shows a less pronounced hydrogen sensitivity than the epithermal energy

range (see Fig. 2.10 in section 2.4). Thus, this section aims at examining the detector response function in view of an appropriate moderator thickness and an additional thermal shield and its benefits for the soil moisture retrieval.

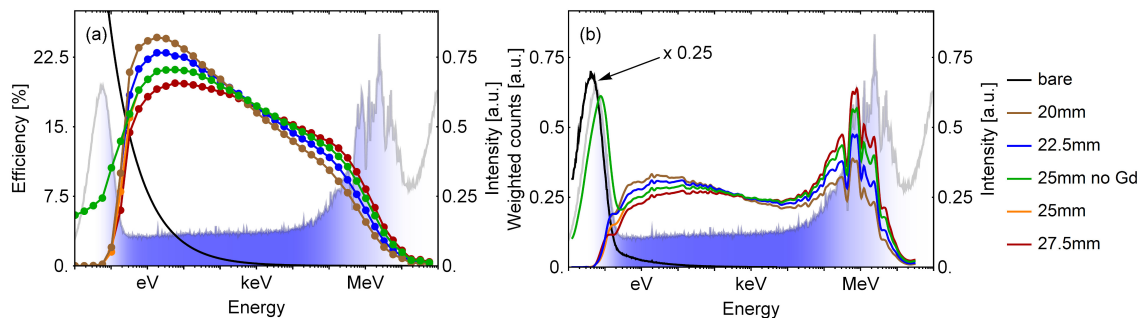


Figure 8.4: (a): Response functions of a bare neutron counter and detectors with moderator thicknesses of 20–27.5 mm in steps of 2.5 mm. All models except for one of the 25 mm versions are equipped with a thermal shield. The thermal shield consists of a Gd_2O_3 layer with a thickness of $90\ \mu\text{m}$ in order to provide a sufficiently high absorption cross section for the thermal peak. The chosen thickness reduces the spectral count rate for energies below 100 meV to approximately 1%. For this study the reference density for the high density polyethylene moderator was chosen to be $0.95\ \text{g}/\text{cm}^3$. The detector model is based on the ^3He Rover, introduced in Desilets et al. (2010) and analyzed by Köhli et al. (2018a). In order to compare energy ranges a cosmic-ray neutron spectrum above the soil at 20 % soil moisture and $15\ \text{g}/\text{m}^3$ air humidity simulated by MCNP is drawn. The dry soil consists to 75 % of SiO_2 and to 25 % of Al_2O_3 . The sensitivity to hydrogen according to Fig. 2.10 in section 2.4 is shown by the shaded blue filling. (b): Weighting of this neutron spectrum with the response functions reveals the total count rate contribution of the different energy domains. The weighted count rate of the bare counter are decreased by a factor of 4 (Weimar et al., 2020).

Fig. 8.4 (a) shows the response functions of neutron counters with various moderator and thermal shield configurations. The standard CRNP configuration is shown in light orange. Folding with the cosmic-ray spectrum yields the spectral count rate, see Fig. 8.4 (b), which, if integrated over all energies, leads to the total count rate. The relative thermal contribution of the signal of the standard CRNP is in particular large for moist soil. The reason for this observation is that the ratio between thermal and epithermal-to-fast neutrons increases with soil moisture, as the thermal intensity is not as sensitive to environmental hydrogen. However, the numbers shown here are subject to a systematic uncertainty since the intensity of the thermal peak additionally depends on the soil chemistry. Following the signal definition in section 8.3 this thermal contamination of standard probes leads to a lower SNR as compared to shielded detectors, see Fig. 8.5 (a). A high SNR is especially achieved for thin moderator configurations as the contamination of evaporation neutrons that did not penetrate the ground is relatively low, indicated in Fig. 8.4 (b). However, excluding the evaporation regime is accompanied by a loss of signal as still a large part of such neutrons probed the soil. The signal normalized to the configuration of 27.5 mm moderator thickness and thermal shield is shown in Fig. 8.5 (b). The subfigures in Fig. 8.5 (c) and (d) are also normalized with respect to the same configuration. Fig. 8.5 (a) and (b) reveal the competition between gain in signal quality by a higher SNR and by higher count rates, i.e. lower statistical uncertainty. Higher SNR leads to higher signal dynamics, i.e. relative count rate change per Vol-% soil moisture change, $\frac{\Delta N}{N}/\Delta\theta$, as depicted in subfigure (c). However, the statistical uncertainty needs to

be sufficiently low in order to resolve these dynamics. Therefore, maximizing

$$\frac{\sqrt{S} \cdot \frac{\Delta N}{N}}{\Delta \theta} \quad (8.5)$$

is suggested as an optimization variable, where S is the signal. This product of statistical and dynamic range precision is shown in Fig. 8.5 (d).

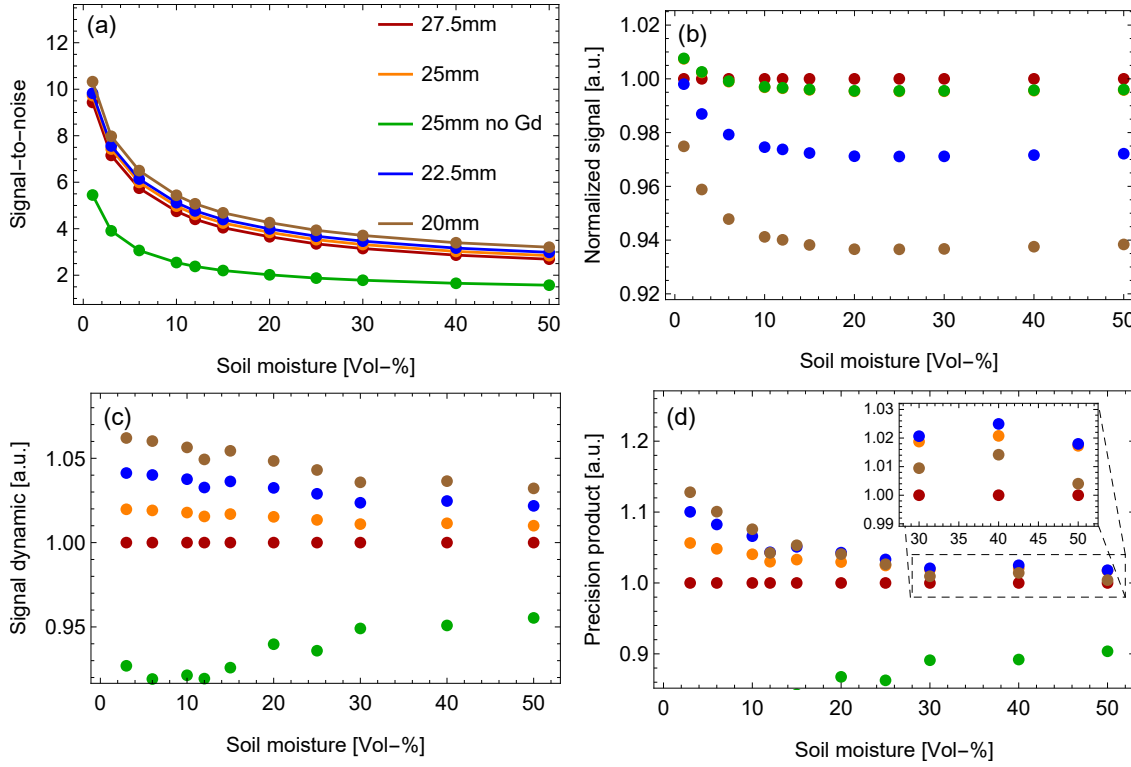


Figure 8.5: Detector response to soil moisture dependent on the moderator thickness. All detector configurations feature a thermal shield except for '25 mm no Gd'. (a): SNR according to the definition of section 8.3. (b): Signal count rates normalized to the detector setup with 27.5 mm moderator thickness and a thermal shield. (c): dynamical range or signal contrast, normalized like (b). (d): Suggested optimization procedure, maximizing the product of statistical and contrast precision according to Eq. 8.5. Figure taken from Weimar et al., 2020.

It features maximum values for 20 mm and 22.5 mm moderator thicknesses in dry and moist conditions, respectively. As for dry conditions the signal dynamic is larger, it is concluded that a 22.5 mm moderator accompanied with a thermal shield shows the best overall performance. Yet, the difference to the 25 mm moderator and thermal shield combination as it was presented by Desilets et al. (2010) is marginal. In some use cases the thickness might be reduced further as for example in high altitude measurements. High altitudes come with the benefit of a high neutron flux and therefore low statistical uncertainty in shorter time frames. It might, thus, be beneficial to opt for a higher SNR with thinner moderators in order to maximize the overall precision. Fig. 8.5 shows the important role of thermal shielding as it significantly improves the dynamic range while keeping the signal count rate constant. If thermal neutrons are not efficiently shielded Eq. 8.5 shifts to thicker moderators and finally yields an optimum of 27.5–30 mm if no thermal shield is applied. The shape of the

response functions is dominated by the moderator thickness but is also slightly influenced by the detector geometry and aspect ratio (Köhli et al., 2018a). Hence, any detailed moderator optimization procedure should be adapted to the individual detector dimensions and might differ slightly from the above analysis.

8.6.2 False positive detections - Neutron counter efficiency to other types of radiation

One important source of detector noise are particles that generate a similar ionisation signature like neutrons inside the neutron counter and therefore may be mistaken for such, see Fig. 3.8, 1(c) in section 3.6. Sources of ionising particles include other cosmic rays, terrestrial radiation and weakly radioactive materials inside the detector itself. In particular, a similar signal compared to neutron conversion is triggered when particles are of the same kind as the conversion products. Such are mainly heavy and highly ionizing particles with short ranges of less than a few millimetres in solid materials. Thus, these particles do not penetrate the neutron counter from outside but if generated in the innermost layer of the tube wall, they can enter and ionize the gas and contribute to the noise. Hence, only material with lowest intrinsic radioactivity should be used for the production of neutron counters. Even a comparably low abundance of radioisotopes may decrease the signal-to-noise ratio significantly due to the small flux of cosmic-ray neutrons.

Standard counting gases feature low mass stopping power for cosmic-ray muons, electrons and protons (see section 3.3 and Fig. 3.3 therein), which leads to a rather low total energy deposition E inside the counter via ionisation as compared to the neutron conversion products. Moreover, that also leads to much longer ionisation track lengths. The significance of such contributions depends on the geometry of the system, which allows or prevents long track length for electrons, and the density of the counting gas. In summary, careful material selection can minimize intrinsic radioactive background that may induce false positive signals. The deposited energy E and the energy loss per distance travelled dE/dx can be used to discriminate between the conversion products and other ionizing particles.

9

Large-scale boron-lined cosmic-ray neutron probes

9.1 Description of the detection system



Figure 9.1: Pictures of the neutron detection system deployed next to a corn crop field. **1:** The neutron detector is mounted on a ground screw. The black polyethylene is covered by a thermal shield with green varnish. The tired scientist's coffee mug is placed on top. The grey box on its left side houses a lead battery, charge controller and the data logger. A antenna on top is used for GNSS and LTE connectivity. Precipitation, atmospheric pressure, humidity and temperature are measured by the small weather station on top of the black pole that comprises a total of 12 sensors (Meter Group, 2022). The solar panel in the rear provides independent power supply. **2:** This detection system contains two neutron counters inside the moderator casing but may be upgraded to five to enhance its count rate. The two tubes are connected via high voltage cables to the readout electronics in the center. **3:** Indoor shot of the logger box setting of a similar system. The data logger's front panel features USB connectivity, an SD and SIM card slot and a display that shows the current status and recently logged data.

The detection system described in this chapter has been designed and developed in close cooperation with Markus Köhli and Ulrich Schmidt, both from Physikalisches Institut, University Heidelberg.

The CRNP design considerations introduced above have led to CRNS-tailored neutron detec-

9. Large-scale boron-lined cosmic-ray neutron probes

tor development. This study introduces the first dedicated approach, a large-area ^{10}B -based neutron detector. It makes use of a multitude of boron-lined proportional counters. These are hermetically sealed aluminium cylinders with an inner diameter of 54 mm and a length of 1250 mm (a picture of the proportional counter is shown in Appendix B.3). The gold plated tungsten wire in the center has a diameter of 25 μm , see schematic setup in Fig. 3.8. The wire is set on a high voltage of 750 V. The cylinder is filled with a gas mixture of 90 % argon and 10 % CO_2 at a pressure of 250 mbar. The B_4C converter layer (96 % enrichment of ^{10}B) is located at the inner cylinder wall and has a thickness of up to 1.5 μm that is sputter-deposited on high purity copper foils. The efficiency of a single counter for thermal neutrons amounts to roughly 10 % (Modzel et al., 2014; Piscitelli, 2013). Another 3 % are absorbed but not detected as the conversion products do not reach the gas or their ionization signature is below the detection limit. The neutron detection via conversion, ionisation and avalanche formation follows the processes described in chapter 3.

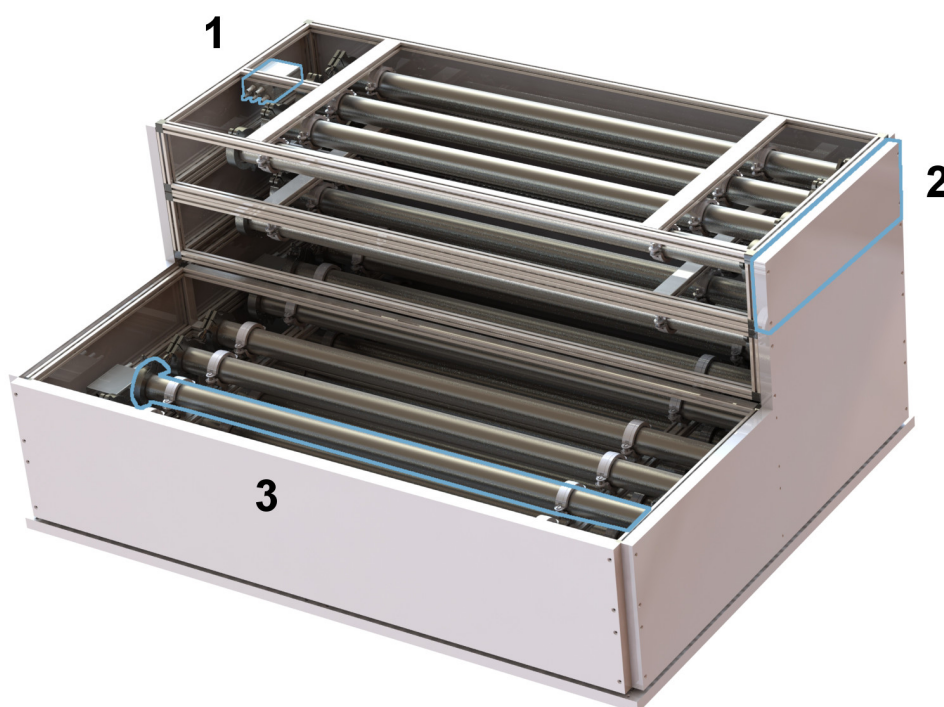


Figure 9.2: Setup of the large-area boron-lined detector for mobile measurements. Six base units are shown, assembled in two rows with two units each and two units on top of the back row. Each base unit contains one readout electronics module (marked as 1 and highlighted in blue) connected to four proportional counters (3). The base units are surrounded by three sides with polyethylene moderator sheets (2). The figure is adapted from Weimar et al., 2020.

Stationary detectors are equipped with up to five counter tubes and a mobile detection system is composed of four rows with eight counters each as indicated in Tab. 9.1. Each row is subdivided into two base units with four neutron counters each (see Fig. 9.2). The detector tubes are surrounded by a modular moderator of 25–35 mm thickness and a removable thermal neutron shield made of Gd_2O_3 . The counters of a base unit and those of a stationary detector are connected to one pulse analysing and digitizing readout electronics module. The readout electronics assigns individual timestamps to each detected event with a temporal resolution of one millisecond. Such information may be used to study the 'ship effect' and

Detection system	Dimensions [cm ³]	Neutron counter	Pseudo efficiency
CRS-1000	40 × 10 × 10	1 (³ He)	3.0±0.2
Stationary (StX-140-5)	140 × 32 × 35	5 (¹⁰ B)	15.8±1.2
Mobile	145 × 120 × 80	8 × 4 (¹⁰ B)	88±5

Table 9.1: Key properties of the mobile and stationary detection system presented in this study and the commonly used CRS-1000 (this detector type is also described in section 2.4.3). Dimensions refer to the size of the moderator casing and the pseudo efficiency follows the definition in Eq. 8.4. It directly relates to the count rate of the system and was calculated using the Monte Carlo code URANOS.

allows for corrections of occasional spikes in the count rate (Aguayo et al., 2013; Kouzes et al., 2008).

A data logger collects the pulse information of the readout electronics and records temperature, relative humidity and air pressure. The data is stored locally on a SD card and can be transmitted remotely via GSM or LTE. GNSS connectivity enables location tracking for mobile measurements but also updates the real time clock of the data logger ensuring stable timing over long periods. Tab. 9.1 shows that the boron-lined detection systems feature a large surface area compared to other systems resulting in a high neutron flux throughput. The neutron counters inside the large moderator housing take up a substantial part of the inner moderator volume. Therefore, moderated neutrons are likely to traverse multiple boron-lined conversion layers, resulting in a moderate response function, which is two times lower than that of a ³He-based CRS-1000 detector. However, due to the larger surface a pseudo efficiency that is approximately five times higher than that of the CRS-1000 detector is achieved (Köhli et al., 2018a). An optional thermal shield reduces the count-rate by 10–20 %, depending on the environmental conditions, but significantly improves the signal-to-noise ratio, see also section 8.6.1.

9.2 Readout electronics

The key feature of any proportional counter is to precisely measure the charge generated in the ionization process by the incoming particle, see section 3.6. A well-adapted analog amplifier stage generates pulses with heights proportional to the energy deposition in the counter. It can therefore discriminate between the dense tracks from the neutron conversion process and weak ionization processes. Energy discrimination can effectively suppress most ionisation events induced weakly ionising cosmic-ray muons, electrons and protons. However, some of these particles can deposit significant amounts of energy in the gas if their track length is large enough. Long ionization traces lead to large differences in the arrival of the primary electrons close to the counter wall and those close to the wire. In general, the projected axial ionization path directly relates to the rise time of the charge pulse. As opposed to electrons, the rise time generated by the ¹⁰B conversion is very short due to the short-ranged and dense ionization processes, see section 3.3. Pulse rise time is therefore another tool for particle discrimination as was shown by Langford et al. (2013) and Izumi et al. (1971).

The readout electronics' design goal is, therefore, to precisely determine the charge pulse's height and rise time, which are coupled to E and dE/dx . Moreover, the outdoor deployment of CRNP demands for insensitivity to temperature drifts, air humidity and low background noise induced by the electronics circuit itself.

9.2.1 Analog input stage and digitising unit

The proportional counter's wire is set to a voltage bias by a low-drift high voltage module. This high voltage is DC-decoupled via capacitor C1, which is transmissible for the high frequencies of the charge pulses generated in the proportional counter (see Fig. 9.3). The input stage is composed of an integrator, that integrates over the charge accumulated in the ionisation processes and amplified at the vicinity of the neutron counter's wire. The product $\tau = RC$ determines the decay of its exponentially shaped output pulse, while C2 its height via $U = Q/C$. C2 takes small values due to the small amount of charge generated. The optimization process of τ mainly depends on the ion drift time scale, which controls the flow velocity of the electrons from the wire onto the readout electronics input (as described in section 3.4). On the one hand τ needs to be high enough in order to integrate over the majority of the electron charge pulse. On the other hand it should be low to decrease the dead time of the detector and the influence of other ionising radiation on the signal.

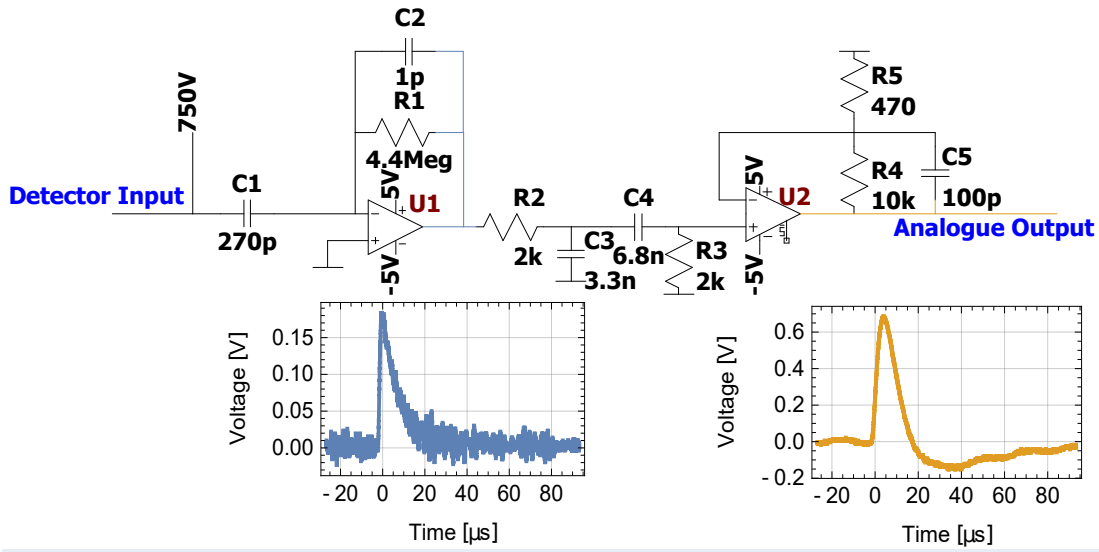


Figure 9.3: Schematic drawing of the analog input stage. The output voltages of the integrator (U1) and the main amplifier (U2) are shown in blue and orange in the corresponding inlets. Note that the pulse was recorded without a casing and, therefore, shows a high noise level.

The change in electric potential at the wire following an avalanche event is a function of the ion drift velocity μ and shows the following time dependency

$$V(t) = -\frac{e}{4\pi\epsilon l} \ln\left(1 + \frac{t}{r_{\text{wire}}^2 \pi\epsilon/\mu C V_0}\right), \quad (9.1)$$

where ϵ denotes the relative permittivity of the gas, e the elementary charge and $C = 2\pi\epsilon/\ln(r_{\text{cyl}}/r_{\text{wire}})$ the capacity between the wire, with radius r_{wire} , and the cylindrical neutron counter shell with length l and radius r_{cyl} . This potential change is then clipped by the integration time constant τ . Fig. 9.4 shows the resulting output signal of an integrator for a neutron counter setup as described above ($\mu \approx 1/6000$ and $\epsilon \approx 1$ were calculated according to Schultz et al., 1977 and Engineering Toolbox, 2010 for a gas mixture of 90% Argon and 10% CO₂). The pulse height represents the integral over the charge pulse. It changes strongly as a function of τ below 3–4 μs and less so for higher τ due to the logarithmic be-

haviour of $V(t)$. An appropriate value of τ was found to be $\approx 4.4 \mu\text{s}$, which was motivated by the ion drift dynamics and optimized experimentally by comparing measured and theoretical pulse-height spectra.

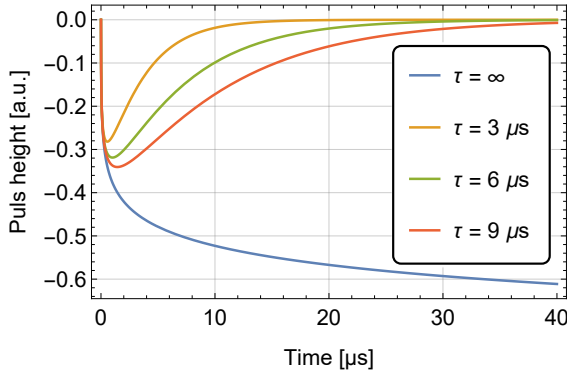


Figure 9.4: Calculated pulse shape according to (Eq. 9.1) cut by an integrating operational amplifier in the input stage of the readout electronics with $\tau = \{3, 6, 9, \infty\} \mu\text{s}$ for a cylindrical shaped neutron counter as described in section 9.1.

The following band-pass filter preselects the desired signal shape. A Fourier analysis of the integrator output signal induced by a neutron conversion reveals its dominant frequencies. The filter's bandwidth is chosen such that most of these frequencies pass but also cuts the pulse tail significantly, i.e. the lower frequencies of the pulse, in order to suppress pulses induced by other ionising radiation that feature longer ionisation tracks (see section 3.3). The subsequent stage amplifies the signal in order to adapt the dynamical range to the analogue-to-digital converter's (ADC) range that digitises the pulse height at a later stage. The main requirements for the operational amplifiers (opamps) are moderate speed in terms of bandwidth and slew rate, low noise, low drift and low power consumption. The first opamp also needs to have a high input impedance, i.e. low input bias and offset currents, in order to not drain the pulse's charge.

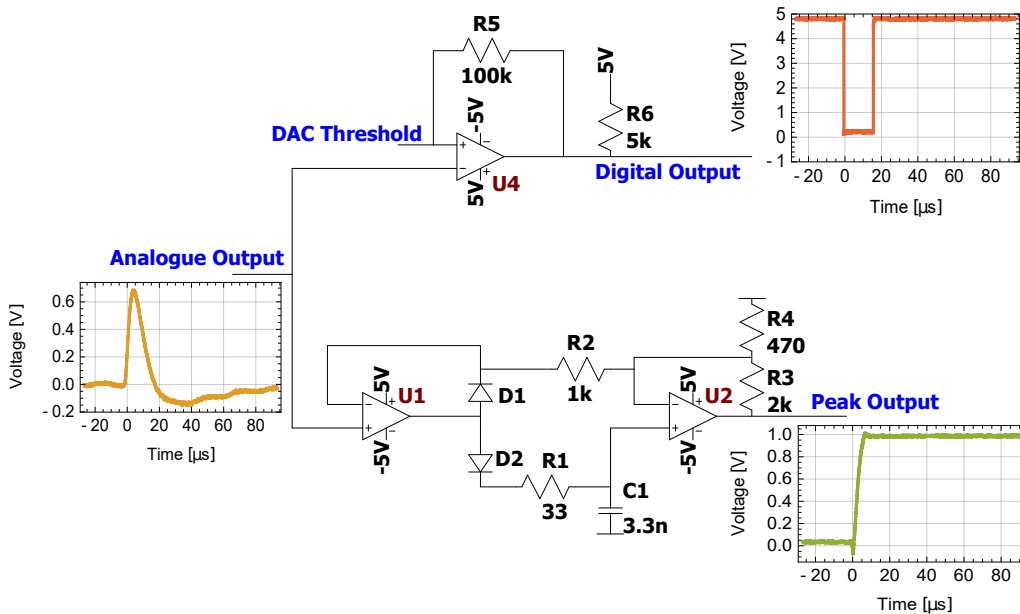


Figure 9.5: Digitising process of the analogue output signal. A comparator measures the time during which an incoming pulse exceeds a set threshold, the pulse length (red signal). It also triggers the readout of a peak detector that outputs the maximum value of the pulse, the pulse height (green signal).

The analogue output signal is then split. One branch is forwarded to a comparator that

provides a logically low signal output if the analogue signal exceeds a threshold set by a digital-to-analogue converter (DAC). Otherwise its output is set to high. Each pulse that exceeds the threshold value triggers a falling edge followed by a rising edge. Their time difference is recorded by the input capture unit of an atmega328p (Atmel, 2016) microcontroller (MCU) embedded in the Arduino Nano platform (Arduino SA, 2022). This interval defines the pulse length as one parameter that describes the recorded pulse shape. The falling edge also triggers the readout of the analogue signal via the 10-bit successive approximation register ADC of the MCU. The ADC's internal clock speed may be set by the programmer: The higher the clock frequency, the faster the analogue sampling but also the higher the uncertainty of the converted value. In order to avoid a compromise between speed and accuracy, a peak detector stage follows the analogue output signal's amplitude and holds the maximum value and also amplifies it (see for detailed description of peak detectors Horowitz et al., 2015). This ensures that the ADC samples the pulse peak, in the following called pulse height, independent of its timing. The ADC's input reference voltage is supplied by a low-drift/noise, high-precision reference. The peak detector is reset to ground after the analogue conversion process is completed using a digital switch. Relative humidity and air temperature are monitored as these are critical parameters that control the performance of the readout electronics.

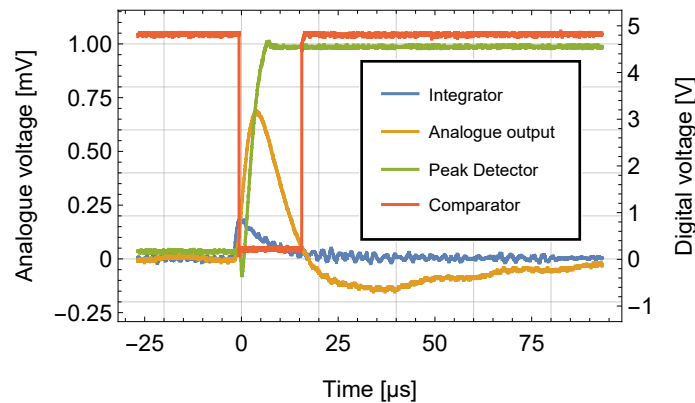


Figure 9.6: The readout electronics signal evolution indicated by the four stages described in Fig. 9.3 and Fig. 9.5. The analogue signal's amplitude (blue, orange and green curve) is given by the left y-axis and the comparators digitalised signal by the right y-axis (red curve).

9.2.2 Board design

The layout of printed circuit boards (PCB) influences the performance of electronic circuits. The ideal spatial placing of the components, the traces that link them and an adequate power supply management depends on a manifold of parameters. The readout electronics houses sensitive analogue electronics, a relatively fast digital part and a high voltage area within less than 80 cm² making an appropriate PCB design a crucial prerequisite to low-noise performance. The digital part can induce electromagnetic interference (EMI) on the analogue part and thereby increase its noise level. Here, a few key remarks on this specific design are made in order to facilitate future improvements and design changes.

Digital and analogue signal separation is critical in mixed systems. The ± 5 V analogue voltage supply is generated in the vicinity of its consuming integrated circuits (IC) with low-noise linear regulators (left of the green rectangle in Fig. 9.7). There is no ground plane below the integrator input stage (blue rectangle) in order to minimize capacitive coupling. Analogue signals are transmitted via slightly larger traces in order to reduce their impedance. The comparator IC (red rectangle) links the analogue circuitry to the digital area. The ground

plane and those traces that link the two compartments do so below the comparator. That is referred to as star point grounding and suppresses interference between the digital and analogue part. The ground plane prevents conductor loops that could lead to EMI because it ensues that the ground return path coincides with the signal trace. The high voltage traces are also followed by a ground plane below, which leads to an electric field that points downward into the PCB rather than pointing in the direction of the analogue circuitry. The latter case would increase the probability of charge creeping and sparks due to discharge, especially during humid conditions. Additionally, the board has several longitudinal mill traces between the high voltage and analogue part to further reduce charge movement (indicated by the thin yellow lines left and on top of the blue rectangle).

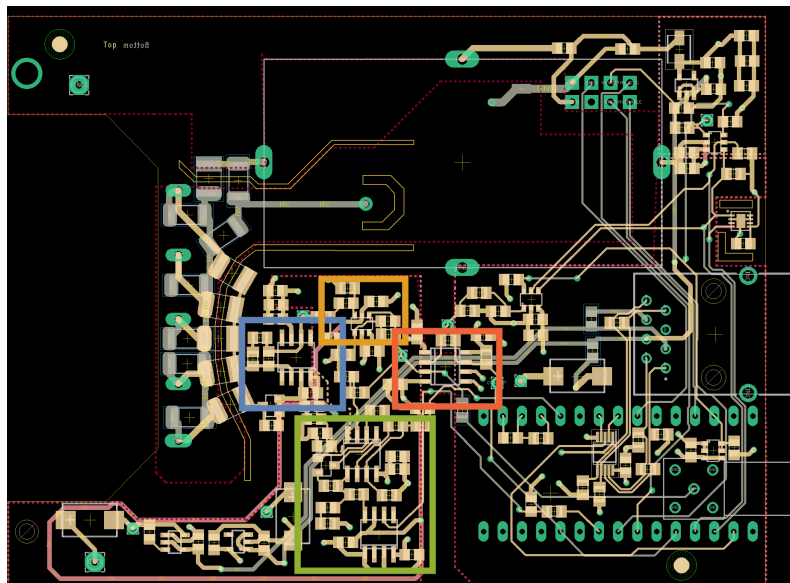


Figure 9.7: Four layer board layout of the read-out electronics with hidden ground and power planes. The four signal stages of the analogue circuitry are colour coded as in Fig. 9.6. The top and bottom layer house signal traces and components (ocher and gray color, respectively). One of the inner layer consists solely of a ground plane ensuring appropriate grounding, while the other is split in several power planes depending on which power supply level is drained the most for a specific area of the board.

9.2.3 Pulse shape analysis

As an upgrade to the commonly used pulse height discrimination, a two-dimensional information about pulse height and length is used, which is shown in Fig. 9.8 and Fig. 9.9. When exposing a boron-lined counter with 1 bar counting gas pressure to a radioactive gamma, beta and neutron source¹ its efficiency to the various particle species can be determined. As suspected, neutrons and electrons populate different but also overlapping regions in the pulse length and height plot, Fig. 9.8 (c), due to their different ionization characteristics, E and dE/dx (see section 3.3)². An event cluster that exclusively contains neutrons depicted in blue can be separated by the orange cluster populated by a mix of particle species. In both, the

¹For these neutron event recordings the in-house ^{252}Cf neutron source at the Physikalische Institut, Heidelberg was used (for more detailed information on this neutron source type see e.g. Smith et al., 1957).

²Note that for this measurement the pulse height and length was recorded after the preamplifier stage, i.e. the integrator, while the rest of the measurements shown here depict pulse height and length measured as described above using the whole signal path. The idea was to record the pulse shape before it was changed by the bandpass filter.

pulse height and pulse length spectrum, these clusters overlap and may not be distinguished completely. Only a combination of the two quantities provides a clear separation. However, a substantial amount of neutron events are contained in the orange cluster that makes up one third of all events. Therefore, a loss in count rate cannot be entirely avoided.

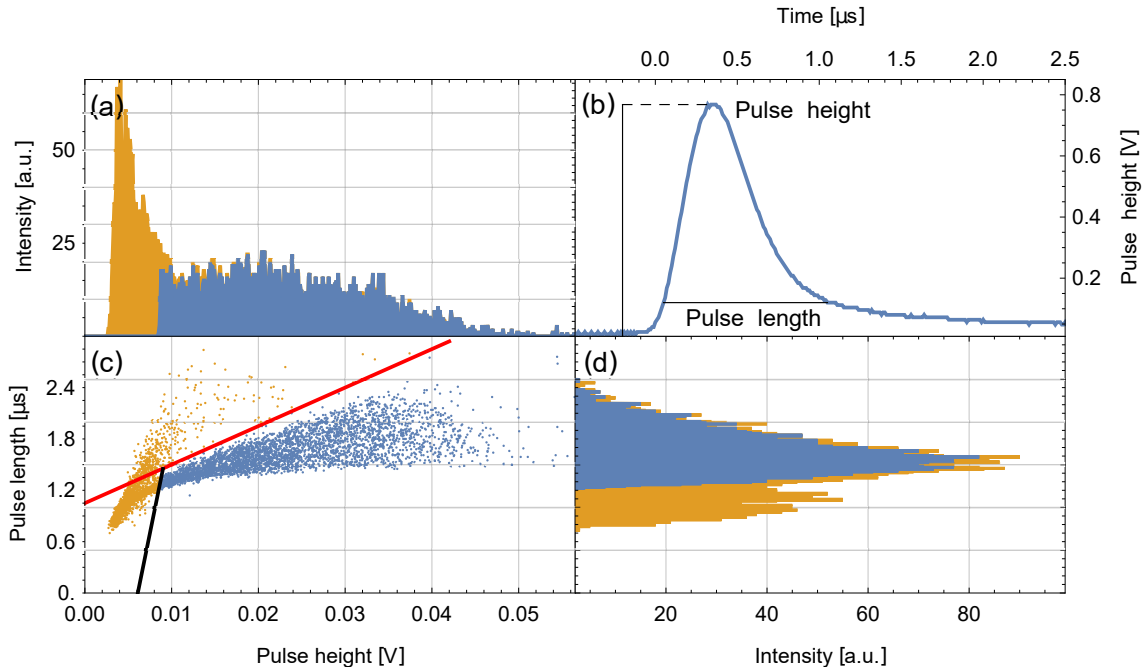


Figure 9.8: Pulse shape analysis for a boron-lined detector at a counting gas pressure of 1 bar. (a) shows the pulse height spectrum of 6200 detected events. (b) displays a pulse generated by the readout electronics corresponding to a neutron event and indicates how pulse height and length are determined. Pulse length corresponds to the time interval during which the pulse exceeds a certain threshold voltage level. The scatter plot (c) depicts the two-dimensional pulse data of the detected events. (d) shows the event pulse length data as a histogram. (a) and (d) are the projections of (c) to the pulse height and length axis, respectively. The blue events could be identified as neutrons whereas the orange cluster contains both electrons and neutrons. These regions can be separated by appropriate thresholds depicted by the red and black line in (c) (Weimar et al., 2020).

The most efficient scheme to reduce the contamination of weakly ionizing particles, however, is to reduce the gas pressure inside the counter tube. Thereby, the ionization per track length $dE/dx \sim \rho$ and so the total energy deposition is reduced. By reducing the gas pressure to 250 mbar, the efficiency for electrons emitted by a radioactive strontium source was measured to be as low as 10^{-9} . The gamma sensitivity is on the same order of magnitude as the gamma rays ionize the gas indirectly by kick-off electrons (Compton scattering). The heavy and highly ionizing conversion products of ^{10}B still deposit the same amount of energy inside the gas, because their track length is still smaller than the radius of the counter tube. The resulting pulse height spectrum Fig. 9.9 (a) resembles the theoretical spectrum Fig. 9.9 (b) simulated by URANOS and convoluted with a Gaussian distribution function with $\sigma = 30$ keV. The convolution is used to simulate the effects of the detector energy resolution. The events in Fig. 9.9 (b) with energies E , $1.47 \text{ MeV} < E < 1.78 \text{ MeV}$ correspond to the ^{10}B decay channel with a probability of 6 %, see section 3.1. Particles with higher energies amount to two percent of all events under typical conditions of a CRNP deployment. These alpha particles can easily

be discriminated against via their pulse height. This event rate is also extrapolated to the boron conversion energy range, shown in Fig. 9.9 (a) and (b) to estimate the background noise by radioisotopes to be (0.74 ± 0.06) mHz, i.e. (64 ± 5) events per day. The main reason for this low intrinsic radioactivity is the $50 \mu\text{m}$ thick, high purity SE-Cu foil inside the boron-lined neutron counter as it has an intrinsic activity that was measured to be as low as (1.05 ± 0.1) events/ (s m^2) in the energy region between 2.6 and 5 MeV. The copper foil also acts as a barrier between the less pure aluminium housing of the counter and the gas filling. It effectively shields alpha and heavier particles from entering and ionising the gas. Further contamination can arise from the decay of ^{222}Rn gas, which accumulates on every surface. However, with typical decay energies above 5 MeV it can be easily discriminated against.

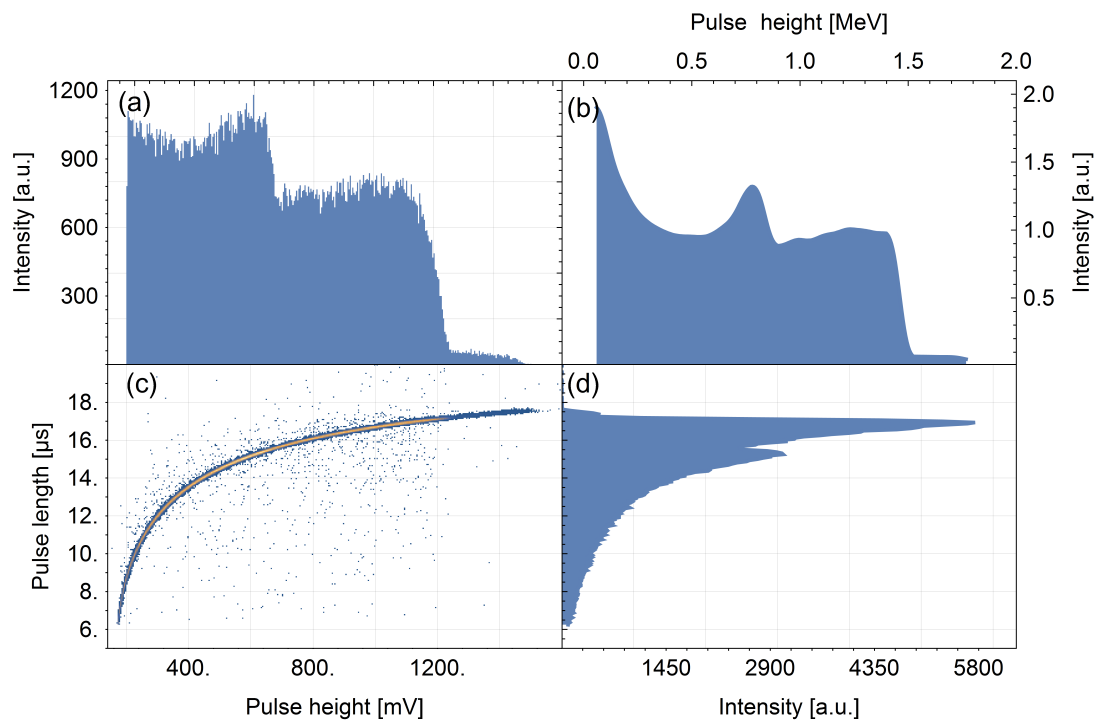


Figure 9.9: Pulse shape analysis for a boron-lined detector at a counting gas pressure of 250 mbar. A total of $\approx 230\,000$ events are recorded. (a) shows the pulse height spectrum and (b) a reference pulse height spectrum simulated by the URANOS Monte Carlo tool for a $1.7 \mu\text{m}$ thick boron layer. (c) shows the two-dimensional pulse shape data and the event pulse lengths are plotted as a histogram in (d) (Weimar et al., 2020).

The hardware discrimination threshold to lower energies is set to be ≈ 100 keV. This lower threshold cuts $\approx 6\%$ of the total ^{10}B pulse height spectrum but also effectively discriminates ionisation traces by electrons. The low electron efficiency could also be confirmed with the Penelope Monte Carlo package (Salvat, 2015) simulating the electron transport and ionization trace inside the counter. The largest energy deposition for 250 mbar amounted to ≈ 50 keV, even for maximum track lengths through the counter volume and thus lies with a large margin below the hardware threshold. The sharp signature of neutron events in the two-dimensional pulse shape plot in Fig. 9.8 (c) allows for a narrow event selection indicated in Fig. 9.10. To the lower end of the spectrum a pulse length threshold is set, which is preferred over pulse height discrimination due to the steep shape of the curve. However, a lower pulse

length threshold leads to a cut in the pulse height spectrum that spans over a small range of values. That is partly the reason for the deviation between the experimental and theoretical spectrum (Fig. 9.9 (a) and (b))³. Approximately, 5–7 % of the ^{10}B conversion spectrum is lost by this lower threshold. To higher values, the spectrum is restricted by a pulse height threshold that excludes higher energetic alpha particles. The neutron event spectrum within these boundaries can be well described by a function that takes the general form

$$\tau_p(h_p) = a_1 - \frac{a_2}{(1 + (a_3 h_p)^{a_4})^{a_5}} + a_6 h_p, \quad (9.2)$$

where τ_p and h_p denote the pulse length and pulse height, respectively. This function along with tolerances that cover the dispersion of the neutron event distribution is used in the data logging unit or remotely to extract the neutron events.

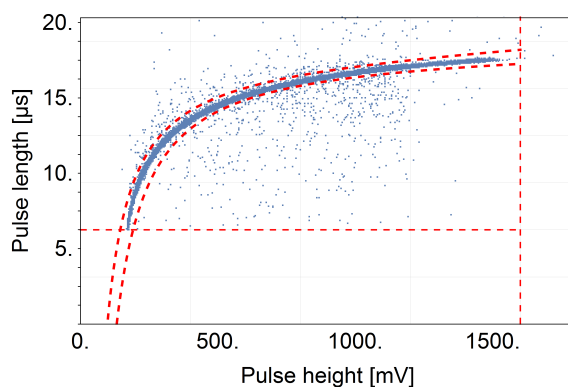


Figure 9.10: Schematic pulse-shape discrimination: The neutron event region is selected via four thresholds: a lower pulse length and upper pulse height criterion along with a lower and upper threshold function described by Eq. 9.2 and a set of tolerance values.

9.2.4 Potential of the two-dimensional pulse discrimination tool

After identifying the two-dimensional neutron pulse-shape signature, it is instructive to examine noise contributions and their appearance in the pulse height and length space. The following examples cover typical pulse-shape structures appearing under certain conditions in the field. Some of these could be reproduced with similar behaviour under controlled conditions. Fig. 9.11, left panel displays the production of noise via a heat gun with moderate heat output that heated the PCB to above 100 degrees Celsius within few minutes. The same PCB was put under mechanical stress by the continuous impact of a screwdriver. Both effects show a similar signature and may be related in their action. Capacitance changes (e.g. C1 in Fig. 9.3) might be caused by both heat and mechanical impact, which could induce signals in the sensitive input amplifier stage.

Humidity is, of course, a threat to sensitive analogue systems that also comprise high voltage. Condensation of water vapour on the PCB results in a multitude of pulse characteristics. Two clusters can be highlighted. One accumulating events with low but long pulses, which might be attributed to slow charge movement due to the lowered resistance between high and low voltage part of the PCB. The second contains several structures alike the neutron cluster but shifted in pulse length. The higher pulses might be induced through discharges when voltage breakdown occurs. These features overlap with the neutron cluster. In particular to lower values of pulse length and height, noise and signal become indistinguishable. Thus, noise by

³It should be noted that, the shown simulated spectrum represents a ^{10}B layer of 1.7 μm thickness. However, the carbon atoms within the boron carbide layer decrease the range of the conversion fragments by roughly 10 % (compare carbon range data from Berger et al., 1999 and Köhli et al., 2016), hence, the relative good agreement between the measured spectrum of a B_4C layer with a thickness of 1.5 μm and the simulated pure ^{10}B layer with a thickness of 1.7 μm .

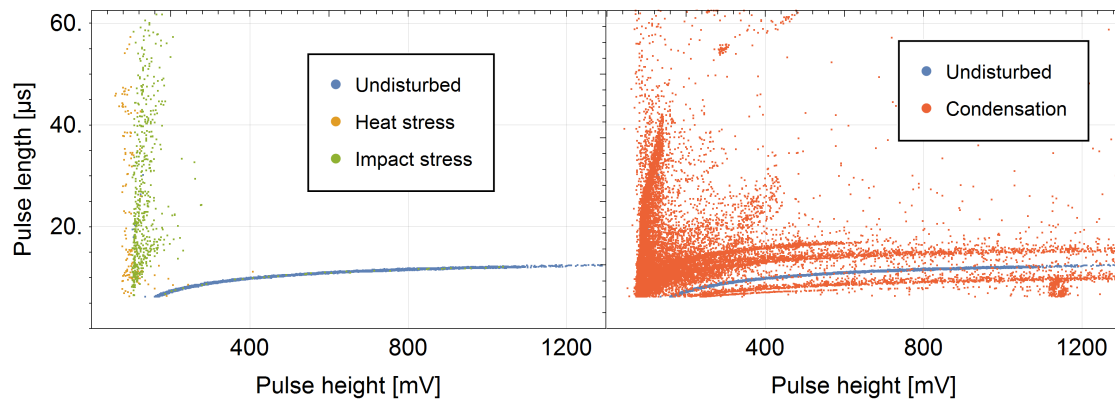


Figure 9.11: Noise signature in the pulse height - length spectrum. Note, that these spectra were recorded using readout electronics with different amplification characteristics than in Fig. 9.9. **Left:** Heat and mechanical stress induce long but low pulses. **Right:** Condensation of water vapour leads to a broad distribution of pulse shapes.

air humidity must be avoided by a suitable sealing. The PCB can also be treated with sealing varnish and high voltage grease.

9.3 Field data of a stationary probe

In mid 2019 the Helmholtz Forschungszentrum Jülich (FZJ) and Climate Service Center Germany (GERICS) launched the ADAPTER project. The goal is to develop and provide real time simulation-based data and forecast products tailored to the needs of agriculture. The data is easily accessible and free of charge and thereby tries to facilitate knowledge transfer between science and data users⁴. The primary goal is to determine the state of the water cycle in Nord-Rhein Westfalen and use models that extrapolate climate and local data in order to provide a regional forecast model. The hydrological simulations are supported by field site monitoring measuring water fluxes locally. Fig. 9.1 shows one of these stations, which measure soil moisture via Cosmic-Ray Neutron Sensing using the boron-lined neutron detection systems described here. The stations also comprise ground truthing via FDR sensors buried next to the CRNP and monitor atmospheric humidity and pressure in order to correct the neutron count rates (the incoming correction is done using the neutron monitor data base). These stations are also part of a Europe-wide network recently described by Bogena et al., 2022.

Here, data from the Nörvenich station, part of the adapter project, during March and April 2022 is examined in order to show the performance of the boron-lined neutron detector. The detector is set up as shown in Fig. 9.1 and is located in-between two agricultural crop fields at a cut-off rigidity of 3.15 GV (lat=50.78104 long=6.53657). Its mean count rate during this period amounted to 1500 neutrons per hour. The underlying soil has a bulk density of 1.25 g/cm³ and during the chosen period no crop was planted on the agricultural fields. The station comprises four FDR sensors buried 5, 15, 30 and 60 cm below the soil surface. The measured neutron flux was corrected for atmospheric pressure, air humidity and incoming radiation and then converted into soil moisture (according to the procedure described by Bogena et al., 2022). The FDR soil moisture values were weighted according to the vertical penetration depth of the signal as suggested by Schrön et al., 2017 applying the functions

⁴<https://www.adapter-projekt.de>

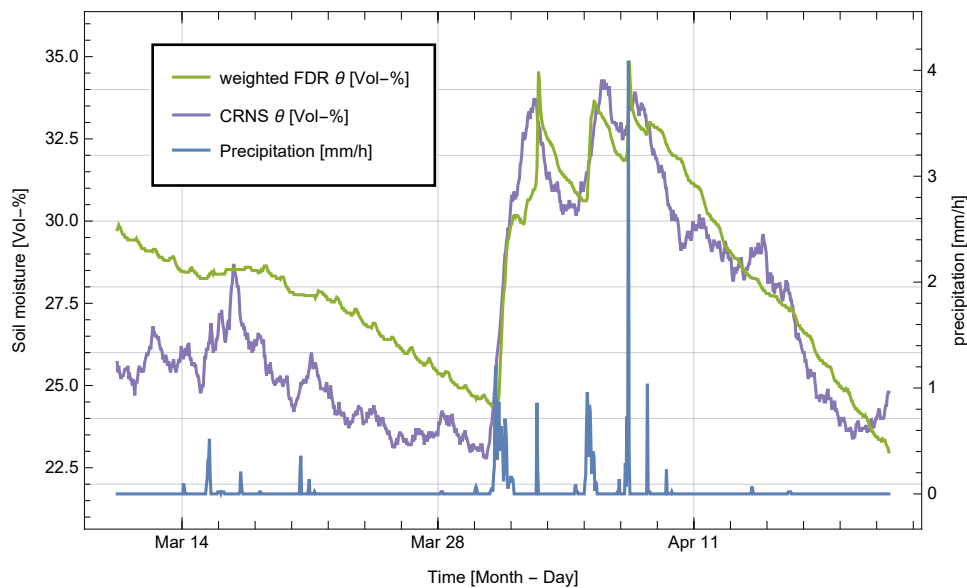


Figure 9.12: Measured soil moisture data at the Nörvenich station by FDR sensors and a CRNP (left y-axis) as well as hourly precipitation (right y-axis). The data span a time period from 10th of March to 21st of April.

of Köhli et al., 2015. Comparing the two soil moisture data sets reveals a first period with significant deviations until a rain event occurred leading to approximately 11 mm rain fall within 30 hours. Before this event, the CRNS derived soil moisture lies below that of the FDR probes. Both show a general process of drying of the soil. Few smaller rain events generate a response in the CRNP signal while the FDR data remains unchanged. This points to the advantage of area-sensitive soil moisture sensing that captures even small precipitation amounts. It should be noted that the CRNP retrieved soil moisture, in general, exhibits more pronounced dynamics and shows some peaks in the data that could not be attributed to any precipitation event. During the following period that is determined by several rain events both data sets show a similar response and coincide quite well in absolute numbers. The CRNP's response features broader structures than that of the FDR probes, which might also be an effect of the area averaging or due to the lower temporal resolution of the CRNP. This data and that of the other CRNP field stations is available here⁵.

9.4 Mobile measurement campaign

Two measurement campaigns were conducted in the region around the Meteorological Observatory Lindenberg, Brandenburg, Germany, using the mobile detection system on a vehicle. This section shows some preliminary results for these campaigns in order to show the potential of the mobile detection unit via a specific use case. The campaign was planned and analysed by Martin Schrön and conducted by Carmen Zengerle, Daniel Altdorf and Mandy Kasner (all UFZ Leipzig, Germany) with on-site support by Frank Beyrich (German Weather Service, Lindenberg, Germany), while the mobile unit was maintained by Markus Köhli and Jannis Weimar (Physikalisches Institut, Heidelberg, Germany). The campaign was carried out in the framework of the FESSTVal project⁶.

Detected neutrons (between 10000–20000 counts per hour) are processed with standard corrections of air pressure, air humidity, incoming cosmic radiation, and soil properties (see sec-

⁵<https://www.adapter-projekt.de/wetter-produkte/beobachtungen.html>

⁶<https://fesstval.de/>

tion 2.4.2), and smoothed over 1 minute (rolling mean) and 20 m radius (weighted by the intensity function W_r , see section 2.4.4). Conversion to soil moisture is performed using Eq. 2.27 and $N_0 = 15447$. The median measured soil moisture on Aug 18th and Aug 27th were 8.7 Vol-% and 16.7 Vol-%, respectively (see Fig. 9.13 (a) and (b)). This corresponds to a change of 8 Vol-% in the mapped area, assuming similar spatial representativeness of both campaigns (see Fig. 9.13 (c)). According to preliminary data from the German Weather Service, the total precipitation in this area was 88.6 mm between the two campaign days, starting with a strong rain event on Aug 22nd (45.4 mm) with ongoing but less intense precipitation until Aug 27th. Hence, the example demonstrates how the mobile detector can be used to map regional soil water storage and to support hydrological process understanding.

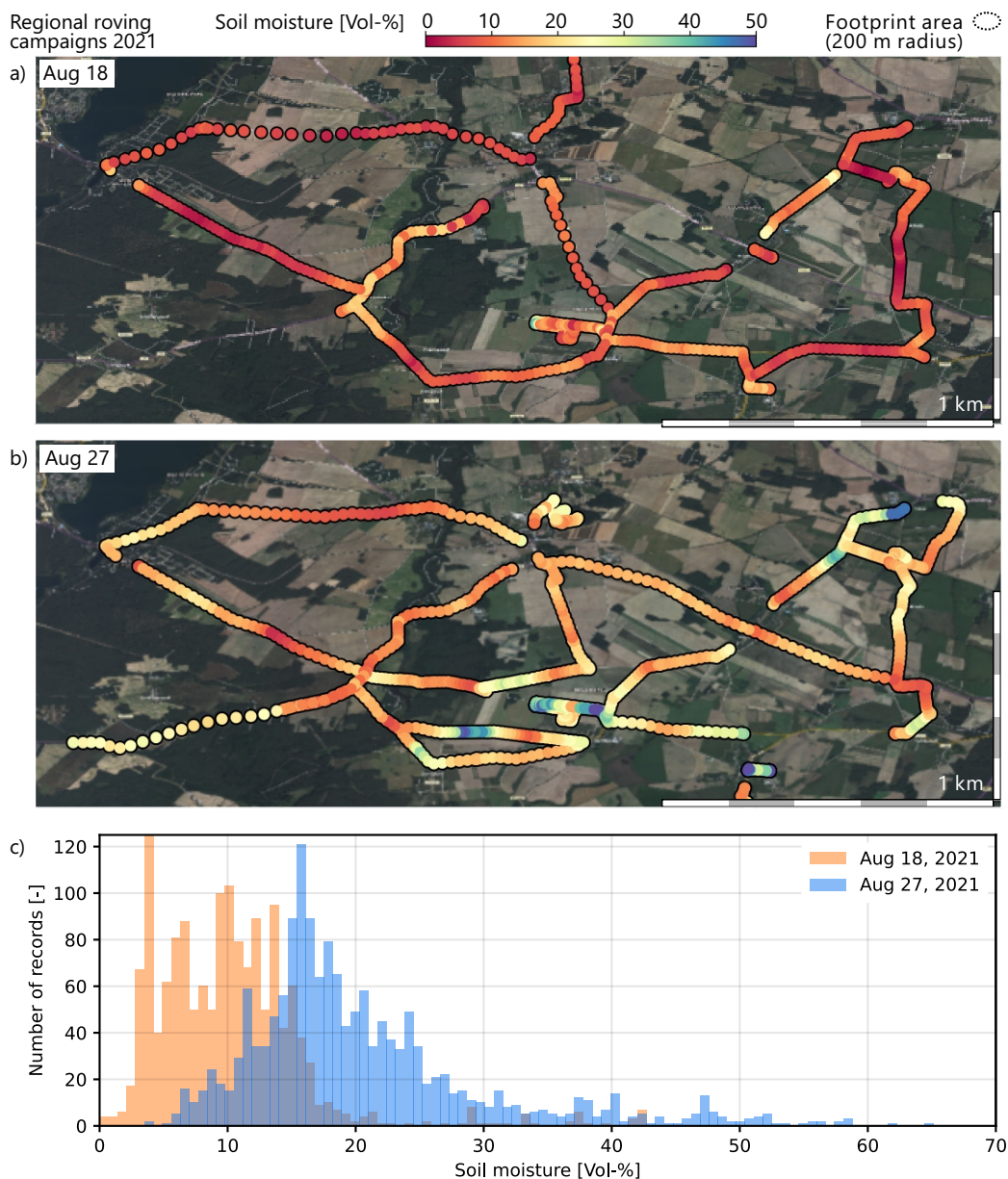


Figure 9.13: Two-days measurement campaign with the mobile detection system on Aug 18th (a) and Aug 27th (b), 2021. Credit: Martin Schrön, UFZ Leipzig, Germany.

Conclusion

This chapter presents a neutron detection system tailored specifically to the needs of Cosmic-Ray Neutron Sensing. A conceptual basis that describes the demands of this neutron detector application was proposed in chapter 8. Putting these ideas into practice the novel detection system shows the following features:

1. **It uses solid ^{10}B as a neutron converter.** Contrary to helium-3 which is extracted from refurbished thermonuclear warheads, boron is widely used as a semiconductor dopant. For radiation hard applications it needs to be depleted in ^{10}B in order to make it more resilient against neutron-induced damages. ^{10}B enriched boron is therefore a by-product of the semiconductor industry making the technology a cost-effective alternative to ^3He -based CRNPs.
2. **It has low statistical uncertainty.** The detection system combines a large surface area of the moderator with moderately efficient proportional counters. This leads to a modular setup that can combine up to five tubes in a stationary system and 32 for a mobile detection unit. This leads to a high count rate, which is approximately five and thirty times higher than that of a standard CRNP, for the two systems.
3. **It features an adapted detector response function.** An aluminium sheet with Gd_2O_3 varnish can be mounted to the outer moderator surface. This leads to a strong suppression of the thermal contamination of standard CRNPs. Since thermal neutrons show a less pronounced and more complex response to soil moisture this varnish improves the signal-to-noise ratio significantly.
4. **It exhibits low efficiency for background radiation.** The proportional counter tubes feature reduced gas pressure at 250 mbar. Thereby the mass stopping power for ionising radiation is decreased by a factor of four as compared to the previous system that operated a 1 bar counting pressure. While the highly ionising boron conversion products still deposit their entire energy within the gas volume, the total energy deposited of weakly ionising cosmic-rays and Compton electrons is suppressed significantly.
5. **Noise event identification.** The pulse-shape analysis of the readout electronics allows for two-dimensional pulse discrimination. Pulse length and height are combined in order to separate the neutron event structure from noise events, which reduces the systematic error.

Both, the stationary and mobile unit were deployed successfully during measurement campaigns and demonstrated their ability to measure soil moisture on the hectare scale and beyond.

This work presents advances in water resource monitoring at the land-atmosphere interface via cosmic-ray neutrons. It is split into two parts. The first part addresses neutron production and transport mechanisms at this interface using the Monte Carlo toolkit MCNP6, while the second part is focused on neutron detector development specifically tailored to the demands of this technique.

Neutron production and transport description via MCNP

In the context of CRNS, neutron flux descriptions have long relied on neutron-only Monte Carlo simulations. Here, MCNP6, a multi-particle Monte Carlo code, was deployed to treat neutron production via other cosmic-rays and their transport mechanisms at the land-atmosphere interface holistically. Three cosmic-ray particle species were identified that contribute significantly to the neutron production at the land-atmosphere interface: high-energy neutrons, protons and muons. In addition to that, short-lived pions act as intermediate particles in the cosmic-ray showers and, thereby, indirectly produce neutrons. While the hadronic species induce most of the neutron production in the upper soil layers, below which their intensity decreases strongly, muons dominate neutron evaporation below 5 m into the soil. The neutron production within the soil, furthermore, depends on the elemental composition. As a general rule, the heavier the target nuclei the more neutrons are evaporated per incident particle.

Following these findings, the effective neutron flux attenuation within three domains, water, air and soil, was examined in more detail and compared to measured data sets. The first represents an easy-to-reproduce setup via simulation due to the simple elemental composition and material density. However, until now the CRNS community used a combination of empirical and simulation-based models to describe the neutron flux propagation through water because hitherto used simulation results indicated attenuation lengths too short to reproduce measured data. Here, it was demonstrated that the measured neutron flux attenuation in water can be reproduced via Monte Carlo simulations with appropriate accuracy and a hadronic attenuation length of 136 cm was obtained. The long attenuation length can be attributed to the additional neutron source terms introduced by cosmic-ray protons.

Furthermore, it was shown that the atmospheric neutron flux propagation can also be reproduced by MCNP within an altitude range from 65 to 3000 m and at cut-off rigidities in the range from 4.2 to 4.8 GV. The inferred atmospheric neutron attenuation length amounts to approximately 143 g/cm^2 . For both, the atmospheric and water domain, the combination of the Bertini, Isabel, Dresner, CEM03.03 and LAQGSM event generators has proven to be an appropriate high-energy model choice for MCNP. Simulated and measured neutron intensities below the soil surface revealed higher discrepancies.

The soil and water case studies also hold promising fields of application. This work presents an analytical function that describes the thermal neutron flux below the soil surface as a function of depth and local soil moisture and demonstrates its value to monitor soil moisture trends at a time scale of several days and up to few meters into the ground. However, below-ground soil moisture sensing via cosmic-ray neutrons exhibits significant dynamics unrelated to soil moisture changes, which are assumed to be an indirect result of natural radioactivity increase. Furthermore analytical functions were determined by fitting the simulated neutron flux through water, in pure water and at the snow-soil interface. These

can be used to infer the snow water equivalent (SWE) of a snowpack above a buried sensor, which is placed on top of a glacier or in soil. Such detectors were expected to measure snow on a local scale of few meters, which was confirmed in this work for intermediate to large snowpacks, while shallow snow cover leads to a spatial broadening of the signal.

The epithermal neutron flux above snow-covered soils was analysed with respect to its spatial transport processes. A total of 192 neutron transport simulation setups, covering a broad range of SWE, soil moisture and air humidity values, were fitted to obtain an analytical description of the radial footprint distribution as a function of these three variables. These indicate a strong decline in the detector's representative measurement area with snow cover increase. Furthermore, the dependence of the epithermal neutron flux above a snow cover with underlying moist soil was examined in order to present a comprehensive treatment of SWE monitoring via cosmic-ray neutrons above a homogeneous snow cover.

Boron-lined cosmic-ray neutron probes

The second part of this work introduces a neutron detection system, based on ^{10}B as a solid neutron converter, which is specifically designed for monitoring soil moisture via cosmic-ray neutrons. High count rates are achieved via a large detector surface area in combination with a modular number of thermal neutron counters. Thereby, sufficiently low statistical uncertainty is obtained for measurement intervals of several 10 minutes to few hours despite the low flux of cosmic-ray neutrons at the land-atmosphere interface. Noise and background radiation interference is suppressed via a two-dimensional pulse-shape analysis in combination with a low pressure counting gas. The latter effectively decreases the signal induced by non-neutron cosmic-rays within the neutron counter, while a combination of pulse length and height allows for a separation of the neutron event signature from noise events.

An adaptation of the standard detector response function was proposed that includes a Gd_2O_3 varnish that shields the detector from thermal contamination and thereby increases its signal-to-noise ratio.

Two models of this detector concept were realised and deployed as stationary and mobile soil moisture sensing probes. Preliminary data indicates their ability to monitor soil moisture patterns and dynamics at the hectare scale and up to several square kilometers.

Open topics

In view of the present work and its results and limitations, two major topics are identified that might be addressed by future studies:

1. The measured and simulated atmospheric neutron flux propagation presented here indicated longer attenuation lengths than those proposed by Desilets et al., 2006. Their analytical functions are commonly referred to when correcting neutron intensities for pressure variations. A CRNS adapted revision could improve this correction procedure, which commonly accounts to up to 20 % of the epithermal neutron flux changes.
2. The presented function for epithermal neutron intensities above snow-covered soils was designed for a horizontally homogeneous snow layer. Although, some studies already addressed neutron dynamics above a heterogeneous snow cover for specific sites, a more general approach could greatly enhance the potential for snow monitoring via CRNS. Furthermore, the homogeneous transfer function should be tested against a larger measured data set than the one presented here.

A

Bibliography

- Abramowski, A and F Aharonian (2016). "Acceleration of petaelectronvolt protons in the Galactic Centre". In: *Nature* 531, pp. 476–479. DOI: [10.1038/nature17147](https://doi.org/10.1038/nature17147).
- Aguayo, E., R. Kouzes, and E. Siciliano (2013). *Ship Effect Neutron Measurements and Impacts on Low-Background Experiments*. Tech. rep. PNNL-22953. Richland, Washington 99352: Pacific Northwest National Laboratory. 77 pp. URL: https://www.pnnl.gov/main/publications/external/technical_reports/PNNL-22953.pdf.
- Aldrich, L. T. and A. O. Nier (1948). "The occurrence of He 3 in natural sources of helium". In: *Physical Review* 74(11), p. 1590. DOI: [10.1103/PhysRev.74.1590](https://doi.org/10.1103/PhysRev.74.1590).
- Andreasen, M., H. K. Jensen, M. Zreda, D. Desilets, H. Bogena, and C. Looms (2016). "Modeling cosmic ray neutron field measurements". In: *Water Resources Research* 52(8), pp. 6451–6471. DOI: [10.1002/2015wr018236](https://doi.org/10.1002/2015wr018236).
- Andreasen, M., K. H. Jensen, D. Desilets, T. E. Franz, M. Zreda, H. R. Bogena, and M. C. Looms (2017a). "Status and perspectives on the cosmic-ray neutron method for soil moisture estimation and other environmental science applications". In: *Vadose Zone Journal* 16(8), pp. 1–11. DOI: [10.2136/vzj2017.04.0086](https://doi.org/10.2136/vzj2017.04.0086).
- Andreasen, M., K. H. Jensen, D. Desilets, M. Zreda, H. R. Bogena, and M. C. Looms (2017b). "Cosmic-ray neutron transport at a forest field site: the sensitivity to various environmental conditions with focus on biomass and canopy interception". In: *Hydrology and Earth System Sciences* 21(4), pp. 1875–1894. DOI: [10.5194/hess-21-1875-2017](https://doi.org/10.5194/hess-21-1875-2017).
- Arduino SA (2022). *Arduino Nano*. URL: <http://store.arduino.cc/products/arduino-nano>.
- Armstrong, T., P Cloth, D Filges, and R. Neef (1984). "A comparison of high-energy fission models". In: *Nuclear Instruments and Methods in Physics Research* 222(3), pp. 540–547. DOI: [10.1016/0167-5087\(84\)90384-3](https://doi.org/10.1016/0167-5087(84)90384-3).
- Atmel (2016). *ATmega328/P Datasheet*. URL: http://www.atmel.com/images/Atmel-7810-Automotive-Microcontrollers-ATmega328P_Datasheet.pdf.
- Auriemma, G., D. Fidanza, G. Pirozzi, and C. Satriano (2003). "Experimental determination of the Townsend coefficient for Argon-CO₂ gas mixtures at high fields". In: *Nuclear Instruments and Methods in Physics Research*. DOI: [10.1016/S0168-9002\(03\)02074-6](https://doi.org/10.1016/S0168-9002(03)02074-6).
- Baatz, R., H. Bogena, H.-J. Hendricks-Franssen, J. Huisman, C. Montzka, and H. Vereecken (2015). "An empirical vegetation correction for soil water content quantification using cosmic ray probes". In: *Water Resources Research* 51(4), pp. 2030–2046. DOI: [10.1002/2014wr016443](https://doi.org/10.1002/2014wr016443).
- Baatz, R., H.-J. Hendricks Franssen, X. Han, T. Hoar, H. R. Bogena, and H. Vereecken (2017). "Evaluation of a cosmic-ray neutron sensor network for improved land surface model prediction". In: *Hydrology and Earth System Sciences* 21(5), pp. 2509–2530. DOI: [10.5194/hess-21-2509-2017](https://doi.org/10.5194/hess-21-2509-2017).
- Berger, M. J., J. S. Coursey, M. A. Zucker, et al. (1999). "ESTAR, PSTAR, and ASTAR: computer programs for calculating stopping-power and range tables for electrons, protons, and helium ions". In: DOI: [10.18434/T4NC7P](https://doi.org/10.18434/T4NC7P).
- Bertini, H. W. (1963). "Low-energy intranuclear cascade calculation". In: *Physical Review* 131(4), p. 1801. DOI: [10.1103/PhysRev.131.1801](https://doi.org/10.1103/PhysRev.131.1801).
- Blasi, P. (2013). "The origin of galactic cosmic rays". In: *The Astronomy and Astrophysics Review* 21(1), pp. 1–73. DOI: [10.1007/s00159-013-0070-7](https://doi.org/10.1007/s00159-013-0070-7).
- Blöschl, G. and M. Sivapalan (1995). "Scale issues in hydrological modelling: a review". In: *Hydrological processes* 9(3-4), pp. 251–290. DOI: [10.1002/hyp.3360090305](https://doi.org/10.1002/hyp.3360090305).
- Bogena, H., J. Huisman, R. Baatz, H.-J. Hendricks-Franssen, and H. Vereecken (2013). "Accuracy of the cosmic-ray soil water content probe in humid forest ecosystems: The

A. Bibliography

- worst case scenario". In: *Water Resources Research* 49(9), pp. 5778–5791. DOI: 10.1002/wrcr.20463.
- Bogena, H. R., J. A. Huisman, A. Güntner, C. Hübner, J. Kusche, F. Jonard, S. Vey, and H. Vereecken (2015). "Emerging methods for noninvasive sensing of soil moisture dynamics from field to catchment scale: A review". In: *Wiley Interdisciplinary Reviews: Water* 2(6), pp. 635–647. DOI: 10.1002/wat2.1097.
- Bogena, H. R., M. Schrön, J. Jakobi, P. Ney, S. Zacharias, M. Andreassen, R. Baatz, D. Boorman, M. B. Duygu, M. A. Eguibar-Galán, et al. (2022). "COSMOS-Europe: a European network of cosmic-ray neutron soil moisture sensors". In: *Earth System Science Data* 14(3), pp. 1125–1151. DOI: 10.5194/essd-14-1125-2022.
- Bottardi, C., M. Albéri, M. Baldoncini, E. Chiarelli, M. Montuschi, K. G. C. Raptis, A. Serafini, V. Strati, and F. Mantovani (2020). "Rain rate and radon daughters' activity". In: *Atmospheric Environment* 238, p. 117728. DOI: 10.1016/j.atmosenv.2020.117728.
- Brall, T., V. Mares, R. Bütikofer, and W. Rühm (2021). "Assessment of neutrons from secondary cosmic rays at mountain altitudes—Geant4 simulations of environmental parameters including soil moisture and snow cover". In: *The Cryosphere* 15(10), pp. 4769–4780. DOI: 10.5194/tc-15-4769-2021.
- Brown, D. A., M. Chadwick, R Capote, A. Kahler, A Trkov, M. Herman, A. Sonzogni, Y Danon, A. Carlson, M Dunn, et al. (2018). "ENDF/B-VIII. 0: The 8th major release of the nuclear reaction data library with CIELO-project cross sections, new standards and thermal scattering data". In: *Nuclear Data Sheets* 148, pp. 1–142. DOI: 10.1016/j.nds.2018.02.001.
- Bustamante, M, P Jez, J. Monroy Montañez, G Carrillo Montoya, G. Romeo, F Padilla Cabal, J. Duarte Chavez, U. Saldaña-Salazar, M Pino Rozas, M Velasquez, et al. (2010). "High-energy cosmic-ray acceleration". In: DOI: 10.5170/CERN-2010-001.533.
- Bykov, A., D. Ellison, A Marcowith, and S. Osipov (2018). "Cosmic ray production in supernovae". In: *Space Science Reviews* 214(1), pp. 1–34. DOI: 10.1007/s11214-018-0479-4.
- Byun, S (2016). "Med Phys 4R06/6R03 radioisotopes and radiation methodology". In: *Dans SH Byun*. URL: https://science.mcmaster.ca/radgrad/images/6R06CourseResources/4R6Notes3_GasFilled_Detectors.pdf.
- Cane, H. V. (2000). "Coronal mass ejections and Forbush decreases". In: *Cosmic rays and Earth*, pp. 55–77. DOI: 10.1023/A:1026532125747.
- Chadwick, J. (1932). "Possible existence of a neutron". In: *Nature* 129(3252), pp. 312–312. DOI: 10.1038/129312a0.
- Chadwick, M. et al. (2011). "ENDF/B-VII.1 Nuclear Data for Science and Technology: Cross Sections, Covariances, Fission Product Yields and Decay Data". In: *Nuclear Data Sheets* 112(12). Special Issue on ENDF/B-VII.1 Library, pp. 2887–2996. DOI: 10.1016/j.nds.2011.11.002.
- Conlin, J. L. and P. Romano (2019). *A compact ENDF (ACE) format specification*. Tech. rep. Los Alamos National Lab.(LANL), Los Alamos, NM (United States).
- Cooper, R, L Garrison, H.-O. Meyer, T Mikev, L Rebenitsch, and R Tayloe (2011). "SciBath: a novel tracking detector for measuring neutral particles underground". In: *arXiv preprint arXiv:1110.4432*. DOI: 10.48550/arXiv.1110.4432.
- Crane, T. and M. Baker (1991). "Neutron detectors". In: *Passive Nondestructive Assay of Nuclear Materials* (13), pp. 1–28. URL: http://www.gammaexplorer.com/lanreports/lan11_a/lib-www/la-pubs/00326408.pdf.
- Crow, W. T., A. A. Berg, M. H. Cosh, A. Loew, B. P. Mohanty, R. Panciera, P. de Rosnay, D. Ryu, and J. P. Walker (2012). "Upscaling sparse ground-based soil moisture observations

- for the validation of coarse-resolution satellite soil moisture products”. In: *Reviews of Geophysics* 50(2). DOI: 10.1029/2011RG000372.
- Degenaar, I, M Blaauw, P Bode, and J de Goeij (2004). “Validation of MCNP for large-sample thermal-beam prompt-gamma neutron activation analysis”. In: *Journal of radioanalytical and nuclear chemistry* 260(2), pp. 311–315. DOI: 10.1023/b:jrnrc.0000027102.53688.54.
- Delunel, R., D. L. Bourles, P. A. van der Beek, F. Schlunegger, I. Leya, J. Masarik, and E. Paquet (2014). “Snow shielding factors for cosmogenic nuclide dating inferred from long-term neutron detector monitoring”. In: *Quaternary Geochronology* 24, pp. 16–26. DOI: 10.1016/j.quageo.2014.07.003.
- Desilets, D. and M. Zreda (2013). “Footprint diameter for a cosmic-ray soil moisture probe: Theory and Monte Carlo simulations”. In: *Water Resource Research* 49, pp. 3566–3575. DOI: 10.1002/wrcr.20187.
- Desilets, D. (n.d.). *Snow Fox: snow-water equivalent depth made easy*. 1316 Wellesley Drive NE, Albuquerque, New Mexico USA: Hydroinnova LLC. URL: https://hydroinnova.com/_downloads/snowfox_v1.pdf.
- Desilets, D., M. Zreda, and T. P. Ferré (2010). “Nature’s neutron probe: Land surface hydrology at an elusive scale with cosmic rays”. In: *Water Resources Research* 46(11). DOI: 10.1029/2009WR008726.
- Desilets, D., M. Zreda, and T Prabu (2006). “Extended scaling factors for in situ cosmogenic nuclides: new measurements at low latitude”. In: *Earth and Planetary Science Letters* 246(3-4), pp. 265–276. DOI: 10.1016/j.epsl.2006.03.051.
- Dorman, L. I. (2004). *Cosmic rays in the Earth’s atmosphere and underground*. Vol. 303. Springer Science & Business Media. ISBN: 978-1-4020-2113-8.
- Dresner, L. (1962). *EVAP—A Fortran Program for Calculating the Evaporation of Various Particles from Excited Compound Nuclei*. Tech. rep. Oak Ridge National Lab., Tenn.
- Dunai, T. J. (2000). “Scaling factors for production rates of in situ produced cosmogenic nuclides: a critical reevaluation”. In: *Earth and Planetary Science Letters* 176(1), pp. 157–169. DOI: 10.1016/S0012-821X(99)00310-6.
- Eidelman, S., K. Hayes, K. e. Olive, M Aguilar-Benitez, C Amsler, D Asner, K. Babu, R. Barnett, J Beringer, P. Burchat, et al. (2006). “Review of particle physics”. In: *Journal of Physics G: Nuclear and particle physics* 33(1), p. 001. DOI: 10.1016/j.physletb.2004.06.001.
- Engineering Toolbox (2010). *Relative Permittivity - the Dielectric Constant*. URL: http://www.engineeringtoolbox.com/relative-permittivity-d_1660.html.
- Esch, E.-I. (2011). “detector development for dark matter research”. PhD thesis. Universität Giessen.
- Fang, B. and V. Lakshmi (2014). “Soil moisture at watershed scale: Remote sensing techniques”. In: *Journal of hydrology* 516, pp. 258–272. DOI: 10.1016/j.jhydrol.2013.12.008.
- Ferrari, A. (2011). *A primer on particle interactions with matter*. Geneva Switzerland. URL: <https://indico.cern.ch/event/152127/sessions/15183/attachments/157061/222187/AFRadDam.pdf>.
- Ferronsky, V. (2015). *Nuclear geophysics: applications in hydrology, hydrogeology, engineering geology, agriculture and environmental science*. Springer. ISBN: 978-3-319-34516-1. DOI: 10.1007/978-3-319-12451-3.
- Fersch, B. et al. (2020). “A dense network of cosmic-ray neutron sensors for soil moisture observation in a pre-alpine headwater catchment in Germany”. In: *Earth System Science Data Discussions* 2020, pp. 1–35. DOI: 10.5194/essd-2020-48.
- Franz, T., M. Zreda, R. Rosolem, B. Hornbuckle, S. Irvin, H. Adams, T. Kolb, C. Zweck, and W. Shuttleworth (2013). “Ecosystem-scale measurements of biomass water using

A. Bibliography

- cosmic ray neutrons". In: *Geophysical Research Letters* 40(1936), pp. 3929–3933. DOI: 10.1002/grl.50791.
- GE Energy (2005). *Reuter Stokes 3-He Neutron Detectors for Homeland Security Radiation Portal Monitors*. Report. GE Energy. Twinsburg, USA. 2 pp. URL: https://www.industrial.ai/sites/g/files/cozyhq596/files/2019-06/reuter_stokes_he-3_neutron_detectors_for_homeland_security_radiation_portal_monitors_english_0.pdf.
- Gaisser, T. (2006). "The Cosmic-ray Spectrum: from the knee to the ankle". In: *Journal of Physics: Conference Series*. Vol. 47. 1. IOP Publishing, p. 002. DOI: 10.1088/1742-6596/47/1/002.
- Gandini, A and G Reffo (1998). "Proceedings of the Workshop Nuclear Reaction Data and Nuclear Reactors: Physics, Design and Safety". In: *Proceedings of the Workshop Nuclear Reaction Data and Nuclear Reactors: Physics, Design and Safety*. World Scientific, pp. 1–1260. DOI: 10.1142/9789814530385.
- Gardner, W. H. (1986). "Methods of Soil Analysis, Part 1. Physical and Mineralogical Methods". In: ed. by Klute, A. 2nd ed. Agronomy Monograph no. 9. American Society of Agronomy-Soil Science Society of America. Chap. Chapter 21: Water Content, pp. 493–544. DOI: <https://doi.org/10.2136/sssabookser5.1.2ed.c21>.
- Gardner, W. and D. Kirkham (1952). "Determination of soil moisture by neutron scattering". In: *Soil Science* 73(5), pp. 391–402.
- Geelhood, B. D., J. H. Ely, R. R. Hansen, R. T. Kouzes, J. E. Schweppe, and R. A. Warner (2003). "Overview of portal monitoring at border crossings". In: *2003 IEEE Nuclear Science Symposium. Conference Record (IEEE Cat. No. 03CH37515)*. Vol. 1. IEEE, pp. 513–517. DOI: 10.1109/NSSMIC.2003.1352095.
- Gerontidou, M, N Katzourakis, H Mavromichalaki, V Yanke, and E Eroshenko (2021). "World grid of cosmic ray vertical cut-off rigidity for the last decade". In: *Advances in Space Research* 67(7), pp. 2231–2240.
- Glasstone, S. and M. C. Edlund (1952). "The elements of nuclear reactor theory". In.
- Goldhagen, P., J. Clem, and J. Wilson (2004). "The energy spectrum of cosmic-ray induced neutrons measured on an airplane over a wide range of altitude and latitude". In: *Radiation Protection Dosimetry* 110(1–4), pp. 387–392. DOI: 10.1093/rpd/nch216.
- Goorley, T. et al. (2012). "Initial MCNP6 Release Overview". In: *Nuclear Technology* 180(3), pp. 298–315. DOI: 10.13182/NT11-135.
- Groom, D., N. Mokhov, and S. Striganov (2001). "Muon stopping power and range tables 10 MeV–100 TeV". In: *Atomic Data and Nuclear Data Tables* 78(2), pp. 183–356. DOI: 10.1006/adnd.2001.0861.
- Gudima, K. K., S. Mashnik, and A. J. Sierk (2001). *User Manual for the code LAQGSM*. Tech. rep. Los Alamos National Lab.(LANL), Los Alamos, NM (United States).
- Gugerli, R., N. Salzmann, M. Huss, and D. Desilets (2019). "Continuous and autonomous snow water equivalent measurements by a cosmic ray sensor on an alpine glacier". In: *The Cryosphere* 13(12), pp. 3413–3434. DOI: 10.5194/tc-13-3413-2019.
- Heidbüchel, I., A. Güntner, and T. Blume (2016). "Use of cosmic-ray neutron sensors for soil moisture monitoring in forests". In: *Hydrology and Earth System Sciences* 20(3), pp. 1269–1288. DOI: 10.5194/hess-20-1269-2016.
- Hillas, A. (2005). "Can diffusive shock acceleration in supernova remnants account for high-energy galactic cosmic rays?" In: *Journal of Physics G: Nuclear and Particle Physics* 31(5), R95.
- Horowitz, P. and W. Hill (2015). *The Art of Electronics Third Edition*. Vol. 3. Cambridge University Press.

- Howat, I. M., S. de la Peña, D. Desilets, and G. Womack (2018). “Autonomous ice sheet surface mass balance measurements from cosmic rays”. In: *The Cryosphere* 12(6), pp. 2099–2108. DOI: [10.5194/tc-12-2099-2018](https://doi.org/10.5194/tc-12-2099-2018).
- IAEA (1970). *Neutron moisture gauges*. Tech. rep. 112. Vienna, Austria: International Atomic Energy Agency. URL: https://inis.iaea.org/collection/NCLCollectionStore/_Public/01/001/1001730.pdf.
- IPCC (2014). “Climate change 2014 synthesis report”. In: *Intergovernmental Panel on Climate Change: Geneva, Switzerland*.
- Iwase, H., K. Niita, and T. Nakamura (2002). “Development of General-Purpose Particle and Heavy Ion Transport Monte Carlo Code”. In: *Journal of Nuclear Science and Technology* 39(11), pp. 1142–1151. DOI: [10.1080/18811248.2002.9715305](https://doi.org/10.1080/18811248.2002.9715305).
- Iwema, J, R Rosolem, R Baatz, T Wagener, and H. Bogena (2015). “Investigating temporal field sampling strategies for site-specific calibration of three soil moisture–neutron intensity parameterisation methods”. In: *Hydrology and Earth System Sciences* 19(7), pp. 3203–3216. DOI: [10.5194/hess-19-3203-2015](https://doi.org/10.5194/hess-19-3203-2015).
- Izumi, S. and Y. Murata (1971). “Pulse risetime analysis of A ³He proportional counter”. In: *Nuclear Instruments and Methods* 94(1), pp. 141–145. DOI: [10.1016/0029-554X\(71\)90351-X](https://doi.org/10.1016/0029-554X(71)90351-X).
- Jakobi, J, J. Huisman, H Vereecken, B Diekkrüger, and H. Bogena (2018). “Cosmic ray neutron sensing for simultaneous soil water content and biomass quantification in drought conditions”. In: *Water Resources Research* 54(10), pp. 7383–7402. DOI: [10.1029/2018WR022692](https://doi.org/10.1029/2018WR022692).
- Jakobi, J, J. A. Huisman, M Köhli, D. Rasche, H. Vereecken, and H. Bogena (2021). “The footprint characteristics of cosmic ray thermal neutrons”. In: *Geophysical Research Letters* 48(15), e2021GL094281. DOI: [10.1029/2021GL094281](https://doi.org/10.1029/2021GL094281).
- Junghans, A., M De Jong, H.-G. Clerc, A. Ignatyuk, G. Kudyaev, and K.-H. Schmidt (1998). “Projectile-fragment yields as a probe for the collective enhancement in the nuclear level density”. In: *Nuclear Physics A* 629(3-4), pp. 635–655. DOI: [10.1016/S0375-9474\(98\)00658-7](https://doi.org/10.1016/S0375-9474(98)00658-7).
- Kimura, A., M. Zerkel, et al. (2020). *Thermal Scattering Law S(α,β): Measurement, Evaluation and Application*. URL: <https://www.oecd-nea.org/upload/docs/application/pdf/2020-03/volume42.pdf>.
- Kinar, N. and J. Pomeroy (2015). “Measurement of the physical properties of the snowpack”. In: *Reviews of Geophysics* 53(2), pp. 481–544. DOI: [10.1002/2015RG000481](https://doi.org/10.1002/2015RG000481).
- Kodama, M., K. Nakai, S. Kawasaki, and M. Wada (1979). “An application of cosmic-ray neutron measurements to the determination of the snow-water equivalent”. In: *Journal of Hydrology* 41(1-2), pp. 85–92. DOI: [10.1016/0022-1694\(79\)90107-0](https://doi.org/10.1016/0022-1694(79)90107-0).
- Köhli, M., M. Schrön, and U. Schmidt (2018a). “Response functions for detectors in cosmic ray neutron sensing”. In: *Nuclear Instruments and Methods in Physics Research Section A: Accelerators, Spectrometers, Detectors and Associated Equipment* 902, pp. 184–189. DOI: [10.1016/j.nima.2018.06.052](https://doi.org/10.1016/j.nima.2018.06.052).
- Köhli, M, M Schrön, and U Schmidt (2018b). “Response functions for detectors in cosmic ray neutron sensing”. In: *Nuclear instruments and methods in physics research section A: Accelerators, spectrometers, detectors and associated equipment* 902, pp. 184–189. DOI: [10.1016/j.nima.2018.06.052](https://doi.org/10.1016/j.nima.2018.06.052).
- Köhli, M, M Schrön, M Zreda, U Schmidt, P Dietrich, and S Zacharias (2015). “Footprint characteristics revised for field-scale soil moisture monitoring with cosmic-ray neutrons”. In: *Water Resources Research* 51(7), pp. 5772–5790. DOI: [10.1002/2015WR017169](https://doi.org/10.1002/2015WR017169).

A. Bibliography

- Köhli, M. O. (2019). “The CASCADE 10B thermal neutron detector and soil moisture sensing by cosmic-ray neutrons”. PhD thesis. Ruprecht-Karls-Universität Heidelberg.
- Köhli, M., J. Weimar, M. Schrön, R. Baatz, and U. Schmidt (2021). “Soil moisture and air humidity dependence of the above-ground cosmic-ray neutron intensity”. In: *Frontiers in Water* 2, p. 66. DOI: [10.3389/frwa.2020.544847](https://doi.org/10.3389/frwa.2020.544847).
- Koning, A. et al. (2011). “Status of the JEFF Nuclear Data Library”. In: *Journal of the Korean Physical Society* 59(2), pp. 1057–1062. DOI: [10.3938/jkps.59.1057](https://doi.org/10.3938/jkps.59.1057).
- Kouzes, R. et al. (2008). “Cosmic-ray-induced ship-effect neutron measurements and implications for cargo scanning at borders”. In: *Nuclear Instruments and Methods in Physics Research Section A: Accelerators, Spectrometers, Detectors and Associated Equipment* 587(1), pp. 89–100. DOI: [10.1016/j.nima.2007.12.031](https://doi.org/10.1016/j.nima.2007.12.031).
- Kowalczyk, A. (2007). “Proton induced spallation reactions in the energy range 0.1 - 10 GeV”. PhD thesis. Jagiellonian University, Cracow, Poland. DOI: [10.48550/arXiv.0801.0700](https://doi.org/10.48550/arXiv.0801.0700).
- Kristensen, K. (1973). “Depth intervals and topsoil moisture measurement with the neutron depth probe”. In: *Hydrology Research* 4(2), pp. 77–85.
- Krüger, H, H Moraal, J. Bieber, J. Clem, P. Evenson, K. Pyle, M. Duldig, and J. Humble (2008). “A calibration neutron monitor: Energy response and instrumental temperature sensitivity”. In: *Journal of Geophysical Research: Space Physics* 113(A8). DOI: [10.1029/2008JA013229](https://doi.org/10.1029/2008JA013229).
- Köhli, M., F. Allmendinger, W. Häußler, T. Schröder, M. Klein, M. Meven, and S. Ulrich (2016). “Efficiency and spatial resolution of the CASCADE thermal neutron detector”. In: *Nuclear Instruments and Methods Phys. Res.* DOI: [10.1016/j.nima.2016.05.014](https://doi.org/10.1016/j.nima.2016.05.014).
- Langford, T., C. Bass, E. Beise, H. Breuer, D. Erwin, C. Heimbach, and J. Nico (2013). “Event identification in ^3He proportional counters using risetime discrimination”. In: *Nuclear Instruments and Methods in Physics Research Section A: Accelerators, Spectrometers, Detectors and Associated Equipment* 717, pp. 51–57. DOI: [10.1016/j.nima.2013.03.062](https://doi.org/10.1016/j.nima.2013.03.062).
- Lechner, A. (2018). “CERN: Particle interactions with matter”. In: *CERN Yellow Rep. School Proc.* 5, p. 47. DOI: [10.23730/CYRSP-2018-005.47](https://doi.org/10.23730/CYRSP-2018-005.47).
- Leo, W. R. (1994). *Techniques for Nuclear and Particle Physics Experiments*. Würzburg: Springer Verlag. DOI: [10.1007/978-3-642-57920-2](https://doi.org/10.1007/978-3-642-57920-2).
- Mancusi, D., S. Lo Meo, N. Colonna, A. Boudard, M. A. Cortés-Giraldo, J. Cugnon, J.-C. David, S. Leray, J. Lerendegui-Marco, C. Massimi, et al. (2017). “On the role of secondary pions in spallation targets”. In: *The European Physical Journal A* 53(5), pp. 1–16. DOI: [10.1140/epja/i2017-12263-0](https://doi.org/10.1140/epja/i2017-12263-0).
- Manukovsky, K., O. Ryazhskaya, N. Sobolevsky, and A. Yudin (2016a). “Neutron production by cosmic-ray muons in various materials”. In: *Physics of Atomic Nuclei* 79(4), pp. 631–640. DOI: [10.1134/S106377881603011X](https://doi.org/10.1134/S106377881603011X).
- (2016b). “Neutron production by cosmic-ray muons in various materials”. In: *Physics of Atomic Nuclei* 79(4), pp. 631–640. DOI: [10.1134/S106377881603011X](https://doi.org/10.1134/S106377881603011X).
- Mashnik, S. G. (2011). “Validation and verification of MCNP6 against intermediate and high-energy experimental data and results by other codes”. In: *The European Physical Journal Plus* 126(5), pp. 1–12. DOI: [10.1140/epjp/i2011-11049-1](https://doi.org/10.1140/epjp/i2011-11049-1).
- Mashnik, S. and A. J. Sierk (2012). *CEM03.03 User Manual*. Tech. rep. Los Alamos National Lab.(LANL), Los Alamos, NM (United States).
- McKinney, G., H. Armstrong, M. R. James, J. Clem, and P. Goldhagen (2012). “MCNP 6 Cosmic-Source Option”. In: *Transactions of the American Nuclear Society* 106, pp. 662–665.

- McMullan, G. A. Faruqi, R Henderson, N Guerrini, R Turchetta, A Jacobs, and G Van Hoften (2009). “Experimental observation of the improvement in MTF from backthinning a CMOS direct electron detector”. In: *Ultramicroscopy* 109(9), pp. 1144–1147. DOI: 10.1016/j.ultramic.2009.05.005.
- Mendoza, E, D Cano-Ott, P Romojaro, V Alcayne, P. G. Abia, V Pseudo, L Romero, and R Santorelli (2020). “Neutron production induced by α -decay with Geant4”. In: *Nuclear Instruments and Methods in Physics Research Section A: Accelerators, Spectrometers, Detectors and Associated Equipment* 960, p. 163659. DOI: 10.1016/j.nima.2020.163659.
- Meter Group (2022). *Atmos 41 manual*. URL: http://library.metergroup.com/Manuals/20635_ATMOS41_Manual_Web.pdf.
- Mewaldt, R. A. (2017). *Cosmic Rays*. URL: http://www.srl.caltech.edu/personnel/dick/cos_encyc.html.
- Minzner, R. (1977). “The 1976 standard atmosphere and its relationship to earlier standards”. In: *Reviews of geophysics* 15(3), pp. 375–384. DOI: 10.1029/RG015i003p00375.
- Mitrofanov, I., A. Kozyrev, D. Lisov, A. Vostrukhin, D. Golovin, M. Litvak, A. Malakhov, M. Mokrousov, S. Y. Nikiforov, and A. Sanin (2016). “Active neutron sensing of the Martian surface with the DAN experiment onboard the NASA “Curiosity” Mars rover: Two types of soil with different water content in the Gale crater”. In: *Astronomy Letters* 42(4), pp. 251–259. DOI: 10.1134/S1063773716040058.
- Modzel, G., M. Henske, A. Houben, M. Klein, M. Köhli, P. Lennert, M. Meven, C. Schmidt, U. Schmidt, and W. Schweika (2014). “Absolute efficiency measurements with the ^{10}B based Jalousie detector”. In: *Nuclear Instruments and Methods in Physics Research Section A: Accelerators, Spectrometers, Detectors and Associated Equipment* 743, pp. 90–95. DOI: 10.1016/j.nima.2014.01.007.
- Mollerach, S. and E. Roulet (2018). “Progress in high-energy cosmic ray physics”. In: *Progress in Particle and Nuclear Physics* 98, pp. 85–118. DOI: 10.1016/j.pnpnp.2017.10.002.
- Montag, B. W., S. L. Bellinger, N. S. Edwards, J. Lage, K. A. Nelson, L. C. Henson, and D. S. McGregor (2019). “Recent progress in the commercialization of the Li Foil multi-wire proportional counter neutron detectors”. In: *Radiation Physics and Chemistry* 155, pp. 158–163. DOI: 10.1016/j.radphyschem.2018.08.003.
- Moraal, H and K. McCracken (2012). “The time structure of ground level enhancements in solar cycle 23”. In: *Space Science Reviews* 171(1), pp. 85–95. DOI: 10.1007/s11214-011-9742-7.
- Nesterenok, A. (2013). “Numerical calculations of cosmic ray cascade in the Earth’s atmosphere - Results for nucleon spectra”. In: *Nuclear Instruments and Methods in Physics Research B* 295, pp. 99–106. DOI: 10.1016/j.nimb.2012.11.005.
- Nesterenok, A. and V. Naidenov (2012). “In situ formation of cosmogenic ^{14}C by cosmic ray nucleons in polar ice”. In: *Nuclear Instruments and Methods in Physics Research Section B: Beam Interactions with Materials and Atoms* 270, pp. 12–18. DOI: 10.1016/j.nimb.2011.09.026.
- Nikolić, S., G. Van De Ven, K. Heng, D. Kupko, B. Husemann, J. C. Raymond, J. P. Hughes, and J. Falcón-Barroso (2013). “An integral view of fast shocks around supernova 1006”. In: *Science* 340(6128), pp. 45–48. DOI: 10.1126/science.1228297.
- Oraby, M, K Verghese, and R. Gardner (1990). “Investigation of an improved-sensitivity neutron-porosity oil-well logging tool”. In: *Nuclear Instruments and Methods in Physics Research Section A: Accelerators, Spectrometers, Detectors and Associated Equipment* 299(1-3), pp. 674–681. DOI: 10.1016/0168-9002(90)90868-7.

A. Bibliography

- Particle Data Group (2020). “Properties of the neutron”. In: *Progress of Theoretical and Experimental Physics* 2020(8), p. 083C01.
- Paul, H. and A. Schinner (2001). “An empirical approach to the stopping power of solids and gases for ions from 3Li to 18Ar”. In: *Nuclear Instruments and Methods in Physics Research Section B: Beam Interactions with Materials and Atoms* 179(3), pp. 299–315. DOI: [10.1016/S0168-583X\(01\)00576-6](https://doi.org/10.1016/S0168-583X(01)00576-6).
- Pfotzer, G. (1936). “Dreifachkoinzidenzen der Ultrastrahlung aus vertikaler Richtung in der Stratosphäre”. In: *Zeitschrift für Physik* 102(1), pp. 23–40. DOI: [10.1007/BF01336829](https://doi.org/10.1007/BF01336829).
- Piscitelli, F. (2013). “Boron-10 layers, Neutron Reflectometry and Thermal Neutron Gaseous Detectors”. PhD thesis. Università degli Studi di Perugia. 186 pp. URL: <https://arxiv.org/pdf/1406.3133.pdf>.
- Raymond, A., A. Inglis, and M. Zreda (2019). “Advances in CRNS with Lithium-Based Neutron Detectors.” In: *Geophysical Research Abstracts*. Vol. 21.
- Rivera Villarreyes, C., G. Baroni, and S. E. Oswald (2011). “Integral quantification of seasonal soil moisture changes in farmland by cosmic-ray neutrons”. In: *Hydrology and Earth System Sciences* 15(12), pp. 3843–3859. DOI: [10.5194/hess-15-3843-2011](https://doi.org/10.5194/hess-15-3843-2011).
- Rosolem, R., W. Shuttleworth, M. Zreda, T. Franz, X. Zeng, and S. Kurc (2013). “The Effect of Atmospheric Water Vapor on Neutron Count in the Cosmic-Ray Soil Moisture Observing System”. In: *Journal of Hydrometeorology* 14(5), pp. 1659–1671. DOI: [10.1175/JHM-D-12-0120.1](https://doi.org/10.1175/JHM-D-12-0120.1).
- Salminen, R., M. Batista, M. Bidovec, A. Demetriades, B. De Vivo, W. De Vos, M. Duris, A. Gilucis, and T. Tarvainen (2005). *Geochemical Atlas of Europe, Part 1, Background Information, Methodology and Maps*. Geological Survey of Finland. ISBN: 951-690-921-3. URL: <http://weppi.gtk.fi/publ/foregsatlas/index.php>.
- Salvat, F. (2015). “The PENELOPE code system. Specific features and recent improvements”. In: ed. by EDP, S. Vol. 82. Barcelona, Spain: Elsevier BV, pp. 98–109. DOI: [10.1016/j.anucene.2014.08.007](https://doi.org/10.1016/j.anucene.2014.08.007).
- Sato, T., H. Yasuda, K. Niita, A. Endo, and L. Sihver (2008). “Development of PARMA: PHITS-based Analytical Radiation Model in the Atmosphere”. In: *Radiation Research* 170(2), pp. 244–259. DOI: [10.1667/RR1094.1](https://doi.org/10.1667/RR1094.1).
- Sato, T. (2015). “Analytical model for estimating terrestrial cosmic ray fluxes nearly anytime and anywhere in the world: Extension of PARMA/EXPACS”. In: *PLoS one* 10(12), e0144679. DOI: [10.1371/journal.pone.0144679](https://doi.org/10.1371/journal.pone.0144679).
- (2016). “Analytical model for estimating the zenith angle dependence of terrestrial cosmic ray fluxes”. In: *PLoS one* 11(8), e0160390. DOI: [10.1371/journal.pone.0160390](https://doi.org/10.1371/journal.pone.0160390).
- Schattan, P., G. Baroni, S. E. Oswald, J. Schöber, C. Fey, C. Kormann, M. Huttenlau, and S. Achleitner (2017). “Continuous monitoring of snowpack dynamics in alpine terrain by aboveground neutron sensing”. In: *Water Resources Research* 53(5), pp. 3615–3634. DOI: [10.1002/2016WR020234](https://doi.org/10.1002/2016WR020234).
- Schattan, P., M. Köhli, M. Schrön, G. Baroni, and S. E. Oswald (2019). “Sensing area-average snow water equivalent with cosmic-ray neutrons: The influence of fractional snow cover”. In: *Water Resources Research* 55(12), pp. 10796–10812.
- Schrön, M. et al. (2018). “Cosmic-ray Neutron Rover Surveys of Field Soil Moisture and the Influence of Roads”. In: *Water Resources Research* 54(9), pp. 6441–6459. DOI: [10.1029/2017WR021719](https://doi.org/10.1029/2017WR021719).
- Schrön, M. (2016). “Cosmic-ray neutron sensing and its applications to soil and land surface hydrology: on neutron physics, method development, and soil moisture estimation across scales”. PhD thesis. Universität Potsdam. ISBN: 978-3-8439-3139-7.

- Schrön, M., M. Köhli, L. Scheiffele, J. Iwema, H. R. Bogena, L. Lv, E. Martini, G. Baroni, R. Rosolem, J. Weimar, et al. (2017). “Improving calibration and validation of cosmic-ray neutron sensors in the light of spatial sensitivity”. In: *Hydrology and Earth System Sciences* 21(10), pp. 5009–5030. DOI: [10.5194/hess-21-5009-2017](https://doi.org/10.5194/hess-21-5009-2017).
- Schultz, G., G. Charpak, and F. Sauli (1977). “Mobilities of Positive Ions in some Gas Mixture Used in Proportional and Drift Chambers”. In: *Revue de Physique Appliquée* 12, pp. 67–70. DOI: [10.1051/rphysap:0197700120106700](https://doi.org/10.1051/rphysap:0197700120106700).
- Serafini, A., M. Albéri, E. Chiarelli, M. Montuschi, K. G. C. Raptis, V. Strati, and F. Mantovani (2020). “Discriminating irrigation and rainfall with proximal gamma-ray spectroscopy”. In: *2020 IEEE International Workshop on Metrology for Agriculture and Forestry (MetroAgriFor)*. IEEE, pp. 191–195. DOI: [10.1109/MetroAgriFor50201.2020.9277556](https://doi.org/10.1109/MetroAgriFor50201.2020.9277556).
- Serber, R. (1947). “Nuclear reactions at high energies”. In: *Physical Review* 72(11), p. 1114. DOI: [10.1103/PhysRev.72.1114](https://doi.org/10.1103/PhysRev.72.1114).
- Sharma, A. (1998). “Properties of some gas mixtures used in tracking detectors”. In: *SLAC* 16(3). DOI: [10.1.1.205.4683](https://doi.org/10.1.1.205.4683).
- Shea, D. A. and D. L. Morgan (2010). *The helium-3 shortage: Supply, demand, and options for congress*.
- Shibata, K. et al. (2011). “JENDL-4.0: A New Library for Nuclear Science and Engineering”. In: *Journal of Nuclear Science and Technology* 48(1), pp. 1–30. DOI: [10.1080/18811248.2011.9711675](https://doi.org/10.1080/18811248.2011.9711675).
- Simmer, G, V Mares, E Weitzenegger, and W Rühm (2010). “Iterative unfolding for Bonner sphere spectrometers using the MSANDB code—Sensitivity analysis and dose calculation”. In: *Radiation measurements* 45(1), pp. 1–9. DOI: [10.1016/j.radmeas.2009.03.023](https://doi.org/10.1016/j.radmeas.2009.03.023).
- Smart, D. F. and M. A. Shea (2004). “A review of geomagnetic cutoff rigidities for earth-orbiting spacecraft”. In: *Advances in Space Research* 36, pp. 2012–2020. DOI: [10.1016/j.nimb.2012.11.005](https://doi.org/10.1016/j.nimb.2012.11.005).
- Smith, A., P. Fields, and J. Roberts (1957). “Spontaneous fission neutron spectrum of Cf 252”. In: *Physical Review* 108(2), p. 411. DOI: [10.1103/PhysRev.108.411](https://doi.org/10.1103/PhysRev.108.411).
- Squires, G. (1978). *Introduction to the Theory of Thermal Neutron Scattering*.
- Stevanato, L., G. Baroni, Y. Cohen, F. Cristiano Lino, S. Gatto, M. Lunardon, F. Marinello, S. Moretto, and L. Morselli (2019). “A Novel Cosmic-Ray Neutron Sensor for Soil Moisture Estimation over Large Areas”. In: *Agriculture* 9(9), p. 202. DOI: [10.3390/agriculture9090202](https://doi.org/10.3390/agriculture9090202).
- Stevanato, L, G Baroni, S. Oswald, M Lunardon, V Mares, F Marinello, S Moretto, M Polo, P Sartori, P Schattan, et al. (2022). “An alternative incoming correction for Cosmic-Ray Neutron Sensing observations using local muon measurement”. In: *Geophysical Research Letters*, e2021GL095383. DOI: [10.1029/2021GL095383](https://doi.org/10.1029/2021GL095383).
- Stowell, P, S Fargher, C Steer, and L. Thompson (2021). “Scintillating thermal neutron detectors for cosmic ray soil moisture monitoring”. In: *Journal of Instrumentation* 16(11), P11039. DOI: [10.1088/1748-0221](https://doi.org/10.1088/1748-0221).
- Tian, Z., Z. Li, G. Liu, B. Li, and T. Ren (2016). “Soil water content determination with cosmic-ray neutron sensor: Correcting aboveground hydrogen effects with thermal/fast neutron ratio”. In: *Journal of Hydrology* 540, pp. 923–933. DOI: [10.1016/j.jhydrol.2016.07.004](https://doi.org/10.1016/j.jhydrol.2016.07.004).
- Tomasi, C. (1984). “Vertical distribution features of atmospheric water vapor in the Mediterranean, Red Sea, and Indian Ocean”. In: *Journal of Geophysical Research: Atmospheres* 89(D2), pp. 2563–2566. DOI: [10.1029/JD089iD02p02563](https://doi.org/10.1029/JD089iD02p02563).
- Truebner GmbH (2021). *SMT100 Soil Moisture Sensor - Flyer*. URL: https://www.truebner.de/download/SMT100_Flyer_EN.pdf.

A. Bibliography

- Van Bavel, C., N. Underwood, and R. Swanson (1956). "Soil moisture measurement by neutron moderation". In: *Soil Science* 82(1), pp. 29–42.
- Vergopolan, N., S. Xiong, L. Estes, N. Wanders, N. W. Chaney, E. F. Wood, M. Konar, K. Caylor, H. E. Beck, N. Gatti, et al. (2021). "Field-scale soil moisture bridges the spatial-scale gap between drought monitoring and agricultural yields". In: *Hydrology and Earth System Sciences* 25(4), pp. 1827–1847. DOI: [10.5194/hess-25-1827-2021](https://doi.org/10.5194/hess-25-1827-2021).
- Vourvopoulos, G and P. Womble (2001). "Pulsed fast/thermal neutron analysis: a technique for explosives detection". In: *Talanta* 54(3), pp. 459–468. DOI: [10.1016/S0039-9140\(00\)00544-0](https://doi.org/10.1016/S0039-9140(00)00544-0).
- WMO (2014). *Guide to Meteorological Instruments and Methods of Observation (CIMO Guide, WMO-No. 8*.
- Wallbank, J. R., S. J. Cole, R. J. Moore, S. R. Anderson, and E. J. Mellor (2021). "Estimating snow water equivalent using cosmic-ray neutron sensors from the COSMOS-UK network". In: *Hydrological Processes* 35(5), e14048. DOI: [10.1002/hyp.14048](https://doi.org/10.1002/hyp.14048).
- Wang, Y.-F., V Balic, G Gratta, A Fasso, S Roesler, and A Ferrari (2001a). "Predicting neutron production from cosmic-ray muons". In: *Physical Review D* 64(1), p. 013012. DOI: [10.1103/PhysRevD.64.013012](https://doi.org/10.1103/PhysRevD.64.013012).
- (2001b). "Predicting neutron production from cosmic-ray muons". In: *Physical Review D* 64(1), p. 013012. DOI: [10.1103/PhysRevD.64.013012](https://doi.org/10.1103/PhysRevD.64.013012).
- Watanabe, Y. et al. (2011). "Status of JENDL High Energy File". In: *Journal of the Korean Physical Society* 59(2(3)), pp. 1040–1045. DOI: [10.3938/jkps.59.1040](https://doi.org/10.3938/jkps.59.1040).
- Waters, L. S., G. W. McKinney, J. W. Durkee, M. L. Fensin, J. S. Hendricks, M. R. James, R. C. Johns, and D. B. Pelowitz (2007). "The MCNPX Monte Carlo radiation transport code". In: *AIP conference Proceedings*. Vol. 896. 1. American Institute of Physics, pp. 81–90. DOI: [10.1063/1.2720459](https://doi.org/10.1063/1.2720459).
- Weimar, J., M. Köhli, C. Budach, and U. Schmidt (2020). "Large-Scale Boron-Lined Neutron Detection Systems as a ^3He Alternative for Cosmic Ray Neutron Sensing". In: *Frontiers in Water* 2, p. 16. DOI: [10.3389/frwa.2020.00016](https://doi.org/10.3389/frwa.2020.00016).
- Werner, C. J., J. S. Bull, C. J. Solomon, F. B. Brown, G. W. McKinney, M. E. Rising, D. A. Dixon, R. L. Martz, H. G. Hughes, L. J. Cox, et al. (2017). *MCNP® USER'S MANUAL Code Version 6.2*. Tech. rep. Los Alamos National Lab.(LANL), Los Alamos, NM (United States).
- Western, A. W., S.-L. Zhou, R. B. Grayson, T. A. McMahon, G. Blöschl, and D. J. Wilson (2004). "Spatial correlation of soil moisture in small catchments and its relationship to dominant spatial hydrological processes". In: *Journal of Hydrology* 286(1-4), pp. 113–134. DOI: [10.1016/j.jhydrol.2003.09.014](https://doi.org/10.1016/j.jhydrol.2003.09.014).
- Whan, K., J. Zscheischler, R. Orth, M. Shongwe, M. Rahimi, E. O. Asare, and S. I. Seneviratne (2015). "Impact of soil moisture on extreme maximum temperatures in Europe". In: *Weather and Climate Extremes* 9, pp. 57–67. DOI: [10.1016/j.wace.2015.05.001](https://doi.org/10.1016/j.wace.2015.05.001).
- Wirtz, K. and K. H. Beckurts (1964). *Neutron physics*. Springer-Verlag. ISBN: 978-3-642-87614-1.
- Woolson, W. and M. Gritzner (1980). "Evaluation Models for Uranium Exploration by Active Neutron Logging". In: *Nuclear Technology* 49(3), pp. 410–425. DOI: [10.13182/NT80-A17689](https://doi.org/10.13182/NT80-A17689).
- Yariv, Y. and Z. Fraenkel (1979). "Intranuclear cascade calculation of high-energy heavy-ion interactions". In: *Physical Review C* 20(6), p. 2227. DOI: [10.1103/PhysRevC.20.2227](https://doi.org/10.1103/PhysRevC.20.2227).
- Yasin, Z. and M. I. Shahzad (2010). "From conventional nuclear power reactors to accelerator-driven systems". In: *Annals of Nuclear Energy* 37(2), pp. 87–92. DOI: [10.1016/j.anucene.2009.11.003](https://doi.org/10.1016/j.anucene.2009.11.003).

- Ziegler, J. F. (1996). "Terrestrial cosmic rays". In: *IBM journal of research and development* 40(1), pp. 19–39. DOI: [10.1147/rd.401.0019](https://doi.org/10.1147/rd.401.0019).
- Zreda, M., W. J. Shuttleworth, C. Zeng, C. Zweck, D. Desilets, T. Franz, and R. Rosolem (2012). "COSMOS: the COsmic-ray Soil Moisture Observing System". In: DOI: [10.5194/hess-16-4079-2012](https://doi.org/10.5194/hess-16-4079-2012).
- Zreda, M., D. Desilets, T. Ferré, and R. L. Scott (2008). "Measuring soil moisture content non-invasively at intermediate spatial scale using cosmic-ray neutrons". In: *Geophysical research letters* 35(21). DOI: [10.1029/2008GL035655](https://doi.org/10.1029/2008GL035655).
- Zweck, C., M. Zreda, and D. Desilets (2013). "Snow shielding factors for cosmogenic nuclide dating inferred from Monte Carlo neutron transport simulations". In: *Earth and Planetary Science Letters* 379, pp. 64–71. DOI: [10.1016/j.epsl.2013.07.023](https://doi.org/10.1016/j.epsl.2013.07.023).

B Appendix

B.1 Thermal neutron intensities 500 cm below the soil surface

Here, a supplementary plot of thermal neutron intensities 500 cm below the soil surface is shown that corresponds to section 6.2. The FDR data shows almost no change in soil moisture except for a slow wetting that amounts to a change of less than 1 Vol-%. The CRNS retrieved data exhibits much higher variability. The data was recorded subsequent to the data sets shown in section 6.2, thus the dynamics of this data set cannot be compared to those. The count rate of the detector at this depth was as low as 3–12 counts per hour. Hence, the dynamic shown here is mostly statistical noise.

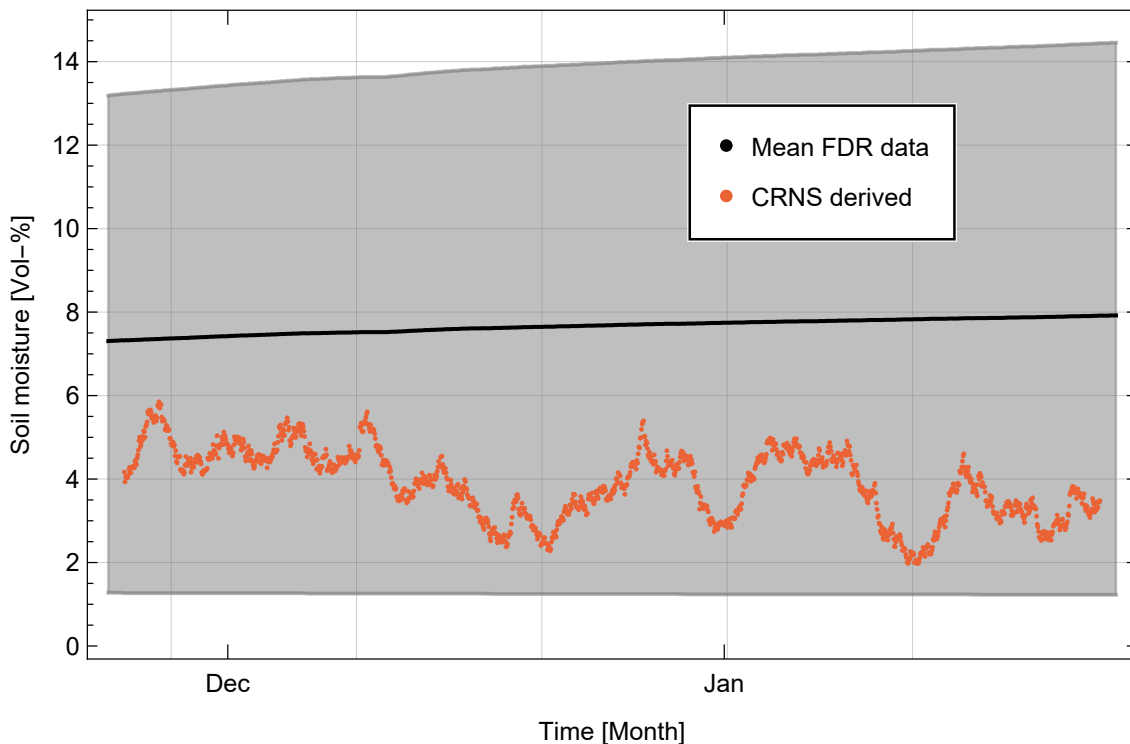


Figure B.1: Measured soil moisture dynamics at 500 cm below the soil surface corresponding to ≈ 487 cm or 810 g/cm^2 actual probing depth of the neutron detector. See caption of Fig. 6.12 for more information.

B.2 Fitting of neutron dynamics above snow covered soils.

Parameter fitting that describe the detector's footprint

Five parameters of Eq. 7.1 show dependencies on the SWE value of the snow cover. Here, it is shown how these parameters evolve with SWE along with the fitted functions described by Eq. 7.2–Eq. 7.7. Although some of them are also influenced by the hydrogen content in air and the soil, these second order effects are not shown here.

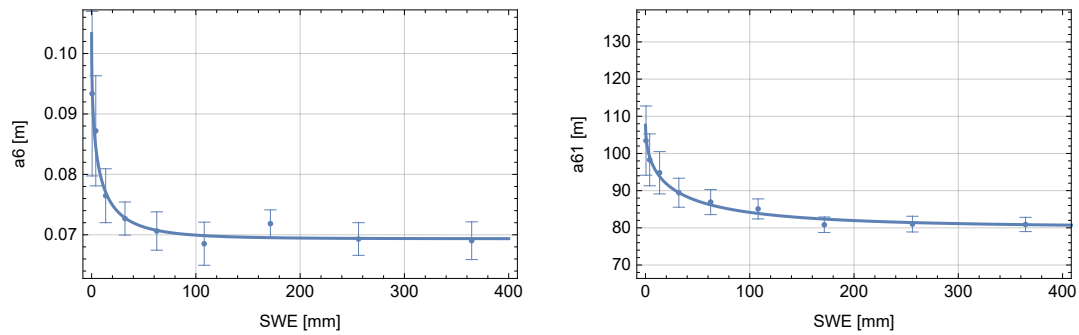


Figure B.2: Fit of parameters a_6 and a_{61} in Eq. 7.1 that describe the far field of the radial footprint function.

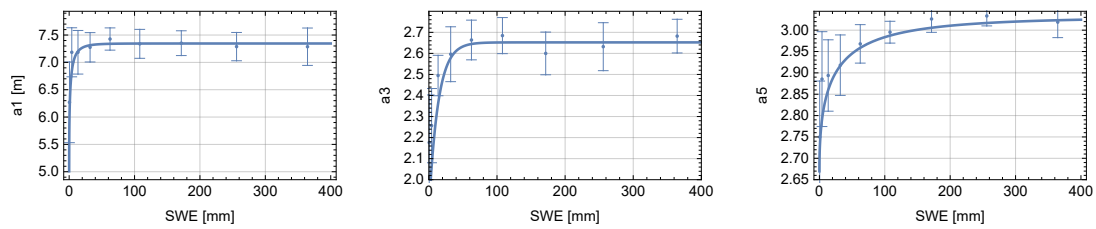


Figure B.3: Fit of parameters a_1 , a_3 and a_5 in Eq. 7.10 that describe the near field of the radial footprint function.

B.2.1 Detected neutron intensities above snow covered soil

Here, the fitting procedure in section 7.2.2 is shown in more detail. Fig. B.4 reveals that a simple hyperbola is not suitable to describe the epithermal intensity above snow covered soils. The transfer function takes the form

$$N(h_{\text{swe}}, h_{\text{sm}}) = b_1 \frac{b_2 + b_3 h_{\text{swe}}}{b_2 + h_{\text{swe}}} \left(1 + b_4 \text{Exp} \left[-\frac{h_{\text{swe}}}{b_5} \right] \right) \quad (\text{B.1})$$

already shown in the referenced chapter. First $N(h_{\text{swe}})$ was fitted for all soil moisture values (1, 3, 6, 10, 12, 15, 20, 25, 30, 40, 50 Vol-%). The resulted parameter arrays for b_i were subsequently fitted against the soil moisture content in order to attain $N(h_{\text{swe}}, h_{\text{sm}})$. The fits of b_i against soil moisture content describing the hyperbola are shown in Fig. B.5 and those determining the exponential part in Fig. B.6.

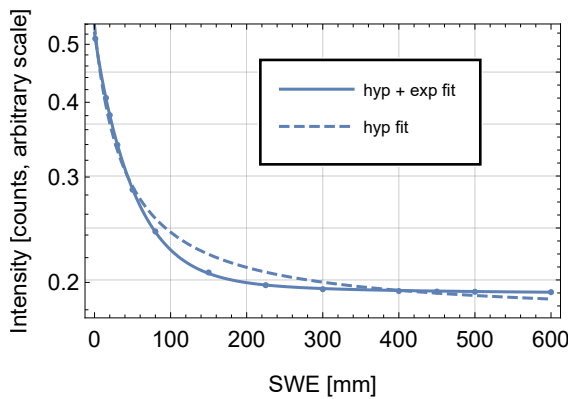


Figure B.4: Fit of a hyperbola as suggested by Schattan et al., 2017 and using Eq. 7.10 that adds an exponential term. The data is taken from a simulation run featuring 10 Vol-% soil moisture content.

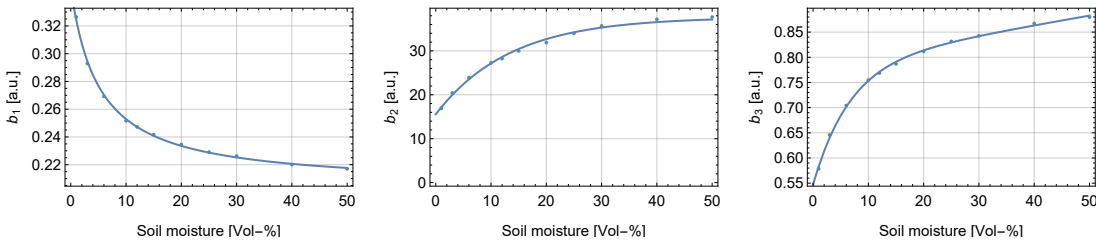


Figure B.5: Fit of parameters b_1 – b_3 in Eq. 7.10 that describe the hyperbolic term.

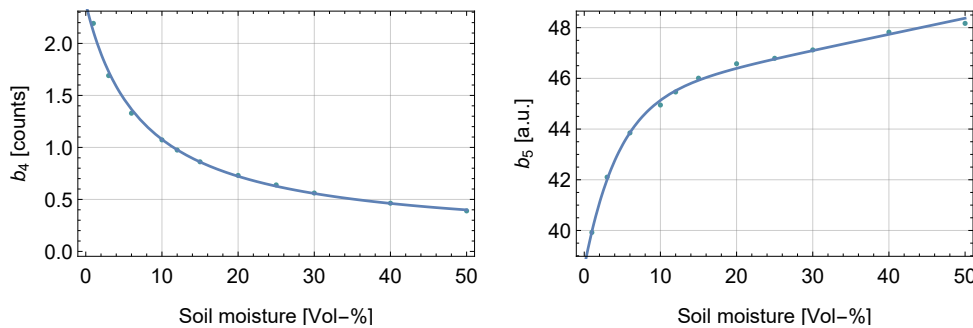


Figure B.6: Fit of parameters b_4 – b_5 in Eq. 7.10 that describe the exponential term.

B.3 Neutron counter and copper foil

Fig. B.7, left shows a high-purity SE-copper foil which was coated with boron-carbide via sputter deposition. This technique allows for a layer thickness precision of the coating on the order of few per cent. Fig. B.7, right displays a proportional counter designed and used for this study. Its setup is described in more detail in section 9.1. The inlet for the counting gas is on the rear. On the front lid a hermetically sealed MHV high voltage connector is placed that connects the wire of the proportional counter to the readout electronics. In order to guarantee a gas-proof sealing ISO-KF flanges are deployed to connect the tube with the front and rear lid.



Figure B.7: **Left:** High-purity SE-copper foil coated with a 1.5 μm thick B_4C layer. **Right:** Picture of a proportional neutron counter, which is the basis for, both, the stationary and mobile system as described in section 9.1.

C

Acknowledgements

Dieser letzte Teil meiner Dissertation soll in deutsch verfasst sein, um den Menschen, die mich in den letzten 3,5 Jahren wissenschaftlich begleitet und diese Zeit zu einer sehr fröhlichen und interessanten Phase meines Lebens gemacht haben, in meiner Muttersprache nochmal einen großen Dank auszusprechen.

Zuallererst einen großen Dank an Utz Schmidt, der mir als Betreuer immer viel Freiheiten gelassen hat meine Ideen und Vorstellungen zur Forschung zu verwirklichen und trotzdem immer bereit war seine Perspektive auf die Dinge zu teilen und zu diskutieren. Ein großer Dank gebührt auch Markus Köhli als partner in crime in fast allen Belangen meiner wissenschaftlichen Arbeit und für viele zehrende aber fruchtbare Diskussionen. Auch Fabian Allmendinger, Benjamin Brauneis und Matthias Janke haben mir viel Input geliefert bei Diskussionen zu Tisch oder zwischen Tür und Angel.

An der Stelle möchte ich mich auch noch bei Max Riede und Klaus Schneeberger bedanken, dafür, dass sie mir meinen Aufenthalt in Innsbruck ermöglicht und mich vor Ort unterstützt haben. Gleiches gilt für den Rest des alpS Teams die mich mit großer Gastfreundschaft willkommen geheißen haben und für Stefan Achleitner und Pepsi. Natürlich möchte ich mich dabei aber auch vor allem bei Paul Schattan bedanken, der fast eineinhalb Jahre mit mir an Schneemessungen und Simulationen dazu getüftelt hat. Ich finde mittlerweile kann man sagen, dass da auch einiges bei rum kam.

Das Cosmic-Sense Team soll nicht unerwähnt bleiben und vor allem die gute Kooperation der Doktorantengruppe mit Skype meetings und gemeinsamen Forschungsprojekten. Vor allem die gemeinsame Arbeit an der Grundwasserschachtsidee mit Daniel Rasche um 9 Uhr ct war immer ein guter Start in den Tag.

Vielen Dank auch an Benjamin Fersch, Rebecca Gugerli und Martin Schrön für die vielen Ideen und Beiträge zu den SnowFox Simulationen. Vor allem letzterem möchte ich nochmal danke sagen, dass er meine lange Email vor nun schon fast acht Jahren mit einer noch längeren Mail beantwortet und mich damit in dieses Forschungsfeld geführt hat.

Ein großer Dank gebührt auch dem Team der Uni Potsdam und dem FZ Jülich für ihre Wartungsarbeiten und ihren Input zu unserem Detektorsystem. Ihr hattet es nicht immer leicht mit uns, wir dafür Glück mit euch.

Leider werde ich an ein paar Personen, die mich in den letzten Jahren wissenschaftlich begleitet haben genau in diesem Moment nicht denken, davor wahrscheinlich umso mehr. Fühlt euch bedankt.